New methods for the detection and characterization of exoplanets

Thesis by
Jorge Llop-Sayson

In Partial Fulfillment of the Requirements for the
Degree of
Doctor of Philosophy in Physics

Caltech

CALIFORNIA INSTITUTE OF TECHNOLOGY
Pasadena, California

2022
Defended October 13, 2021

Jorge Llop-Sayson
ORCID: 0000-0002-3414-784X

ACKNOWLEDGEMENTS

First, I would like to thank my advisor, Dimitri Mawet. He has fostered a fantastic research environment that I have been honoured to be part of. These have been some wonderful years. I couldn't have asked for a better advisor. Thank you to Nem Jovanovic, this thesis would look very different without him. Thank you as well to AJ Riggs for great mentoring and also for fighting the JPL bureaucracy for me. I would also like to thank Chas Beichman for giving me the opportunity to work with him in the α Cen project. I would like to thank all the postdocs who have mentored me, especially Garreth Ruane, and also: Jason Wang, Marie Ygouf, and Elodie Choquet. Thank you to all the collaborators and friends for all the excellent conversations, at Caltech or at conferences, and all the encouragement. To name some: Dan Echeverri, Jackie Pezzato, Jacques Delorme, Carl Coker, Niyati Desai, JB Ruffio, Neelay Fruitwala, Camilo Mejia-Prada, Hari Subedi, and Kevin Fogarty. I have been part of an amazing community of remarkable people.

I would like to thank the Caltech PMA division and Physics department. This great department received me and helped me find a home in Cahill. Thank you also to the Caltech international offices filled with wonderful people always compassionate and willing to help.

I would also like to thank all the folks at Goddard. Special word of thanks to Mike McElwain, a fantastic mentor. I must also thank Karl Stapelfeldt, who backed the IFS at Goddard and pointed me to Dimitri.

To the friends I made during these years: thank you for all the climbing evenings, Sierras adventures, backyard brunches, paellas, and dinners. My friends at Caltech are great scientists and such wonderful people. To all my friends around the LA area, in particular the Dominican community in Eagle Rock. Special mention to Tara Causland, Dan Roberts, Fr. Michael Chaberek, OP, Stephanie Breunig, Brian Garcia.

To my parents and brothers. For all the love.

To Hayley, the first Dr. Llop. From all the blessings mentioned here, you are my favourite one.

ABSTRACT

Advancements in detection technologies have allowed the discovery of thousands of exoplanets. These discoveries have revolutionized our understanding of the Universe; not only are planets ubiquitous, but the planetary systems they populate are as diverse as the complex processes that govern their formation allow. This thesis compiles several studies on the development and application of exoplanet detection and characterization methods, in particular for direct imaging and spectroscopy. From all the planets discovered to date, only a marginal portion have been imaged. This is due to the limited access of high contrast instruments into the parameter space where most exoplanets habitate. Developments in high contrast are key to reaching a full understanding of the exoplanet population. In particular, direct methods allow for an effective characterization of the atmospheric compositions, making it possible to probe exoplanet atmospheres in search of biosignatures.

A sure pathway to enhance exoplanet characterization capabilities is by taking full advantage of synergies between detection methods. In Chapter 2 these synergies are explored in the context of ϵ Eridani's elusive companion: three different methods are combined to constrain its mass and orbital parameters. Combining astrometry, radial velocity, and direct imaging data offers a complementarity that enhances the overall constraining power. In Chapter 3, the α Centauri system is reviewed regarding the possibility of imaging an exoplanet with the JWST observatory in the infrared. The following chapters deal with technological development for high contrast imaging and spectroscopy instruments. In Chapter 4 a coronagraph design study is presented in which new design tools are discussed and evaluated, demonstrating better coronagraph performance. In this chapter the case study is the Nancy Grace Roman Space Telescope Coronagraph Instrument, in which its heavily obstructed pupil constitutes a huge challenge for coronagraph design. Along the same lines, Chapter 5 presents the technology demonstration of the apodized vortex coronagraph (AVC). The AVC is a coronagraph concept that effectively deals with the telescope pupil discontinuities. Chapters 6 and 7 introduce a novel wavefront sensing and control algorithm for the high contrast concept of a fiber injection unit in the image plane of a coronagraph. A single mode fiber (SMF) is placed in the position of the planet to extract its light and feed it into a spectrograph. Our algorithm leverages the synergies of the coronagraph and the mode selectivity of the SMF to maximize the signal-to-noise ratio of the planet.

PUBLISHED CONTENT AND CONTRIBUTIONS

Llop-Sayson, J., C. T. Coker, et al. (2021). "Laboratory Demonstration of Wavefront Control through a Single Mode Fiber over a 20% Bandwidth for the Characterization of Exoplanet Atmospheres". In: *Submitted to Journal of Astronomical Telescopes, Instruments, and Systems*.
I performed the simulations, prepared and performed the laboratory experiments, and prepared the manuscript.

Llop-Sayson, J., C. Kappel, et al. (2021). "New method to achieve the proper polarization state for a vector vortex coronagraph". In: *Techniques and Instrumentation for Detection of Exoplanets X*. Ed. by S. B. Shaklan and G. J. Ruane. Vol. 11823. International Society for Optics and Photonics. SPIE, pp. 230–237. URL: `https://doi.org/10.1117/12.2594871`.
I developed the method and tested it in the laboratory. I prepared the manuscript.

Llop-Sayson, J., A. J. E. Riggs, et al. (2021). "Coronagraph Design with the Electric Field Conjugation Algorithm". In: *Submitted to Journal of Astronomical Telescopes, Instruments, and Systems*.
I participated in the conception of the methods presented, performed all the simulations with the FALCO code by A J Riggs (of which I am a contributor), and prepared the manuscript.

Llop-Sayson, J., J. J. Wang, J.-B. Ruffio, D. Mawet, S. Blunt, O. Absil, C. Bond, C. Brinkman, B. P. Bowler, M. Bottom, A. Chontos, P. A. Dalba, B. J. Fulton, S. Giacalone, M. Hill, L. A. Hirsch, A. W. Howard, H. Isaacson, M. Karlsson, J. Lubin, A. Madurowicz, K. Matthews, E. Morris, M. Perrin, B. Ren, M. Rice, L. J. Rosenthal, G. Ruane, R. Rubenzahl, H. Sun, N. Wallack, J. W. Xuan, and M. Ygouf (Oct. 2021). "Constraining the Orbit and Mass of epsilon Eridani b with Radial Velocities, Hipparcos IAD-Gaia DR2 Astrometry, and Multiepoch Vortex Coronagraphy Upper Limits". In: *The Astronomical Journal* 162.5. DOI: `10.3847/1538-3881/ac134a`. URL: `https://doi.org/10.3847/1538-3881/ac134a`.
I performed the orbit fits using my own code based on code by J. Wang and J.-B. Ruffio, and orbit fitting code, and prepared the manuscript.

Beichman, C. et al. (Jan. 2020). "Searching for Planets Orbiting α Cen A with the James Webb Space Telescope". In: *Publications of the Astronomical Society of the Pacific* 132.1007. DOI: `10.1088/1538-3873/ab5066`. arXiv: `1910.09709 [astro-ph.IM]`.
My contribution to this work was on the simulation of the observations and the development of data reduction strategies. I simulated the MIRI observations using the MIRISim IDL tool. A wide variety of plausible planet configurations were considered: several planet sizes, temperatures, and positions were explored. I modified the MIRISim code to account for telescope jitter and wavefront error

evolution due to thermal changes and rapid solar angle change. To assess the sensitivity of the observations I performed post-processing on the simulated products. I used PCA while taking advantage of the diversity provided by the short exposure frames. My contributions led to the expected sensitivity of the observations presented in the paper, and the observation strategy definition, namely pointing out the importance of the change of solar angle of the telescope to mitigate wavefront error changes.

Llop-Sayson, J., N. Jovanovic, et al. (2020). "Wavefront control experiments with a single mode fiber at the High-Contrast Spectroscopy Testbed for Segmented Telescopes (HCST)". In: *Space Telescopes and Instrumentation 2020: Optical, Infrared, and Millimeter Wave*. Ed. by M. Lystrup et al. Vol. 11443. International Society for Optics and Photonics. SPIE, pp. 517–523. URL: `https://doi.org/10.1117/12.2562973`.
I prepared and performed the laboratory experiments, and prepared the manuscript.

Llop-Sayson, J., G. Ruane, D. Mawet, N. Jovanovic, C. T. Coker, et al. (Feb. 2020). "High-contrast Demonstration of an Apodized Vortex Coronagraph". In: *The Astronomical Journal* 159.3. DOI: `10.3847/1538-3881/ab6329`. URL: `https://doi.org/10.3847`.
I performed the simulations, prepared and performed the laboratory experiments, and prepared the manuscript.

Llop-Sayson, J., G. Ruane, N. Jovanovic, et al. (2019). "The high-contrast spectroscopy testbed for segmented telescopes (HCST): new wavefront control demonstrations". In: *Techniques and Instrumentation for Detection of Exoplanets IX*. Ed. by S. B. Shaklan. Vol. 11117. International Society for Optics and Photonics. SPIE, pp. 610–619. URL: `https://doi.org/10.1117/12.2530670`.
I prepared and performed the laboratory experiments, and prepared the manuscript.

Llop-Sayson, J., G. Ruane, D. Mawet, N. Jovanovic, B. Calvin, et al. (2019). "Demonstration of an electric field conjugation algorithm for improved starlight rejection through a single mode optical fiber". In: *Journal of Astronomical Telescopes, Instruments, and Systems* 5.1. DOI: `10.1117/1.JATIS.5.1.019004`. URL: `https://doi.org/10.1117/1.JATIS.5.1.019004`.
I developed the mathematical formalism of the algorithm presented. I performed the simulations, prepared and performed the laboratory experiments, and prepared the manuscript.

Llop-Sayson, J., D. Mawet, et al. (2018). "Wavefront control for minimization of speckle coupling into a fiber injection unit based on the electric field conjugation algorithm". In: *Adaptive Optics Systems VI*. Ed. by L. M. Close, L. Schreiber, and D. Schmidt. Vol. 10703. International Society for Optics and Photonics. SPIE, pp. 1529–1537. URL: `https://doi.org/10.1117/12.2313657`.
I performed the simulations, prepared and performed the laboratory experiments, and prepared the manuscript.

TABLE OF CONTENTS

LIST OF ILLUSTRATIONS

LIST OF TABLES

Chapter 1

INTRODUCTION

Our predecessors in ancient Mesopotamia were the first to use arithmetic and geometry in order to predict patterns and celestial events of the night. Interestingly, their primitive knowledge was never solely linked to practical purposes, such as season prediction and cartography; rather, the pursuit of knowledge was an integral part of their culture as well as their societal attitudes and dynamism. This behaviour is not exclusive to the people in Mesopotamia and those who were influenced by it, like the ancient Greeks and Egyptians. The Mayans independently developed a complex system of mathematics and primitive astronomy. By measuring the casting of shadows and using sophisticated calendars, they were able to measure the tropical year and the position of Venus, among many other events. And like their counterparts across the ocean, the seeking of knowledge was not merely a survival skill, it was central to their civilization. We inevitably follow in their footsteps since the ambition of unveiling the secrets of the cosmos is part of our nature and not something we can escape from.

There is one the fundamental question that has haunted humanity for millennia: are we alone in the Universe? Only recently do we seem to know what the path to answering this looks like. Indeed, since the invention of the telescope and the development of calculus, the field of astronomy has advanced in giant steps. Mathematical models and precise observations have given us an ever-growing understanding of the Universe. In 1992, the first planetary system outside the solar system was discovered. By precisely measuring the pulse timing of a pulsar, Wolszczan et al. (1992) were able to infer the presence of two planets orbiting the pulsar. In 1995, Mayor and Queloz (1995) discovered a Jupiter-mass planet orbiting a Sun-like star by inferring its presence "from observations of periodic variations in the stars radial velocity". Interest in the subject of extra-solar planets (or exoplanets) has since exponentially increased, bringing more brilliant minds and talent to the field. Subsequently, rapid advancements in discovery methods and overall technology development have put us at reach of answering some of the fundamental questions in astrophysics.

In this thesis I present a synthesis of my work on the advancement of methods and technologies for detection and characterization of exoplanets. Every chapter is an adaptation of a scientific article, published or in the process of submission, in which I am first author or have made a significant contribution. In this chapter I intend to give an overview of the state of the exoplanet science field, with a particular emphasis on direct imaging techniques.

1.1 Exoplanet demographics

To this date there are over 4500 exoplanets confirmed. While this may seem like plenty, the real number, in our galaxy alone, is likely inapprehensible (I direct the future reader to check the current number to see how we are doing: https://exoplanets.nasa.gov/discovery/discoveries-dashboard/). Fig. 1.1 shows all the exoplanet detections to date, each labeled with its detection technique, thus illustrating how our knowledge is somewhat biased by the technology available. Different detection techniques have different limited reach into the star and planet characteristics parameter space. For instance, transit photometry, the most successful detection technique, has access to short orbit periods of planets that are relatively big compared to their host star. Indeed, the vast majority of planets in Fig. 1.1 are at low separations. The Solar System, the only planetary system known until only a few years ago, has half of its planets orbiting at more than 5 AU.

Since the first exoplanet discovery in 1992, astronomers have been unveiling a surprising truth: there is not much to extrapolate from the Solar System. Planetary systems are very diverse. Planets seem to form in all kinds of stellar systems; they are commonly found around M-dwarfs (Dressing et al., 2015; Sabotta et al., 2021), they form around giant stars (Jones et al., 2014), and are even found around pulsars (Wolszczan et al., 1992; Bailes et al., 2011). Indeed, most of the known planetary systems are very different from the Solar System. Fig. 1.2 shows a distribution of planets per star versus planet size for periods less than 100 days; sub-Neptunes and super-Earths are the most commonly found types of planets (Fulton, Petigura, Howard, et al., 2017), neither of which can be found in our own system. Only small rocky planets are orbiting close-in in the Solar System. The gap in planet occurrence between 1.5 and 2 $R_{\oplus}$ is due to the physics of planet formation processes. An interesting case in terms of planet formation theory is that of hot Jupiters, i.e. close-in, typically <10 days period, giant, >0.1 M_{Jup}, planets (e.g. Marcy et al. (1996) and Wright, Marcy, et al. (2012)). Their occurrence rate has been a hot topic in exoplanet statistics; transit surveys yield occurrence rates of ~0.4 % (Howard, Marcy, et al., 2012; Zhou et al., 2019), while RV surveys estimate a factor of two higher Mayor, Marmier, et al. (2011). Moe et al. (2019) determined

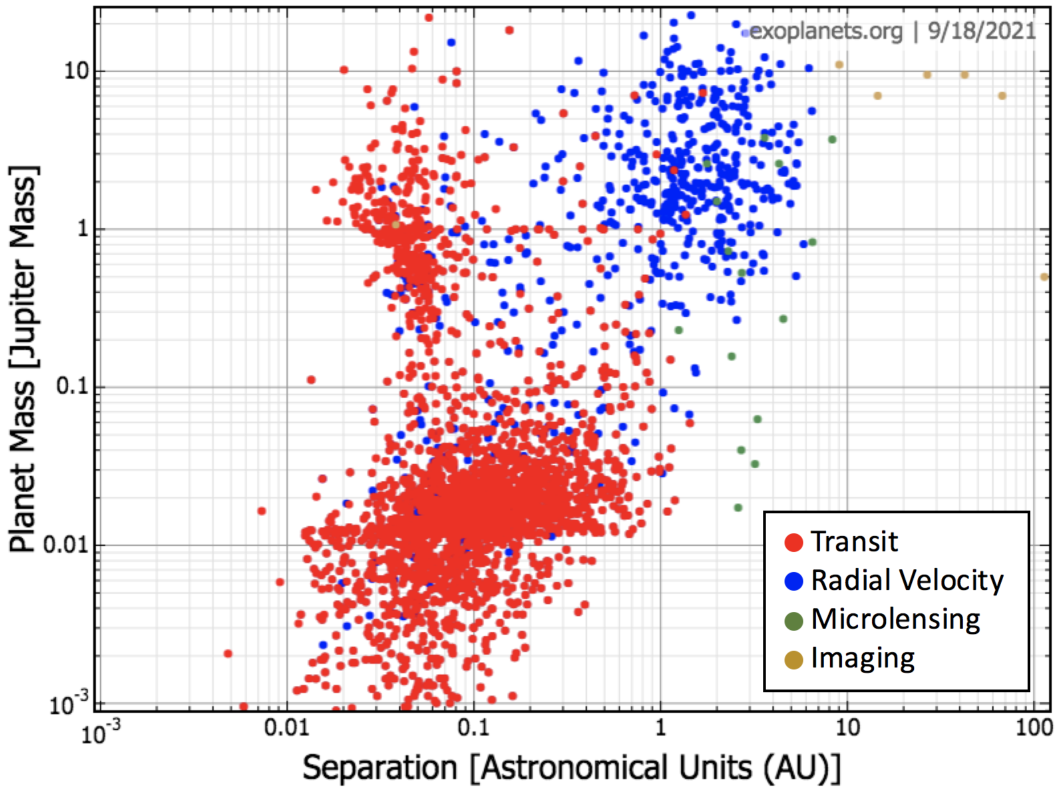

Figure 1.1 Detected exoplanets to date.

that this is probably due to a sample selection issue. Exoplanet occurrence rate in general is hard to constrain given the lack of completeness of the available sample; however, occurrence rates can be corrected and predicted via extrapolation (e.g. Fressin et al. (2013)). Of particular interest is the occurrence rate of rocky planets in the habitable zone of solar type stars, $\eta_\oplus$. Although hardly constrained, current estimates point towards $\eta_\oplus$ ~0.37 (Bryson et al., 2021).

Orbits are very diverse too. The planets in the Solar System roughly orbit in the same plane with small mutual inclination, but there is no evidence that this type of configuration is commonplace (Tremaine et al., 2012). Many of the discovered multi-planet systems present dispersed inclinations (e.g. Bean et al. (2009) and McArthur et al. (2010)), and predictions anticipate a substantial population of systems of this kind (Zhu et al., 2018). Similarly, while all orbits in the Solar System are close to circular, exoplanets exhibit a wide range of eccentricities (Limbach et al., 2015). Interestingly, eccentricity and planetary mass show a correlation (Wright, Upadhyay, et al., 2009): lower mass planets show close to zero eccentricity, while massive planets show a broad distribution between 0 and 0.5.

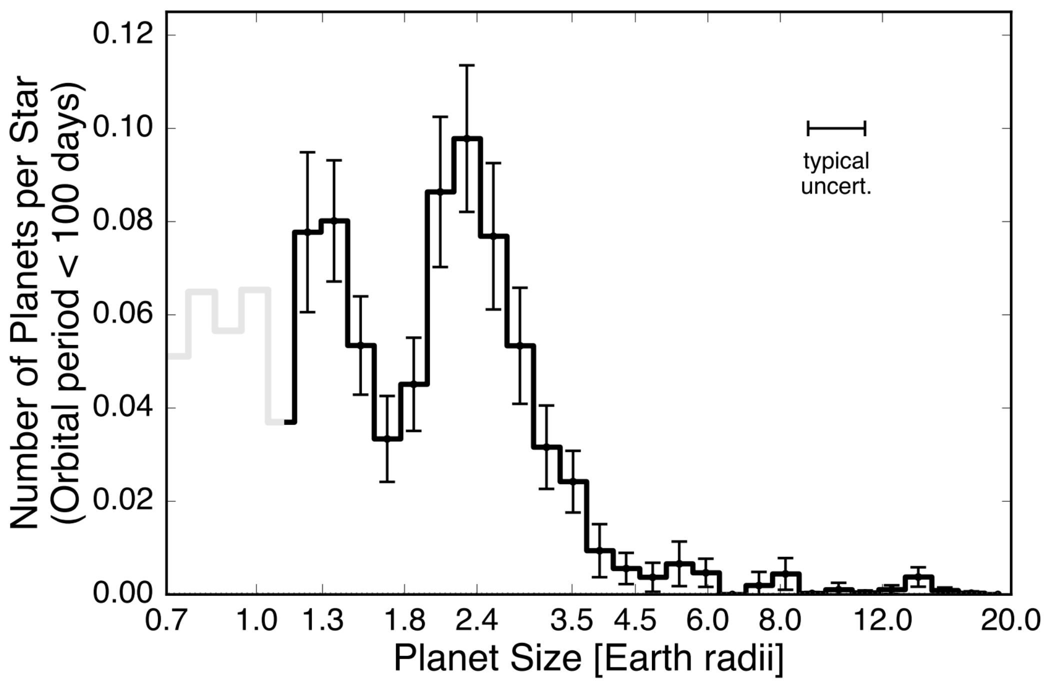

Figure 1.2 Planets per star as a function of planet size for periods less than 100 days. Taken from Fulton, Petigura, Howard, et al. (2017).

Planetary mass is a particularly interesting characteristic. For instance, a mass estimate is critical to constrain atmospheric compositions (von Paris et al., 2013). Furthermore, a measurement of the density constrains the planet's core properties (Valencia et al., 2007; Dorn et al., 2015), e.g. determine core size or distinguish between rocky and icy cores. Besides, in the same way that a size distribution, such as the one seen in Fig. 1.1, provides valuable information about planet formation processes, similarly, finding a mass-separation function is key to understanding the formation mechanisms (Suzuki, Bennett, Ida, et al., 2018).

1.2 Exoplanet detection and characterization methods

Transits and microlensing

The presence of an exoplanet can be inferred if a planetary transit occurs, i.e. if the planet periodically passes over the host star in the observer's line of sight causing a dip in the observed star brightness. The detection and characterization of exoplanets following this measurement is known as *transit photometry and spectroscopy*. Over 3300 exoplanets have been detected with this technique, the vast majority with the Kepler NASA mission (Borucki et al., 2010; Howell et al., 2014) that monitored 100,000s stars in search of periodical dimming events. Although the probability of this phenomenon is small, this has been the most successful detection method to date. In our supposedly isotropic galaxy, the probability of transit is inversely proportional to the semi-major axis of the planet's orbit, $p \propto 1/a$ (Winn, 2010).

The characteristics of the transit allow for the characterization of the system. For instance, the times of transit and occultation, i.e. when the planet passes behind the star, provided that the occultation can be measured, leads to the computation of the eccentricity. The transit depth, δ, is the measurement of the dimming, or how deep the transit is. A radius estimate for the planet can be obtained since the transit depth is

$$\delta = \left(\frac{R_p}{R_s}\right)^2, \tag{1.1}$$

provided that the planet is fully transiting the star and the star is well characterized. In Fig. 1.3 a sketch of the fundamentals of a transit is shown. Moreover, transit spectroscopy, where the spectra of the transit event is analyzed, has obtained many successful atmospheric composition measurements (e.g. Charbonneau et al. (2002), Mandell et al. (2013), Saba et al. (2021)), with some prominent molecular and atomic species detections, e.g. H_2O, CO, CH_4, CO_2, TiO, and VO (Madhusudhan, 2019).

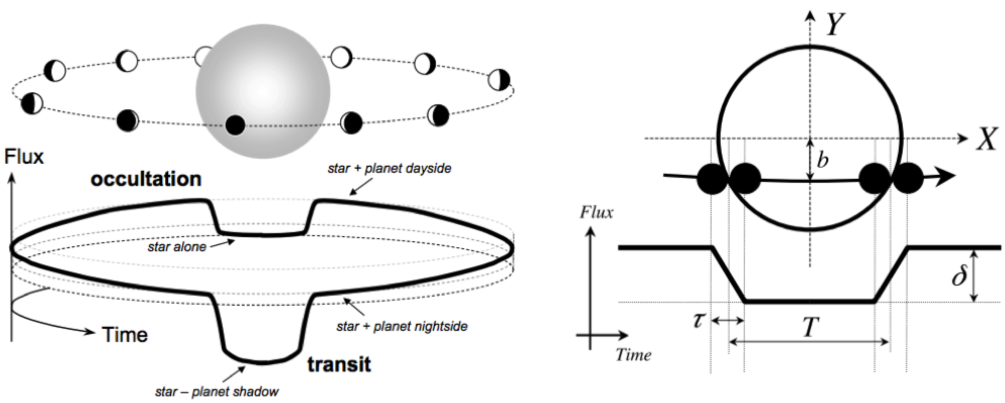

Figure 1.3 A schematic of a planetary transit with its main features. Explanation in the text. Adapted from the Winn (2010).

However, the transit method has its limitations. As stated above, the number of exoplanets that undergo planetary transits is relatively small. Therefore, transits are able to detect a particular set of exoplanets that orbit relatively close to their host. Regarding spectroscopic characterization, transit spectroscopy is limited to strong molecule and atomic absorption (Madhusudhan, 2019). Indeed, the signal from the planet is small compared to the host star's, which is not attenuated and is a major source of uncertainty. Besides, the signal from the atmosphere is dependent on the scale height: $H = kT/mg$, where k is the Boltzmann constant, T is the temperature, m is the mean mass of the molecule, and g is the local gravitational acceleration. Hence, a small scale height will produce a small signal. Furthermore, the presence of clouds heavily hinders the detection of molecules and atomic species since they blur the spectral features.

Gravitational microlensing is another detection technique that exploits the spacetime warping caused by the presence of an exoplanet. A background *source* is magnified by a *lens* object, the mass of which modifies the spacetime grid around itself resulting in the lens effect. The light from the source is bent in such a way that the source is observed to have an arc or ring shape. In the perfect alignment case, the observation phenomenon is known as the Einstein ring; otherwise, a distorted arc is observed. Resolving the arc is not possible with current observatories. Gravitational microlensing is based on the light amplification resolved in a lightcurve that a microlensing event produces, see Fig. 1.4. The focusing of the source light by the star acting as a lens results in a distinct symmetric peak of the lightcurve when observing the source; if a companion passes by as well, there will be another superimposed peak product of the microlensing event from the planet. The more massive the planet is, the brighter the event and broader in time. I defer a detailed explanation of this method to Gaudi (2010).

Only a handful of planets have been discovered by this method to date. This method is the only one capable of finding sub-stellar objects that do not orbit a star (Sumi et al., 2011). These are called free-floating planets (FFPs). FFPs seem to be common, and their population has some surprising trends. For instance, (1) there seems to be a gap for Jupiter-mass planets (Mroz et al., 2017) and (2) Neptune-mass planets are likely the most common (Suzuki, Bennett, Sumi, et al., 2016). Ground based observatories have limited access to Earth-mass planets, where the timescales of the microlensing event is relatively short, 0.1-0.5 days, and rather dim. However, it has been speculated that Earth to super-Earth-mass planets are probably very common (Mroz et al., 2017). The Galactic Bulge Time Domain Survey, one of the Nancy Grace Roman Space Telescope's highest priority surveys, is predicted to discover $\sim$1400 exoplanets, from which $\sim$200 will be $\lesssim 3\ M_{\oplus}$ (Penny et al., 2019).

Although it is a remarkably powerful technique, with the potential to bear a tremendous yield, it has some limitations. The vast majority of the systems (and all the FFPs) that this kind of survey has access to are beyond the reach of other detection

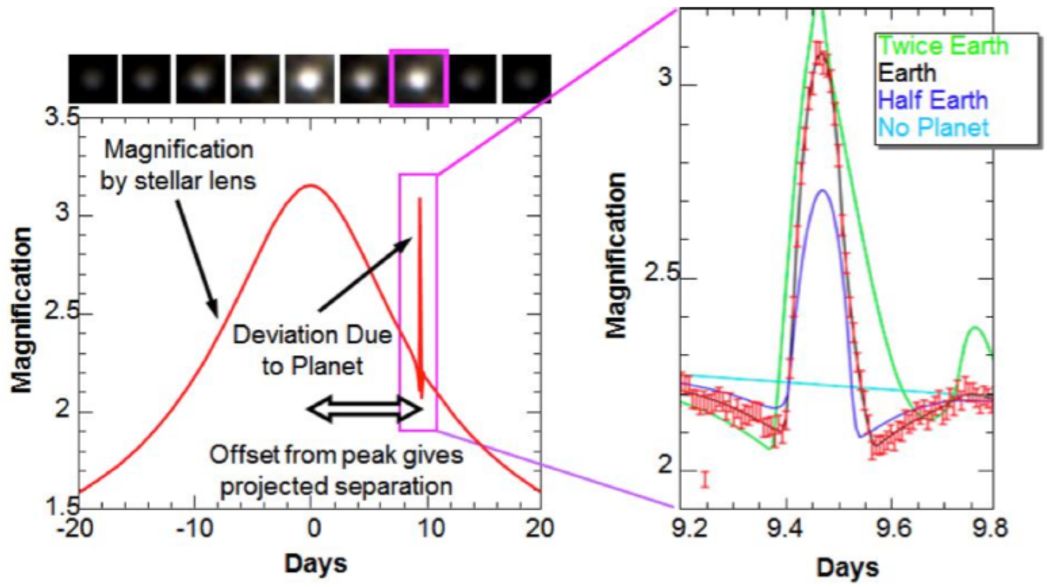

Figure 1.4 A typical lightcurve from a microlensing event. Otherwise symmetric, the presence of the planet adds a superimposed peak to the host star ordinary lensing curve. The shape and distance from the main peak inform us about the size and separation of the planet. Adapted from the Nancy Grace Roman Space Telescope team, GSFC (roman.gsfc.nasa.gov/galactic_bulge_time_domain_survey.html).

techniques and will not have a follow-up observation. Moreover, the light detected is neither from the host star nor from the exoplanet, so any characterization of the atmosphere, spin, or surface is not available.

Radial velocities

The radial velocity (RV) method is a widely successful method that accounts for over 20% of known exoplanets. It is only surpassed by transit photometry given the bountiful yield of the Kepler NASA mission. RV was one of the earliest exoplanet detection concepts (Campbell et al., 1988), and after Mayor and Queloz (1995) detection of a hot Jupiter, it quickly became a prolific detection technique used in many observatories. Early examples of dedicated instruments include ELODIE (Baranne et al., 1996) and HARPS (Mayor, Pepe, et al., 2003). Today, the state-of-the-art standard is set by HIRES (Vogt et al., 1994; Howard, Johnson, et al., 2010), HARPS3 (Thompson et al., 2016), ESPRESSO (Pepe, Molaro, et al., 2014) and CARMENES (Quirrenbach et al., 2018). Although it started exclusively as a technique to discover planetary systems, RV has slowly transitioned into a means to also confirm and characterize transit exoplanet candidates (Fischer et al., 2016; Kempton et al., 2018).

As the name suggests, RV uses radial velocity measurements from the host star, the changes of which indicate the presence of one or multiple planets. The radial velocity is measured via Doppler spectroscopy; the light from the star moving away from the observer is redshifted (or blueshifted when moving towards the observer), which can be captured with a high enough spectral resolution data point and precise calibration. The spectral shift is thus a direct measurement of the star's line-of-sight motion, from which the orbit of a planet can be inferred if a periodic sinusoidal-like variation is detected. Neglecting relativistic effects, the wavelength shift and the line-of-sight component of the star's velocity, v_r, is computed to be:

$$v_r = c\frac{\lambda_B - \lambda_0}{\lambda_0}, \tag{1.2}$$

where λ_B is the wavelength measured in the International Celestial Reference System (ICRS) at the observer's position after barycentric correction and λ_0 is the wavelength measured at the source position. This fundamental equation of RV may appear to be simple, however, obtaining a precise estimation of λ_B is exceptionally difficult. Indeed, a spectral line may be easily recognizable by the observer, even at the suitable spectral resolution, but the precision to which it needs to be calibrated is very strict, especially when targeting the RVs of the most compelling (small and rocky) cases. To give an idea, an Earth analogue, i.e. orbiting a solar-mass star at 1 AU, has an RV signal of 9 cm/s (when viewed edge on, more on this later in this section). The corresponding Doppler shift is tiny; therefore, sources of uncertainty have to be scrutinized carefully. I list some of the more important ones here, that are associated with astrophysical effects:

- Barycentric correction: the Earth's velocity vector has to be calibrated out. Moreover, to reach an uncertainety level of $\sim$1 cm/s RMS, second order sources have to be tackled: gravitational redshifting, precession, nutation, and the bending of light passing close to the Sun (Wright and Eastman, 2014).
- Stellar activity: commonly known as *stellar jitter*, consists of quasi periodic signals from the star's activity that can be particularly hard to model (Davis et al., 2017; Lubin et al., 2021). These can cause false detections (Dumusque, 2018).
- Starspots: the temperature of these is generally lower than the photosphere. Hence, large enough starspots can contaminate the signal (Prato et al., 2008).

- Stellar properties: the effective temperature, surface gravity, and metallicity also have an non-negligible effect on the velocity uncertainty (Beatty et al., 2015).

- Solar contamination: the reflection from the moon and atmospheric scattering of sunlight can contaminate the spectra (Roy et al., 2020).

And, some of the instrumental sources, identified by Podgorski et al. (2014) and Halverson et al. (2016):

- Instrument instability: temperature gradients and changes cause optical aberrations, such as defocus. Other mechanical instabilities, namely vibrations, have an effect on lateral shifts and defocus.

- Telescope focus errors and optical imperfections: these have an impact on the defocus.

- Detector errors: many effects enter this category. For instance, an inter-pixel change in quantum efficiency biases the centroiding of spectral lines. Also, fabrication techniques of CCDs lead to small sudden changes in the detector that cause systematic errors (Dumusque et al., 2015). Furthermore, temperature changes can make the read-out noise vary with time.

- Stray light: can be mitigated by baffling and ghost mitigation protocols, such as tilting the detector. Seems to be poorly understood and hard to analyze (Halverson et al., 2016).

- Imperfect atmospheric dispersion corrector (ADC): the ADC performance determines the wavelength offsets caused by chromatic errors from the atmosphere's dispersion. These can also affect barycentric correction via chromatic errors (Blackman et al., 2019).

Last, but not least:

- Telluric contamination: absorption lines from Earth's atmosphere have to be calibrated out. Although not Doppler shifted and thus relatively easy to spot, changes in humidity and pressure can make this process challenging (Meier Valdés et al., 2021). Furthermore, reaching levels of 10 cm/s precision requires dealing with micro-telluric lines (Cunha et al., 2014; Bedell et al., 2019).

It is worth mentioning the photon noise, which evidently haunts high resolution spectrographs; even for relatively bright stars, instruments are typically photon starved (Pepe, Ehrenreich, et al., 2014). Substantial efforts are being made to mitigate these sources of uncertainty. Stellar jitter being one of the most challenging sources of error, it has been the focus of many research efforts into mitigating this effect via modeling (Kjeldsen et al., 1995; Del Moro, 2004) and statistical analysis (Davis et al., 2017; Collier Cameron et al., 2021; Holzer et al., 2021). An interesting approach to dealing with unknown small systematic errors is to calibrate RV data by monitoring quiet stars (Tal-Or, Trifonov, et al., 2019).

Wavelength calibration technology, a key element in precise RV, has seen remarkable advancements in the last two decades (McCracken et al., 2017). Historically, wavelength calibration has been performed by internal sources like Th-Ar lamps and I2 cells, but their degradation with aging and limited accuracy have motivated the development and use of laser frequency combs (LFCs) (Murphy et al., 2007). Probst et al. (2020) recently demonstrated the long term stability of LFCs to the precision of 1 cm/s.

Once an estimate of λ_B is obtained, v_r can be computed from Eq. 1.2, and thus the RV curve is assembled. It is worth noting the problem with aliasing. Gaps in the data, sampling, spurious peaks, etc. induce aliasing of the periodic signal (Dawson et al., 2010). Especially in low signals, aliasing can hinder the estimation of the exoplanet's period (Stock et al., 2020). In general, the best way to avoid this problem seems to be to monitor the radial velocities for as many periods of the candidate orbit as possible.

To characterize the planetary system with the RV time series a phase-folded RV curve solution is obtained, from which the RV orbit is computed. In Fig. 1.5 an example of an eccentric orbit and its corresponding phase-folded RV curve is shown with its most significant parameters. A Keplerian orbit imprints a particular RV-phase curve shape, from which most orbital parameters can be derived. Not all. A planet's orbit can be fully characterized with 6 parameters, typically: the semi-major axis, a, the eccentricity, e, the inclination, i, the argument of the periastron, ω, the longitude of the ascending node, Ω, and a time reference, say, the time of passage of conjunction, t_c. Given an RV curve, we can find a solution for the period, P, e, ω and t_c. P is directly related to a through Kepler's third law. Therefore, with RV we can compute all orbital parameters but i and Ω, for purely geometrical reasons. To obtain the RV orbit we solve the following system of equations associated with a Keplerian orbit:

$$M = E - e \sin E \tag{1.3}$$

$$\nu = 2 \tan^{-1} \left(\sqrt{\frac{1+e}{1-e}} \tan \frac{E}{2} \right) \tag{1.4}$$

$$v_r = K[\cos(\nu + \omega) + e \cos \omega] \tag{1.5}$$

M is the mean anomaly, E is the eccentric anomaly, ν is the true anomaly, and K is the semi-amplitude of the radial velocity. We solve this with iterative methods.

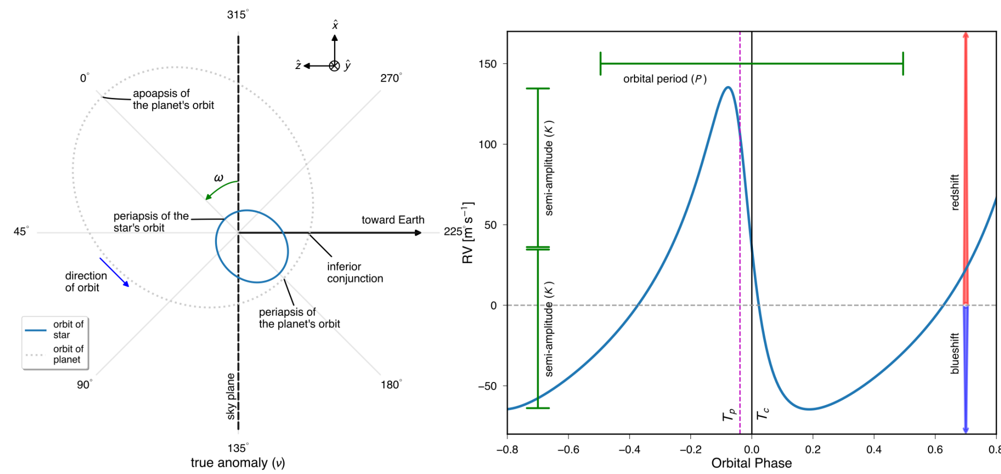

Figure 1.5 Most of the characteristics of an exoplanet orbit (*left*) can be derived from the RV phase solution (*right*) taken from the RV data of a star's Doppler spectroscopy observations. Details of the method in text. Taken from Fulton, Petigura, Blunt, et al. (2018).

An estimate of the lower bound of the planetary mass is available with RV. With this purpose, we consider the radial velocity semi-amplitude, K, which is $K = (v_{r,max} - v_{r,min})/2$. After some algebra, this provides an expression that relates K, e, and P to $m_p \sin i$:

$$K_1 = \frac{28.4329}{\sqrt{1-e^2}} \frac{m_p \sin i}{M_{Jup}} \left(\frac{m_s + m_p}{M_\odot}\right)^{-2/3} \left(\frac{a}{1AU}\right)^{-1/2} \tag{1.6}$$

Mass and inclination cannot be disentangled, so RV only has access to the minimum mass, i.e. the corresponding to $i = 90°$. It is worth noting that at 90°, the planet transits, so the degeneracy is broken and the density can be measured. To get an upper bound for the mass other characterization methods have to be used. RV, however, is one of the only two detection techniques that can directly measure mass and is the only one with prospects of reaching Earth-like planets in the near future (Crass et al., 2021).

Absolute Astrometry

The tracking of a star's absolute astrometry in search for periodic movements superimposed to its proper motion is another indirect method of detection and characterization of exoplanets. I will refer to it as simply *astrometry*. The principle of this method is straightforward: if the stars moves in the sky in periodic wobbles instead of in a rectilinear way, the most probable explanation is that a companion is perturbing its motion. Indeed, a companion-hosting star will have three movements super-imposed: its proper motion, parallax, and the orbit motion around the barycenter of the system.

Therefore, if one is able to effectively subtract the parallax and proper motion, only the reflex motion due to the orbit remains. Characterizing the orbit of the star around the barycenter directly provides the orbit of the planet given their relative mass, m_s/m_p. Astrometry, as opposed to RV, has access to all six orbital parameters and the planet mass. That is, provided that the observation has enough sensitivity to the star motion. An astrometry instrument has to be capable to detect very small motions in the order of μas. The astrometry signal amplitude, A_{astr}, depends solely on the relative mass between the star and planet, the semi-major axis, a, and the distance from the observer, d. It can be expressed as:

$$A_{astr} = 3\left(\frac{a}{1AU}\right)\left(\frac{m_p}{1M_{\oplus}}\right)\left(\frac{m_s}{1M_{\odot}}\right)^{-1}\left(\frac{d}{1pc}\right)^{-1}\mu as \tag{1.7}$$

For instance, an Earth analogue at 10 pc would have a signal amplitude of 0.3 μas, and a Jupiter-analogue in the same system, 495 μas (Malbet, Sozzetti, et al., 2010). Interestingly, this method favors wider orbits. The bad news is that the signal is always small: current estimates indicate that the vast majority of nearby exoplanets would have an astrometric signal of <1 mas (Malbet and Sozzetti, 2018). In the 'diffraction limited case, the astrometric precision, σ_{astr}, of an instrument scales with the telescope size, D:

$$\sigma_{astr} \propto \frac{\lambda}{D} \tag{1.8}$$

Although this relationship seems to indicate that we cannot do better than 1 mas precision with a reasonably sized telescope, the strategy for measuring precise astrometry allows for much better than the diffraction limit angular size. An astrometric measurement is done by repeatedly imaging the target and background sources to monitor their relative motion (Pravdo et al., 1996). Observations from ground-based telescopes, although generally limited by atmospheric turbulence (J. Sahlmann, 2013), have consistently achieved sub-mas precisions (Lazorenko, 2006). However, only a handful of exoplanets have been discovered with this method (the exoplanet catalog at http://exoplanet.eu/catalog credits astrometry with 15 detections as of this date), e.g. a low mass companion orbiting HD 176051 is considered the first confirmed astrometry exoplanet (Muterspaugh et al., 2010), and the recent exoplanet candidate TVLM 513b with a mass measurement of $m_p = 0.35 - 0.42\ M_{Jup}$ (Curiel et al., 2020).

Several ground-based observatories have developed astrometry capabilities, such as the VLT with the FORS2 camera (Lazorenko et al., 2014) and the CAPSCam at Las Campanas (Boss et al., 2009). Single aperture observations are able to achieve an astrometric precision of $\sim$100 μas, although this may be degraded by the lack of bright enough reference sources (Sahlmann et al., 2016). With optical interferometry the precision can be pushed by an order of magnitude (Lane et al., 2004): this is based on observing two stars simultaneously in order to measure interferometric fringes to precisely monitor their relative movement. The Very Long Baseline Array is a fine example of the power of interferometry (Bower, Bolatto, Ford, and Kalas, 2009; Bower, Bolatto, Ford, Fries, et al., 2011), in this case radio interferometry is used to achieve $\sim$10 μas astrometric precision (Reid et al., 2014). GRAVITY at the VLT (Lacour et al., 2014) supports an optical interferometer that is already producing exciting exoplanet science, e.g. Gravity Collaboration et al. (2019) and Kammerer et al. (2021). I refer the reader to Lacour et al. (2014) for a comprehensive explanation of the interferometric technique.

Space-based observatories are not limited by the atmosphere distortion, and thus projected to reach significantly better astrometric precision (Janson, Brandeker, et al., 2018). Several dedicated observatories have been proposed, e.g. the Space Interferometry Mission (SIM, Shao et al., 2007) and the Nearby Earth Astrometric Telescope (NEAT, Malbet, Léger, et al., 2012). Most exciting are the Gaia prospects (Perryman, de Boer, et al., 2001; de Bruijne, 2012). Gaia's exquisite astrometric precision over a long baseline is projected to yield 40000 detections (Perryman, Hartman, et al., 2014). As we wait for its final data release, ingenious ways of using the currently available data from the data release 2 (Gaia DR2, Gaia Collaboration, 2018) and the early data release 3 (eDR3, Gaia Collaboration, 2021) have been developed. For instance, using the proper motion anomalies between the Hipparcos catalog (Hipparcos Collaboration, 1997) and Gaia's (Kervella et al., 2019). This consists on computing a long term proper motion between the Hipparcos and Gaia epochs, and comparing it to the *instantaneous* proper motion measured by each mission; a proper motion anomaly would indicate an acceleration due to the presence of a companion. To use astrometry from different catalogs one should be aware of the difference between their frame of reference, Brandt (2018) (and Brandt (2021) for eDR3) performed a cross-calibration between both catalogs in order to confidently make use of the long term proper motions and proper motion anomalies.

Capabilities in space astrometry are projected to continue to grow after Gaia. Future small observatory Small-JASMINE (Yano et al., 2012) is programmed to do Gaia follow-ups at precisions of $\sim$10 μas. The Roman Space Telescope will carry out an astrometry program that is also estimated to achieve $\sim$10 μas astrometric precision (WFIRST Astrometry Working Group et al., 2019; Melchior et al., 2018), although this number has been deemed optimistic (Tal-Or, Zucker, et al., 2019). Astrometry could also be carried out with HabEx Workhorse camera at sub-μas precision, as proposed by Bendek, Martin, et al. (2021).

We list some of these challenges as identified by Malbet and Sozzetti (2018), Malbet, Abbas, et al. (2019), Maire et al. (2021), Lacour et al. (2014), and Reid et al. (2014):

- Adaptive optics: atmospheric turbulence is the main limitation of ground-based observations; adaptive optics help mitigate its effects. I will delve deeper into adaptive optics technology later in this chapter.

- Detectors: typical detector defects like the ones discussed in the previous section in the context of RV observations are also an important limitation for astrometry. Similarly to RV, in astrometry, precise centroiding on the detector chip can be negatively affected by detector systematic errors.

- Calibration and metrology: astrometry relies on the precise astrometric measurements over an extended period of time. Hence, precise calibration of the instrument is required to confidently use all measurements taken at different epochs. Laser metrology is used to account for optical distortions in the instrument in such a way that aberrations can be calibrated out (Crouzier, Malbet, Hénault, et al., 2016; Crouzier, Malbet, Henault, et al., 2016).

- Influence of giant wide-separation planets on smaller planets: Malbet and Sozzetti (2018) identify this problem in which, since a bigger planet at wider separation would have a much stronger signal, such a signal would confuse the detection of a smaller closer-in planet. I do not think this should be a problem provided that the smaller signal is captured; orbit fitting methods, such as the ones based on MCMC model fitting, should easily probe the parameter space in search for the two superimposed orbits simultaneously.

- Astrometric jitter: Although astrometry is much less affected by stellar activity than RV (Makarov et al., 2010; Lagrange, Meunier, Desort, et al., 2011), this effect starts to be a major limitation at very high precision, typically at sub-μas (Lagrange, Meunier, Desort, et al., 2011). Spots, plages, granulation of the target star contaminate the astrometric measurement by shifting the photocenter from the barycenter (Eriksson et al., 2007; Meunier et al., 2020). This effect has a dependence on inclination, metallicity, and active-region nesting (Sowmya et al., 2021).

The many efforts dealing with these limitations will hopefully result in a breakthrough in astrometry detections, mass measurements, and orbit characterizations that this technique has long been promising to deliver.

Direct methods

After a review of the most relevant indirect techniques, it is time to turn our eyes to direct methods of finding and characterizing exoplanets. Yes, transit photometry measures the photometry from the host star, RV and astrometry look for reflex motions of the host star due a possible orbit, and microlensing does not even measure the host star, it infers a companion by the microlensing magnification of a background source. In this section I will go over techniques that detect light coming directly from the exoplanet itself.

Direct detection of exoplanets is a very powerful characterization method. Firstly, imaging an exoplanet and computing its relative astrometry with respect to the host star, at three or more epochs, gives us constraining information about its orbital parameters. Only the astrometry technique has also the full orbit parameters available since RV suffers from a geometrical degeneracy that impedes the measurement of the inclination and longitude of the ascending node. Second, the light from the planet can be fed into a spectrograph to obtain information about the composition of its atmosphere. The transit method can infer atmospheric properties from the absorption lines in a transit spectrum, however, these are usually hard to obtain due to the limitations of this technique as discussed in Sec.1.2. Characterizing the atmosphere of exoplanets is of paramount importance to fully understand planetary systems and how they form. Hence, the potential to access atmospheric compositions, and namely biomarkers, makes direct methods key. Although more futuristic, it is worth mentioning that direct methods could potentially resolve the surface of an exoplanet. This would require gigantic telescopes, although some creative ideas have been proposed, e.g. Turyshev et al. (2020).

While a powerful technique, it is also probably the most challenging, mainly due to the small planet-to-star flux ratio. When looking for an exoplanet, the light from the star overwhelms the image leaving no trace of the companion. Direct detection methods deal with isolating the signal from the planet from the unwanted starlight signal. Unfortunately, achieving the sensitivity needed to detect a significant amount of exoplanets with respect to the actual population is extremely hard. In Fig. 1.6 some of the current and projected capabilities of direct imaging instruments are shown, plotted are also simulated exoplanets in nearby systems with occurrence rates as in Kopparapu et al. (2018). Current high contrast instruments have access to only a small fraction of exoplanets (see also Fig. 1.1). Indeed, planets at separations that we are currently able to probe are rare (Bowler, 2016). Given the relevance of this topic in this thesis, in the following sections I will go into more details on the technical challenges of a high contrast imaging system.

The light from a planet can either come from thermal emission or from reflected light from the host star. Given the temperatures of star and planet, strong reflected signal is expected in the optical, and thermal emission, particularly for young self-luminous planets, in the near- and mid-infrared. Ideally, one would want to combine information from both reflected and thermal emission. In this case, one can account for the planet's energy budget and climate (J. Wang, Meyer, et al., 2019). Furthermore, clouds in an exoplanet's atmosphere have a significant effect on how the light is reflected and emitted (Morley et al., 2015): a cloud covered atmosphere presents a black-body-like spectrum in thermal emission, and in reflected light, certain molecules in the clouds are likely to be have strong features. Clouds are not necessarily an annoyance since they are an indicator of the metallicity of an

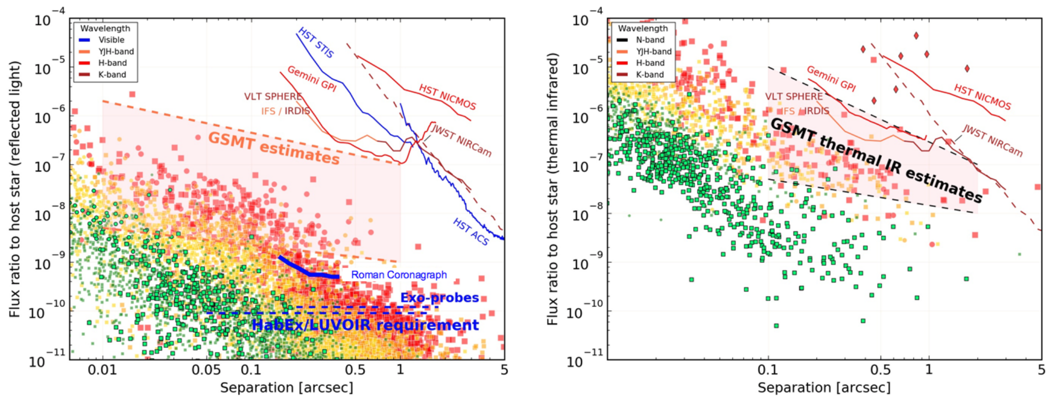

Figure 1.6 Lines indicate the performance of an instrument/observatory in terms of planet-to-star flux ratio versus angular separation. Dots represent simulated exoplanets in around stars in the vicinity of the Solar System. *Left:* Flux ratio in reflected light; *right:* in thermal emission. Round markers denote for planets around cool stars (T_{eff} < 4000 K), square markers denote planets around warmer stars (T_{eff} > 4000 K), and dimaond markers indicate planets that have already been imaged. The color of the marker indicates the size of the planet: red denotes giant planets; orange, Neptune-sized planets; yellow, mini-Neptunes; dark green, super-Earth and Earth-size planets; and light green, temperate super-Earth and Earth-size planets. Credit: D. Mawet, B. Macintosh, T. Meshkat, V. Bailey, D. Savransky (https://github.com/nasavbailey/DI-flux-ratio-plot).

atmosphere (Burrows et al., 2011). Understanding the effect of clouds in the spectra obtained in reflected light is an interesting field of current research. For instance, its polarization effects versus cloud particle size and its interplay with the planetary phase (the azimuthal distance with respect to the observer direction) and albedo (Millar-Blanchaer et al., 2015; Sanghavi et al., 2021). Reflected light is significantly harder to detect with respect to thermal emission, so much so that the hope of yielding a substantial number of detections in reflected light is left to the next generation telescopes, in particular space-based (Lopez-Morales et al., 2019). This is illustrated in Fig. 1.6: young, self-luminous exoplanets are more favourable in term of flux ratio between star and planet in the thermal infrared.

Although the number of direct detections has been less than what was hoped for (B. Macintosh, 2013), astronomers have been able to characterize and learn from the small set available. I list here some of the crowd's favourites, and show some of their images in Fig. 1.7:

- β Pictoris: so far, two planets have been discovered in this system. Planet b was discovered by Lagrange, Gratadour, et al. (2009), and has since been extensively studied. It has a mass of 15.4±3.0 M_{Jup}, and is almost edge-on ($i \sim 90$). It is so edge-on that until 2015 it was hoped that it would transit (B. Macintosh, Graham, Ingraham, et al., 2014); sadly, further constrains in its orbits denied this possibility (Millar-Blanchaer et al., 2015). Kenworthy et al. (2021) recently investigated the possibility of a transit in the previous possible transit epoch in 1981, where there is available photometry data of the star; again, sadly, the transit most probably did not happen. With high-resolution spectroscopy, I. A. G. Snellen et al. (2014) were able to measure the spin of the planet. A second planet was discovered through RV, and then confirmed through a direct detection (Lagrange, Meunier, Rubini, et al., 2019; Nowak et al., 2020), with a dynamical mass of 8.2±0.8 M_{Jup}. This is considered the first direct detection of an RV planet.

- HR 8799: the first three planets of this system were discovered by Marois, B. Macintosh, et al. (2008), and the fourth just a couple of years later (Marois, Zuckerman, et al., 2010). Since, this system has been the aim of many research efforts, e.g. Bonnefoy et al. (2016) and Greenbaum et al. (2018). The planet orbits are currently fairly well characterized (J. J. Wang, Graham, et al., 2018; Ruffio et al., 2019), and their masses have been since constrained to: 5.8±0.5 M_{Jup} for the outer planet, and 7.2±0.7 M_{Jup} for the inner three (J. J. Wang, Graham, et al., 2018; Goździewski et al., 2020). Low to high resolution spectra has been obtained from all four planets, from which individual molecules have been detected (water, methane, and carbon monoxide) (Konopacky et al., 2013; T. S. Barman et al., 2015), C/O ratio has been constrained (Mollière et al., 2020), and even spin measurements have been obtained (J. J. Wang, Ruffio, et al., 2021).

- 51 Eridani: this system hosts a Jupiter-like exoplanet that was discovered by B. Macintosh, Graham, T. Barman, et al. (2015). It has a measured mass of 2.6±0.3 M_{Jup}. Astrometry was used to further constrain the dynamical mass of 51 Eridani b, but the data combining the Hipparcos and Gaia catalogs was inconsistent, which can be explained, if not by systematics between the two catalogs, by another companion (De Rosa et al., 2020).

- Fomalhaut: the presence of a planet around Fomalhaut was suspected due to the asymmetry in the debris disk by Stapelfeldt et al. (2004). Shortly after a candidate companion was imaged with HST (Kalas et al., 2005). This exciting discovery was followed by surprising non-detections in the infrared (Janson,

J. C. Carson, et al., 2012) that challenged the existance of a companion, e.g. Poppenhaeger et al. (2017) and Gaspar et al. (2020). The main case against it is that it cannot have a big enough mass to disturb the debris disk in the way that the debris disk seems to be distorted from observations. However, Pearce et al. (2021) recently offered an argument for planet b based on it being in mean-motion resonance with the disk.

- κ Andromedae: a giant planet was discovered around κ Andromedae by J. Carson et al. (2013). Without reliable astrometry and RV data, the mass estimate of this planet is completely model dependent. The age estimate, taken from its measured flux profile, drives the mass estimate. Hence, its mass has been believed to be between ~13 M_{Jup}, for a younger (~30 Myr) planet (J. Carson et al., 2013), to ~50 M_{Jup}, for an older (~200 Myr) planet (Hinkley et al., 2013). Current studies tend to favor a the younger planet model, putting the planet mass estimate at ~10-13 M_{Jup}, see e.g. Uyama et al. (2020).

- PDS 70: two protoplanets, b and c, in PDS 70 were recently discovered by Mesa et al. (2019) and Haffert et al. (2019) respectively. Due to their protoplanetary nature, it has been challenging to detect individual molecules from their atmospheres (J. J. Wang, Ginzburg, et al., 2020; Stolker et al., 2020; Cugno et al., 2021). Particularly hard to characterize is PDS 70 c, from which little is known; the mass of the planet b has an upper bound of 10 M_{Jup}, planet c's mass is currently unconstrained (J. J. Wang, Vigan, et al., 2021).

Direct imaging methods account for single aperture imaging, which would be the most intuitive way to think of detecting an exoplanet, and interferometric methods. The former I will examine thoroughly for most of the rest of this chapter, but before that, let me go over a brief review of the latter. Most of direct detections are using conventional imaging systems, however, interferometry offers a pathway to reach enhanced starlight rejection and resolution. For instance, nulling interferometry is based on combining the light from multiple beams, in which light from planet and star is present, to produce destructive interference of the unwanted starlight. This was first conceived by Bracewell (1978): two separated apertures combine their beams with a π phase shift between the two on-axis beams, the light from an off-axis source would appear among the fringes if its separation coincides with the separation of the bright interference fringes. To be sure to capture the planet light the interferometer rotates along the line-of-sight, which makes the fringes rotate, but not the planet

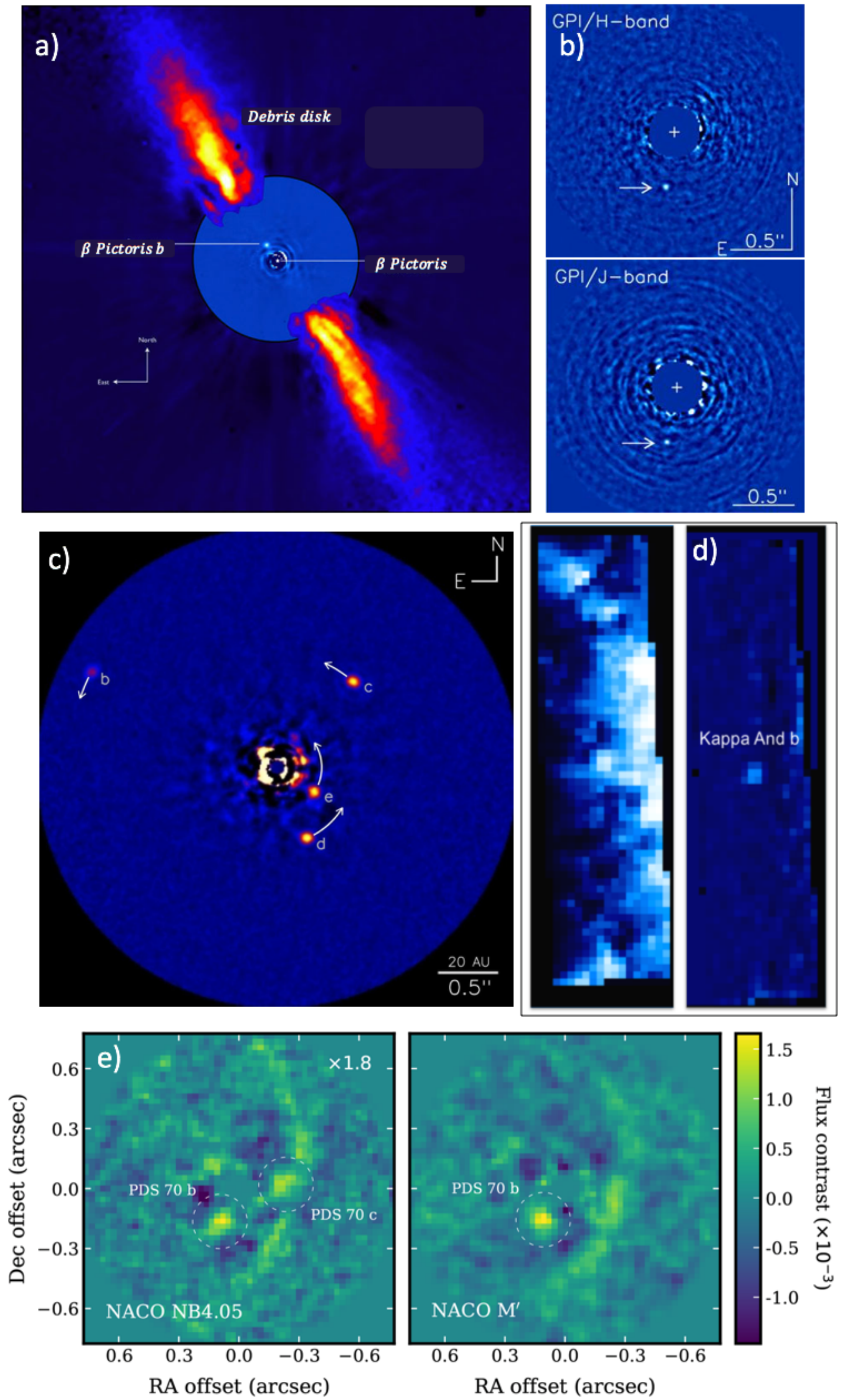

Figure 1.7 Images of directly imaged exoplanets, more information about them in the text. *a)* β Pictoris, credit: A-M. Lagrange et al., *b)* 51 Eridani, credit: Macintosh et al., *c)* HR 8799, credit: C. Marois, *d)* κ Andromedae IFS image, taken from Wilcomb et al. (2020), *e)* PDS 70, taken from Stolker et al. (2020).

signal. This signal shows as a modulation of intensity over the residual starlight. In the late 1990s and 2000s, this method grew in popularity as with exciting prospects to detect Earth-like exoplanets, see e.g. Woolf et al. (1998) and P. M. Hinz et al. (1998). The Terrestrial Planet Finder NASA mission had an interferometer version, the TPF-I, that was programmed to consist of three telescopes with a baseline of over 100 m to probe ~150 nearby stars in search for habitable planets (Lawson et al., 2007). On the ground, several interferometer concepts were developed, e.g. at the Large Binocular Telescope Interferometer (LBTI) (P. Hinz et al., 2014) or the Palomar Fiber Nuller, an interferometer concept that used a single mode fiber (B. Mennesson et al., 2011).

Unfortunately, interferometers in the infrared never did better than a $\sim 10^{-4}$ null (Gravity Collaboration et al., 2019). Two of the main limitations of optical and infrared interferometry, as identified by Gravity Collaboration (2017), are:

- Partial coherence of the beams due to atmospheric distortion and optical aberrations.
- Short coherence time due to atmospheric turbulence.

Lessons learned from radio interferometry and advances in adaptive optics have led to the remarkable improvements in interferometric capabilities of the GRAVITY instrument at VLT (Eisenhauer et al., 2011). Furthermore, the use of single mode fibers helps with the spatial filtering of atmospheric turbulence effects. The exciting science coming from GRAVITY (Gravity Collaboration et al., 2019; Kammerer et al., 2021; Nowak et al., 2020) has put interferometry back in the picture. Besides, a novel concept, the vortex fiber nuller (VFN, G. Ruane, J. Wang, et al. (2018)), is set to see light at Keck (Echeverri et al., 2020). These exciting prospects may be a sign of a new era in interferometry for exoplanets.

1.3 High Contrast Imaging and Spectroscopy

At the end of last section we went over the direct detection methods, where I tried to convey why they are key to exoplanetary science. As we saw, direct methods are still far from probing a substantial fraction of the exoplanet population within a few parsecs of the Earth; such technology is not yet available. In this section I present some of the technological challenges and areas of advancement to image and characterize exoplanets with high contrast imaging. I focus on coronagraphy because of its importance in this thesis. Besides, coronagraphy offers a pathway to achieve the yield of characterized exoplanets needed to reach a comprehensive understanding of the planetary systems in the galactic vicinity.

The Exoplanet Exploration Program, in their 2019 Technology Plan Appendix[1], identified a set of challenges and pathways to maturing key technologies that are expected to enable the great science goals of the next decades. Some of these are addressed in this thesis: coronagraph instrument design, wavefront sensing and control algorithms, and post-processing and integrated observation strategies.

The coronagraph instrument

A coronagraph comes in many forms. The common denominator of them all being to increase the signal-to-noise ratio (SNR) of the planet signal. In the stellar photon noise limit (G. Ruane, A. J. Riggs, et al., 2018):

$$SNR \propto \frac{\eta_p}{\sqrt{\eta_s}}, \tag{1.9}$$

where η_p and η_s are the fraction of planet and star light detected respectively. All a coronagraph can do is fight the noise related to the starlight, while maintaining enough fraction of the planet signal intact. Other sources of noise, such as background and detector noise, although important, are not considered part of a coronagraph optimization. Therefore, a coronagraph is designed to minimize η_s/η_p^2.

The coronagraph was invented by Bernard Lyot in 1931, and, as its name indicates, it was conceived to observe the solar corona (Lyot, 1939). His concept was based on imaging the sun at a plane where an obscuration would diffract the light from the bright center; by virtue of optical diffraction this light appears at the outer edge of the subsequent pupil plane: there, an optical stop, named Lyot stop in honor of its inventor, blocks the diffracted light. At the image plane the light from the bright center is gone, revealing the corona. We use this concept, with surprisingly little variations, almost a hundred years later, to image objects around stars.

The architecture of a typical coronagraph instrument is shown in Fig. 1.8. A pair of deformable mirrors (DMs) correct for wavefront errors. Depending on the type of coronagraph, either an apodizer or focal plane mask (FPM), or a combination of both, is used to diffract the light. The Lyot stop at a pupil plane blocks the diffracted light. Only the residuals of the starlight remain after the Lyot stop, and the objects around it are revealed. I will not consider *interferometric* coronagraphs (although the use of phase tricks and DMs makes all coronagraphs interferometric) since their

[1]https://exoplanets.nasa.gov/exep/technology/gap-lists/

operation is quite different and are not as relevant in this thesis. For some examples see Baudoz, Rabbia, et al. (2000) or B. P. Mennesson et al. (2003).

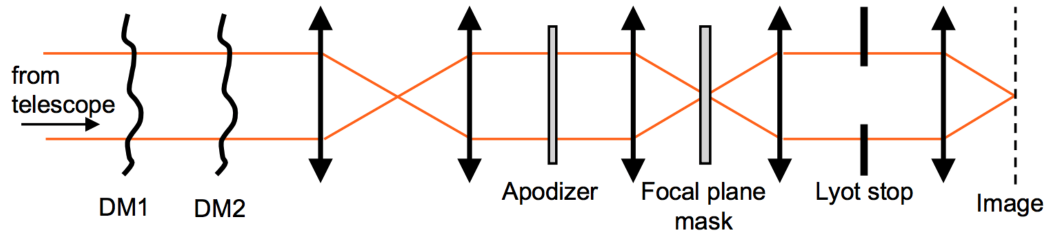

Figure 1.8 Typical coronagraph architecture. DM1, the apodizer and the Lyot stop are all in conjugated pupil planes. Taken from G. Ruane, A. Riggs, et al. (2018).

Since it consists of optical transformations, a coronagraph instrument can be represented by a linear operator, $C\{\cdot\}$. In such a way that

$$E_{im} = C\{E_{tel}\}, \tag{1.10}$$

where E_{im} and E_{tel} are the electric fields at the final image plane and at the entrance of the telescope respectively. Following the mathematical framework introduced by Belikov et al. (2021), we can do a singular value decomposition (SVD) on the coronagraph operator, $C = UTV^*$, in order to inspect the action of a coronagraph. From the SVD we obtain two orthonormal basis, u_n and v_n, associated to U and V respectively. Given that fields E_{tel} and E_{im} can be represented in any orthonormal basis, let us represent with these basis:

$$E_{tel} = \sum_n a_n v_n \tag{1.11}$$

$$E_{im} = \sum_n b_n u_n, \tag{1.12}$$

where $a_n = \langle E_{tel}, v_n \rangle$, and likewise for b_n. Applying the coronagraph operation we obtain:

$$E_{im} = \sum_n a_n t_n v_n, \tag{1.13}$$

where t_n are the singular values from the SVD of C, i.e. the diagonal elements of T. Hence, from a coronagraph we ideally want:

- The t_n singular values associated with v_n modes that correspond to the on-axis source, i.e. the starlight, to be zero.

- The t_n singular values associated with v_n modes that correspond to the science object, to be one.
- The C operator to be insensitive to as many aberration modes as possible. Since a representation of aberration modes is not orthogonal with, say, an off-axis source, a trade-off has to be made between number of aberration modes to which C is insensitive and the throughput of an off-axis source. Here is where we need the concept of inner working angle (IWA), which we define as the separation from the on-axis center at which the throughput of an off-axis source is at 50%. There exists an optimal IWA that monotonically grows with the amount of aberration modes that C is insensitive to.
- The IWA to be as small as possible.

In practice, going from the coronagraph operator C to a real system is not easy. Instead, using the architecture shown in Fig. 1.8, the optical elements are optimized to achieve the four points above. The fourth point concerning IWA becomes more general, since, in practice, we end up not having much control over the t_n singular values; thus it becomes: to maximize the throughput of the off-axis source.

Let us take a look to the specific case of the coronagraph instrument laid out in Fig. 1.8. The two DMs can be expressed as a single operator, DM, in the pupil plane:

$$E_2 = DM \cdot E_{tel}. \tag{1.14}$$

The apodizer can be expressed, too, operator, Ap, in the pupil plane:

$$E_3 = Ap \cdot E_2. \tag{1.15}$$

To work on the focal plane we perform a Fourier transform to the operands and fields, and express the result of this operation with a *hat*: $x \xrightarrow{\mathcal{F}} \hat{x}$. Hence, at the FPM mask plane:

$$E_{im,3} = F\hat{P}M \cdot \hat{E}_3, \tag{1.16}$$

where $E_{im,3}$ in the pupil plane is E_4. Back to the pupil plane to apply the effect of the Lyot stop, LS:

$$E_5 = LS \cdot E_4, \tag{1.17}$$

where $E_{im} = \hat{E}_5$ is the final electric field in the image plane. Hence, with all the operators explicitly:

$$E_5 = LS \cdot (FPM * (Ap \cdot DM \cdot E_{tel})), \tag{1.18}$$

where $*$ denotes a convolution. From this expression we can consider a few things about coronagraphs:

- Although from Eq. 1.18 it seems like the DMs and the apodizer are redundant, this is obviously not true: the DMs are active surfaces to correct quasi-static optical errors and atmospheric turbulence, while the apodizer is a passive element. However, this is an indication that the apodizer can be designed to help alleviate the work from the DMs, see e.g. G. Ruane, Jewell, et al. (2016).
- Ignoring the DMs and apodizer, and assuming a flat wavefront upstream of the FPM, E_{flat}, a pair of operators FPM and LS can be calculated so as to conjugate E_{flat}. Kuchner et al. (2002) used this to come up with the band limited coronagraph.
- Without the FPM, the Lyot stop is redundant. As mentioned before, the Lyot stop blocks the light diffracted by the FPM. Without this diffraction, the Lyot stop is equivalent to the apodizer.
- Without the FPM, the apodizer has to control the full wavefront. Solutions to this problem require an apodizer that controls the complex amplitude to create an area in the image plane suitable for high contrast. See Kasdin, Vanderbei, et al. (2003) for an analysis on this type of coronagraphs. In practice, most designs include an FPM (G. Ruane, A. J. Riggs, et al., 2018). Some coronagraphs that combine apodizer, FPM and Lyot stop are: the apodized pupil Lyot coronagraph (Soummer, 2005), the phase induced amplitude apodization, or PIAA coronagraph (Guyon, Pluzhnik, Galicher, et al., 2005), and its variant PIAACMC (Guyon, Martinache, et al., 2010), and the apodized vortex coronagraph (AVC, G. Ruane, Jewell, et al. (2016)). In Chapter 5 the AVC concept is discussed in detail.

Many advancements have been made in the design of coronagraphs, for a thorough review see Guyon, Pluzhnik, Kuchner, et al. (2006) and G. Ruane, A. J. Riggs, et al. (2018). The main challenge that remains in coronagraph design is the sensitivity to low-order aberrations in the case of telescope pupils with a central obscuration. This is illustrated in Fig. 1.9, where the yield of a mission such as HabEx or LUVOIR is plotted against telescope size for on-axis, i.e. with an obscured pupil, and off-axis, un-obscured. Firstly, looking at the off-axis case, the monolith aperture and the segmented aperture have a seemingly perfect continuity in terms of yield, which indicates that we can deal well with this kind of discontinuities in the pupil. Second, the central obscuration results in a significant loss in yield. Over-plotted are the curves from the theoretical limits for an ideal coronagraph, computed by Belikov et al. (2021). These limits do not necessarily imply a realistic instrument that would achieve such performance, but indicate that there is room for major improvement.

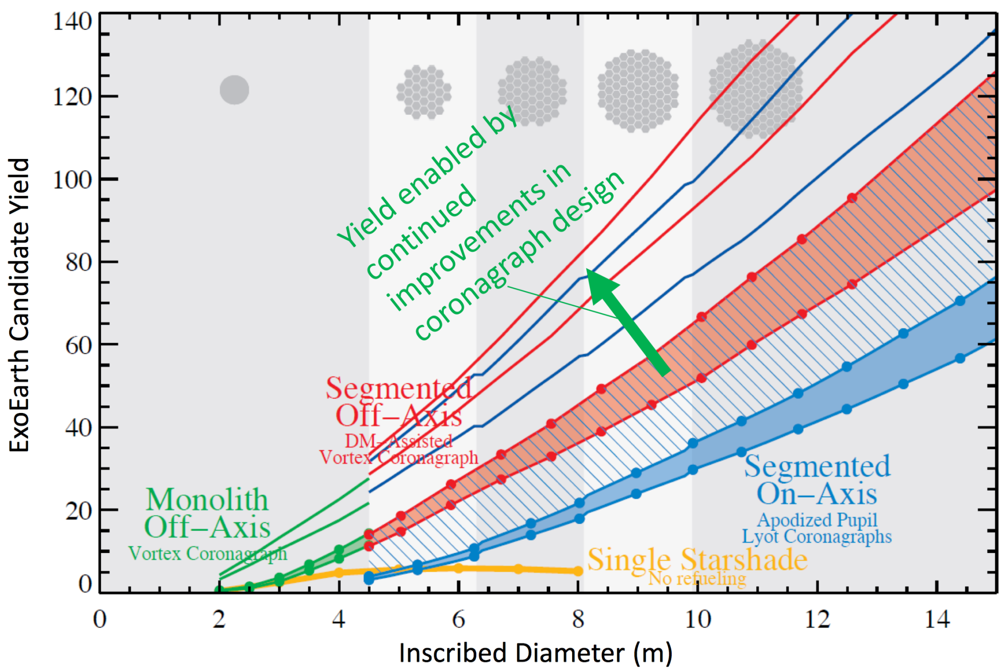

Figure 1.9 ExoEarth yield versus telescope diameter for a HabEx/LUVOIR-like mission. More information in the text. Taken from Belikov et al. (2021).

Wavefront sensing and control

An adaptive optics system is generally understood as having the function of maximizing the Strehl ratio, or bringing the PSF closer to the diffraction limit. A wavefront sensor computes an estimation of the wavefront aberrations, which are then corrected. This process is referred to as wavefront sensing and control (WFSC), although this term is commonly used in the context of correcting for high spatial frequencies and dark hole digging, i.e. creating a dark area in the image plane free from stellar noise in which the planet is hoped to be found. In this section I will first give a brief overview of WFSC in ground based telescopes concerning atmospheric disturbances, and second I will introduce WFSC in the context of dark hole digging.

Typically, an adaptive optics system follows the layout shown in Fig. 1.10. The beamsplitter sends a spectral bandpass outside the science bandpass to the wavefront sensor, where the aberrations are estimated. The control is thus computed in terms of DM commands to correct the wavefront. This process has to be rapid so as to match the short timescales that characterize atmospheric turbulence. Effective WFSC for atmospheric disturbances requires at least 1 kHz control rate (Madec, 2012). Therefore, a fast sensor and DM are critical. Moreover, a bright enough source is necessary to achieve the sensitivity needed to compute the aberrations. This can be done by either having a bright astronomical source near the science target, or by artificially creating a bright point source with laser beams (Beckers, 1993).

A widely used wavefront sensing solution is the Shack-Hartman sensor (SHS); the principles by which an SHS measures aberrations have been known for a long time (Scheiner, 1619). In adaptive optics applications, the pupil is divided into sub-apertures that are focused onto a detector; each sub-image displacement indicates a local tilt of the wavefront. The set of tilts indicates the wavefront aberrations. Its simplicity and robustness make it a popular option for adaptive optics, see e.g. B. A. Macintosh et al. (2012), Beuzit et al. (2019), and, in particular, the SHS at Keck (Wizinowich et al., 2000) from which we will see some images in Chapter 2. Some limitations of this concept include: (1) only the slopes are measured, so there is no information on step discontinuity of the pupil (2) at the spatial frequency set by the sub-aperture spacing the correction is optimal, but it degrades for low spatial frequencies, which are the most important when correcting for atmospheric turbulence, (3) the sub-aperture spacing also leads to aliasing, (4) the need for a high flux (Guyon, 2010), (5) it is poorly suited for dealing with the island effect, i.e. piston errors caused by air temperature gradients at the telescope secondary mirror structures (N'Diaye et al., 2018). The pyramid wavefront sensor (PyWFS) is a more sophisticated alternative to the SHS that has been demonstrated to have better sensitivity to aberrations in closed loop with respect to the SHS (Vérinaud, 2004). A four-sided glass prism is used to create four images of the pupil; the distribution of light in the four images is used to reconstruct the wavefront. A common thread in the advancement of high contrast instruments on ground-based observatories is the introduction of a PyWFS, see e.g. Jovanovic et al. (2015), Bond et al. (2020) or Males et al. (2020).

With the layout shown in Fig. 1.10 the wavefront sensor pick up aberrations associated with optics out of the science beam path. These are called non-common path aberrations (NCPAs). Since atmospheric aberrations are the limiting factor,

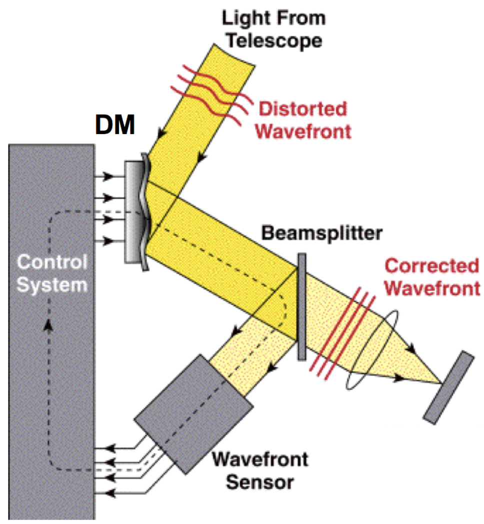

Figure 1.10 Typical layout of an adaptive optics system. Credit: C. Max, Lawrence Livermore National Laboratory and NSF Center for Adaptive Optics..

NCPAs were rightly neglected in first generation adaptive optics systems. However, with the advances in WFSC technology, an important limitation after atmospheric related noise are quasi-static speckles. These originate from errors in the optics, and may vary slowly with temperature changes, or telescope pointing. NCPAs are an important source of systematic errors (Sauvage et al., 2007). Advanced wavefront sensing concepts have been trying to deal with this issue, see e.g. Ren et al. (2012), Hénault (2019) or Lamb et al. (2021). Moving the wavefront sensor closer to the science camera helps mitigate NCPA related errors. An ingenious example of a way to integrate the wavefront sensor with the coronagraph is the Zernike wavefront sensor (N'Diaye et al., 2018). In this concept, the light reflected from the FPM is used to reconstruct the wavefront. Since aberrations before the FPM are known to be more constraining than downstream (the light is mostly gone) the Zernike wavefront sensor picks up the light in a key location. However, the ultimate objective would be to do wavefront sensing at the science camera, which would solve the NCPA problem, this is commonly known as common path wavefront sensing. Many research efforts have led to clever ways of doing doing common path wavefront sensing; I list here some interesting examples:

- The self-coherent camera (SCC, Baudoz, Boccaletti, et al. (2006)), in which the speckles in the image plane coherently interfere with a light probe from the same source. The probe can be sent with a hole in the Lyot stop, the light of which is imaged on the camera. This creates Fizeau interference fringes from which the wavefront can be reconstructed.

- MEDUSAE (Ygouf et al., 2013) uses a probabilistic framework in which wavefront sensing and object estimation are done simultaneously. A maximum likelihood model of optical aberrations and object is estimated using Bayesian inference making use of as many constrains as possible: namely, wavelength diversity, or any other priors, such as knowledge of the instrument, and estimated position of planets. ANDROMEDA (Cantalloube et al., 2015) and COFFEE (Paul et al., 2013) use a similar approach.

- Pair-wise probing: similarly to the SCC, probes can be sent using the DM; a known probe adds sufficient diversity in the speckle field so as to allow for a direct estimate of the wavefront in the image plane. This technique will be discussed in detail in Chapter 6.

- A machine learning approach was recently proposed by Orban de Xivry et al. (2021). They demonstrate in simulations improved sensitivity for broad range of flux levels without the need for an iterative process. The biggest drawback is the need for considerable computing power.

As mentioned before, WFSC can also be used to create a dark area in the image plane, or dark hole (DH), where the stellar noise is nulled to isolate the science object signal. This is done in the case where the limitation is quasi-static speckles. The idea is similar to what we have seen: an estimation of the wavefront is computed and fed to a controller in order to find a DM shape that results in the DH. In this case, the light remaining in the image plane after the coronagraph is made to interfere with itself to create the DH. There are several algorithms to achieve this, and I list here a few examples:

- Electric field conjugation (EFC, Give'on et al. (2007)): EFC uses a Jacobian of the optical system with respect to the DMs to find a DM shape that minimizes the intensity at the image plane. EFC is currently among the preferred WFSC solutions for systems limited by quasi-static speckles (Groff et al., 2016), and is planned to be tested in the Roman Coronagraph Instrument (Kasdin, Bailey, et al., 2020), and HabEx and LUVOIR (The HabEx Team, 2019; The LUVOIR Team, 2019). This algorithm is used extensively in this thesis, and it will be discussed in depth in Chapters 4 and 6.

- Stroke minimization: introduced by Pueyo et al. (2011) it follows a similar approach to EFC, only that the null solution is chosen to minimize the stroke of the DM in order to avoid excessive throughput (of planet light) loss. In reality, stroke minimization is mathematically identical to EFC, when EFC uses a Tikhonov regularization (Groff et al., 2016).

- Speckle nulling: a similar method to EFC, it deals with speckles one at a time requiring little knowledge about the optical system. It assumes that a speckle is perfectly coherent, and, with a DM sinusoidal probe, an artificial speckle of supplementary phase, or anti-speckle, nulls it by destructively interfering with it. A formal review of speckle nulling is given by Bordé et al. (2006).

- L-BFGS-B: phase retrieval using L-BFGS-B has been proposed in the past (Jurling et al., 2014), and was recently introduced as a WFSC algorithm, as an alternative to EFC (Will et al., 2021). Its main advantage with respect to EFC is memory saving, which is important for space based systems in which memory is a scarce resource.

Although MEDUSAE and COFFEE were mentioned as a wavefront sensing method earlier in this section, they could well be considered in the list above. MEDUSAE, for instance, can be used in an iterative fashion, and can potentially be used to form a DH, provided that there is enough constraining information (Ygouf et al., 2013).

Last, but definitely not least concerning WFSC is DM technology. Two main families of DMs are used in high contrast imaging applications that are categorized depending on the actuation technology: electrostrictive actuators (Ealey et al., 2004) and electrostatical microelectromechanical system (MEMS) actuators (Bifano, 2011). In electrostrictive DMs, the actuator is physically attached to the mirror membrane: voltage is applied to the actuator, which changes size and thus shapes the mirror membrane. In a MEMS DM, the actuator is not in contact with the membrane; the shape of the membrane is changed by applying a charge to the actuator electrode and keeping the membrane at ground voltage. Fig. 1.11 shows a schematic of both actuator technologies. The important characteristics of a DM that drive its performance are:

- Inter-actuator distance. MEMS DM manufacturing allows for more compact actuators with respect to electrostrictive. That means that for the same number of actuators, the MEMS DM can be smaller. This becomes important when using two DMs. The use of two DMs is necessary when digging a DH correcting for amplitude aberrations for a symmetric DH shape (when using WFSC algorithms that take linearization assumptions such as EFC) (Pueyo et al., 2009). There exists an optimal separation between the DMs when doing this correction that depends on the actuator pitch; this separation is typically a few meters, and can become unpractical if the actuator pitch is not small enough. This is more constraining in space-based systems where having a compact optical layout is an important requirement.

- Number of actuators. The number of actuators inscribed in the pupil drives the control area in the image plane: the Nyquist limit sets the outer working angle (OWA) to OWA $= N_{act}/2\ \lambda/D$. However, there are are solutions to reach beyond the Nyquist limit by using coherent light from diffracted satellite spots (Sirbu et al., 2017).

- Achievable stroke. This is usually identified as being more important for ground-based systems, where aberrations from atmospheric aberrations require significantly more stroke than any other source of aberrations (Madec, 2012). However, in space based telescopes with obstructed apertures, if the DMs are in charge of performing the apodization, the DM stroke needed is high (Trauger et al., 2016).

- Actuator height resolution. The number of logical bits provided by the DM electronics and the available total stroke set the height resolution. With more modest raw contrast requirements, ground-based telescopes do not need as much resolution. On the other hand, when aiming to achieve 10^{-10} raw contrast in space-based telescopes the requirements are very stringent: <10 pm resolution is needed to reduce quantization errors (G. Ruane, Echeverri, et al., 2020).

- Temporal response. The electronics drive the temporal response of a DM. Providing compact DM electronics is important in space-based systems (Bendek, G. J. Ruane, et al., 2020), but rapid correction rates are a key aspect of ground-based systems to beat the atmospheric turbulence time scales.

- Stability. Surface shape stability, including shape repeatability and hysteresis, is an important requirement for space-based observatories where the WFSC process and target acquisition take a long time, of the order of hours, see e.g. J. E. Krist et al. (2015), Prada, Serabyn, et al. (2019) or Redmond et al. (2021).

- Surface quality. A limiting aspect of MEMS DMs is their printed through surface, commonly known as quilting. This limits the achievable contrast introducing chromatic errors when working with two DMs (J. Krist et al., 2019). Quilting has to be <1 nm RMS to meet contrast requirements of 10^{-10} (A. J. E. Riggs et al., 2021).

- Environmental factors. Since MEMS DMs have a gap between the actuator and the membrane they are less likely to produce unwanted shapes due to environmental changes (Bendek, G. J. Ruane, et al., 2020). For the same reason, humidity and pressure are an important factor with MEMS DMs: an electrical discharge between actuator and membrane can permanently damage actuators. For space based systems, the electronics and DM must operate in vacuum conditions, at certain temperature ranges, and must subsist launch vibrations (Prada, Liu, et al., 2021).

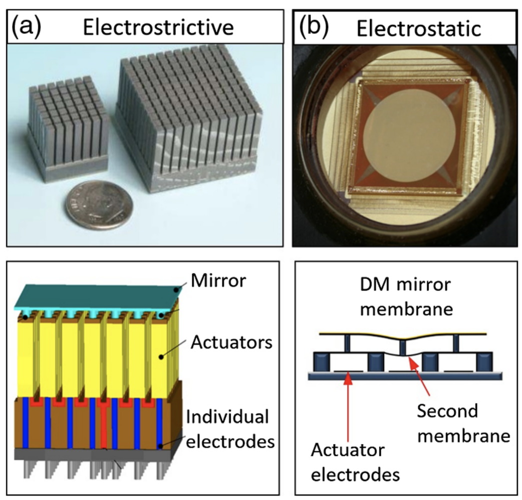

Figure 1.11 The two main deformable mirror technologies are electrostrictive (*left*) and electrostatic MEMS (*right*). Taken from Bendek, G. J. Ruane, et al. (2020)

Observation strategy and post-processing

Observation strategies are carefully designed to tackle the speckle noise. In this section I discuss speckle noise related to quasi-static aberrations. These speckles, given their nature, behave in certain ways that are utilized by astronomers to their advantage. First, speckles scale in size with wavelength; this fact is exploited by spectral differential imaging (SDI, Racine et al. (1999)). SDI helps discriminate the science object from the speckles by acquiring multiple images in different spectral channels; the speckles *move out* proportionally with wavelength. See Fig. 1.12 for a graphical illustration of this, and the following methods. Second, the position of the speckles does not depend on the roll rotation of the telescope, they depend on the rotation of the instrument and telescope optics with respect to the detector chip, which generally rotate jointly. This is exploited by angular differential imaging (ADI, Marois, Lafrenière, et al. (2006)). Multiple images are taken at different roll angles, the sky rotates in each image, but not the speckles. The speckles for each roll angle are subtracted using a model of the PSF. Finally, by de-rotating the images, the residual speckles can be subtracted since they are randomly distributed. Third, the speckle field does not depend on the target star, in other words, two identical stars with the same brightness and spectral features, produce the same speckles for a given coronagraph instrument, weather either hosts a planet or not. Therefore, subtracting one star's image from another one with similar properties is done to eliminate speckles. This is called reference differential imaging (RDI, see e.g. Lafrenière et al. (2007) and G. Ruane, Ngo, et al. (2019)).

These three strategies have been widely successful and are an integral part of any observational strategy nowadays. However, they all have certain limitations. For instance, ADI is only effective for a large enough angle or, equivalently, if the object is at enough angular separation, if not, the resulting image suffers from self-subtraction of the science object (Esposito et al., 2014). RDI requires reference images, for which time of acquisition required is comparable to the time of acquisition of a science target image; this results in less time available for science. While this is generally true, RDI can take advantage of a reference library of PSF, in which certain resemblance to the target image is hoped to be found and utilised. A successful method to do so is by creating a reference image with PCA with a set of reference images. This was introduced by Soummer et al. (2012) with the name of Karhunen-Loève image projection (KLIP). KLIP works as follows: an orthogonal basis is derived from the reference library via PCA, then the target image is projected onto that basis to create a reference image.

SDI is particularly interesting since the spectral information, not only provides diversity to filter out the speckles, but it also is of scientific interest. A popular instrument concept to simultaneously obtain spatial and spectral information is the integral field spectrograph (IFS, AKA integral field unit, IFU). The IFS divides the image plane in multiple sub-apertures, or *spaxels*, the light of which is collimated and sent through a disperser element and, finally, the spectra of all spaxels are

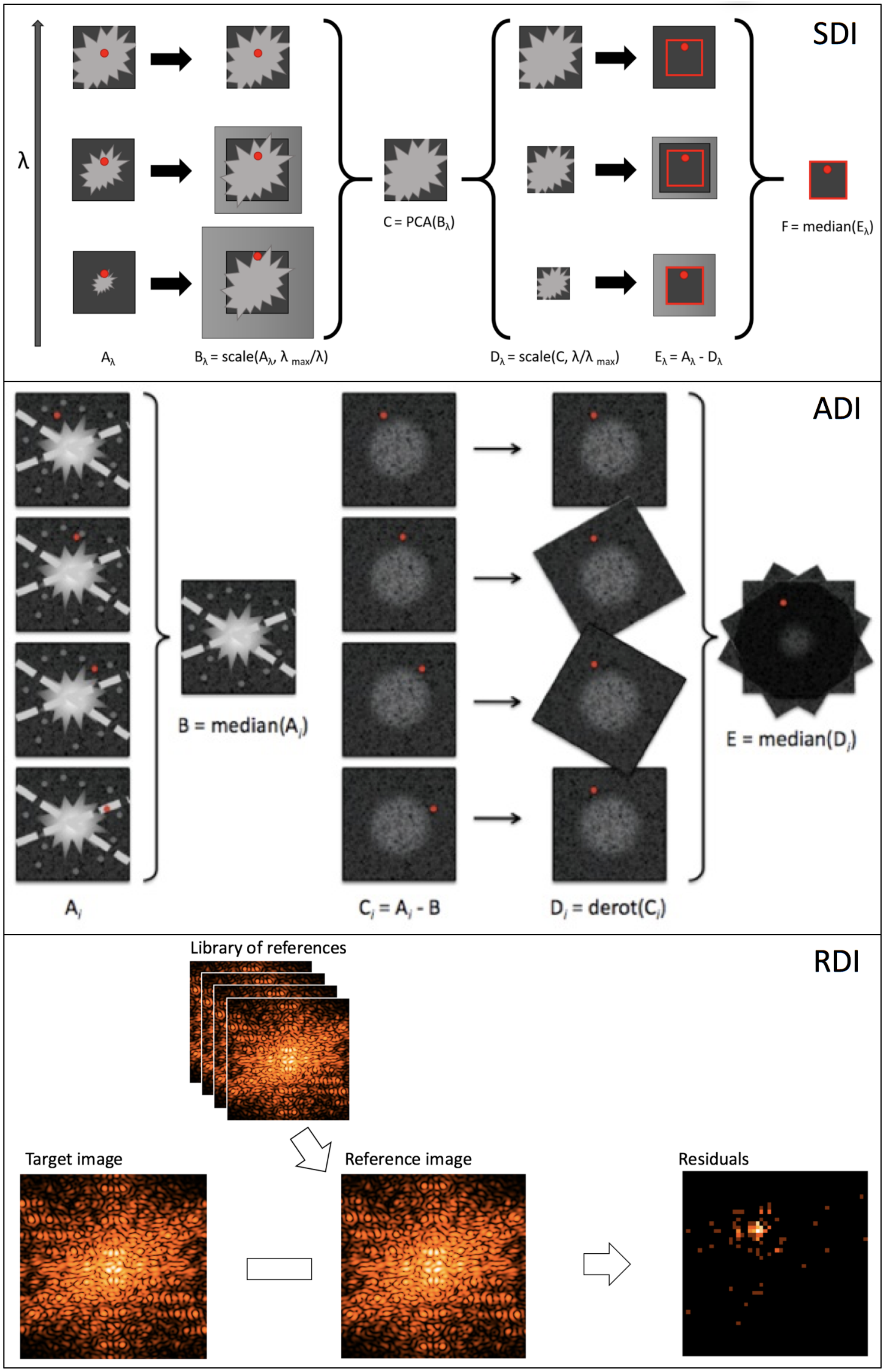

Figure 1.12 *Top:* spectral differential imaging, taken from Kiefer, S. et al. (2021), *middle:* angular differential imaging, credit: Thalmann, *bottom:* reference differential imaging. The illustration for SDI includes a principal component analysis (PCA) based method, which is more sophisticated than simply visually inspection.

imaged on the same detector. In Fig. 1.13 I show an IFS explanatory graphic of a common version of IFS in which the image plane is sampled with a lenslet array. In the same spirit, MKIDs (Microwave Kinetic Inductance Detectors, Mazin et al. (2012)) detectors are being developed and tested to fight speckle noise. MKIDs are very fast detectors with the capability of identifying the photon's energy at each arrival. Furthermore, these are read-out noise-free and dark current-free detectors. They have been tested at Subaru with promising results (Walter et al., 2020).

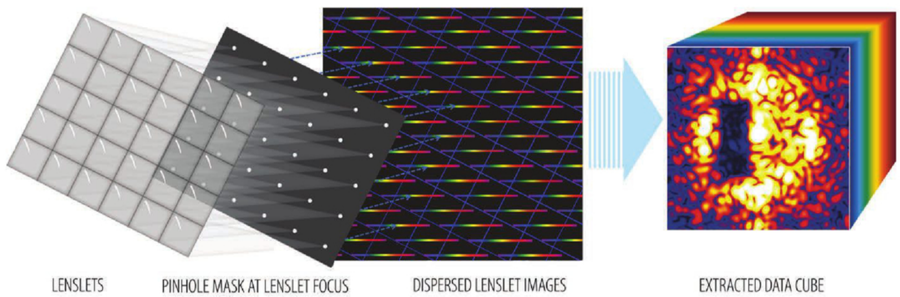

Figure 1.13 Lenslet-based IFS. In this particular example, taken from McElwain et al. (2016), a pinhole array stops the diffraction from the spaxels to avoid spectral crosstalk in the image plane.

Combining all three post-processing approaches when data or capabilities is available seems to always be beneficial (Marois, Zuckerman, et al., 2010; Rameau et al., 2015; Gerard and Marois, 2016; Gerard, Marois, et al., 2019). I have not mentioned dual-mode polarimetric imaging, which adds more diversity from polarizing astrophysical events, which, when it comes to combating speckles, the more the merrier. Indeed, as they say, information is power, and it certainly applies to high contrast imaging (Ygouf et al., 2013; Guyon, Norris, et al., 2021). All of these methods consist on modulating, someway or another, the coherent signal from the star to differentiate the signal from the planet. Which brings us to the next section.

Combining high contrast and high resolution spectroscopy

High dispersion coronagraphy (HDC) (Kawahara et al., 2014; Sparks et al., 2002; Kok et al., 2014; I. Snellen et al., 2015; J. Wang, Mawet, G. Ruane, et al., 2017; Mawet et al., 2017) combines high contrast imaging with high resolution spectroscopy to enhance the planet SNR. In this concept, the coronagraph acts as a spatial filter: as seen earlier in this chapter, the coronagraph filters out the starlight in the image plane favoring the discrimination of the planet signal. The high resolution component of HDC acts as a spectral filter: (1) at medium resolution, speckles can be distinguished by their spectral features, which replicate those of the star, (2) at high resolution, the RV of the planet can be distinguished from the star's; a Doppler shift difference between planet and star occurs for any non-face-on orbits.

High spectral resolution allows the probing of molecular and atomic abundances in an exoplanet atmosphere through cross-correlation methods (Konopacky et al., 2013; T. S. Barman et al., 2015; Wilcomb et al., 2020). But that's not all. Doppler shift RV measurements provide information that is used to compute the orbit, as discussed in Sec. 1.2. Besides, the RV signal in terms of Doppler shift is much stronger from the planet; the planet moves much faster. Furthermore, RV measurements, provided that the position of the planet is known, can break the eccentricity-inclination degeneracy that occur when the planet is not imaged at enough epochs relative to its period (I. A. G. Snellen et al., 2014; Ruffio et al., 2019). The rotational velocity, or spin, of a planet can be inferred by measuring the broadening of absorption lines in the spectrum (I. A. G. Snellen et al., 2014; Bryan et al., 2018; J. J. Wang, Ruffio, et al., 2021). Finally, with enough measurements spanning the rotation period, the spot coverage over the companion, due to weather phenomena, can be inferred with Doppler mapping (Crossfield et al., 2014).

HDC leverages the technology available to enhance the science output. This is already leading to amazing results, and is projected to improve future observatories capabilities (J. Wang, Mawet, Hu, et al., 2018). Indeed, exploring technology synergies is a sure pathway to maximize the scientific yield in this field. The next chapter is a good example of this: the combination of different detection methods is exploited to improve our knowledge of a notoriously elusive exoplanet, ϵ Eridani b.

BIBLIOGRAPHY

Bailes, M. et al. (Sept. 2011). “Transformation of a Star into a Planet in a Millisecond Pulsar Binary”. In: *Science* 333.6050, p. 1717. DOI: 10.1126/science.1208890. arXiv: 1108.5201 [astro-ph.SR].

Baranne, A. et al. (Oct. 1996). “ELODIE: A spectrograph for accurate radial velocity measurements.” In: *Astronomy and Astrophysics, Supplement* 119, pp. 373–390.

Barman, T. S. et al. (May 2015). “Simultaneous Detection of Water, Methane, and Carbon Monoxide in the Atmosphere of Exoplanet HR8799b”. In: *Astrophysical Journal* 804.1, 61, p. 61. DOI: 10.1088/0004-637X/804/1/61. arXiv: 1503.03539 [astro-ph.EP].

Baudoz, P., A. Boccaletti, et al. (Jan. 2006). “The Self-Coherent Camera: a new tool for planet detection”. In: *IAU Colloq. 200: Direct Imaging of Exoplanets: Science & Techniques*. Ed. by C. Aime and F. Vakili, pp. 553–558. DOI: 10.1017/S174392130600994X.

Baudoz, P., Y. Rabbia, and J. Gay (Jan. 2000). “Achromatic interfero coronagraphy I. Theoretical capabilities for ground-based observations”. In: *Astronomy and Astrophysics, Supplement* 141, pp. 319–329. DOI: 10.1051/aas:2000120.

Bean, J. L. and A. Seifahrt (Mar. 2009). “The architecture of the GJ 876 planetary system. Masses and orbital coplanarity for planets b and c”. In: *Astronomy and Astrophysics* 496.1, pp. 249–257. DOI: 10.1051/0004-6361/200811280. arXiv: 0901.3144 [astro-ph.EP].

Beatty, T. G. and B. S. Gaudi (Dec. 2015). “Astrophysical Sources of Statistical Uncertainty in Precision Radial Velocities and Their Approximations”. In: *Publications of the ASP* 127.958, p. 1240. DOI: 10.1086/684264. arXiv: 1507.00780 [astro-ph.SR].

Beckers, J. M. (Jan. 1993). “Adaptive Optics for Astronomy: Principles, Performance, and Applications”. In: *Annual Review of Astronomy and Astrophysics* 31, pp. 13–62. DOI: 10.1146/annurev.aa.31.090193.000305.

Bedell, M. et al. (Oct. 2019). “WOBBLE: A Data-driven Analysis Technique for Time-series Stellar Spectra”. In: *Astronomical Journal* 158.4, 164, p. 164. DOI: 10.3847/1538-3881/ab40a7. arXiv: 1901.00503 [astro-ph.IM].

Belikov, R. et al. (2021). “Theoretical performance limits for coronagraphs on obstructed and unobstructed apertures: how much can current designs be improved?” In: *Techniques and Instrumentation for Detection of Exoplanets X*. Ed. by S. B. Shaklan and G. J. Ruane. Vol. 11823. International Society for Optics and Photonics. SPIE, pp. 293–312. URL: https://doi.org/10.1117/12.2594855.

Bendek, E. A., S. Martin, and O. Guyon (2021). "Astrometry exoplanet detection using the Habex Workhorse camera". In: *Techniques and Instrumentation for Detection of Exoplanets X*. Ed. by S. B. Shaklan and G. J. Ruane. Vol. 11823. International Society for Optics and Photonics. SPIE. URL: https://doi.org/10.1117/12.2594996.

Bendek, E. A., G. J. Ruane, et al. (2020). "Microelectromechanical deformable mirror development for high-contrast imaging, part 1: miniaturized, flight-capable control electronics". In: *Journal of Astronomical Telescopes, Instruments, and Systems* 6.4, pp. 1–20. DOI: 10.1117/1.JATIS.6.4.045001. URL: https://doi.org/10.1117/1.JATIS.6.4.045001.

Beuzit, J. .-L. et al. (Nov. 2019). "SPHERE: the exoplanet imager for the Very Large Telescope". In: *Astronomy and Astrophysics* 631, A155, A155. DOI: 10.1051/0004-6361/201935251. arXiv: 1902.04080 [astro-ph.IM].

Bifano, T. (2011). "MEMS deformable mirrors". In: *Nature Photonics* 5.1, pp. 21–23. DOI: 10.1038/nphoton.2010.297. URL: https://doi.org/10.1038/nphoton.2010.297.

Blackman, R. T., J. M. J. Ong, and D. A. Fischer (July 2019). "The Measured Impact of Chromatic Atmospheric Effects on Barycentric Corrections: Results from the EXtreme PREcision Spectrograph". In: *Astronomical Journal* 158.1, 40, p. 40. DOI: 10.3847/1538-3881/ab24c3. arXiv: 1906.01653 [astro-ph.EP].

Bond, C. Z. et al. (July 2020). "Adaptive optics with an infrared pyramid wavefront sensor at Keck". In: *Journal of Astronomical Telescopes, Instruments, and Systems* 6, 039003, p. 039003. DOI: 10.1117/1.JATIS.6.3.039003.

Bonnefoy, M. et al. (Mar. 2016). "First light of the VLT planet finder SPHERE. IV. Physical and chemical properties of the planets around HR8799". In: *Astronomy and Astrophysics* 587, A58, A58. DOI: 10.1051/0004-6361/201526906. arXiv: 1511.04082 [astro-ph.EP].

Bordé, P. J. and W. A. Traub (Feb. 2006). "High-Contrast Imaging from Space: Speckle Nulling in a Low-Aberration Regime". In: *Astrophysical Journal* 638.1, pp. 488–498. DOI: 10.1086/498669. arXiv: astro-ph/0510597 [astro-ph].

Borucki, W. J. et al. (Feb. 2010). "Kepler Planet-Detection Mission: Introduction and First Results". In: *Science* 327.5968, p. 977. DOI: 10.1126/science.1185402.

Boss, A. P. et al. (Nov. 2009). "The Carnegie Astrometric Planet Search Program". In: *Publications of the ASP* 121.885, p. 1218. DOI: 10.1086/647960. arXiv: 0909.2008 [astro-ph.IM].

Bower, G. C., A. Bolatto, E. B. Ford, A. Fries, et al. (Oct. 2011). "Radio Interferometric Planet Search. II. Constraints on Sub-jupiter-mass Companions to GJ 896A". In: *Astrophysical Journal* 740.1, 32, p. 32. DOI: 10.1088/0004-637X/740/1/32. arXiv: 1107.3180 [astro-ph.SR].

Bower, G. C., A. Bolatto, E. B. Ford, and P. Kalas (Aug. 2009). “Radio Interferometric Planet Search. I. First Constraints On Planetary Companions For Nearby, Low-Mass Stars From Radio Astrometry”. In: *Astrophysical Journal* 701.2, pp. 1922–1939. DOI: 10.1088/0004-637X/701/2/1922. arXiv: 0907.1680 [astro-ph.EP].

Bowler, B. P. (Oct. 2016). “Imaging Extrasolar Giant Planets”. In: *Publications of the ASP* 128.968, p. 102001. DOI: 10.1088/1538-3873/128/968/102001. arXiv: 1605.02731 [astro-ph.EP].

Bracewell, R. N. (1978). “Detecting nonsolar planets by spinning infrared interferometer”. In: *Nature* 274.5673, pp. 780–781. DOI: 10.1038/274780a0. URL: https://doi.org/10.1038/274780a0.

Brandt, T. D. (Dec. 2018). “The Hipparcos-Gaia Catalog of Accelerations”. In: *Astrophysical Journal, Supplement* 239.2, 31, p. 31. DOI: 10.3847/1538-4365/aaec06. arXiv: 1811.07283 [astro-ph.SR].

– (May 2021). “The Hipparcos-Gaia Catalog of Accelerations: Gaia EDR3 Edition”. In: *arXiv e-prints*, arXiv:2105.11662, arXiv:2105.11662. arXiv: 2105.11662 [astro-ph.GA].

Bryan, M. L. et al. (2018). “Constraints on the spin evolution of young planetary-mass companions”. In: *Nature Astronomy* 2.2, pp. 138–144. DOI: 10.1038/s41550-017-0325-8. URL: https://doi.org/10.1038/s41550-017-0325-8.

Bryson, S. et al. (Jan. 2021). “The Occurrence of Rocky Habitable-zone Planets around Solar-like Stars from Kepler Data”. In: *Astronomical Journal* 161.1, 36, p. 36. DOI: 10.3847/1538-3881/abc418. arXiv: 2010.14812 [astro-ph.EP].

Burrows, A., K. Heng, and T. Nampaisarn (July 2011). “The Dependence of Brown Dwarf Radii on Atmospheric Metallicity and Clouds: Theory and Comparison with Observations”. In: *Astrophysical Journal* 736.1, 47, p. 47. DOI: 10.1088/0004-637X/736/1/47. arXiv: 1102.3922 [astro-ph.SR].

Campbell, B., G. A. H. Walker, and S. Yang (Aug. 1988). “A Search for Substellar Companions to Solar-type Stars”. In: *Astrophysical Journal* 331, p. 902. DOI: 10.1086/166608.

Cantalloube, F. et al. (Oct. 2015). “Direct exoplanet detection and characterization using the ANDROMEDA method: Performance on VLT/NaCo data”. In: *Astronomy and Astrophysics* 582, A89, A89. DOI: 10.1051/0004-6361/201425571. arXiv: 1508.06406 [astro-ph.IM].

Carson, J. et al. (Jan. 2013). “DIRECT IMAGING DISCOVERY OF A “SUPER-JUPITER” AROUND THE LATE B-TYPE STAR κ And”. In: *The Astrophysical Journal* 763.2, p. L32. DOI: 10.1088/2041-8205/763/2/l32. URL: https://doi.org/10.1088/2041-8205/763/2/l32.

Charbonneau, D. et al. (Mar. 2002). “Detection of an Extrasolar Planet Atmosphere”. In: *Astrophysical Journal* 568.1, pp. 377–384. DOI: 10.1086/338770. arXiv: astro-ph/0111544 [astro-ph].

Collier Cameron, A. et al. (Aug. 2021). “Separating planetary reflex Doppler shifts from stellar variability in the wavelength domain”. In: *Monthly Notices of the RAS* 505.2, pp. 1699–1717. DOI: 10.1093/mnras/stab1323. arXiv: 2011.00018 [astro-ph.EP].

Crass, J. et al. (July 2021). “Extreme Precision Radial Velocity Working Group Final Report”. In: *arXiv e-prints*, arXiv:2107.14291, arXiv:2107.14291. arXiv: 2107.14291 [astro-ph.IM].

Crossfield, I. J. M. et al. (2014). “A global cloud map of the nearest known brown dwarf”. In: *Nature* 505.7485, pp. 654–656. DOI: 10.1038/nature12955. URL: https://doi.org/10.1038/nature12955.

Crouzier, A., F. Malbet, F. Henault, et al. (Nov. 2016). “A detector interferometric calibration experiment for high precision astrometry”. In: *Astronomy and Astrophysics* 595, A108, A108. DOI: 10.1051/0004-6361/201526321. arXiv: 1609.02477 [astro-ph.IM].

Crouzier, A., F. Malbet, F. Hénault, et al. (July 2016). “The latest results from DICE (Detector Interferometric Calibration Experiment)”. In: *Space Telescopes and Instrumentation 2016: Optical, Infrared, and Millimeter Wave*. Ed. by H. A. MacEwen et al. Vol. 9904. Society of Photo-Optical Instrumentation Engineers (SPIE) Conference Series, 99045G. DOI: 10.1117/12.2234304. arXiv: 1608.00360 [astro-ph.IM].

Cugno, G. et al. (Sept. 2021). “Molecular mapping of the PDS70 system. No molecular absorption signatures from the forming planet PDS70 b”. In: *Astronomy and Astrophysics* 653, A12, A12. DOI: 10.1051/0004-6361/202140632. arXiv: 2106.03615 [astro-ph.EP].

Cunha, D. et al. (Aug. 2014). “Impact of micro-telluric lines on precise radial velocities and its correction”. In: *Astronomy and Astrophysics* 568, A35, A35. DOI: 10.1051/0004-6361/201423723. arXiv: 1407.0181 [astro-ph.EP].

Curiel, S. et al. (Sept. 2020). “An Astrometric Planetary Companion Candidate to the M9 Dwarf TVLM 513-46546”. In: *Astronomical Journal* 160.3, 97, p. 97. DOI: 10.3847/1538-3881/ab9e6e. arXiv: 2008.01595 [astro-ph.EP].

Davis, A. B. et al. (Sept. 2017). “Insights on the Spectral Signatures of Stellar Activity and Planets from PCA”. In: *Astrophysical Journal* 846.1, 59, p. 59. DOI: 10.3847/1538-4357/aa8303. arXiv: 1708.00491 [astro-ph.EP].

Dawson, R. I. and D. C. Fabrycky (Oct. 2010). “Radial Velocity Planets De-aliased: A New, Short Period for Super-Earth 55 Cnc e”. In: *Astrophysical Journal* 722.1, pp. 937–953. DOI: 10.1088/0004-637X/722/1/937. arXiv: 1005.4050 [astro-ph.EP].

de Bruijne, J. H. J. (Sept. 2012). "Science performance of Gaia, ESA's space-astrometry mission". In: *Astrophysics and Space Science* 341.1, pp. 31–41. DOI: 10.1007/s10509-012-1019-4. arXiv: 1201.3238 [astro-ph.IM].

De Rosa, R. J. et al. (Jan. 2020). "An Updated Visual Orbit of the Directly Imaged Exoplanet 51 Eridani b and Prospects for a Dynamical Mass Measurement with Gaia". In: *Astronomical Journal* 159.1, 1, p. 1. DOI: 10.3847/1538-3881/ab4da4. arXiv: 1910.10169 [astro-ph.EP].

Del Moro, D. (Dec. 2004). "Solar granulation properties derived from three different time series". In: *Astronomy and Astrophysics* 428, pp. 1007–1015. DOI: 10.1051/0004-6361:20040466.

Dorn, C. et al. (May 2015). "Can we constrain the interior structure of rocky exoplanets from mass and radius measurements?" In: *Astronomy and Astrophysics* 577, A83, A83. DOI: 10.1051/0004-6361/201424915. arXiv: 1502.03605 [astro-ph.EP].

Dressing, C. D. and D. Charbonneau (June 2015). "THE OCCURRENCE OF POTENTIALLY HABITABLE PLANETS ORBITING M DWARFS ESTIMATED FROM THE FULLKEPLERDATASET AND AN EMPIRICAL MEASUREMENT OF THE DETECTION SENSITIVITY". In: *The Astrophysical Journal* 807.1, p. 45. DOI: 10.1088/0004-637x/807/1/45. URL: https://doi.org/10.1088/0004-637x/807/1/45.

Dumusque, X. (Nov. 2018). "Measuring precise radial velocities on individual spectral lines. I. Validation of the method and application to mitigate stellar activity". In: *Astronomy and Astrophysics* 620, A47, A47. DOI: 10.1051/0004-6361/201833795. arXiv: 1809.01548 [astro-ph.SR].

Dumusque, X. et al. (Aug. 2015). "Characterization of a Spurious One-year Signal in HARPS Data". In: *Astrophysical Journal* 808.2, 171, p. 171. DOI: 10.1088/0004-637X/808/2/171. arXiv: 1508.00596 [astro-ph.EP].

Ealey, M. A. and J. T. Trauger (2004). "High-density deformable mirrors to enable coronagraphic planet detection". In: *UV/Optical/IR Space Telescopes: Innovative Technologies and Concepts*. Ed. by H. A. MacEwen. Vol. 5166. International Society for Optics and Photonics. SPIE, pp. 172–179. URL: https://doi.org/10.1117/12.512729.

Echeverri, D. et al. (Dec. 2020). "Detecting and characterizing close-in exoplanets with vortex fiber nulling". In: *Society of Photo-Optical Instrumentation Engineers (SPIE) Conference Series*. Vol. 11446. Society of Photo-Optical Instrumentation Engineers (SPIE) Conference Series, p. 1144619. DOI: 10.1117/12.2563142. arXiv: 2012.04239 [astro-ph.IM].

Eisenhauer, F. et al. (Mar. 2011). "GRAVITY: Observing the Universe in Motion". In: *The Messenger* 143, pp. 16–24.

Eriksson, U. and L. Lindegren (Dec. 2007). “Limits of ultra-high-precision optical astrometry. Stellar surface structures”. In: *Astronomy and Astrophysics* 476.3, pp. 1389–1400. DOI: 10.1051/0004-6361:20078031. arXiv: 0706.1646 [astro-ph].

Esposito, T. M. et al. (Jan. 2014). “Modeling Self-subtraction in Angular Differential Imaging: Application to the HD 32297 Debris Disk”. In: *Astrophysical Journal* 780.1, 25, p. 25. DOI: 10.1088/0004-637X/780/1/25. arXiv: 1310.7026 [astro-ph.EP].

Fischer, D. A. et al. (May 2016). “State of the Field: Extreme Precision Radial Velocities”. In: *Publications of the Astronomical Society of the Pacific* 128.964, p. 066001. DOI: 10.1088/1538-3873/128/964/066001. URL: https://doi.org/10.1088/1538-3873/128/964/066001.

Fressin, F. et al. (Apr. 2013). “The False Positive Rate of Kepler and the Occurrence of Planets”. In: *Astrophysical Journal* 766.2, 81, p. 81. DOI: 10.1088/0004-637X/766/2/81. arXiv: 1301.0842 [astro-ph.EP].

Fulton, B. J., E. A. Petigura, S. Blunt, et al. (Apr. 2018). “RadVel: The Radial Velocity Modeling Toolkit”. In: *Publications of the Astronomical Society of the Pacific* 130.986, p. 044504. DOI: 10.1088/1538-3873/aaaaa8. arXiv: 1801.01947 [astro-ph.IM].

Fulton, B. J., E. A. Petigura, A. W. Howard, et al. (Sept. 2017). “The California-Kepler Survey. III. A Gap in the Radius Distribution of Small Planets”. In: *Astronomical Journal* 154.3, 109, p. 109. DOI: 10.3847/1538-3881/aa80eb. arXiv: 1703.10375 [astro-ph.EP].

Gaia Collaboration (Aug. 2018). “Gaia Data Release 2. Summary of the contents and survey properties”. In: *Astronomy and Astrophysics* 616, A1, A1. DOI: 10.1051/0004-6361/201833051. arXiv: 1804.09365 [astro-ph.GA].

– (May 2021). “Gaia Early Data Release 3. Summary of the contents and survey properties”. In: *Astronomy and Astrophysics* 649, A1, A1. DOI: 10.1051/0004-6361/202039657. arXiv: 2012.01533 [astro-ph.GA].

Gaspar, A. and G. Rieke (Apr. 2020). “New HST data and modeling reveal a massive planetesimal collision around Fomalhaut”. In: *Proceedings of the National Academy of Science* 117.18, pp. 9712–9722. DOI: 10.1073/pnas.1912506117. arXiv: 2004.08736 [astro-ph.EP].

Gaudi, B. S. (Feb. 2010). “Exoplanetary Microlensing”. In: *arXiv e-prints*, arXiv:1002.0332, arXiv:1002.0332. arXiv: 1002.0332 [astro-ph.EP].

Gerard, B. L. and C. Marois (July 2016). “Planet detection down to a few λ/D: an RSDI/TLOCI approach to PSF subtraction”. In: *Adaptive Optics Systems V*. Ed. by E. Marchetti, L. M. Close, and J.-P. Véran. Vol. 9909. Society of Photo-Optical Instrumentation Engineers (SPIE) Conference Series, p. 990958. DOI: 10.1117/12.2231905. arXiv: 1609.08692 [astro-ph.IM].

Gerard, B. L., C. Marois, et al. (July 2019). “A Chromaticity Analysis and PSF Subtraction Techniques for SCExAO/CHARIS Data”. In: *The Astronomical Journal* 158.1, p. 36. DOI: 10.3847/1538-3881/ab21d4. URL: https://doi.org/10.3847/1538-3881/ab21d4.

Give’on, A. et al. (2007). “Broadband wavefront correction algorithm for high-contrast imaging systems”. In: *Astronomical Adaptive Optics Systems and Applications III*. Ed. by R. K. Tyson and M. Lloyd-Hart. Vol. 6691. International Society for Optics and Photonics. SPIE, pp. 63–73. URL: https://doi.org/10.1117/12.733122.

Goździewski, K. and C. Migaszewski (Oct. 2020). “An Exact, Generalized Laplace Resonance in the HR 8799 Planetary System”. In: *The Astrophysical Journal* 902.2, p. L40. DOI: 10.3847/2041-8213/abb881. URL: https://doi.org/10.3847/2041-8213/abb881.

Gravity Collaboration (June 2017). “First light for GRAVITY: Phase referencing optical interferometry for the Very Large Telescope Interferometer”. In: *Astronomy and Astrophysics* 602, A94, A94. DOI: 10.1051/0004-6361/201730838. arXiv: 1705.02345 [astro-ph.IM].

Gravity Collaboration et al. (Mar. 2019). “First direct detection of an exoplanet by optical interferometry. Astrometry and K-band spectroscopy of HR 8799 e”. In: *Astronomy and Astrophysics* 623, L11, p. L11. DOI: 10.1051/0004-6361/201935253. arXiv: 1903.11903 [astro-ph.EP].

Greenbaum, A. Z. et al. (May 2018). “GPI Spectra of HR 8799 c, d, and e from 1.5 to 2.4 μm with KLIP Forward Modeling”. In: *The Astronomical Journal* 155.6, p. 226. DOI: 10.3847/1538-3881/aabcb8. URL: https://doi.org/10.3847/1538-3881/aabcb8.

Groff, T. D. et al. (2016). “Methods and limitations of focal plane sensing, estimation, and control in high-contrast imaging”. In: *J. Astron. Telesc. Instrum. Syst.* 2.1, p. 011009. DOI: 10.1117/1.JATIS.2.1.011009.

Guyon, O., E. A. Pluzhnik, M. J. Kuchner, et al. (Nov. 2006). “Theoretical Limits on Extrasolar Terrestrial Planet Detection with Coronagraphs”. In: *Astrophysical Journal, Supplement* 167.1, pp. 81–99. DOI: 10.1086/507630. arXiv: astro-ph/0608506 [astro-ph].

Guyon, O. (Jan. 2010). “High Sensitivity Wavefront Sensing with a Nonlinear Curvature Wavefront Sensor”. In: *Publications of the ASP* 122.887, p. 49. DOI: 10.1086/649646. arXiv: 0911.1310 [astro-ph.IM].

Guyon, O., F. Martinache, et al. (Oct. 2010). “High Performance PIAA Coronagraphy with Complex Amplitude Focal Plane Masks”. In: *Astrophysical Journal, Supplement* 190.2, pp. 220–232. DOI: 10.1088/0067-0049/190/2/220.

Guyon, O., B. Norris, et al. (2021). "High contrast imaging at the photon noise limit with self-calibrating WFS/C systems". In: *Techniques and Instrumentation for Detection of Exoplanets X*. Ed. by S. B. Shaklan and G. J. Ruane. Vol. 11823. International Society for Optics and Photonics. SPIE, pp. 376–386. URL: https://doi.org/10.1117/12.2594885.

Guyon, O., E. A. Pluzhnik, R. Galicher, et al. (Mar. 2005). "Exoplanet Imaging with a Phase-induced Amplitude Apodization Coronagraph. I. Principle". In: *Astrophysical Journal* 622.1, pp. 744–758. DOI: 10.1086/427771. arXiv: astro-ph/0412179 [astro-ph].

Haffert, S. Y. et al. (June 2019). "Two accreting protoplanets around the young star PDS 70". In: *Nature Astronomy* 3, pp. 749–754. DOI: 10.1038/s41550-019-0780-5. arXiv: 1906.01486 [astro-ph.EP].

Halverson, S. et al. (Aug. 2016). "A comprehensive radial velocity error budget for next generation Doppler spectrometers". In: *Ground-based and Airborne Instrumentation for Astronomy VI*. Ed. by C. J. Evans, L. Simard, and H. Takami. Vol. 9908. Society of Photo-Optical Instrumentation Engineers (SPIE) Conference Series, 99086P. DOI: 10.1117/12.2232761. arXiv: 1607.05634 [astro-ph.IM].

Hénault, F. (Sept. 2019). "New concepts for calibrating non-common path aberrations in adaptive optics and coronagraph systems". In: *Society of Photo-Optical Instrumentation Engineers (SPIE) Conference Series*. Vol. 11117. Society of Photo-Optical Instrumentation Engineers (SPIE) Conference Series, p. 1111711. DOI: 10.1117/12.2527897. arXiv: 1909.05224 [astro-ph.IM].

Hinkley, S. et al. (Dec. 2013). "The κ Andromedae System: New Constraints on the Companion Mass, System Age, and Further Multiplicity". In: *Astrophysical Journal* 779.2, 153, p. 153. DOI: 10.1088/0004-637X/779/2/153. arXiv: 1309.3372 [astro-ph.EP].

Hinz, P. et al. (2014). "Commissioning the LBTI for use as a nulling interferometer and coherent imager". In: *Optical and Infrared Interferometry IV*. Ed. by J. K. Rajagopal, M. J. Creech-Eakman, and F. Malbet. Vol. 9146. International Society for Optics and Photonics. SPIE, pp. 241–250. URL: https://doi.org/10.1117/12.2057340.

Hinz, P. M. et al. (1998). "Imaging circumstellar environments with a nulling interferometer". In: *Nature* 395.6699, pp. 251–253. DOI: 10.1038/26172. URL: https://doi.org/10.1038/26172.

The HIPPARCOS and TYCHO catalogues. Astrometric and photometric star catalogues derived from the ESA HIPPARCOS Space Astrometry Mission (Jan. 1997). Vol. 1200. ESA Special Publication.

Holzer, P. H. et al. (June 2021). "A Stellar Activity F-statistic for Exoplanet Surveys (SAFE)". In: *Astronomical Journal* 161.6, 272, p. 272. DOI: 10.3847/1538-3881/abf5e0. arXiv: 2104.04887 [astro-ph.EP].

Howard, A. W., J. A. Johnson, et al. (Oct. 2010). "The California Planet Survey. I. Four New Giant Exoplanets". In: *Astrophysical Journal* 721.2, pp. 1467–1481. DOI: 10.1088/0004-637X/721/2/1467. arXiv: 1003.3488 [astro-ph.EP].

Howard, A. W., G. W. Marcy, et al. (June 2012). "PLANET OCCURRENCE WITHIN 0.25 AU OF SOLAR-TYPE STARS FROM KEPLER". In: *The Astrophysical Journal Supplement Series* 201.2, p. 15. DOI: 10.1088/0067-0049/201/2/15. URL: https://doi.org/10.1088/0067-0049/201/2/15.

Howell, S. B. et al. (Apr. 2014). "The K2 Mission: Characterization and Early Results". In: *Publications of the Astronomical Society of the Pacific* 126.938, p. 398. DOI: 10.1086/676406. arXiv: 1402.5163 [astro-ph.IM].

J. Sahlmann, e. a. (2013). "Astrometric detection of exoplanets from the ground". In: *Techniques and Instrumentation for Detection of Exoplanets VI*. Ed. by S. Shaklan. Vol. 8864. International Society for Optics and Photonics. SPIE, pp. 481–489. URL: https://doi.org/10.1117/12.2023929.

Janson, M., A. Brandeker, et al. (2018). "Future Astrometric Space Missions for Exoplanet Science". In: *Handbook of Exoplanets*. Ed. by H. J. Deeg and J. A. Belmonte. Cham: Springer International Publishing, pp. 1331–1342. ISBN: 978-3-319-55333-7. DOI: 10.1007/978-3-319-55333-7_87. URL: https://doi.org/10.1007/978-3-319-55333-7_87.

Janson, M., J. C. Carson, et al. (Mar. 2012). "Infrared Non-detection of Fomalhaut b: Implications for the Planet Interpretation". In: *Astrophysical Journal* 747.2, 116, p. 116. DOI: 10.1088/0004-637X/747/2/116. arXiv: 1201.4388 [astro-ph.EP].

Jones, M. I. et al. (June 2014). "The properties of planets around giant stars". In: *Astronomy and Astrophysics* 566, A113, A113. DOI: 10.1051/0004-6361/201323345. arXiv: 1406.0884 [astro-ph.EP].

Jovanovic, N. et al. (Sept. 2015). "The Subaru Coronagraphic Extreme Adaptive Optics System: Enabling High-Contrast Imaging on Solar-System Scales". In: *Publications of the Astronomical Society of the Pacific* 127, p. 890. DOI: 10.1086/682989. arXiv: 1507.00017 [astro-ph.IM].

Jurling, A. S. and J. R. Fienup (July 2014). "Applications of algorithmic differentiation to phase retrieval algorithms". In: *J. Opt. Soc. Am. A* 31.7, pp. 1348–1359. DOI: 10.1364/JOSAA.31.001348. URL: http://josaa.osa.org/abstract.cfm?URI=josaa-31-7-1348.

Kalas, P., J. R. Graham, and M. Clampin (June 2005). "A planetary system as the origin of structure in Fomalhaut's dust belt". In: *Nature* 435.7045, pp. 1067–1070. DOI: 10.1038/nature03601. arXiv: astro-ph/0506574 [astro-ph].

Kammerer, J. et al. (Aug. 2021). "GRAVITY K-band spectroscopy of HD 206893 B. Brown dwarf or exoplanet". In: *Astronomy and Astrophysics* 652, A57, A57. DOI: 10.1051/0004-6361/202140749. arXiv: 2106.08249 [astro-ph.EP].

Kasdin, N. J., V. P. Bailey, et al. (2020). "The Nancy Grace Roman Space Telescope Coronagraph Instrument (CGI) technology demonstration". In: *Space Telescopes and Instrumentation 2020: Optical, Infrared, and Millimeter Wave*. Ed. by M. Lystrup et al. Vol. 11443. International Society for Optics and Photonics. SPIE, pp. 300–313. URL: `https://doi.org/10.1117/12.2562997`.

Kasdin, N. J., R. J. Vanderbei, et al. (Jan. 2003). "Extrasolar Planet Finding via Optimal Apodized-Pupil and Shaped-Pupil Coronagraphs". In: *The Astrophysical Journal* 582.2, pp. 1147–1161. DOI: `10.1086/344751`. URL: `https://doi.org/10.1086/344751`.

Kawahara, H. et al. (June 2014). "Spectroscopic Coronagraphy for Planetary Radial Velocimetry of Exoplanets". In: *The Astrophysical Journal Supplement Series* 212.2, p. 27. DOI: `10.1088/0067-0049/212/2/27`.

Kempton, E. M. .-R. et al. (Nov. 2018). "A Framework for Prioritizing the TESS Planetary Candidates Most Amenable to Atmospheric Characterization". In: *Publications of the ASP* 130.993, p. 114401. DOI: `10.1088/1538-3873/aadf6f`. arXiv: `1805.03671 [astro-ph.EP]`.

Kenworthy, M. A. et al. (Apr. 2021). "The β Pictoris b Hill sphere transit campaign. I. Photometric limits to dust and rings". In: *Astronomy and Astrophysics* 648, A15, A15. DOI: `10.1051/0004-6361/202040060`. arXiv: `2102.05672 [astro-ph.EP]`.

Kervella, P. et al. (2019). "Stellar and substellar companions of nearby stars from Gaia DR2 - Binarity from proper motion anomaly". In: *A&A* 623, A72. DOI: `10.1051/0004-6361/201834371`. URL: `https://doi.org/10.1051/0004-6361/201834371`.

Kiefer, S. et al. (2021). "Spectral and angular differential imaging with SPHERE/IFS - Assessing the performance of various PCA-based approaches to PSF subtraction". In: *A&A* 652, A33. DOI: `10.1051/0004-6361/202140285`. URL: `https://doi.org/10.1051/0004-6361/202140285`.

Kjeldsen, H. and T. R. Bedding (Jan. 1995). "Amplitudes of stellar oscillations: the implications for asteroseismology." In: *Astronomy and Astrophysics* 293, pp. 87–106. arXiv: `astro-ph/9403015 [astro-ph]`.

Kok, R. J. de et al. (Jan. 2014). "Identifying new opportunities for exoplanet characterisation at high spectral resolution". In: *Astronomy and Astrophysics* 561, A150, A150. DOI: `10.1051/0004-6361/201322947`. arXiv: `1312.3745`.

Konopacky, Q. M. et al. (Mar. 2013). "Detection of Carbon Monoxide and Water Absorption Lines in an Exoplanet Atmosphere". In: *Science* 339.6126, pp. 1398–1401. DOI: `10.1126/science.1232003`. arXiv: `1303.3280 [astro-ph.EP]`.

Kopparapu, R. K. et al. (Apr. 2018). "Exoplanet Classification and Yield Estimates for Direct Imaging Missions". In: *Astrophysical Journal* 856.2, 122, p. 122. DOI: `10.3847/1538-4357/aab205`. arXiv: `1802.09602 [astro-ph.EP]`.

Krist, J. et al. (2019). "Numerical modeling of the Habex coronagraph". In: *Techniques and Instrumentation for Detection of Exoplanets IX*. Ed. by S. B. Shaklan. Vol. 11117. International Society for Optics and Photonics. SPIE, pp. 85–100. URL: https://doi.org/10.1117/12.2530462.

Krist, J. E., B. Nemati, and B. P. Mennesson (2015). "Numerical modeling of the proposed WFIRST-AFTA coronagraphs and their predicted performances". In: *Journal of Astronomical Telescopes, Instruments, and Systems* 2.1, pp. 1–26. DOI: 10.1117/1.JATIS.2.1.011003. URL: https://doi.org/10.1117/1.JATIS.2.1.011003.

Kuchner, M. J. and W. A. Traub (May 2002). "A Coronagraph with a Band-limited Mask for Finding Terrestrial Planets". In: *Astrophysical Journal* 570.2, pp. 900–908. DOI: 10.1086/339625. arXiv: astro-ph/0203455 [astro-ph].

Lacour, S. et al. (July 2014). "Reaching micro-arcsecond astrometry with long baseline optical interferometry. Application to the GRAVITY instrument". In: *Astronomy and Astrophysics* 567, A75, A75. DOI: 10.1051/0004-6361/201423940. arXiv: 1404.1014 [astro-ph.IM].

Lafrenière, D. et al. (May 2007). "A New Algorithm for Point-Spread Function Subtraction in High-Contrast Imaging: A Demonstration with Angular Differential Imaging". In: *Astrophysical Journal* 660.1, pp. 770–780. DOI: 10.1086/513180. arXiv: astro-ph/0702697 [astro-ph].

Lagrange, A. .-M., D. Gratadour, et al. (Jan. 2009). "A probable giant planet imaged in the β Pictoris disk. VLT/NaCo deep L'-band imaging". In: *Astronomy and Astrophysics* 493.2, pp. L21–L25. DOI: 10.1051/0004-6361:200811325. arXiv: 0811.3583 [astro-ph].

Lagrange, A. .-M., N. Meunier, M. Desort, et al. (Apr. 2011). "Using the Sun to estimate Earth-like planets detection capabilities . III. Impact of spots and plages on astrometric detection". In: *Astronomy and Astrophysics* 528, L9, p. L9. DOI: 10.1051/0004-6361/201016354. arXiv: 1101.2512 [astro-ph.SR].

Lagrange, A. .-M., N. Meunier, P. Rubini, et al. (Aug. 2019). "Evidence for an additional planet in the β Pictoris system". In: *Nature Astronomy* 3, pp. 1135–1142. DOI: 10.1038/s41550-019-0857-1.

Lamb, M. P. et al. (Aug. 2021). "Simultaneous estimation of segmented telescope phasing errors and non-common path aberrations from adaptive-optics-corrected images". In: *Monthly Notices of the RAS* 505.3, pp. 3347–3360. DOI: 10.1093/mnras/stab1247. arXiv: 2104.14609 [astro-ph.IM].

Lane, B. F. and M. W. Muterspaugh (Feb. 2004). "Differential Astrometry of Subarcsecond Scale Binaries at the Palomar Testbed Interferometer". In: *Astrophysical Journal* 601.2, pp. 1129–1135. DOI: 10.1086/380760. arXiv: astro-ph/0308381 [astro-ph].

Lawson, P. R. et al. (Mar. 2007). *Terrestrial Planet Finder Interferometer Science Working Group Report*. NASA STI/Recon Technical Report N.

Lazorenko, P. F. (Apr. 2006). "Astrometric precision of observations at VLT/FORS2". In: *Astronomy and Astrophysics* 449.3, pp. 1271–1279. DOI: 10.1051/0004-6361:20054244. arXiv: astro-ph/0512502 [astro-ph].

Lazorenko, P. F. et al. (May 2014). "Astrometric planet search around southern ultracool dwarfs. II. Astrometric reduction methods and a deep astrometric catalogue". In: *Astronomy and Astrophysics* 565, A21, A21. DOI: 10.1051/0004-6361/201323271. arXiv: 1403.4619 [astro-ph.SR].

Limbach, M. A. and E. L. Turner (Jan. 2015). "Exoplanet orbital eccentricity: Multiplicity relation and the Solar System". In: *Proceedings of the National Academy of Science* 112.1, pp. 20–24. DOI: 10.1073/pnas.1406545111. arXiv: 1404.2552 [astro-ph.EP].

Lopez-Morales, M. et al. (May 2019). "Detecting Earth-like Biosignatures on Rocky Exoplanets around Nearby Stars with Ground-based Extremely Large Telescopes". In: *Bulletin of the AAS* 51.3, 162, p. 162. arXiv: 1903.09523 [astro-ph.EP].

Lubin, J. et al. (Aug. 2021). "Stellar Activity Manifesting at a One-year Alias Explains Barnard b as a False Positive". In: *Astronomical Journal* 162.2, 61, p. 61. DOI: 10.3847/1538-3881/ac0057.

Lyot, B. (June 1939). "The study of the solar corona and prominences without eclipses (George Darwin Lecture, 1939)". In: *Monthly Notices of the RAS* 99, p. 580. DOI: 10.1093/mnras/99.8.580.

Macintosh, B., J. R. Graham, T. Barman, et al. (Oct. 2015). "Discovery and spectroscopy of the young jovian planet 51 Eri b with the Gemini Planet Imager". In: *Science* 350.6256, pp. 64–67. DOI: 10.1126/science.aac5891. arXiv: 1508.03084 [astro-ph.EP].

Macintosh, B., J. R. Graham, P. Ingraham, et al. (Sept. 2014). "First light of the Gemini Planet Imager". In: *Proceedings of the National Academy of Science* 111, pp. 12661–12666. DOI: 10.1073/pnas.1304215111. arXiv: 1403.7520 [astro-ph.EP].

Macintosh, B. (Jan. 2013). *The Gemini Planet Imager Exoplanet Survey*. NASA OSS Proposal.

Macintosh, B. A. et al. (Sept. 2012). "The Gemini Planet Imager: integration and status". In: *Ground-based and Airborne Instrumentation for Astronomy IV*. Ed. by I. S. McLean, S. K. Ramsay, and H. Takami. Vol. 8446. Society of Photo-Optical Instrumentation Engineers (SPIE) Conference Series, 84461U. DOI: 10.1117/12.926721.

Madec, P.-Y. (2012). "Overview of deformable mirror technologies for adaptive optics and astronomy". In: *Adaptive Optics Systems III*. Ed. by B. L. Ellerbroek, E. Marchetti, and J.-P. Véran. Vol. 8447. International Society for Optics and Photonics. SPIE, pp. 22–39. URL: https://doi.org/10.1117/12.924892.

Madhusudhan, N. (Aug. 2019). "Exoplanetary Atmospheres: Key Insights, Challenges, and Prospects". In: *Annual Review of Astronomy and Astrophysics* 57, pp. 617–663. DOI: 10.1146/annurev-astro-081817-051846. arXiv: 1904.03190 [astro-ph.EP].

Maire, A. .-L. et al. (July 2021). "Lessons learned from SPHERE for the astrometric strategy of the next generation of exoplanet imaging instruments". In: *arXiv e-prints*, arXiv:2107.14341, arXiv:2107.14341. arXiv: 2107.14341 [astro-ph.IM].

Makarov, V. V., D. Parker, and R. K. Ulrich (July 2010). "Astrometric Jitter of the Sun as a Star". In: *Astrophysical Journal* 717.2, pp. 1202–1205. DOI: 10.1088/0004-637X/717/2/1202. arXiv: 1005.4888 [astro-ph.SR].

Malbet, F., U. Abbas, et al. (Oct. 2019). "ESA Voyage 2050 white paper – Faint objects in motion: the new frontier of high precision astrometry". In: *arXiv e-prints*, arXiv:1910.08028, arXiv:1910.08028. arXiv: 1910.08028 [astro-ph.IM].

Malbet, F., A. Sozzetti, et al. (Oct. 2010). "Review from the Blue Dots Astrometry Working Group". In: *Pathways Towards Habitable Planets*. Ed. by V. CoudÃ© du Foresto, D. M. Gelino, and I. Ribas. Vol. 430. Astronomical Society of the Pacific Conference Series, p. 84. arXiv: 0912.0400 [astro-ph.EP].

Malbet, F., A. Léger, et al. (Oct. 2012). "High precision astrometry mission for the detection and characterization of nearby habitable planetary systems with the Nearby Earth Astrometric Telescope (NEAT)". In: *Experimental Astronomy* 34.2, pp. 385–413. DOI: 10.1007/s10686-011-9246-1. arXiv: 1107.3643 [astro-ph.EP].

Malbet, F. and A. Sozzetti (2018). "Astrometry as an Exoplanet Discovery Method". In: *Handbook of Exoplanets*. Ed. by H. J. Deeg and J. A. Belmonte. Cham: Springer International Publishing, pp. 689–704. ISBN: 978-3-319-55333-7. DOI: 10.1007/978-3-319-55333-7_196. URL: https://doi.org/10.1007/978-3-319-55333-7_196.

Males, J. R. et al. (Dec. 2020). "MagAO-X first light". In: *Society of Photo-Optical Instrumentation Engineers (SPIE) Conference Series*. Vol. 11448. Society of Photo-Optical Instrumentation Engineers (SPIE) Conference Series, p. 114484L. DOI: 10.1117/12.2561682.

Mandell, A. M. et al. (Dec. 2013). "Exoplanet Transit Spectroscopy Using WFC3: WASP-12 b, WASP-17 b, and WASP-19 b". In: *Astrophysical Journal* 779.2, 128, p. 128. DOI: 10.1088/0004-637X/779/2/128. arXiv: 1310.2949 [astro-ph.EP].

Marcy, G. W. and R. P. Butler (June 1996). "A Planetary Companion to 70 Virginis". In: *Astrophysical Journal, Letters* 464, p. L147. DOI: 10.1086/310096.

Marois, C., D. Lafrenière, et al. (Apr. 2006). "Angular Differential Imaging: A Powerful High-Contrast Imaging Technique". In: *Astrophysical Journal* 641.1, pp. 556–564. DOI: 10.1086/500401. arXiv: astro-ph/0512335 [astro-ph].

Marois, C., B. Macintosh, et al. (Nov. 2008). "Direct Imaging of Multiple Planets Orbiting the Star HR 8799". In: *Science* 322.5906, p. 1348. DOI: 10.1126/science.1166585. arXiv: 0811.2606 [astro-ph].

Marois, C., B. Zuckerman, et al. (Dec. 2010). "Images of a fourth planet orbiting HR 8799". In: *Nature* 468.7327, pp. 1080–1083. DOI: 10.1038/nature09684. arXiv: 1011.4918 [astro-ph.EP].

Mawet, D. et al. (2017). "Observing Exoplanets with High-dispersion Coronagraphy. II. Demonstration of an Active Single-mode Fiber Injection Unit". In: *Astrophys. J.* 838, p. 92. DOI: 10.3847/1538-4357/aa647f.

Mayor, M., M. Marmier, et al. (Sept. 2011). "The HARPS search for southern extra-solar planets XXXIV. Occurrence, mass distribution and orbital properties of super-Earths and Neptune-mass planets". In: *arXiv e-prints*, arXiv:1109.2497, arXiv:1109.2497. arXiv: 1109.2497 [astro-ph.EP].

Mayor, M., F. Pepe, et al. (Dec. 2003). "Setting New Standards with HARPS". In: *The Messenger* 114, pp. 20–24.

Mayor, M. and D. Queloz (1995). "A Jupiter-mass companion to a solar-type star". In: *Nature* 378.6555, pp. 355–359. DOI: 10.1038/378355a0. URL: https://doi.org/10.1038/378355a0.

Mazin, B. A. et al. (Jan. 2012). "A superconducting focal plane array for ultraviolet, optical, and near-infrared astrophysics". In: *Optics Express* 20.2, p. 1503. DOI: 10.1364/OE.20.001503. arXiv: 1112.0004 [astro-ph.IM].

McArthur, B. E. et al. (June 2010). "New Observational Constraints on the υ Andromedae System with Data from the Hubble Space Telescope and Hobby-Eberly Telescope". In: *Astrophysical Journal* 715.2, pp. 1203–1220. DOI: 10.1088/0004-637X/715/2/1203.

McCracken, R. A., J. M. Charsley, and D. T. Reid (June 2017). "A decade of astrocombs: recent advances in frequency combs for astronomy". In: *Opt. Express* 25.13, pp. 15058–15078. DOI: 10.1364/OE.25.015058. URL: http://www.opticsexpress.org/abstract.cfm?URI=oe-25-13-15058.

McElwain, M. W. et al. (2016). "PISCES: an integral field spectrograph technology demonstration for the WFIRST coronagraph". In: *Space Telescopes and Instrumentation 2016: Optical, Infrared, and Millimeter Wave*. Ed. by H. A. MacEwen et al. Vol. 9904. International Society for Optics and Photonics. SPIE, pp. 446–463. URL: https://doi.org/10.1117/12.2231671.

Meier Valdés, E. A., B. M. Morris, and B. .-O. Demory (May 2021). "Monitoring precipitable water vapour in near real-time to correct near-infrared observations using satellite remote sensing". In: *Astronomy and Astrophysics* 649, A132, A132. DOI: 10.1051/0004-6361/202039629. arXiv: 2103.05326 [astro-ph.IM].

Melchior, P., D. Spergel, and A. Lanz (Feb. 2018). "In the Crosshair: Astrometric Exoplanet Detection with WFIRST's Diffraction Spikes". In: *Astronomical Journal* 155.2, 102, p. 102. DOI: 10.3847/1538-3881/aaa422. arXiv: 1708.00022 [astro-ph.IM].

Mennesson, B. et al. (June 2011). "NEW CONSTRAINTS ON COMPANIONS AND DUST WITHIN A FEW AU OF VEGA". In: *The Astrophysical Journal* 736.1, p. 14. DOI: 10.1088/0004-637x/736/1/14. URL: https://doi.org/10.1088/0004-637x/736/1/14.

Mennesson, B. P. et al. (2003). "Optical Planet Discoverer: how to turn a 1.5-m telescope into a powerful exo-planetary systems imager". In: *High-Contrast Imaging for Exo-Planet Detection*. Ed. by A. B. Schultz and R. G. Lyon. Vol. 4860. International Society for Optics and Photonics. SPIE, pp. 32–44. URL: https://doi.org/10.1117/12.457646.

Mesa, D. et al. (Dec. 2019). "VLT/SPHERE exploration of the young multiplanetary system PDS70". In: *Astronomy and Astrophysics* 632, A25, A25. DOI: 10.1051/0004-6361/201936764. arXiv: 1910.11169 [astro-ph.EP].

Meunier, N., A. .-M. Lagrange, and S. Borgniet (Dec. 2020). "Activity time series of old stars from late F to early K. V. Effect on exoplanet detectability with high-precision astrometry". In: *Astronomy and Astrophysics* 644, A77, A77. DOI: 10.1051/0004-6361/202038710. arXiv: 2011.02158 [astro-ph.SR].

Millar-Blanchaer, M. A. et al. (Sept. 2015). "Beta Pictoris' Inner Disk in Polarized Light and New Orbital Parameters for Beta Pictoris b". In: *Astrophysical Journal* 811.1, 18, p. 18. DOI: 10.1088/0004-637X/811/1/18. arXiv: 1508.04787 [astro-ph.EP].

Moe, M. and K. M. Kratter (Dec. 2019). "Impact of Binary Stars on Planet Statistics – I. Planet Occurrence Rates, Trends with Stellar Mass, and Wide Companions to Hot Jupiter Hosts". In: *arXiv e-prints*, arXiv:1912.01699, arXiv:1912.01699. arXiv: 1912.01699 [astro-ph.EP].

Mollière, P. et al. (Aug. 2020). "Retrieving scattering clouds and disequilibrium chemistry in the atmosphere of HR 8799e". In: *Astronomy and Astrophysics* 640, A131, A131. DOI: 10.1051/0004-6361/202038325. arXiv: 2006.09394 [astro-ph.EP].

Morley, C. V. et al. (Dec. 2015). "Thermal Emission and Reflected Light Spectra of Super Earths with Flat Transmission Spectra". In: *Astrophysical Journal* 815.2, 110, p. 110. DOI: 10.1088/0004-637X/815/2/110. arXiv: 1511.01492 [astro-ph.EP].

Mroz, P. et al. (Aug. 2017). "No large population of unbound or wide-orbit Jupiter-mass planets". In: *Nature* 548.7666, pp. 183–186. DOI: 10.1038/nature23276. arXiv: 1707.07634 [astro-ph.EP].

Murphy, M. T. et al. (Sept. 2007). “High-precision wavelength calibration of astronomical spectrographs with laser frequency combs”. In: *Monthly Notices of the RAS* 380.2, pp. 839–847. DOI: 10.1111/j.1365-2966.2007.12147.x. arXiv: astro-ph/0703622 [astro-ph].

Muterspaugh, M. W. et al. (Oct. 2010). “THE PHASES DIFFERENTIAL ASTROMETRY DATA ARCHIVE. V. CANDIDATE SUBSTELLAR COMPANIONS TO BINARY SYSTEMS”. In: *The Astronomical Journal* 140.6, pp. 1657–1671. DOI: 10.1088/0004-6256/140/6/1657. URL: https://doi.org/10.1088/0004-6256/140/6/1657.

N’Diaye, M. et al. (Feb. 2018). “Calibration of the island effect: Experimental validation of closed-loop focal plane wavefront control on Subaru/SCExAO”. In: *Astronomy and Astrophysics* 610, A18, A18. DOI: 10.1051/0004-6361/201731985. arXiv: 1712.03963 [astro-ph.IM].

Nowak, M. et al. (Oct. 2020). “Direct confirmation of the radial-velocity planet β Pictoris c”. In: *Astronomy and Astrophysics* 642, L2, p. L2. DOI: 10.1051/0004-6361/202039039. arXiv: 2010.04442 [astro-ph.EP].

Orban de Xivry, G. et al. (Aug. 2021). “Focal plane wavefront sensing using machine learning: performance of convolutional neural networks compared to fundamental limits”. In: *Monthly Notices of the RAS* 505.4, pp. 5702–5713. DOI: 10.1093/mnras/stab1634. arXiv: 2106.04456 [astro-ph.IM].

Paul, B. et al. (Dec. 2013). “High-order myopic coronagraphic phase diversity (COFFEE) for wave-front control in high-contrast imaging systems.” In: *Opt. Express* 21.26, pp. 31751–31768. DOI: 10.1364/OE.21.031751. URL: http://www.opticsexpress.org/abstract.cfm?URI=oe-21-26-31751.

Pearce, T. D. et al. (June 2021). “Fomalhaut b could be massive and sculpting the narrow, eccentric debris disc, if in mean-motion resonance with it”. In: *Monthly Notices of the RAS* 503.4, pp. 4767–4786. DOI: 10.1093/mnras/stab760. arXiv: 2103.04977 [astro-ph.EP].

Penny, M. T. et al. (Mar. 2019). “Predictions of the WFIRST Microlensing Survey. I. Bound Planet Detection Rates”. In: *Astrophysical Journal, Supplement* 241.1, 3, p. 3. DOI: 10.3847/1538-4365/aafb69. arXiv: 1808.02490 [astro-ph.EP].

Pepe, F., P. Molaro, et al. (Jan. 2014). “ESPRESSO: The next European exoplanet hunter”. In: *Astronomische Nachrichten* 335.1, p. 8. DOI: 12.1002/asna.201312004.

Pepe, F., D. Ehrenreich, and M. R. Meyer (Sept. 2014). “Instrumentation for the detection and characterization of exoplanets”. In: *Nature* 513.7518, pp. 358–366. DOI: 10.1038/nature13784. arXiv: 1409.5266 [astro-ph.EP].

Perryman, M., K. S. de Boer, et al. (Apr. 2001). “GAIA: Composition, formation and evolution of the Galaxy”. In: *Astronomy and Astrophysics* 369, pp. 339–363. DOI: 10.1051/0004-6361:20010085. arXiv: astro-ph/0101235 [astro-ph].

Perryman, M., J. Hartman, et al. (Dec. 2014). “Astrometric Exoplanet Detection with Gaia”. In: *Astrophysical Journal* 797.1, 14, p. 14. DOI: 10.1088/0004-637X/797/1/14. arXiv: 1411.1173 [astro-ph.EP].

Podgorski, W. et al. (July 2014). “A novel systems engineering approach to the design of a precision radial velocity spectrograph: the GMT-Consortium Large Earth Finder (G-CLEF)”. In: *Ground-based and Airborne Instrumentation for Astronomy V*. Ed. by S. K. Ramsay, I. S. McLean, and H. Takami. Vol. 9147. Society of Photo-Optical Instrumentation Engineers (SPIE) Conference Series, 91478W. DOI: 10.1117/12.2056329.

Poppenhaeger, K., K. Auchettl, and S. J. Wolk (July 2017). “A test of the neutron star hypothesis for Fomalhaut b”. In: *Monthly Notices of the RAS* 468.4, pp. 4018–4024. DOI: 10.1093/mnras/stx565. arXiv: 1703.03279 [astro-ph.SR].

Prada, C. M., D. Liu, et al. (2021). “Environmental testing of high-actuator-count MEMS deformable mirrors for space-based applications”. In: *Techniques and Instrumentation for Detection of Exoplanets X*. Ed. by S. B. Shaklan and G. J. Ruane. Vol. 11823. International Society for Optics and Photonics. SPIE, pp. 209–221. URL: https://doi.org/10.1117/12.2594263.

Prada, C. M., E. Serabyn, and F. Shi (2019). “High-contrast imaging stability using MEMS deformable mirror”. In: *Techniques and Instrumentation for Detection of Exoplanets IX*. Ed. by S. B. Shaklan. Vol. 11117. International Society for Optics and Photonics. SPIE, pp. 112–118. URL: https://doi.org/10.1117/12.2525628.

Prato, L. et al. (Nov. 2008). “A Young-Planet Search in Visible and Infrared Light: DN Tauri, V836 Tauri, and V827 Tauri”. In: *Astrophysical Journal, Letters* 687.2, p. L103. DOI: 10.1086/593201. arXiv: 0809.3599 [astro-ph].

Pravdo, S. H. and S. B. Shaklan (July 1996). “Astrometric Detection of Extrasolar Planets: Results of a Feasibility Study with the Palomar 5 Meter Telescope”. In: *Astrophysical Journal* 465, p. 264. DOI: 10.1086/177417.

Probst, R. A. et al. (2020). “A crucial test for astronomical spectrograph calibration with frequency combs”. In: *Nature Astronomy* 4.6, pp. 603–608. DOI: 10.1038/s41550-020-1010-x. URL: https://doi.org/10.1038/s41550-020-1010-x.

Pueyo, L. et al. (Nov. 2009). “Optimal dark hole generation via two deformable mirrors with stroke minimization”. In: *Appl. Opt.* 48.32, pp. 6296–6312. DOI: 10.1364/AO.48.006296. URL: http://ao.osa.org/abstract.cfm?URI=ao-48-32-6296.

– (Nov. 2011). “Optimal Dark Hole Generation via Two Deformable Mirrors with Stroke Minimization”. In: *arXiv e-prints*, arXiv:1111.5111, arXiv:1111.5111. arXiv: 1111.5111 [astro-ph.IM].

Quirrenbach, A. et al. (July 2018). "CARMENES: high-resolution spectra and precise radial velocities in the red and infrared". In: *Ground-based and Airborne Instrumentation for Astronomy VII*. Ed. by C. J. Evans, L. Simard, and H. Takami. Vol. 10702. Society of Photo-Optical Instrumentation Engineers (SPIE) Conference Series, 107020W. DOI: 10.1117/12.2313689.

Racine, R. et al. (May 1999). "Speckle Noise and the Detection of Faint Companions". In: *Publications of the ASP* 111.759, pp. 587–594. DOI: 10.1086/316367.

Rameau, J. et al. (Sept. 2015). "Detection limits with spectral differential imaging data". In: *Astronomy and Astrophysics* 581, A80, A80. DOI: 10.1051/0004-6361/201525879.

Redmond, S. F. et al. (Aug. 2021). "Dark zone maintenance results for segmented aperture wavefront error drift in a high contrast space coronagraph". In: *Proceeding of SPIE*, arXiv:2108.08216, arXiv:2108.08216. arXiv: 2108.08216 [astro-ph.IM].

Reid, M. J. and M. Honma (Aug. 2014). "Microarcsecond Radio Astrometry". In: *Annual Review of Astronomy and Astrophysics* 52, pp. 339–372. DOI: 10.1146/annurev-astro-081913-040006. arXiv: 1312.2871 [astro-ph.IM].

Ren, D. et al. (Mar. 2012). "Correction of Non-Common-Path Error for Extreme Adaptive Optics". In: *Publications of the ASP* 124.913, p. 247. DOI: 10.1086/664947.

Riggs, A. J. E. et al. (2021). "High contrast imaging with MEMS deformable mirrors in the Decadal Survey Testbed". In: *Techniques and Instrumentation for Detection of Exoplanets X*. Ed. by S. B. Shaklan and G. J. Ruane. Vol. 11823. International Society for Optics and Photonics. SPIE, pp. 259–267. URL: https://doi.org/10.1117/12.2593459.

Roy, A. et al. (Apr. 2020). "Solar Contamination in Extreme-precision Radial-velocity Measurements: Deleterious Effects and Prospects for Mitigation". In: *Astronomical Journal* 159.4, 161, p. 161. DOI: 10.3847/1538-3881/ab781a. arXiv: 2002.09468 [astro-ph.IM].

Ruane, G., A. J. Riggs, et al. (Aug. 2018). "Review of high-contrast imaging systems for current and future ground- and space-based telescopes I: coronagraph design methods and optical performance metrics". In: *Space Telescopes and Instrumentation 2018: Optical, Infrared, and Millimeter Wave*. Ed. by M. Lystrup et al. Vol. 10698. Society of Photo-Optical Instrumentation Engineers (SPIE) Conference Series, 106982S. DOI: 10.1117/12.2312948. arXiv: 1807.07042 [astro-ph.IM].

Ruane, G., A. Riggs, et al. (Aug. 2018). "Fast linearized coronagraph optimizer (FALCO) IV: coronagraph design survey for obstructed and segmented apertures". In: *Proceedings of the SPIE*. Vol. 10698. Society of Photo-Optical Instrumentation Engineers (SPIE) Conference Series, 106984U. DOI: 10.1117/12.2312973. arXiv: 1807.06758 [astro-ph.IM].

Ruane, G., D. Echeverri, et al. (Oct. 2020). "Microelectromechanical deformable mirror development for high-contrast imaging, part 2: the impact of quantization errors on coronagraph image contrast". In: *Journal of Astronomical Telescopes, Instruments, and Systems* 6, 045002, p. 045002. DOI: 10.1117/1.JATIS.6.4.045002. arXiv: 2010.03704 [astro-ph.IM].

Ruane, G., J. Jewell, et al. (July 2016). "Apodized vortex coronagraph designs for segmented aperture telescopes". In: *Proceedings of the SPIE*. Vol. 9912. Society of Photo-Optical Instrumentation Engineers (SPIE) Conference Series, p. 99122L. DOI: 10.1117/12.2231715. arXiv: 1607.06400 [astro-ph.IM].

Ruane, G., H. Ngo, et al. (Mar. 2019). "Reference Star Differential Imaging of Close-in Companions and Circumstellar Disks with the NIRC2 Vortex Coronagraph at the W. M. Keck Observatory". In: *Astronomical Journal* 157.3, 118, p. 118. DOI: 10.3847/1538-3881/aafee2. arXiv: 1901.04090 [astro-ph.IM].

Ruane, G., J. Wang, et al. (Nov. 2018). "Efficient Spectroscopy of Exoplanets at Small Angular Separations with Vortex Fiber Nulling". In: *Astrophysical Journal* 867.2, 143, p. 143. DOI: 10.3847/1538-4357/aae262. arXiv: 1809.06483 [astro-ph.IM].

Ruffio, J.-B. et al. (Nov. 2019). "Radial Velocity Measurements of HR 8799 b and c with Medium Resolution Spectroscopy". In: *Astronomical Journal* 158.5, 200, p. 200. DOI: 10.3847/1538-3881/ab4594. arXiv: 1909.07571 [astro-ph.EP].

Saba, A. et al. (Aug. 2021). "The transmission spectrum of WASP-17 b from the optical to the near-infrared wavelengths: combining STIS, WFC3 and IRAC datasets". In: *arXiv e-prints*, arXiv:2108.13721, arXiv:2108.13721. arXiv: 2108.13721 [astro-ph.EP].

Sabotta, S. et al. (July 2021). "The CARMENES search for exoplanets around M dwarfs – Planet occurrence rates from a subsample of 71 stars". In: *arXiv e-prints*, arXiv:2107.03802, arXiv:2107.03802. arXiv: 2107.03802 [astro-ph.EP].

Sahlmann, J. et al. (Nov. 2016). "The mass of planet GJ 676A b from ground-based astrometry. A planetary system with two mature gas giants suitable for direct imaging". In: *Astronomy and Astrophysics* 595, A77, A77. DOI: 10.1051/0004-6361/201628854. arXiv: 1608.00918 [astro-ph.EP].

Sanghavi, S., R. West, and J. Jiang (Jan. 2021). "Cloudy Atmospheres on Directly Imaged Exoplanets: The Need for Accurate Particulate Representation in Photopolarimetric Simulations". In: *Astrophysical Journal* 907.1, 30, p. 30. DOI: 10.3847/1538-4357/abcd99.

Sauvage, J.-F. et al. (Aug. 2007). "Calibration and precompensation of noncommon path aberrations for extreme adaptive optics". In: *Journal of the Optical Society of America A* 24.8, pp. 2334–2346. DOI: 10.1364/JOSAA.24.002334. arXiv: astro-ph/0703077 [astro-ph].

Scheiner, C. (1619). "Oculus, sive fundamentum opticum". In: *Oculus, sive fundamentum opticum*.

Shao, M. et al. (2007). “Finding Earth clones with SIM: the most promising near-term technique to detect, find masses for, and determine three-dimensional orbits of nearby habitable planets”. In: *Techniques and Instrumentation for Detection of Exoplanets III*. Ed. by D. R. Coulter. Vol. 6693. International Society for Optics and Photonics. SPIE, pp. 118–125. URL: https://doi.org/10.1117/12.734671.

Sirbu, D. et al. (Nov. 2017). “Techniques for High-contrast Imaging in Multi-star Systems. II. Multi-star Wavefront Control”. In: *Astrophysical Journal* 849.2, 142, p. 142. DOI: 10.3847/1538-4357/aa8e02. arXiv: 1704.05441 [astro-ph.IM].

Snellen, I. et al. (Apr. 2015). “Combining high-dispersion spectroscopy with high contrast imaging: Probing rocky planets around our nearest neighbors”. In: *Astronomy and Astrophysics* 576, A59, A59. DOI: 10.1051/0004-6361/201425018.

Snellen, I. A. G. et al. (2014). “Fast spin of the young extrasolar planet Î²Pictoris b”. In: *Nature* 509.7498, pp. 63–65. DOI: 10.1038/nature13253. URL: https://doi.org/10.1038/nature13253.

Soummer, R. (Jan. 2005). “Apodized Pupil Lyot Coronagraphs for Arbitrary Telescope Apertures”. In: *Astrophysical Journal, Letters* 618.2, pp. L161–L164. DOI: 10.1086/427923. arXiv: astro-ph/0412221 [astro-ph].

Soummer, R., L. Pueyo, and J. Larkin (Aug. 2012). “Detection and Characterization of Exoplanets and Disks Using Projections on Karhunen-Loève Eigenimages”. In: *Astrophysical Journal, Letters* 755.2, L28, p. L28. DOI: 10.1088/2041-8205/755/2/L28. arXiv: 1207.4197 [astro-ph.IM].

Sowmya, K. et al. (July 2021). “Predictions of Astrometric Jitter for Sun-like Stars. II. Dependence on Inclination, Metallicity, and Active-Region Nesting”. In: *arXiv e-prints*, arXiv:2107.01493, arXiv:2107.01493. arXiv: 2107.01493 [astro-ph.SR].

Sparks, W. B. and H. C. Ford (Oct. 2002). “Imaging Spectroscopy for Extrasolar Planet Detection”. In: *Astrophysical Journal* 578, pp. 543–564. DOI: 10.1086/342401. eprint: astro-ph/0209078.

Stapelfeldt, K. R. et al. (Sept. 2004). “First Look at the Fomalhaut Debris Disk with the Spitzer Space Telescope”. In: *The Astrophysical Journal Supplement Series* 154.1, pp. 458–462. DOI: 10.1086/423135. URL: https://doi.org/10.1086/423135.

Stock, S. et al. (Apr. 2020). “The CARMENES search for exoplanets around M dwarfs. Characterization of the nearby ultra-compact multiplanetary system YZ Ceti”. In: *Astronomy and Astrophysics* 636, A119, A119. DOI: 10.1051/0004-6361/201936732. arXiv: 2002.01772 [astro-ph.EP].

Stolker, T. et al. (Dec. 2020). “MIRACLES: atmospheric characterization of directly imaged planets and substellar companions at 4-5 μm. II. Constraints on the mass and radius of the enshrouded planet PDS 70 b”. In: *Astronomy and Astrophysics*

644, A13, A13. DOI: 10.1051/0004-6361/202038878. arXiv: 2009.04483 [astro-ph.EP].

Sumi, T. et al. (May 2011). "Unbound or distant planetary mass population detected by gravitational microlensing". In: *Nature* 473.7347, pp. 349–352. DOI: 10.1038/nature10092. arXiv: 1105.3544 [astro-ph.EP].

Suzuki, D., D. P. Bennett, T. Sumi, et al. (Dec. 2016). "THE EXOPLANET MASS-RATIO FUNCTION FROM THE MOA-II SURVEY: DISCOVERY OF A BREAK AND LIKELY PEAK AT A NEPTUNE MASS". In: *The Astrophysical Journal* 833.2, p. 145. DOI: 10.3847/1538-4357/833/2/145. URL: https://doi.org/10.3847/1538-4357/833/2/145.

Suzuki, D., D. P. Bennett, S. Ida, et al. (Dec. 2018). "Microlensing Results Challenge the Core Accretion Runaway Growth Scenario for Gas Giants". In: *Astrophysical Journal, Letters* 869.2, L34, p. L34. DOI: 10.3847/2041-8213/aaf577. arXiv: 1812.11785 [astro-ph.EP].

Tal-Or, L., S. Zucker, et al. (Mar. 2019). "Prospects for detecting the astrometric signature of Barnard's Star b". In: *Astronomy and Astrophysics* 623, A10, A10. DOI: 10.1051/0004-6361/201834643. arXiv: 1811.05920 [astro-ph.EP].

Tal-Or, L., T. Trifonov, et al. (Mar. 2019). "Correcting HIRES/Keck radial velocities for small systematic errors". In: *Monthly Notices of the RAS* 484.1, pp. L8–L13. DOI: 10.1093/mnrasl/sly227. arXiv: 1810.02986 [astro-ph.EP].

The HabEx Team (2019). *The HabEx Final Report*. https://www.jpl.nasa.gov/habex/pdf/HabEx-Final-Report-Public-Release-LINKED-0924.pdf.

The LUVOIR Team (2019). *The Large UV Optical Infrared Surveyor (LUVOIR) final report*. https://asd.gsfc.nasa.gov/luvoir/resources/docs/LUVOIR_FinalReport_2019-08-26.pdf.

Thompson, S. J. et al. (Aug. 2016). "HARPS3 for a roboticized Isaac Newton Telescope". In: *Ground-based and Airborne Instrumentation for Astronomy VI*. Ed. by C. J. Evans, L. Simard, and H. Takami. Vol. 9908. Society of Photo-Optical Instrumentation Engineers (SPIE) Conference Series, 99086F. DOI: 10.1117/12.2232111. arXiv: 1608.04611 [astro-ph.IM].

Trauger, J. et al. (Jan. 2016). "Hybrid Lyot coronagraph for WFIRST-AFTA: coronagraph design and performance metrics". In: *Journal of Astronomical Telescopes, Instruments, and Systems* 2, 011013, p. 011013. DOI: 10.1117/1.JATIS.2.1.011013.

Tremaine, S. and S. Dong (Mar. 2012). "THE STATISTICS OF MULTI-PLANET SYSTEMS". In: *The Astronomical Journal* 143.4, p. 94. DOI: 10.1088/0004-6256/143/4/94. URL: https://doi.org/10.1088/0004-6256/143/4/94.

Turyshev, S. G. et al. (Feb. 2020). “Direct Multipixel Imaging and Spectroscopy of an Exoplanet with a Solar Gravity Lens Mission”. In: *arXiv e-prints*, arXiv:2002.11871, arXiv:2002.11871. arXiv: 2002.11871 [astro-ph.IM].

Uyama, T. et al. (Feb. 2020). “Atmospheric Characterization and Further Orbital Modeling of κ Andromeda b”. In: *Astronomical Journal* 159.2, 40, p. 40. DOI: 10.3847/1538-3881/ab5afa. arXiv: 1911.09758 [astro-ph.EP].

Valencia, D., D. D. Sasselov, and R. J. O’Connell (Aug. 2007). “Detailed Models of Super-Earths: How Well Can We Infer Bulk Properties?” In: *Astrophysical Journal* 665.2, pp. 1413–1420. DOI: 10.1086/519554. arXiv: 0704.3454 [astro-ph].

Vérinaud, C. (Mar. 2004). “On the nature of the measurements provided by a pyramid wave-front sensor”. In: *Optics Communications* 233.1-3, pp. 27–38. DOI: 10.1016/j.optcom.2004.01.038.

Vogt, S. S. et al. (June 1994). “HIRES: the high-resolution echelle spectrometer on the Keck 10-m Telescope”. In: *Instrumentation in Astronomy VIII*. Ed. by D. L. Crawford and E. R. Craine. Vol. 2198. Society of Photo-Optical Instrumentation Engineers (SPIE) Conference Series, p. 362. DOI: 10.1117/12.176725.

von Paris, P. et al. (Mar. 2013). “Characterization of potentially habitable planets: Retrieval of atmospheric and planetary properties from emission spectra”. In: *Astronomy and Astrophysics* 551, A120, A120. DOI: 10.1051/0004-6361/201220009. arXiv: 1301.0217 [astro-ph.EP].

Walter, A. B. et al. (Dec. 2020). “The MKID Exoplanet Camera for Subaru SCExAO”. In: *Publications of the ASP* 132.1018, 125005, p. 125005. DOI: 10.1088/1538-3873/abc60f. arXiv: 2010.12620 [astro-ph.IM].

Wang, J., D. Mawet, R. Hu, et al. (2018). “Baseline requirements for detecting biosignatures with the HabEx and LUVOIR mission concepts”. In: *J. Astron. Telesc. Instrum. Syst.* 4.3, p. 035001. DOI: 10.1117/1.JATIS.4.3.035001.

Wang, J., D. Mawet, G. Ruane, et al. (Apr. 2017). “Observing Exoplanets with High Dispersion Coronagraphy. I. The Scientific Potential of Current and Next-generation Large Ground and Space Telescopes”. In: *Astron. J.* 153, 183, p. 183. DOI: 10.3847/1538-3881/aa6474. arXiv: 1703.00582 [astro-ph.EP].

Wang, J. J., A. Vigan, et al. (Mar. 2021). “Constraining the Nature of the PDS 70 Protoplanets with VLTI/GRAVITY”. In: *Astronomical Journal* 161.3, 148, p. 148. DOI: 10.3847/1538-3881/abdb2d. arXiv: 2101.04187 [astro-ph.EP].

Wang, J. J., S. Ginzburg, et al. (June 2020). “Keck/NIRC2 L’-band Imaging of Jovian-mass Accreting Protoplanets around PDS 70”. In: *Astronomical Journal* 159.6, 263, p. 263. DOI: 10.3847/1538-3881/ab8aef. arXiv: 2004.09597 [astro-ph.EP].

Wang, J. J., J. R. Graham, et al. (Oct. 2018). “Dynamical Constraints on the HR 8799 Planets with GPI”. In: *The Astronomical Journal* 156.5, p. 192. DOI: 10.3847/1538-3881/aae150. URL: https://doi.org/10.3847/1538-3881/aae150.

Wang, J. J., J.-B. Ruffio, et al. (July 2021). “Detection and Bulk Properties of the HR 8799 Planets with High Resolution Spectroscopy”. In: *arXiv e-prints*, arXiv:2107.06949, arXiv:2107.06949. arXiv: 2107.06949 [astro-ph.EP].

Wang, J., M. Meyer, et al. (May 31, 2019). “New Frontiers for Terrestrial-sized to Neptune-sized Exoplanets In the Era of Extremely Large Telescopes”. In: *Bulletin of the AAS* 51.3. https://baas.aas.org/pub/2020n3i200. URL: https://baas.aas.org/pub/2020n3i200.

WFIRST Astrometry Working Group et al. (Oct. 2019). “Astrometry with the Wide-Field Infrared Space Telescope”. In: *Journal of Astronomical Telescopes, Instruments, and Systems* 5, 044005, p. 044005. DOI: 10.1117/1.JATIS.5.4.044005. arXiv: 1712.05420 [astro-ph.IM].

Wilcomb, K. K. et al. (Nov. 2020). “Moderate-resolution K-band Spectroscopy of Substellar Companion κ Andromedae b”. In: *Astronomical Journal* 160.5, 207, p. 207. DOI: 10.3847/1538-3881/abb9b1. arXiv: 2009.08959 [astro-ph.EP].

Will, S. D., T. D. Groff, and J. R. Fienup (Jan. 2021). “Jacobian-free coronagraphic wavefront control using nonlinear optimization”. In: *Journal of Astronomical Telescopes, Instruments, and Systems* 7, 019002, p. 019002. DOI: 10.1117/1.JATIS.7.1.019002.

Winn, J. N. (Jan. 2010). “Transits and Occultations”. In: *arXiv e-prints*, arXiv:1001.2010, arXiv:1001.2010. arXiv: 1001.2010 [astro-ph.EP].

Wizinowich, P. et al. (Mar. 2000). “First Light Adaptive Optics Images from the Keck II Telescope: A New Era of High Angular Resolution Imagery”. In: *Publications of the ASP* 112.769, pp. 315–319. DOI: 10.1086/316543.

Wolszczan, A. and D. A. Frail (1992). “A planetary system around the millisecond pulsar PSR1257 + 12”. In: *Nature* 355.6356, pp. 145–147. DOI: 10.1038/355145a0. URL: https://doi.org/10.1038/355145a0.

Woolf, N. and J. R. Angel (1998). “ASTRONOMICAL SEARCHES FOR EARTH-LIKE PLANETS AND SIGNS OF LIFE”. In: *Annual Review of Astronomy and Astrophysics* 36.1, pp. 507–537. DOI: 10.1146/annurev.astro.36.1.507. eprint: https://doi.org/10.1146/annurev.astro.36.1.507. URL: https://doi.org/10.1146/annurev.astro.36.1.507.

Wright, J. T. and J. D. Eastman (Sept. 2014). “Barycentric Corrections at 1 cm s^{-1} for Precise Doppler Velocities”. In: *Publications of the ASP* 126.943, p. 838. DOI: 10.1086/678541. arXiv: 1409.4774 [astro-ph.IM].

Wright, J. T., G. W. Marcy, et al. (July 2012). "The Frequency of Hot Jupiters Orbiting nearby Solar-type Stars". In: *Astrophysical Journal* 753.2, 160, p. 160. DOI: 10.1088/0004-637X/753/2/160. arXiv: 1205.2273 [astro-ph.EP].

Wright, J. T., S. Upadhyay, et al. (Mar. 2009). "Ten New and Updated Multiplanet Systems and a Survey of Exoplanetary Systems". In: *Astrophysical Journal* 693.2, pp. 1084–1099. DOI: 10.1088/0004-637X/693/2/1084. arXiv: 0812.1582 [astro-ph].

Yano, T. et al. (2012). "The scientific goal of the Japanese small astrometric satellite, Small-JASMINE". In: *Proceedings of the International Astronomical Union* 8.S289, pp. 433–436. DOI: 10.1017/S1743921312021898.

Ygouf, M. et al. (Mar. 2013). "Simultaneous exoplanet detection and instrument aberration retrieval in multispectral coronagraphic imaging". In: *Astronomy and Astrophysics* 551, A138, A138. DOI: 10.1051/0004-6361/201220318. arXiv: 1302.7045 [astro-ph.IM].

Zhou, G. et al. (Sept. 2019). "Two New HATNet Hot Jupiters around A Stars and the First Glimpse at the Occurrence Rate of Hot Jupiters from TESS". In: *The Astronomical Journal* 158.4, p. 141. DOI: 10.3847/1538-3881/ab36b5. URL: https://doi.org/10.3847/1538-3881/ab36b5.

Zhu, W. et al. (June 2018). "About 30% of Sun-like Stars Have Kepler-like Planetary Systems: A Study of Their Intrinsic Architecture". In: *Astrophysical Journal* 860.2, 101, p. 101. DOI: 10.3847/1538-4357/aac6d5. arXiv: 1802.09526 [astro-ph.EP].

Chapter 2

CONSTRAINING THE ORBIT AND MASS OF ϵ ERIDANI B

Llop-Sayson, J., J. J. Wang, J.-B. Ruffio, D. Mawet, S. Blunt, O. Absil, C. Bond, C. Brinkman, B. P. Bowler, M. Bottom, A. Chontos, P. A. Dalba, B. J. Fulton, S. Giacalone, M. Hill, L. A. Hirsch, A. W. Howard, H. Isaacson, M. Karlsson, J. Lubin, A. Madurowicz, K. Matthews, E. Morris, M. Perrin, B. Ren, M. Rice, L. J. Rosenthal, G. Ruane, R. Rubenzahl, H. Sun, N. Wallack, J. W. Xuan, and M. Ygouf (Oct. 2021). "Constraining the Orbit and Mass of epsilon Eridani b with Radial Velocities, Hipparcos IAD-Gaia DR2 Astrometry, and Multiepoch Vortex Coronagraphy Upper Limits". In: *The Astronomical Journal* 162.5. DOI: 10.3847/1538-3881/ac134a. URL: https://doi.org/10.3847/1538-3881/ac134a.

ABSTRACT

ϵ Eridani is a young planetary system hosting a complex multi-belt debris disk and a confirmed Jupiter-like planet orbiting at 3.48 AU from its host star. Its age and architecture are thus reminiscent of the early Solar System. The most recent study of Mawet et al. (2019), which combined radial velocity (RV) data and Ms-band direct imaging upper limits, started to constrain the planet's orbital parameters and mass, but are still affected by large error bars and degeneracies. Here we make use of the most recent data compilation from three different techniques to further refine ϵ Eridani b's properties: RVs, absolute astrometry measurements from the *Hipparcos* and *Gaia* missions, and new Keck/NIRC2 Ms-band vortex coronagraph images. We combine this data in a Bayesian framework. We find a new mass, M_b = $0.66^{+0.12}_{-0.09}$ M_{Jup}, and inclination, $i = 78.81^{\circ +29.34}_{-22.41}$, with at least a factor 2 improvement over previous uncertainties. We also report updated constraints on the longitude of the ascending node, the argument of the periastron, and the time of periastron passage. With these updated parameters, we can better predict the position of the planet at any past and future epoch, which can greatly help define the strategy and planning of future observations and with subsequent data analysis. In particular, these results can assist the search for a direct detection with JWST and the Nancy Grace Roman Space Telescope's coronagraph instrument (CGI).

2.1 Introduction

ϵ Eridani is a nearby K2V dwarf star (Table 2.1) surrounded by a prominent multi-belt debris disk and a confirmed Jupiter-like planet on a 7.4-year orbit (Mawet et al., 2019). Its relative young age, spectral type, and architecture are reminiscent of the early Solar System. Its proximity (3.2 pc) and thus apparent brightness ($V = 3.73$ mag.) make it an excellent laboratory to study the early formation and evolution of planetary systems analogous to the Solar System.

Since the discovery of its debris disk by the Infrared Astronomical Satellite (IRAS, Aumann, 1985), ϵ Eridani has been the subject of increased scrutiny culminating with the discovery of decade-long radial velocity (RV) variations by Hatzes et al. (2000) pointing towards the presence of a $\simeq$ 1.5 M_J giant planet with a period $P = 6.9$ yr ($\simeq$ 3 AU orbit) and a high eccentricity ($e = 0.6$). This early orbital solution was dynamically incompatible with the multi-belt disk configuration of ϵ Eridani, raising the possibility of false alarm or at the very least confusion due to stellar jitter. Benedict et al. (2006) attempted at modelling the perturbation caused by the companion using RV combined with HST astrometry. Recently, Mawet et al. (2019) revisited this poster-child system by combining three decades of RV measurements with the most sensitive direct imaging data set ever obtained. The RV data, its state-of-the-art treatment of stellar noise, and direct imaging upper limits were combined in an innovative joint Bayesian analysis, providing new constraints on the mass and orbital parameters of the elusive planet. Mawet et al. (2019) reported a mass of $0.78^{+0.38}_{-0.12}$ M_{Jup}, semi-major axis (SMA) of 3.48 ± 0.02 AU with a period of 7.37 ± 0.07 years, and an eccentricity of $0.07^{+0.06}_{-0.05}$, an order of magnitude smaller than earlier estimates and consistent with a circular orbit. These new orbital parameters were found to be dynamically compatible to the most recent picture of ϵ Eridani's disk architecture (Su et al., 2017; Booth et al., 2017; Ertel et al., 2018). However, the joint RV-direct imaging upper limit analysis of Mawet et al. (2019) left some orbital parameters such as inclination i, longitude of ascending node Ω, and argument of periapsis ω, largely unconstrained, making future pointed direct detection attempts (e.g. with JWST) more difficult.

In this paper, we compiled data from recent *Gaia* data release 2 (DR2) forming a 25-year time baseline with archival *Hipparcos* astrometric data, plus new RV and deep direct imaging observations, to perform a joint astrometry-RV-direct imaging analysis aimed at refining the orbital elements of ϵ Eridani b. The paper is organized as follows. In Sec. 2.2 we present the observations, namely, we include absolute

Table 2.1. Properties of ϵ Eridani

Property	Value	Ref.
RA (hms)	03 32 55.8 (J2000)	van Leeuwen (2007)
Dec (dms)	-09 27 29.7 (J2000)	van Leeuwen (2007)
Spectral type	K2V	Keenan et al. (1989)
Mass ($M_\odot$)	0.82 ± 0.02	Baines et al. (2011)
Distance (pc)	3.216 ± 0.0015	van Leeuwen (2007)
V mag.	3.73	Ducati (2002)
K mag.	1.67	Ducati (2002)
L mag.	1.60	Cox (2000)
M mag.	1.69	Cox (2000)
Age (Myr)	400-800	Mamajek et al. (2008) and Janson et al. (2015)

astrometry measurements of ϵ Eridani to help constrain the orbital parameters and mass. We include an updated set of RV measurements, and new direct imaging observations with Keck/NIRC2. Sec. 2.3 describes the methods used to constrain the orbit and mass of ϵ Eridani by combining the three different observation techniques. At the end of this section, the new constraints are presented. In Sec. 5.5 we discuss the findings, update the planet-disk interaction parameters with respect to Mawet et al. (2019) and discuss the prospects of a detection with JWST.

2.2 Observations

Radial Velocities

ϵ Eridani has been targeted by five multi-year radial velocity (RV) planet searches over the past 30 years. Most of the resulting RV measurements are presented and discussed in Mawet et al. (2019). Since the publication of that paper, we have obtained 76 additional spectra of ϵ Eridani with Keck/HIRES (Vogt, Allen, et al., 1994), and 172 spectra with the Levy Spectrograph on the Automated Planet Finder (APF) telescope (M. V. Radovan et al. 2014; Vogt, M. Radovan, et al. 2014). These new measurements are given in Table 2.5. As in Mawet et al. (2019), new HIRES observations were taken using the standard iodine cell configuration used for the California Planet Survey (Howard et al., 2010). Observations were taken through either the B5 ($0.''87 \times 3.''5$) or C2 ($0.''87 \times 14.''0$) decker, yielding R $\simeq$ 55,000 spectral resolution. Spectra had a median of 293,000 counts per exposure, corresponding to a median extracted flux of 67,000 counts (SNR = 260) at 550 nm. The same template spectrum described in Mawet et al. (2019), taken in 2010 using the B3 decker, was used to derive RVs from all new spectra obtained for this work.

New APF measurements were also taken using the standard configuration described in Mawet et al. (2019). Most APF measurements were acquired through the W decker (1″ x 3″), with a spectral resolution of R $\simeq$ 110,000. The median exposure time across observations was 26 s, yielding a per-pixel SNR of 120 at 550 nm. The same template spectrum described in Mawet et al. (2019), taken in 2014 using the N decker, was used to derive RVs from all new spectra obtained for this work. For our analysis, all exposures taken with a single instrument within 10 hours were binned.

Absolute Astrometry Data

We obtain the astrometry data for ϵ Eridani from the *Hipparcos* catalog Hip2 (van Leeuwen, 2007), and the Gaia DR2 catalog (Gaia Collaboration, 2018), as well as the intermediate astrometry data (IAD) available from the *Hipparcos* mission.

Hipparcos Intermediate Astrometry Data

The *Hipparcos* data is generally used in its reduced form, consisting of a five-element parameter set: the right-ascension α, declination δ, the proper motion (PM) vector μ_α and μ_δ, and the parallax. However, the IAD contains all individual measurements taken by the mission, in the case of ϵ Eridani, from 1990.036 to 1992.563. The orbit period of ϵ Eridani b being ~7.31 years, *Hipparcos* IAD baseline is ~0.35 times that period. Therefore, *Hipparcos* IAD may include changes in astrometry that contain signs of the presence of a companion. Indeed, a companion perturbs the otherwise constant rectilinear motion of the photocenter into a Keplerian motion around the barycenter. By using the IAD, we fit our model orbit to the curve described by the measured positions of ϵ Eridani's photocenter during the *Hipparcos* mission.

The *Hipparcos* mission performed its measurements on a 1D scan, the acquisition protocol of which allowed for a reconstruction of the 1D points into 2D positions on the sky. The orbital direction of the scan, along with the precise epoch of each measurement are recorded in order to retrieve the final position. We use data from van Leeuwen, 2007 that consists of the IAD residuals from the fit to the data (van Leeuwen, 2007), the scan direction, epochs, and the errors associated with the original data. Using the fit from van Leeuwen, 2007 and the residuals combined with the scan direction data, we reconstruct the one dimensional scan measurements following the method used in Nielsen et al., 2020. The available data consists of 78 data points; Table 2.6 lists the complete set of data points used.

Gaia DR2

Unlike with *Hipparcos*, the IAD for *Gaia* is not yet public. We thus utilise the reduced data consisting of five astrometric parameters: the right-ascension α_G, declination δ_G, the proper motion vectors $\mu_{\alpha,G}$ and $\mu_{\delta,G}$, and the parallax. Although the velocity in the data is recorded as a proper motion, in reality, in the presence of a companion, this velocity contains both the proper motion and the velocity induced by the movement of the photocenter around the barycenter of the system. The deviation of the velocity from the actual proper motion is often called the proper motion anomaly, which stems from the movement of the photocenter around the barycenter.

Due to ϵ Eridani's proximity and the long baseline between *Hipparcos* and *Gaia*, we need to account for the 3D effects of different tangential planes where the PMs of each dataset are published. In other words, we account for the effect of the curvature when comparing the two coordinate systems. Correcting for this effect when propagating from the *Hipparcos*'s to *Gaia*'s epoch accounts for an error of ~0.25 mas for the PM in the RA direction, which, although being below one sigma, is large enough to affect the model fit. We use the `SkyCoord` tool in the `astropy` Python package to propagate between epochs that accounts for the difference in epochs and position in spherical coordinates. This allows us to work combining velocities from both datasets. We follow a similar approach to Kervella et al. (2019).

Furthermore, we correct for systematics from Gaia's rotating frame of reference according to the method described in Lindegren et al., 2018.

Gaia eDR3

We use the *Gaia* eDR3 to do a different fit to the proper motion anomalies between the *Hipparcos* and *Gaia* proper motions. We use the calibrated proper motions from Brandt (2021). This catalog includes the proper motions from the *Hipparcos* epoch, from the *Gaia* eDR3 epoch, and the long term proper motion computed with the positions at the two epochs and the time difference. The difference between the *Hipparcos* or *Gaia* proper motion and the long baseline proper motion is the proper motion anomaly, which is caused by the presence of the planet. For this fit we do not use the *Hipparcos* IAD.

Direct Imaging Data

Building upon the work presented by Mawet et al., 2019, we present additional Ms-band observations on the ϵ Eridani system acquired in 2019 with Keck/NIRC2 and its vector vortex coronagraph (Serabyn et al., 2017). The observations are summarized in Tab. 2.2. Except for the night of the 2019-12-08, the new data was acquired using the newly installed infrared pyramid wavefront sensor (Bond et al., 2020) instead of the facility Shack-Hartmann wavefront sensor. The alignment of the star behind the coronagraph is ensured at the 2 mas level by the quadrant analysis of coronagraphic images for tip-tilt sensing (QACITS; Huby, Baudoz, et al. (2015) and Huby, Bottom, et al. (2017)). The telescope was used in pupil tracking mode to allow speckle subtraction with angular differential imaging (Marois et al., 2008).

The data was corrected for bad pixels, flat-fielded, sky-subtracted, and registered following the method detailed in Xuan et al. (2018). Similar to Mawet et al. (2019), the stellar point spread function was subtracted using principal component analysis combined with a matched filter (FMMF; Ruffio, Macintosh, Wang, et al., 2017) from the open-source Python package pyKLIP (Wang, Ruffio, et al., 2015). After high-pass filtering the images with a Gaussian filter with a length scale of twice the PSF full width at half maximum (FWHM), the PSF FWHM is ~10 pixels (~0.1″) in Ms band. Stellar speckles are subtracted using 30 principal components. For each science frame, the principal components are only calculated from images featuring an azimuthal displacement of the planet on the detector of more than 0.5 FWHM. The final sensitivity of each epoch is plotted in Fig. 2.1 as a function of projected separation. The nightly performance in 2019 was lower than in 2017 resulting in a similar combined sensitivity for each year despite the longer combined exposure time. A weighted mean is used to combine different epochs together. As a way to correct for any correlation between frames, the noise of the combined images is then normalized following the standard procedure of dividing by the standard deviation calculated in concentric annuli. With the exception of the 2019-12-08 observation, the epochs in 2017 and 2019 are close enough in time for the planet to not move significantly compared to the PSF size with a full width at half-maximum of ~10 pixels.

2.3 Analysis

Radial Velocity Model

Mawet et al. (2019) performed a thorough series of tests to evaluate the possibility that ϵ Eridani b is an artifact of stellar activity, finding that the ~7 yr orbital period is

Table 2.2. Summary of observations of ϵ Eridani with Keck/NIRC2 in Ms band. From left to right: UT date of the observation, total exposure time, exposure time per integration, number of coadds, number of exposures, total paralactic angle rotation for angular differential imaging, 5σ sensitivity expressed as the planet-to-star flux ratio at 2 projected separation (0.4 and 1.0"), and finally the wavefront sensor (WFS) used (Shack-Hartmann or Pyramid).

Epoch	Tot. time (s)	Exp. time (s)	Coadds	# of exp.	Angle rot. (deg)	5σ 0.4"	5σ 1.0"	WFS
2017-01-09	6300	0.5	60	210	88.6	4.8e-05	1.1e-05	SH
2017-01-10	7800	0.5	60	260	100.2	4.9e-05	1.1e-05	SH
2017-01-11	4800	0.5	60	160	69.5	6.3e-05	1.0e-05	SH
Combined 2017	5.25h					3.3e-05	7.0e-06	
2019-10-20	5190	0.25	120	173	84.9	5.1e-05	2.0e-05	Pyramid
2019-10-21	5850	0.25	120	195	82.0	3.9e-05	1.8e-05	Pyramid
2019-10-22	7170	0.25	120	239	89.3	5.4e-05	2.0e-05	Pyramid
2019-11-04	6660	0.25	120	222	68.2	6.3e-05	1.8e-05	Pyramid
2019-11-05	6510	0.25	120	217	68.0	4.6e-05	1.3e-05	Pyramid
2019-12-08	6510	0.3	100	217	103.7	1.0e-04	2.4e-05	SH
Combined 2019	10.5h					2.3e-05	7.9e-06	

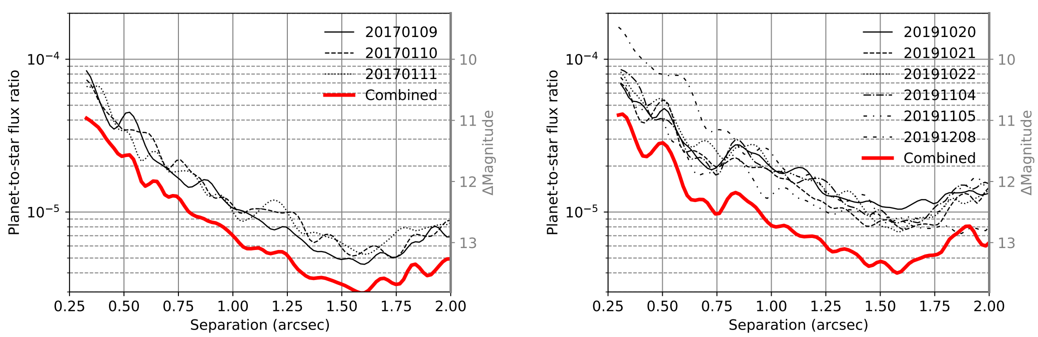

Figure 2.1 Planet sensitivity for each observations in 2017 (left) and 2019 (right). The planet sensitivity is expressed as the 5σ planet-to-star flux ratio. The December 8, 2019 epoch was not included in the combined sensitivity curve for 2019 as the planet would have moved by an amount comparable to the size of the point spread function.

distinct from periods and harmonics of the periodicities in the S_{HK} activity indicator timeseries. Our aim is not to recapitulate their analysis, but to update their orbital solution using the additional data obtained since the paper's publication, which spans approximately half of one orbital period of ϵ Eridani b.

Mawet et al. (2019) identified three peaks in a Lomb-Scargle periodogram of the RVs that rose above the 1% eFAP: one at the putative planet period of 7.3 yr, one at 2.9 yr, and one at 11d. Applying `RVSearch` (Rosenthal et al. 2021) to the full dataset, we recover this structure of peaks. Like Mawet et al. (2019), we also identify two major periods in the S_{HK} timeseries for both HIRES and APF, which coincide with the 11 d and 2.9 yr periods in the RVs. We interpret these as the signatures of rotationally-modulated stellar activity and a long-term activity cycle, respectively. To investigate the effects of these signals on the physical parameters of planet b, we performed two separate RV orbit-fits using `RadVel` (Fulton et al., 2018) to try different priors on the Gaussian Process (GP) timescale for modeling the stellar activity. In each of these fits, we assume a one-planet orbital solution, parameterized as $\sqrt{e_b}\cos\omega_b$, $\sqrt{e_b}\sin\omega_b$, $T_{conj,b}$, P_b, K_b. We also included RV offset (γ) and white noise (σ) parameters for each instrument in the fit, treating the four Lick velocity datasets independently to account for instrumental upgrades as in Mawet et al. (2019). Finally, we allowed an RV trend $\dot{\gamma}$.

In the first fit, we included a GP noise model to account for the impact of rotationally-modulated magnetic activity on the RVs (Rajpaul et al., 2015). We used a quasi-periodic kernel, following (Mawet et al., 2019). This kernel has hyperparameters η_2, the exponential decay timescale (analagous to the lifetime of active regions on the stellar disk), η_3, the stellar rotation period, and η_4, which controls the number of local maxima in the RVs per rotation period, and η_1, the amplitude of the GP mean function, which we treated as independent for each instrument dataset. Following Lopez-Morales et al. (2016), we fixed η_4 to 0.5, which allows approximately two local maxima per rotation period. In this first fit, we allowed η_2 and η_3 to vary in the range (0, 100d). We calculated a Markov chain representation of the posterior using `emcee` (Foreman-Mackey et al., 2013), We visually inspected the chains to ensure appropriate burn-in and production periods. In total, the chain contained 450080 samples. The resulting orbital and nuisance parameters are given in Table 2.3. Both the orbital parameters and the GP hyperparameters are well constrained; in particular, the marginalized posterior over the rotation period η_3 is Gaussian about the expected period of 11d. The data allow a trend, although the value is consistent with no trend at the 1σ level, which allows us to conclude that there is no evidence in the current data for a RV trend. One non-intuitive feature of this fit is a preference for extremely small values (10^{-6} m/s) of white noise jitter for the second Lick dataset. Even when we ran a fit requiring that all jitter values be at least 0.5 m/s, the posterior peaked at this lower bound. This may be evidence that much of the noise in this particular dataset is correlated, and therefore well-modeled by the GP noise model. It could also indicate that the reported observational uncertainties are overestimated for this dataset. Whatever the reason, there are fewer than 10 measurements that are affected by the value of this jitter parameter, and neither the orbital parameters nor the GP timescale parameters are affected by its particular value.

To investigate the impact of the long-term activity cycle on the marginalized orbital parameter posteriors, we performed another fit identical to the one described above, except we required that η_2 and η_3 vary between 1yr and the $\sim$ 30 yr observation baseline. The marginalized posteriors for η_2 and η_3 were broad, with power across the entire allowed space, although the period parameter η_3 showed local maxima at both $\sim$ 1100 d and $\sim$ 2000 d. The marginalized 1 d posteriors for both of these parameters did not vary with those of any of the orbital parameters, allowing us to conclude that the long-term activity cycle, while somewhat present in the RVs, did not significantly affect the derived values of the orbital parameters. We therefore adopt the rotation-only GP fit described above.

Our derived orbital parameters, accounting for the effect of rotationally-modulated stellar noise, are very similar to those of Mawet et al. (2019) (see their Table 3). We derive an orbital period of 2671^{+17}_{-23} days, a slightly reduced median semiamplitude of 10.3 m/s, and a low median eccentricity of 0.067. We show the series of RV measurements, the residuals to the fit and the phase folded RV curve in Fig. 2.2.

Combining Direct Imaging, Astrometry, and Radial Velocity Data

We use the RV posterior distributions presented in Sec. 2.3 that we obtain from the `RadVel` orbit fit as the prior probabilities for the model fit to the astrometry and direct imaging data. The set of priors from the RV fit consists of: a, e, ω, τ, and $M \sin i$. We use the same orbital parameter convention as in Blunt, Wang, et al. (2020). However, since the fit to the astrometry and direct imaging data will obtain a separate distribution for both the mass and inclination, we draw a set of correlated values for i and M from the $M \sin i$ distribution. We assume a *sine* distribution as a prior probability for i, which corresponds to an unconstrained prior for i.

Such a set of parameters presents a complex covariance that is practically impossible to reproduce if trying to represent these distributions in a parametric way. Instead, we choose to use a Kernel Density Estimator (KDE) to translate the posteriors to priors. A KDE smooths a probability density by convolving a Gaussian kernel with the discrete points of the MCMC chain. It allows one to preserve the covariance information contained in the original posteriors while allowing for a reliable reproduction of the shapes in the distributions. We use the `scipy.stats` package

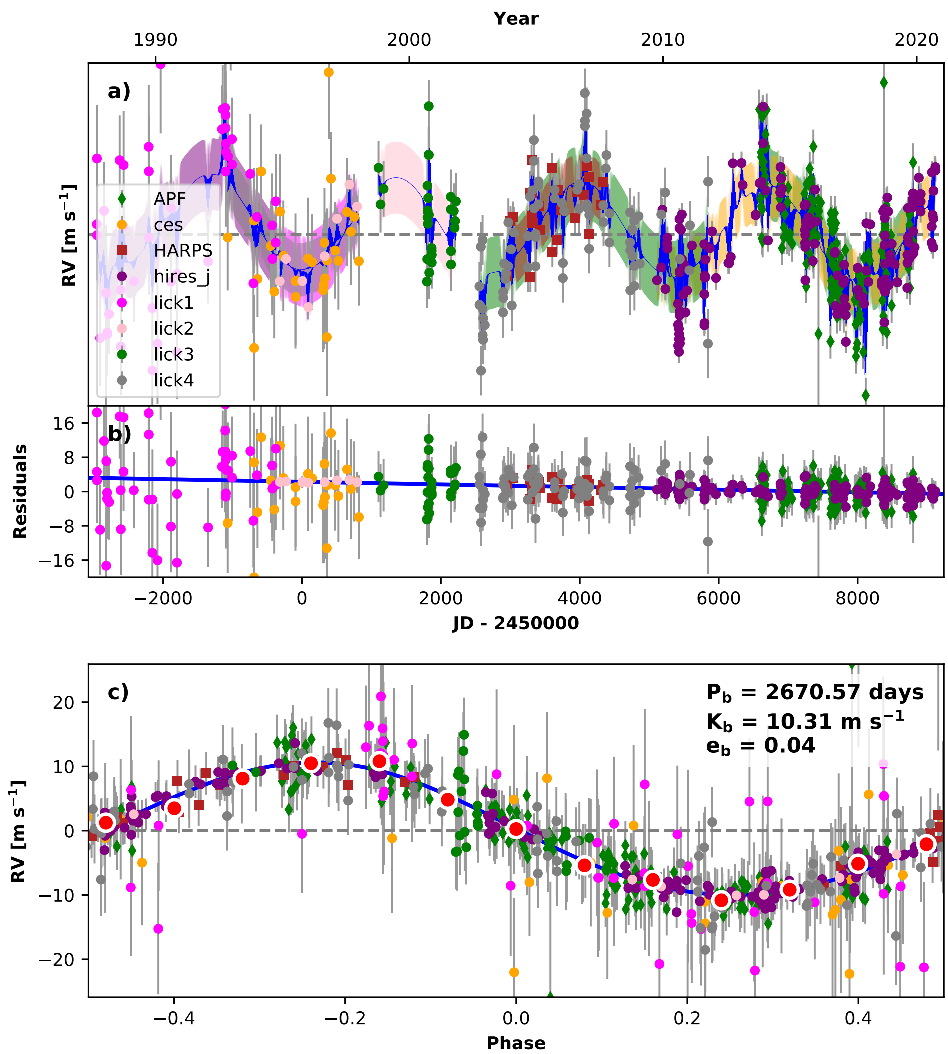

Figure 2.2 (a) Time series of radial velocities from all data sets, (b) residuals to the RV fit, (c) phase-folded RV curve. The maximum probability one-planet model is overplotted (*blue*), as well as the binned data (*red dots*).

Table 2.3. RV Fit MCMC Posteriors

Parameter	Credible Interval	Maximum Likelihood	Units
Modified MCMC Step Parameters			
P_b	2671^{+17}_{-23}	2661	days
$Tconj_b$	2460017^{+76}_{-32}	2460023	JD
$Tperi_b$	2460054^{+680}_{-690}	2460235	JD
e_b	$0.055^{+0.067}_{-0.039}$	0.046	
ω_b	$57.3^{+80.2}_{-154.7}$	2.1	$\circ$
K_b	$10.34^{+0.95}_{-0.93}$	10.33	m s^{-1}
Other Parameters			
γ_{lick4}	$-1.0^{+2.7}_{-2.6}$	−0.9	m s^{-1}
γ_{lick3}	10.0 ± 4.9	9.9	m s^{-1}
γ_{lick2}	$7.5^{+5.6}_{-5.7}$	7.6	m s^{-1}
γ_{lick1}	$4.4^{+6.2}_{-6.1}$	4.5	m s^{-1}
γ_{hires_j}	2 ± 1	2	m s^{-1}
γ_{harps}	$16442.5^{+3.2}_{-3.1}$	16442.4	m s^{-1}
γ_{ces}	$16446.6^{+5.7}_{-5.5}$	16446.6	m s^{-1}
γ_{apf}	-0.9 ± 1.3	−0.9	m s^{-1}
$\dot{\gamma}$	$-0.00026^{+0.00063}_{-0.0006}$	−0.00026	m s^{-1} d^{-1}
$\ddot{\gamma}$	$\equiv 0.0$	$\equiv 0.0$	m s^{-1} d^{-2}
σ_{lick4}	$5.17^{+1.1}_{-0.95}$	5	$m\ s^{-1}$
σ_{lick3}	$5.6^{+2.1}_{-2.3}$	5.3	$m\ s^{-1}$
σ_{lick2}	$2.3^{+3.6}_{-1.4}$	0.5	$m\ s^{-1}$
σ_{lick1}	$7.2^{+3.5}_{-3.7}$	7.4	$m\ s^{-1}$
σ_{hires_j}	$2.36^{+0.46}_{-0.41}$	2.26	$m\ s^{-1}$
σ_{harps}	$4.8^{+2.2}_{-2.7}$	4.3	$m\ s^{-1}$
σ_{ces}	$8.1^{+3.8}_{-4.5}$	7.3	$m\ s^{-1}$
σ_{apf}	$3.64^{+0.62}_{-0.55}$	3.51	$m\ s^{-1}$
$\eta_{1,apf}$	$7.82^{+0.97}_{-0.92}$	7.71	m s^{-1}
$\eta_{1,hires_j}$	$6.92^{+0.64}_{-0.59}$	6.78	m s^{-1}
$\eta_{1,ces}$	$7.5^{+4.1}_{-4.7}$	7.0	m s^{-1}
$\eta_{1,harps}$	$5.7^{+2.3}_{-3.0}$	5.3	m s^{-1}
$\eta_{1,lick,fischer}$	$8.7^{+1.3}_{-1.4}$	8.0	
η_2	$37.6^{+6.4}_{-5.4}$	36.4	days
η_3	$11.68^{+0.14}_{-0.13}$	11.66	days
η_4	$\equiv 0.5$	$\equiv 0.5$	

Note. — 436160 links saved. Reference epoch for γ,$\dot{\gamma}$,$\ddot{\gamma}$: 2457454.642028 implementation of a KDE, which allows for a customized value of the KDE bandwidth parameter. The choice of the bandwidth is critical to maintain the fidelity of the RV fit for the fit of the astrometry and direct imaging data. We explain the process to compute the optimal bandwidth for our data in Appendix 2.6.

The combined astrometric and imaging model consists of thirteen parameters: the six orbital parameters ($a, e, i, \omega, \Omega, \tau$), the mass of the companion M_b, the total mass of the system M_{tot}, the parallax, the position of the barycenter of the system at an arbitrary epoch (we choose the *Hipparcos* epoch at 1992.25, $\alpha_{1992.25}$ and $\delta_{1992.25}$), and the proper motion vector of the barycenter $\mu = [\mu_\alpha, \mu_\delta]$.

Astrometric Model

For the astrometric model, we use a similar approach to De Rosa, Esposito, et al., 2019 and Nielsen et al., 2020 while also fitting for the parallax and M_{tot}. This framework consists on deriving from the model a displacement of the photocenter from the barycenter induced by the presence of a companion. The orbital parameters and the relative mass are used to compute this relative motion of the photocenter about the barycenter. Then, to compare to the astrometry data, we obtain absolute astrometry quantities propagating from a reference RA/Dec position with the proper motion of the barycenter, and adding the relative displacement. For this reason we add to our model the reference position $\alpha_{1992.25}$ and $\delta_{1992.25}$, and the proper motion of the barycenter μ. We assume that the brightness of the planet is negligible compared to the host star (below 10 ppb reflected light in the visible); consequently making the photocenter and the star positions coincide.

We compute the goodness of fit to the astrometric data by deriving two distinct terms for both the *Hipparcos* and *Gaia* data: $\chi^2_{astrom} = \chi^2_H + \chi^2_G$. For the *Hipparcos* IAD, we calculate the expected position of the barycenter at all IAD epochs (α_H and δ_H) by propagating $\alpha_{1992.25}$ and $\delta_{1992.25}$ with μ. The displacement of the photocenter with respect to the barycenter ($\Delta\alpha_H$ and $\Delta\delta_H$) is computed using the expected orbit from the model orbital parameters, and the relative mass. We compare this values to the corresponding α_{IAD} and δ_{IAD} that we calculate from the 1D scans from IAD. We compute χ^2_H in the same way as in Nielsen et al., 2020.

Similarly for the *Gaia* data, we propagate the reference position of the barycenter, $\alpha_{1992.25}$ and $\delta_{1992.25}$, to the *Gaia* epoch: α_G and δ_G, and we compute the displacement of the photocenter with respect to the barycenter ($\Delta\alpha_G$ and $\Delta\delta_G$) with the orbital parameters and the relative mass. We compare this derived quantity to the

Gaia DR2 positional data, i.e. the RA/Dec from the *Gaia* DR2 catalog $\alpha_{G,GDR2}$ and $\delta_{G,GDR2}$. We can fit to the *Gaia* DR2 proper motion data by adding an instantaneous proper motion disturbance to the reference proper motion calculated by deriving an average linear velocity of the star due to its orbital motion over a few epochs around 2015.5. The χ^2_G associated with the *Gaia* data is then calculated in the same way as described in De Rosa, Esposito, et al. (2019).

The analysis of the *Hipparcos*-*Gaia* eDR3 acceleration data is done in the way described in Kervella et al. (2019).

Direct Imaging Model

The part of the likelihood function associated with the direct imaging data described in Sec. 2.2 is computed based on the method described in Mawet et al. (2019). The logarithm of the direct imaging likelihood ($\mathcal{P}$) (Ruffio, Mawet, et al., 2018) for a single epoch can be written as:

$$\log \mathcal{P}(d|I,x) = -\frac{1}{2\sigma_x^2}(I^2 - 2I\tilde{I}_x) \tag{2.1}$$

Where I is the planet flux corresponding to the planet mass in the orbital model, $\tilde{I}_x$ is the estimated flux from the data at the location x, and σ_x is the uncertainty of this estimate. Individual epochs are not combined in the main analysis of this work. The direct imaging epochs are assumed to be independent such that their log-likelihoods are simply added together. While this assumption is not perfect, it should not significantly affect the upper limit as the framework marginalizes over the spatial direction which will factor in any brighter speckles. To compute I from the planet mass, we use the COND evolutionary model (Baraffe et al., 2003) and we adopt an upper bound age of 800 Myr for the system (Janson et al., 2015). To compare with this age, we also run model fits with an age of 400 Myr, corresponding to the lower bound. $\tilde{I}_x$ is the flux measured in the image where the planet is predicted to be based on a given set of orbital parameters.

MCMC Results

The fit to the astrometry and direct imaging data using the `RadVel` posteriors as priors is performed using the `orbitize!`[1] package (Blunt, Endl, et al., 2019). We implement a Markov-chain Monte Carlo (MCMC) (Foreman-Mackey et al., 2013) analysis to fit for the six orbital parameters and the mass of planet b. MCMC has

[1]https://github.com/sblunt/orbitize

been extensively used to do orbit fitting, e.g. first by Hou et al. (2012) and more recently by Blunt, Endl, et al. (2019), Nowak et al. (2020), Hinkley et al. (2021) and Wang, Vigan, et al. (2021). As discussed in Sec. 2.3 we also fit for the mass of ϵ Eridani, as well as for the astrometric parameters α and δ, and μ_α and μ_δ. Therefore we fit for thirteen parameters; six orbital parameters, the parallax, the photocenter position vector and the proper motion vector, and the masses of the star and planet.

The knowledge of ϵ Eridani's mass is accounted with a Gaussian prior $0.82 \pm 0.02\ M_\odot$ (Baines et al., 2011). The priors for the astrometric parameters are set to uniform distributions centered at the *Hipparcos* values with broad ranges of $\pm 20\sigma$ to allow for deviations of the data from the nominal proper motion and photocenter position. The RV fits do not provide any constraints on the longitude of the ascending node, Ω, for which we set a uniform prior distribution. As discussed in Sec. 2.3, although the RV fits do not constrain the inclination, i, we assume a *sine* distribution to draw correlated values for the mass, M_b, and the inclination. The fit is performed with 550 walkers, and 18000 steps per walker.

The MCMC fits converge to yield the orbital parameters and mass posteriors shown in Table 2.4. Two fits are presented for both ends of the current bounds on the system's age, i.e., 400 and 800 Myr. A corner plot showing some of these and their correlations, for the 800 Myr fit, is shown in Fig. 2.3. A complete corner plot is shown in Appendix 2.6.

In order to assess the constraining power of the direct imaging data, given that our data consists of nondetections, we performed an MCMC run to only fit for the astrometry data. Fig. 2.4 show the posterior distribution compared to the prior distribution, i.e. the posteriors from the RV fit.

The use of the astrometry data results in a significantly improved constraining of the inclination of the planet with respect to the results presented in Mawet et al., 2019. Starting with a *sine* distribution as the prior, which is centered at 90°, the walkers converge onto an inclination of $i = 78.81^{\circ +29.34}_{-22.41}$. The addition of the astrometry data also yields a different model for the mass of the companion; by using the RV and direct imaging data we obtain a distribution of $M_b = 0.73^{+0.34}_{-0.13}$ M$_{Jup}$ (800 Myr), by adding the astrometry, $M_b = 0.66^{+0.12}_{-0.09}$ M$_{Jup}$ (800 Myr). The astrometry data from *Hipparcos* and *Gaia* seem to favor a lower mass planet and more edge-on inclinations. We compute the most probable perturbation semi-major axis: $\alpha_A = 0.89$ mas, which is a factor of ~2 away from the result reported by Benedict et al. (2006), i.e. 1.88 mas. More details on the perturbed orbit can be found in

Table 2.4. MCMC posteriors for different sets of data and assumptions for the age of the system.

	RV and Direct Imaging	RV, Astrometry, and Direct Imaging		RV and Astrometry	RV, Astrometry (eDR3 acc.), and Direct Imaging
	800 Myr	400 Myr	800 Myr	*No age assumption*	800 Myr
M_b (M_{Jup})	$0.74^{+0.37}_{-0.15}$	$0.66^{+0.11}_{-0.10}$	$0.66^{+0.12}_{-0.09}$	$0.65^{+0.10}_{-0.09}$	$0.64^{+0.09}_{-0.09}$
a_b (AU)	$3.52^{+0.04}_{-0.04}$	$3.53^{+0.04}_{-0.03}$	$3.53^{+0.03}_{-0.04}$	$3.53^{+0.04}_{-0.04}$	$3.52^{+0.04}_{-0.04}$
e	$0.07^{+0.07}_{-0.05}$	$0.07^{+0.07}_{-0.05}$	$0.07^{+0.07}_{-0.05}$	$0.07^{+0.07}_{-0.05}$	$0.07^{+0.07}_{-0.05}$
ω (°)	$-29.01^{+107.96}_{-111.95}$	$-28.37^{+75.90}_{-99.58}$	$-19.15^{+88.27}_{-94.80}$	$-19.54^{+97.09}_{-87.06}$	$-29.84^{+104.59}_{-115.85}$
Ω (°)	$181.27^{+124.60}_{-125.02}$	$195.06^{+127.20}_{-72.21}$	$198.18^{+127.29}_{-63.14}$	$195.08^{+122.64}_{-73.72}$	$190.06^{+108.72}_{-151.74}$
i (°)	$89.15^{+45.03}_{-43.16}$	$75.77^{+29.47}_{-19.94}$	$78.81^{+29.34}_{-22.41}$	$80.95^{+27.55}_{-21.39}$	$89.70^{+25.49}_{-25.08}$
τ_{peri}	$0.52^{+0.33}_{-0.35}$	$0.42^{+0.34}_{-0.29}$	$0.35^{+0.33}_{-0.24}$	$0.37^{+0.32}_{-0.25}$	$0.52^{+0.34}_{-0.36}$
$\Delta\alpha_H$ (mas)		$-0.33^{+0.54}_{-0.41}$	$-0.25^{+0.53}_{-0.47}$	$-0.20^{+0.51}_{-0.48}$	
$\Delta\delta_H$ (mas)		$0.27^{+0.32}_{-0.46}$	$0.30^{+0.32}_{-0.47}$	$0.25^{+0.32}_{-0.49}$	
PM_H^{α}		$-975.20^{+0.02}_{-0.02}$	$-975.20^{+0.02}_{-0.02}$	$-975.20^{+0.02}_{-0.02}$	
PM_H^{δ}		$19.95^{+0.02}_{-0.02}$	$19.95^{+0.02}_{-0.02}$	$19.95^{+0.02}_{-0.02}$	

Appendix 2.6.

We add the fit to the *Hipparcos-Gaia* eDR3 acceleration in the last column of Table 2.4. The results of this fit are largely consistent with the *Hipparcos* IAD-*Gaia* DR2 fits. Two main differences can be appreciated: (1) the inclination median is ~90°; however, the posterior probabilities converge to a similar inclination with respect to our other fits, i.e. ~75°, and to its supplementary angle, i.e. ~105°. This is probably because the rotation information available from the IAD is not accessible when using the proper motion anomalies. (2) The upper mass bound (see Fig. 2.4) is slightly lower, which brings the mass to a lower mass solution.

This result is an order of magnitude better than previously published (Mawet et al., 2019). The argument of periapsis, ω, reported in Mawet et al. (2019) is the stellar ω, which is the reason it is ~180° off with respect to the result presented here.

2.4 Discussion

Debris Disk

The interaction between the debris disk and planet in the ϵ Eridani system was thoroughly discussed in Mawet et al. (2019). Here we build on this analysis with our updated orbital constraints. ϵ Eridani's debris disk is currently known to be composed of three rings (Backman et al., 2008): a main ring from 35-90 AU, an inner belt at ~3 AU, an intermediate belt at ~20 AU. Planet b sits between the two inner belts. Extensive characterization of the disk has been carried out over the years; see Backman et al. (2008), MacGregor et al. (2015), and Booth et al.

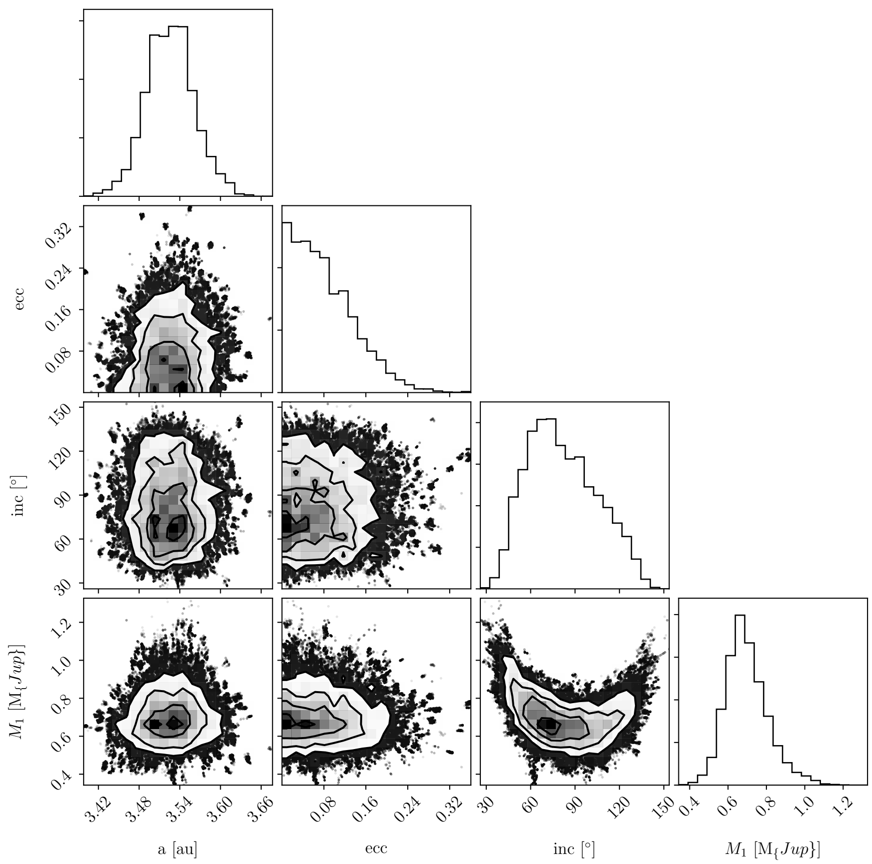

Figure 2.3 Corner plot of the posterior distributions and their correlation. These are the posteriors for the model fit to the RV, astrometry, and direct imaging data assuming an age of 800 Myr. We make use of `corner.py` (Foreman-Mackey, 2016) to produce corner plots.

(2017). In particular, Booth et al. (2017) analysis concluded the presence of a gap in emission in the circumstellar disk between ~20 and ~60 AU, which would indicate the presence of one or more companions in this range of separations. The inclination of the main ring was constrained to 34° ± 2 (Booth et al., 2017).

The orbital parameters and mass of planet b can set constraints on the edges of the inner belts (Wisdom, 1980). We follow the same analysis as Mawet et al. (2019) given that the eccentricity of the planet is expected to be well below 0.3, in which case the chaotic zone structure carved by the planet is independent of the eccentricity (Quillen et al., 2006). With the results of our MCMC fit (see Table 2.4), in particular the semi-major axis and relative mass, we expect there to be no particles from 2.97 to 4.29 AU. The edges are slightly moved outwards with respect to Mawet et al.

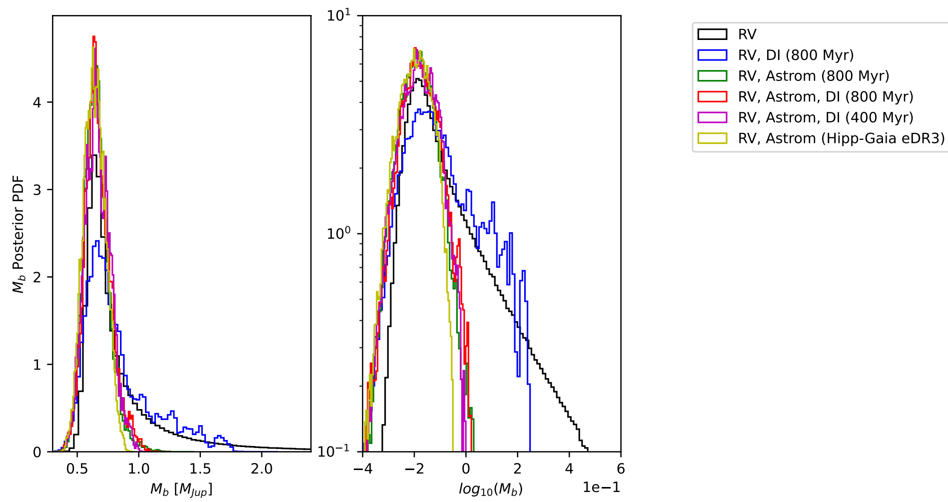

Figure 2.4 Mass posteriors PDF for different fits in linear (*left*) and logarithmic (*right*) scale. The astrometry data has a bigger constraining power on both ends of the mass bounds with respect to the direct imaging data available. In all fits except the RV only fit (*black*) we have utilized the KDE to include the RV posteriors as priors to the fit; an artifact thus appears at the extreme of lower bound in which the distribution slightly separates from the prior. A detailed explanation of this can be found in Appendix 2.6. However, closer to the median, the effect of adding the astrometry, for which a lower mass is allowed, is real, as it can be appreciated in the difference between the distributions with and without astrometry.

(2019) since the semi-major axis posterior of the planet is now larger, it was then reported no particles from 2.7 and 4.3 AU. The mass posterior is lower, which reduces the width of the chaotic zone by ∼4%.

It was concluded in Mawet et al. (2019) that the inner belt and outer ring were most likely to be self-stirred, i.e. collisions between disk particles are driven by particle-to-particle gravitational interactions, as opposed to being stirred by the presence of the planet (see Sec. 5.3.2. and Fig. 15 in Mawet et al. (2019)). The timescale for the planet to stir and shape the main ring is ∼1 Gyr, which, combined with the distance between the two, makes their dynamical coupling probably not significant. As for the intermediate belt, the timescales of self-stirring and planet-stirring were computed to be similar in the range of separations of the belt. The new orbital parameters from our MCMC fit (see Table 2.4), namely a lower mass for the planet and a slightly higher semi-major axis, contribute to larger planet-stirring timescales: an 18% increase in the planet-stirring timescale estimation with respect to Mawet

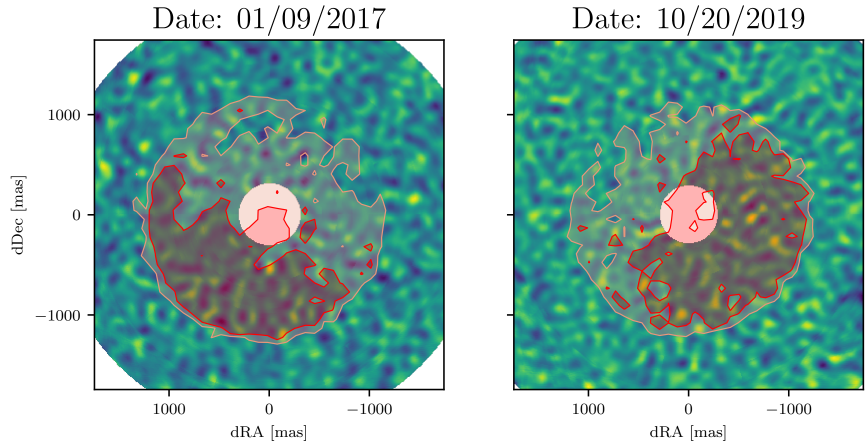

Figure 2.5 Keck/NIRC2 reduced data for two of the nine observing epochs (see Table 2.2), the 1- and 2-σ contours of the posteriors of the position are overplotted. The posteriors are for the model fit to the RV, astrometry and direct imaging data assuming an age of 800 Myr. The addition of the astrometry and direct imaging data breaks the degeneracy on the inclination, and the position of the companion is better constrained.

et al. (2019). However, this does not rule out the contribution of planet induced stirring process for the intermediate belt.

The inclination of ϵ Eridani b is constrained to $75.77^{\circ+29.92}_{-21.32}$ thanks to the inclusion of the astrometry data (see Sec. 2.3). This result indicates that the planet orbit is likely inclined with respect to the main ring, for which $i = 34^{\circ} \pm 2^{\circ}$, which is $\sim 2\sigma$ away from the most probable inclination. The origin of such a mutual inclination is unknown but could possibly be due to the dynamical effects of a third body.

A mutual inclination could be causing a warping on the main ring. Indeed, the vertical warp in the β Pictoris inner disk is believed to have been produced by its mutual inclination with β Pictoris b (e.g., Dawson et al., 2011). Using a similar analysis as presented in Dawson et al. (2011) based on secular interactions, we find that in the case of ϵ Eridani the minimum mass of planet at 3 AU to excite the inclination of dust particles in the ring at 70 AU after 800 Myr is of $\sim 0.5\ M_{Jup}$. This indicates that planet b could be in the regime of starting to drive a warp in the main ring if it is indeed misaligned with the disk plane. A coplanar solution is still allowed by the data since an inclination of 32° is $\sim 1\sigma$ away from the most probable inclination of the planet. It is worth noting that Benedict et al. (2006) yielded a solution for the inclination of the companion of $30.1° \pm 3.8°$.

Gaia's Future Sensitivity

De Rosa, Nielsen, et al. (2020) recently published the prospects for constraining mass of 51 Eridani b with *Gaia*'s final data release. They simulated sets of *Gaia* data with different astrometric error estimates, and found that the detection was possible only with optimistic mass and astrometric uncertainties. We performed a similar analysis computing the astrometric signal of ϵ Eridani b and comparing it to the sensitivity results of Fig. 11 on De Rosa, Nielsen, et al. (2020). We expect ϵ Eridani to have a similar astrometric error due to its brightness since the brightness of the star sets the uncertainty in the scans. We get an estimate for this at Lindegren et al. (2018): ~50 μas.

We find that the amplitude of the astrometric signal for ϵ Eridani b is an order of magnitude stronger than that of 51 Eridani b. Indeed, the shorter distance to the system and the period the planet both favorable factors for a stronger astrometric signal. For the nominal *Gaia* mission span of 5 years and for an astrometric uncertainty in the scans of 50 μa, ϵ Eridani b is detectable at ~1 M_{Jup}, which falls on the higher end of our mass posterior probability. However, for the extended mission span of 8 years, for which 51 Eridani is only detectable for a high mass estimate, ϵ Eridani b is readily detectable even at ~0.5 M_{Jup}, which is on the lower than the median mass of the posterior probability presented in this paper.

The final data release of Gaia's mission is a particularly exciting prospect for the exoplanet science field. Gaia final release will probably have access to constraining the dynamic mass of ϵ Eridani b. However, as the work presented in this paper aims at showing, it is by using this data combined with other observations that the best science is attainable.

Advantages of Combining Different Methods

The results presented in this paper are another example of the power of combining different methods to constrain a system's characteristics. By adding the astrometry data, we have identified new constraints for the inclination and longitude of the ascending node, both of which are inaccessible to an RV orbit fit. The direct imaging data, although it being a nondetection, sets upper limits on the mass. The distribution of most likely planet positions shown in Fig. 2.5 and how it prefers certain areas and fluxes is no coincidence; the MCMC walkers converge easier where the estimated flux from the coronagraph images is higher.

Although the constraints on the position shown in Fig. 2.5 are far from ideal, direct imaging planet hunters will take advantage of any position knowledge however small it may be. Indeed, data reduction techniques in direct imaging greatly benefit from a prior knowledge of the position of the object. For instance, in principal component analysis (PCA) (Soummer et al., 2012) based methods, a great deal of speckle subtraction power is gained by treating the data by patches; knowing where the planet is more likely to be reduces the computing time and allows the algorithm to focus on a constrained area of interest.

The synergies between RV, astrometry, and direct imaging data are currently being explored, and more work is being done in this direction (GRAVITY Collaboration et al., 2020).

Prospects for a Direct Detection with JWST

The James Webb Space Telescope (JWST) will provide the community with unprecedented capabilities to do infrared exoplanet science. In this section we discuss the prospect for a detection of ϵ Eridani b with JWST's NIRSPEC and MIRI instruments. In Fig. 2.6 we show the probability contour for the position of the planet at an epoch in JWST's Cycle 1.

MIRI

The Mid-Infrared Instrument (MIRI) aboard JWST is equipped with a coronagraph, and is expected to reach 10^{-4} levels of raw contrast at $\lambda = 10\ \mu m$ (mode F1065C) with conventional star subtraction (Boccaletti et al., 2015). We performed a more sophisticated data reduction as was done for MIRI in Beichman et al. (2020) to get a more accurate representation of the expected performance of MIRI on ϵ Eridani. We use the `IDL` library `MIRImSIM`[2], and the wavefront error drift predictions presented in Perrin et al. (2018). We make use of as much diversity as possible from the jitter of the telescope to perform a reference star subtraction based on principal component analysis (PCA, Soummer et al. (2012)). A more detailed description of the data processing can be found in Beichman et al. (2020).

In Fig. 2.7 we show some simulation results for MIRI observations. We find that, even for a perfect pointing accuracy of the telescope, MIRI would require ~75 hours to reach SNR>5.

[2]https://jwst.fr/wp/?p=30

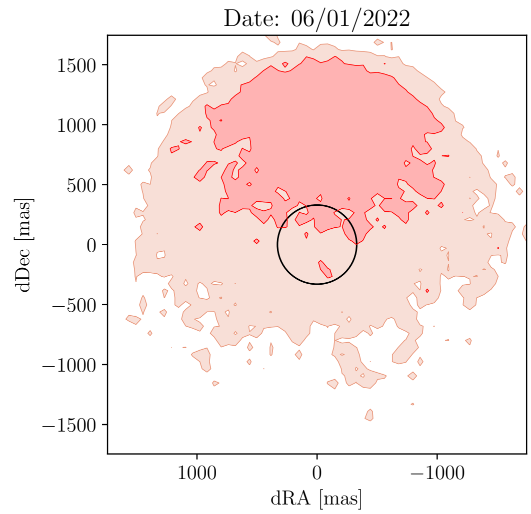

Figure 2.6 1- and 2-σ contours of the planet's position at a possible JWST epoch. This information can be useful for observers; for instance, when using the 4QPM coronagraph, the user will want to avoid the *gaps* falling on the most probable position of planet b. The black circle indicates the inner working angle of MIRI's F1065 mode Boccaletti et al. (2015). The posteriors used for this contours are taken from the fit to the RV, astrometry, and direct imaging data, assuming an 800 Myr age.

NIRSpec

A new avenue to imaging ϵ Eridani b is by using the moderate spectral resolution integral field spectroscopy mode of NIRSPEC (G395H/F290LP, with its 3x3" field of view). Atmospheric models predict a large excess emission around 4.5 μm from the atmosphere of exoplanets such as ϵ Eridani b (Marley et al., 2018). Ground-based medium resolution spectrographs ($R \sim 4000$) like OSIRIS and SINFONI have made clear detections of exoplanets as close as $0.4''$ from their star detector water and carbon monoxyde (Konopacky et al., 2013; Barman et al., 2015; Hoeijmakers et al., 2018; Wilcomb et al., 2020). The advantage of a higher spectral resolution is the possibility to subtract the starlight continuum with a high-pass filter and then use cross-correlation techniques to detect the molecular spectral signature of the planet. Like NIRSpec, these instruments were not designed for exoplanet detection, but the increased resolution can overcome a lack of a coronagraph and achieve comparable, if not better, detections of imaged exoplanets. Furthermore, the fact that these are spectroscopic detections opens up rich capabilities in atmospheric characterization that are simply not possible through imaging alone. Houlle et al.

(2021) demonstrated the power of high spectral resolution integral spectroscopy in the context of HARMONI, a first light instrument to the extremely large telescope, showing that it could detect planets 10 times fainter than angular differential imaging. NIRSpec is expected to excel at this technique thanks to the stability of a space observatory and the absence of variable telluric lines, which can be the source of spurious detection of molecules as discussed in Petit dit de la Roche et al. (2018).

To assess the feasibility of detecting these planets, we simulated NIRSpec observations with the JWST exposure time calculator (ETC) and implemented a forward modeling approach similar to Hoeijmakers et al. (2018) and Ruffio, Macintosh, Konopacky, et al. (2019) to NIRSpec in which a starlight and a planet model are jointly fitted. The planet model consists of a Sonora atmospheric (Marley et al., 2018) modulated by the transmission of the instrument. The same simulation is used to derive the sensitivity of NIRSpec as a function of separation, shown in Fig. 2.7. The JWST ETC does not include many of the likely source of errors that will affect the calibration of the data so the final sensitivity remains uncertain. However, cross correlation techniques are not sensitive to speckle variability and chromaticity, or telescope pointing precision unlike conventional speckle subtraction techniques. The observations are dominated by the photon noise from the diffracted starlight, so it is critical to minimize the effect of the diffraction spikes in the JWST PSF. They are more than an order of magnitude brighter than the rest of the PSF at a given separation. To avoid chance alignments of the planets with the diffraction spikes, two visits per star with a 30° pupil rotation can be used to double the average sensitivity of the observation, which is twice as efficient as simply increasing the integration time (Fig. 2.7). Even in the fastest reading mode and shortest available integration time, the core of the PSF will heavily saturate around 0.6″ which is limiting the inner working angle. We note that the planets only emit toward the redder part of the band (4.2 μm) where the starlight is dimmer, so any wavelength shorter than 4.2 μm is allowed to saturate with no consequence. Any detector persistence in pixels previously saturated in an earlier dither position will appear like slightly elevated stellar signal, and will naturally be removed by the high pass filtering as if it were speckle noise.

Prospective for a Detection in Reflected Light with the Roman Coronagraph Instrument

Carrion-González et al. (2021) assessed the potential of detecting reflected light from a set of exoplanets in nearby systems with the Roman coronagraph instrument

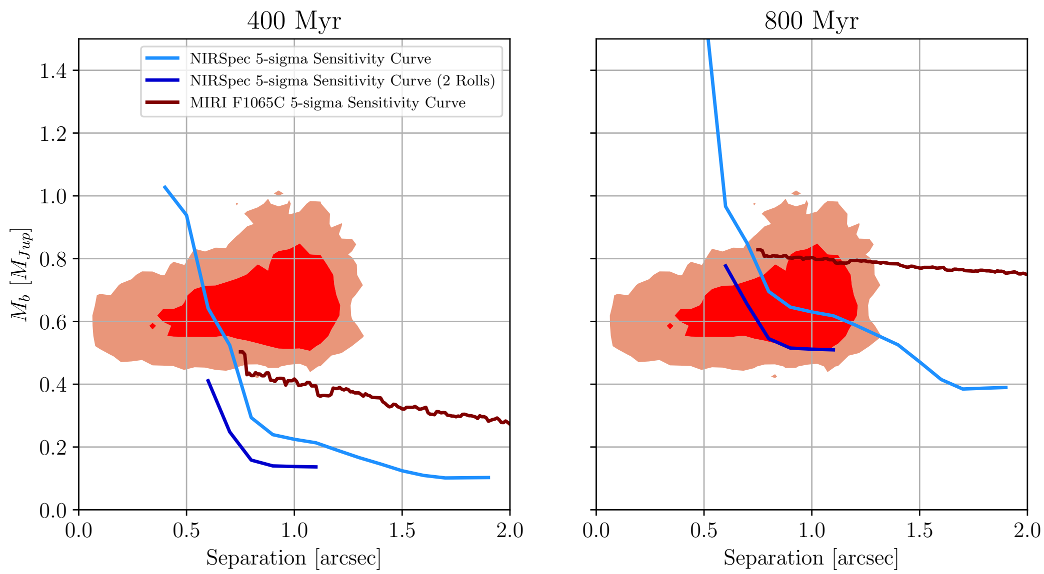

Figure 2.7 Expected 5σ sensitivity for NIRSpec and MIRI using our data reduction techniques, compared to the expected location and mass of the companion; *red*: 1- and 2-σ contours at an epoch close to the expected maximum elongation, i.e. January 2024. The upper sensitivity curve for NIRSpec corresponds to 2 hours of exposure times, while the two-roll case corresponds to a total of 4 hours with a 30° pupil rotation between two rolls to mitigate the effect of the diffraction spikes of the JWST point spread function. The MIRI simulations require ~75 hours of exposure time to get enough signal-to-noise. These results indicate that NIRSpec is the most sensitive instrument for this science case.

(CGI). In particular, ϵ Eridani stands out as a particularly notable, yet risky target; like most targets for the Roman CGI, it would require thousands of hours to get a detection. They conclude that ϵ Eridani b would be *Roman-accessible* at a probability of 57.99%, in the optimistic case, and 51.29% in the pessimistic case. However, they argue that the inclination "is the key factor affecting the detectability of this planet." Indeed, as it can be seen in their Fig. C.5, a more edge-on orbit is more favorable to avoiding the outer working angle. Our result for the inclination, i = $78.81^{\circ+29.34}_{-22.41}$, indicates that the orbit should be more favorable for detection, since Carrion-González et al. (2021) assume face-on as the most probable orbit.

Prospects for Ground Based Observatories

A recent publication by Pathak et al. (2021) presented new observations of ϵ Eridani at 10 μm with the VLT/VISIR. They obtained comparable sensitivities to the Keck/NIRC2 results presented here. They claim that a sensitivity to 1 M_{Jup} can be attained with 70 hours of exposure time, assuming an age of 700 Myr and the current setup for the instrument. Unfortunately, the results presented here indicate that the mass is likely lower than 1 M_{Jup}. However, there are envisioned ways to upgrading VISIR which would improve its sensitivity at smaller separations (Kasper et al., 2019).

Although a formidable task for current ground based observatories, imaging ϵ Eridani b should be much easier with future 30-meter class telescopes. High-contrast imaging at L, M and N bands with METIS at the ELT will essentially be background-limited at the angular separation of ϵ Eridani b (Carlomagno et al., 2020). METIS is expected to have access to Earth-like planets around α Centauri A with 5 h of exposure time N band (Brandl et al., 2021), which would make ϵ Eridani b detectable in the order of minutes. Similarly, the TMT with its second generation instrument PSI is expected to reach 10^{-8} final contrast at 2 λ/D (Fitzgerald et al., 2019), well above the sensitivity needed to image ϵ Eridani b.

2.5 Conclusion

We combine observations of ϵ Eridani from three different methods: radial velocities spanning three decades, the combined astrometry data from *Hipparcos* IAD and GRD2, and vortex coronagraph images with Keck/NIRC2. We perform a fit to this data using MCMC and obtain the best constraints to date for the orbital parameters and mass of ϵ Eridani b. Namely, a lower mass posterior with respect to previous analysis (Mawet et al., 2019), $M_b = 0.66^{+0.12}_{-0.09}$ M$_{Jup}$, and new constraints for the inclination, $i = 78.81^{\circ+29.34}_{-22.41}$. The new inclination seems to indicate that the planet orbit is not co-planar with the main ring structure, at $i = 34° \pm 2°$. Our results are consistent with a small eccentricity, and we improved the accuracy of the time of conjunction to ~81 days.

These improved constraints translate in a more confident prediction of the position at any epoch as (see Figs. 2.5 and 2.6). We show how this information can be useful when planning the observing strategy, and data reduction, with future missions like the JWST. The JWST is a particularly exciting prospect: we show how NIRSpec could obtain a detection with a reasonable exposure time of just a few hours. More work is expected to be done in this regard. Another exciting landmark for the field of exoplanetary science is the final release of *Gaia*'s data; we show how, with the expected sensitivity, *Gaia* will most likely have access to a dynamic mass measurement of ϵ Eridani b.

In this paper, we show that the combination of data sets from different observing methods has the power to yield previously inaccessible planetary characteristics from the elusive ϵ Eridani b. As more RV data continues to be collected, and RV facilities and instruments continue to be improved, plus the prospects of Gaia's final data release, and future coronagraph images, the prospects for studying this planet are promising.

2.6 Appendix

Radial Velocity Measurements

The new RV measurements are shown in Table 2.5.

Table 2.5: Radial Velocities

Time (JD)	RV ($m\ s^{-1}$)	RV Unc. ($m\ s^{-1}$)	Inst.
2457830.7206	-13.32	1.10	$hires_j$
2457957.0042	-9.42	2.67	apf
2457957.0049	-18.75	2.72	apf
2457957.0055	-18.07	2.86	apf
2457971.9799	-19.64	2.61	apf
2457971.9806	-21.74	2.51	apf
2457971.9814	-20.58	2.53	apf
2457975.9705	-29.90	2.50	apf
2457975.9712	-26.60	2.55	apf
2457975.9720	-26.59	2.45	apf
2457983.0029	-25.13	2.36	apf
2457983.0036	-28.48	2.19	apf
2457983.0044	-23.69	2.33	apf
2457991.9333	-19.97	2.54	apf
2457991.9342	-19.61	2.37	apf
2457991.9350	-20.31	2.42	apf
2457993.0151	-23.62	2.13	apf
2457993.0158	-30.11	2.32	apf
2457993.0166	-21.83	2.05	apf
2458000.1544	-4.85	0.90	$hires_j$
2458001.1525	-4.85	0.95	$hires_j$
2458003.1521	-9.65	0.92	$hires_j$

2458011.8651	-6.39	3.20	apf
2458011.8658	-14.24	3.06	apf
2458011.8665	-8.81	2.98	apf
2458011.9773	-3.93	2.69	apf
2458011.9779	-9.78	2.72	apf
2458011.9786	-13.28	2.60	apf
2458024.9756	-9.99	2.20	apf
2458024.9763	-10.66	2.23	apf
2458024.9770	-9.56	2.46	apf
2458027.8153	-18.68	3.08	apf
2458027.8173	-16.81	3.07	apf
2458027.8191	-19.40	2.79	apf
2458027.9419	-18.22	4.21	apf
2458027.9427	-18.13	2.92	apf
2458027.9434	-18.38	3.45	apf
2458029.9391	-11.04	1.07	hires_j
2458031.9469	-16.01	2.19	apf
2458031.9477	-15.41	2.34	apf
2458031.9485	-17.23	2.22	apf
2458032.9383	-9.09	2.28	apf
2458032.9392	-6.62	2.20	apf
2458032.9400	-10.73	2.25	apf
2458039.8294	-12.02	2.29	apf
2458039.8301	-12.76	2.25	apf
2458039.8309	-10.73	2.37	apf
2458040.9596	-14.86	2.28	apf
2458040.9604	-15.63	2.28	apf
2458040.9612	-15.16	2.30	apf
2458041.9011	-17.38	2.27	apf
2458041.9019	-20.79	2.03	apf
2458041.9027	-20.04	2.10	apf
2458051.7346	-9.28	3.29	apf
2458051.7353	-13.60	3.34	apf
2458051.7360	-10.66	3.23	apf
2458063.8317	-9.47	3.22	apf
2458063.8324	-18.04	3.19	apf

2458063.8332	-11.10	3.49	apf
2458065.9048	-11.21	1.16	hires_j
2458080.8503	-28.17	2.22	apf
2458080.8511	-28.91	2.42	apf
2458080.8519	-23.24	2.28	apf
2458086.7355	-10.09	2.62	apf
2458086.7362	-17.91	2.75	apf
2458086.7369	-13.81	2.65	apf
2458088.6965	-8.24	2.75	apf
2458088.6971	-8.44	2.70	apf
2458088.6978	-6.73	2.93	apf
2458088.8101	-3.59	2.29	apf
2458088.8108	-7.83	2.24	apf
2458088.8116	-3.13	2.32	apf
2458091.9103	-12.71	1.17	hires_j
2458115.6819	-32.50	2.89	apf
2458115.6826	-37.07	2.71	apf
2458115.6832	-38.80	2.76	apf
2458119.7231	-11.88	3.31	apf
2458119.7238	-9.47	2.80	apf
2458119.7245	-8.95	3.07	apf
2458124.8560	4.97	1.04	hires_j
2458125.6912	-5.43	0.96	hires_j
2458131.6676	-15.23	2.81	apf
2458131.6683	-3.72	2.92	apf
2458131.6690	-9.99	2.99	apf
2458154.7030	-7.90	1.15	hires_j
2458156.6999	-6.81	2.40	apf
2458156.7009	-6.12	2.39	apf
2458156.7018	-2.55	2.40	apf
2458175.6205	-4.60	2.54	apf
2458175.6222	-9.71	2.26	apf
2458175.6236	-5.39	2.21	apf
2458181.7462	4.72	1.36	hires_j
2458343.0008	-3.22	2.55	apf
2458343.0017	-4.83	2.48	apf

2458343.0025	-5.67	2.54	apf
2458346.1447	-7.86	0.93	hires$_j$
2458350.1449	-8.76	1.00	hires$_j$
2458356.9155	-1.36	2.23	apf
2458356.9162	-4.72	2.17	apf
2458356.9170	2.84	2.08	apf
2458357.9251	-12.01	2.49	apf
2458357.9258	-16.35	2.32	apf
2458357.9266	-17.44	2.35	apf
2458359.9026	-19.24	2.44	apf
2458359.9035	-25.73	2.50	apf
2458359.9043	-20.22	2.51	apf
2458367.0466	7.57	1.00	hires$_j$
2458369.0367	-8.97	2.19	apf
2458369.0375	-7.22	2.23	apf
2458369.0382	-6.04	2.14	apf
2458370.0423	-18.25	2.27	apf
2458370.0430	-18.08	2.26	apf
2458370.0437	-20.25	2.41	apf
2458377.0051	32.40	38.87	apf
2458379.0183	-4.80	2.39	apf
2458379.0189	-5.50	2.50	apf
2458379.0196	-7.38	2.29	apf
2458384.0611	-16.79	1.01	hires$_j$
2458386.0254	-9.85	1.06	hires$_j$
2458387.0174	0.19	1.08	hires$_j$
2458387.9630	3.39	2.26	apf
2458387.9637	1.27	2.42	apf
2458387.9645	-0.11	2.23	apf
2458387.9940	8.09	1.10	hires$_j$
2458390.0029	1.72	2.50	apf
2458390.0042	2.69	2.37	apf
2458390.0042	-2.89	2.47	apf
2458390.0479	6.12	0.96	hires$_j$
2458390.9784	-3.06	2.26	apf
2458390.9792	3.35	2.41	apf

2458390.9801	2.41	2.38	apf
2458392.0595	2.27	1.08	$hires_j$
2458394.0773	-7.38	1.04	$hires_j$
2458396.0349	-10.04	1.19	$hires_j$
2458396.9693	-3.90	1.23	$hires_j$
2458398.8491	4.51	3.30	apf
2458398.8499	-2.61	3.38	apf
2458398.8506	-2.75	3.02	apf
2458398.9204	0.82	2.90	apf
2458398.9211	4.59	3.02	apf
2458398.9217	-5.49	2.89	apf
2458399.9857	-0.15	2.55	apf
2458399.9866	1.95	2.51	apf
2458399.9874	1.36	2.44	apf
2458400.9738	0.34	2.46	apf
2458400.9746	-0.60	2.37	apf
2458400.9753	0.62	2.41	apf
2458410.9247	-12.64	2.46	apf
2458410.9254	-7.35	2.31	apf
2458410.9261	-8.92	2.35	apf
2458414.8894	9.86	2.17	apf
2458414.8902	4.71	2.10	apf
2458414.8909	1.61	2.29	apf
2458418.8942	-21.68	2.42	apf
2458418.8950	-25.37	2.40	apf
2458418.8958	-20.21	2.35	apf
2458419.9035	-13.62	2.99	apf
2458419.9045	-11.57	2.79	apf
2458419.9067	-11.59	2.07	apf
2458426.9223	10.59	1.04	$hires_j$
2458439.0088	7.54	1.28	$hires_j$
2458443.8821	-10.76	1.18	$hires_j$
2458443.8827	-6.02	1.02	$hires_j$
2458443.8832	-10.14	1.22	$hires_j$
2458462.8538	-2.77	1.02	$hires_j$
2458462.8544	-1.14	1.04	$hires_j$

2458462.8549	-2.01	1.01	hires_j
2458476.7717	-3.32	1.02	hires_j
2458476.7722	-2.91	1.05	hires_j
2458476.7727	-3.41	0.97	hires_j
2458480.7128	-4.31	2.48	apf
2458480.7139	2.18	2.60	apf
2458480.7150	-0.89	2.54	apf
2458487.6420	-4.39	2.37	apf
2458487.6427	-4.97	2.28	apf
2458487.6434	-6.74	2.41	apf
2458488.6304	-16.61	2.84	apf
2458488.6311	-17.42	2.53	apf
2458488.6317	-15.66	2.40	apf
2458490.7571	2.75	1.04	hires_j
2458490.7577	0.01	1.05	hires_j
2458490.7582	-1.50	1.06	hires_j
2458532.7200	-4.04	1.12	hires_j
2458568.7106	-7.45	1.08	hires_j
2458568.7112	-8.92	1.17	hires_j
2458568.7117	-7.60	1.12	hires_j
2458569.7117	-7.98	1.00	hires_j
2458569.7123	-7.88	1.10	hires_j
2458569.7128	-8.14	1.02	hires_j
2458714.1492	-9.22	1.08	hires_j
2458715.1508	-1.96	0.93	hires_j
2458716.1499	-3.73	0.89	hires_j
2458723.1549	8.30	0.96	hires_j
2458724.1550	1.85	0.93	hires_j
2458732.0204	-7.99	2.41	apf
2458732.0230	-9.53	2.27	apf
2458732.0252	-7.23	2.32	apf
2458733.1529	0.70	1.04	hires_j
2458744.1572	-2.81	1.16	hires_j
2458746.8760	-2.41	2.33	apf
2458746.8768	3.22	2.40	apf
2458746.8777	1.49	2.39	apf

2458746.8785	2.54	2.26	apf
2458747.8382	6.14	2.72	apf
2458747.8391	0.56	2.66	apf
2458747.8401	2.39	2.84	apf
2458747.8410	5.68	2.69	apf
2458749.8802	1.21	2.64	apf
2458749.8812	5.31	2.52	apf
2458749.8822	3.23	2.64	apf
2458752.9836	-15.60	2.07	apf
2458752.9844	-11.82	2.24	apf
2458752.9852	-10.04	2.22	apf
2458752.9860	-12.86	2.27	apf
2458765.8514	0.59	2.51	apf
2458765.8523	-1.54	2.25	apf
2458765.8533	-5.55	2.65	apf
2458776.9385	-2.09	1.14	$hires_j$
2458794.9139	10.33	1.06	$hires_j$
2458795.9719	11.51	0.96	$hires_j$
2458796.9731	8.51	1.17	$hires_j$
2458797.9759	3.21	1.01	$hires_j$
2458798.8832	15.73	3.20	apf
2458798.8838	15.91	4.46	apf
2458798.8844	10.47	5.65	apf
2458798.9255	9.65	1.05	$hires_j$
2458800.7426	0.40	8.44	apf
2458800.7431	-11.34	10.11	apf
2458800.7437	0.37	8.28	apf
2458802.9074	-1.55	1.04	$hires_j$
2458819.9272	-1.62	1.23	$hires_j$
2458819.9278	2.20	1.17	$hires_j$
2458819.9285	-1.86	1.25	$hires_j$
2458880.7768	14.95	1.09	$hires_j$
2458905.7045	7.52	0.93	$hires_j$
2458906.7048	9.72	1.01	$hires_j$
2458907.7049	11.37	1.05	$hires_j$
2459064.1408	0.66	0.88	$hires_j$

2459067.1418	4.26	0.92	hires_j
2459069.0914	16.14	0.91	hires_j
2459079.1461	6.80	0.97	hires_j
2459088.1435	-0.35	0.83	hires_j
2459089.1488	-0.30	1.06	hires_j
2459090.1506	5.99	0.85	hires_j
2459091.1516	12.06	0.89	hires_j
2459117.1542	16.88	1.01	hires_j
2459118.1551	17.29	0.96	hires_j
2459120.0833	16.54	0.94	hires_j

Hipparcos IAD Measurements

The full list of IAD measurements of ϵ Eridani are shown in Table 2.6.

Table 2.6: *Hipparcos* IAD Measurements

Time (yr)	RA (°)	Dec. (°)
1990.036	52.5116405005777	-9.4583497858903
1990.036	52.5116401584946	-9.4583496322689
1990.036	52.5116403587071	-9.4583497221005
1990.036	52.5116403865140	-9.4583497347661
1990.165	52.5115962411255	-9.4583180708649
1990.165	52.5115959467574	-9.4583177566427
1990.165	52.5115960096074	-9.4583178233896
1990.537	52.5116469916317	-9.4582724641828
1990.537	52.5116469841479	-9.4582725080033
1990.598	52.5116419591556	-9.4582840685775
1990.598	52.5116414487723	-9.4582837747986
1990.598	52.5116417640389	-9.4582839565381
1990.598	52.5116420312751	-9.4582841103275
1990.986	52.5114013929774	-9.4583510281954
1990.986	52.5114013393019	-9.4583509989263
1990.986	52.5114015402335	-9.4583511001388
1990.986	52.5114012050044	-9.4583509320788

1990.986	52.5114009365369	-9.4583507920843
1990.986	52.5114013955396	-9.4583510292821
1990.986	52.5114010690108	-9.4583508624671
1991.033	52.5113714176233	-9.4583447128771
1991.033	52.5113714135922	-9.4583447403729
1991.033	52.5113713999200	-9.4583448169388
1991.033	52.5113714029650	-9.4583448033679
1991.211	52.5113225169863	-9.4582994758077
1991.211	52.5113226736580	-9.4582992298002
1991.211	52.5113224771832	-9.4582995327838
1991.211	52.5113225766121	-9.4582993787588
1991.211	52.5113225353019	-9.4582994446619
1991.211	52.5113226173269	-9.4582993157660
1991.211	52.5113225487930	-9.4582994236099
1991.211	52.5113226206707	-9.4582993113122
1991.233	52.5113235973147	-9.4582931095657
1991.233	52.5113235887250	-9.4582928458202
1991.233	52.5113235967572	-9.4582930845733
1991.233	52.5113236047697	-9.4582933483541
1991.233	52.5113235890592	-9.4582926401783
1991.233	52.5113235894297	-9.4582926262907
1991.233	52.5113235941072	-9.4582930012824
1991.233	52.5113236004370	-9.4582932122974
1991.487	52.5113727458625	-9.4582615280949
1991.487	52.5113727288772	-9.4582614578977
1991.487	52.5113727022689	-9.4582613500171
1991.487	52.5113727581897	-9.4582615765491
1991.487	52.5113728058925	-9.4582617679102
1991.487	52.5113727896355	-9.4582617118418
1991.524	52.5113756856158	-9.4582652690679
1991.524	52.5113756602019	-9.4582652578526
1991.617	52.5113670292940	-9.4582828689332
1991.617	52.5113670158256	-9.4582828932237
1991.618	52.5113670300430	-9.4582826870404
1991.618	52.5113667689413	-9.4582831584554
1991.714	52.5113300285460	-9.4583083881100

1991.714	52.5113300175102	-9.4583083656777
1991.714	52.5113301324919	-9.4583086000961
1991.714	52.5113300055516	-9.4583083406066
1991.714	52.5113299595752	-9.4583082455852
1991.714	52.5113300402794	-9.4583084132933
1991.715	52.5113293922848	-9.4583084348328
1991.715	52.5113293727876	-9.4583083887744
1991.715	52.5113294670004	-9.4583085961528
1992.062	52.5110857608807	-9.4583343386895
1992.062	52.5110853444093	-9.4583341343475
1992.062	52.5110851647440	-9.4583340464981
1992.062	52.5110856265134	-9.4583342719861
1992.062	52.5110853695640	-9.4583341461406
1992.139	52.5110586465189	-9.4583148046891
1992.139	52.5110585719244	-9.4583149218441
1992.139	52.5110585808650	-9.4583149077813
1992.139	52.5110585956311	-9.4583148842530
1992.189	52.5110520744159	-9.4583002913271
1992.189	52.5110521033931	-9.4583003354390
1992.189	52.5110521308103	-9.4583003772504
1992.189	52.5110519452936	-9.4583000936515
1992.563	52.5111043447049	-9.4582660986126
1992.563	52.5111044409491	-9.4582658056901
1992.563	52.5111043696635	-9.4582660220212
1992.563	52.5111043689974	-9.4582660247248

Using the Kernel Density Estimator

The bandwidth is in practice associated with the smoothing of the kernel, and has to be carefully tuned to (1) avoid data artifacts caused by undersmoothing, and (2) retain the distribution tail information and skewed bounds limits that could be lost by oversmoothing. In Fig. 2.8(a) we illustrate these effects and the importance of bandwidth selection. The value of the optimal bandwidth is, however, heavily dependent on the data; a higher amount of data points allows for a more aggressive bandwidth, i.e. lower bandwidth, and a low number of data points is more susceptible to a spurious ridged distribution.

A way of choosing the KDE bandwidth is: 1. Pick an acceptable change in the median and 68th interval limits of the KDE fit w.r.t the actual posterior distribution. This will set a maximum acceptable bandwidth. 2. Pick an acceptable variation of the log-prior probability when evaluating the priors for a SMA around the prior median SMA. This will set a minimum acceptable bandwidth. For this we will loop over a set of bandwidths computing the median and 68th interval limits, and for each bandwidth we will compute the variation of log-prior with a set of SMAs around the prior median SMA: we will fit a Gaussian and the standard deviation of the residuals to the fit will be our cost function.

Perturbed Orbit Solution

The perturbed orbit for the case of 800 Myr is shown in Fig. 2.9; the perturbation size is α_A = 0.89 mas. Overplotted are the estimated positions of ϵ Eridani for the *Hipparcos* and *Gaia* epochs; *Hipparcos* covers ~35% of the orbit, *Gaia* epoch is taken as 2015.5.

Corner Plot

In Fig. 2.10 the full corner plot is shown, with the posterior distributions and their correlation for the six orbital parameters and the masses. These posteriors correspond to the MCMC run for the fit to the RV, astrometry, and direct imaging data assuming an age of 800 Myr.

2.7 Acknowledgments

This work was partially supported by the National Science Foundation AST-ATI Grant 1710210. The material is based upon work supported by NASA under award No. 80NSSC20K0624. J.J.W. is supported by the Heising-Simons Foundation 51 Pegasi b Fellowship. J.J.W. thanks Rob de Rosa and Eric Nielsen for helpful discussions. P. D. is supported by a National Science Foundation (NSF) Astronomy and Astrophysics Postdoctoral Fellowship under award AST-1903811. M.R. is supported by the National Science Foundation Graduate Research Fellowship Program under Grant Number DGE-1752134 Part of this work has received funding from the European Research Council (ERC) under the European Union's Horizon 2020 research and innovation programme (grant agreement No. 819155), and by the Wallonia-Brussels Federation (grant for Concerted Research Actions). J.L.-S. thanks Christopher Mendillo for helpful discussions.

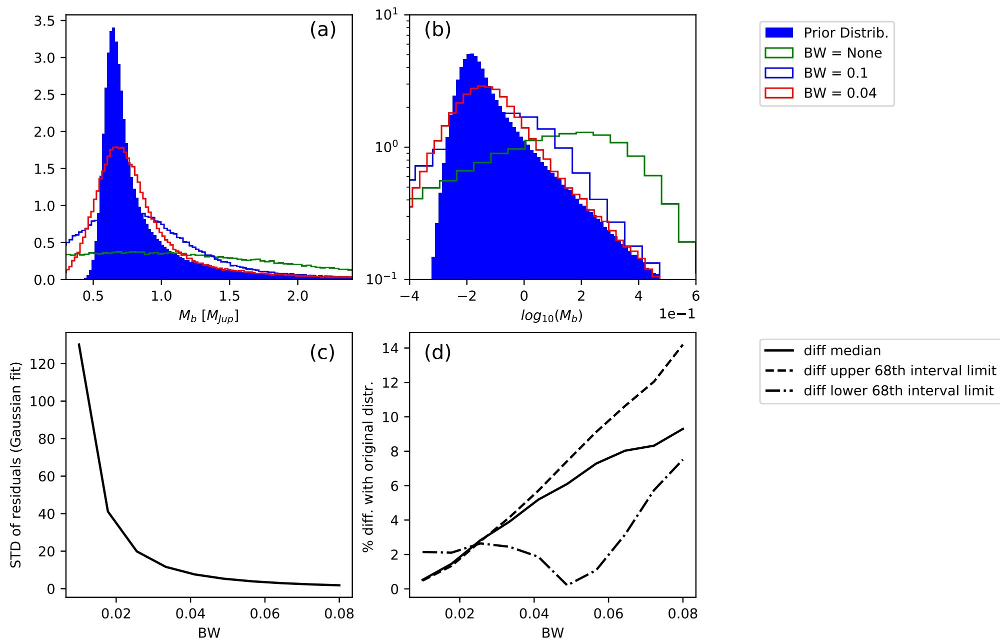

Figure 2.8 (a) Mass-histogram comparing three different KDE bandwidths to fit the 6-correlated parameters from the RV fit. The blue bar histogram represents the distribution from the RV fit, the step histograms are KDE fit to that distribution for different bandwidths. (b) The residuals in prior probability to a Gaussian fit versus the KDE bandwidth. For a set of reasonable SMAs, we compute the prior probabilities, and we fit a Gaussian; the narrower the bandwidth, the more the spurious effects of the RV posterior sampling affect the KDE fit. (c) Difference between the KDE fit and the original prior distribution for the mass distribution. The narrower the bandwidth, the closer to the original distribution. (d) Difference of the confidence intervals with respect to the original distribution. The narrower the bandwidth the more the upper and lower bounds are similar to the original distribution. A balance, thus, needs to be found between a small enough bandwidth so that the upper and lower bounds are well reproduced (see (d)), but not as small as to begin an undersmoothing effect (see (c)).

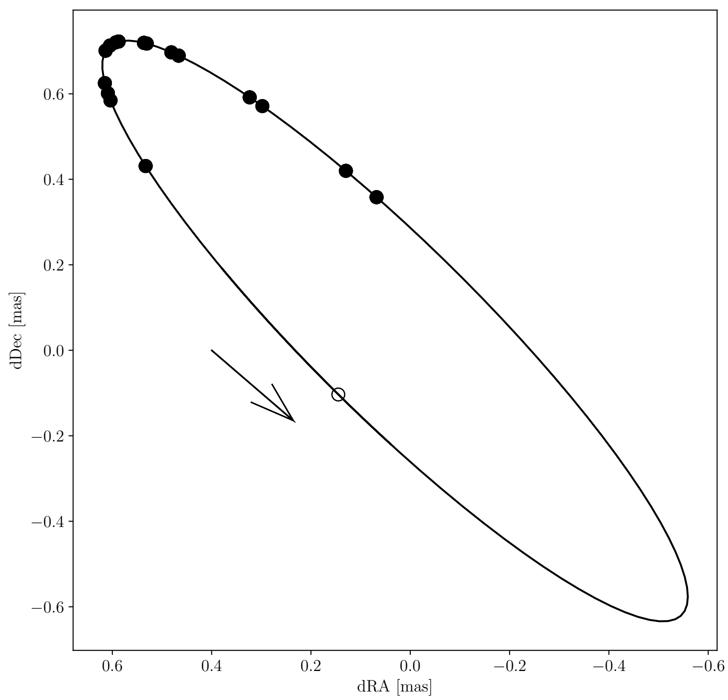

Figure 2.9 ϵ Eridani's perturbed orbit caused by the presence of the companion. Filled circles indicate the estimated position of the star at the *Hipparcos* IAD epochs, the empty circle indicates the *Gaia* DR2 epoch. The arrow indicates the direction of motion.

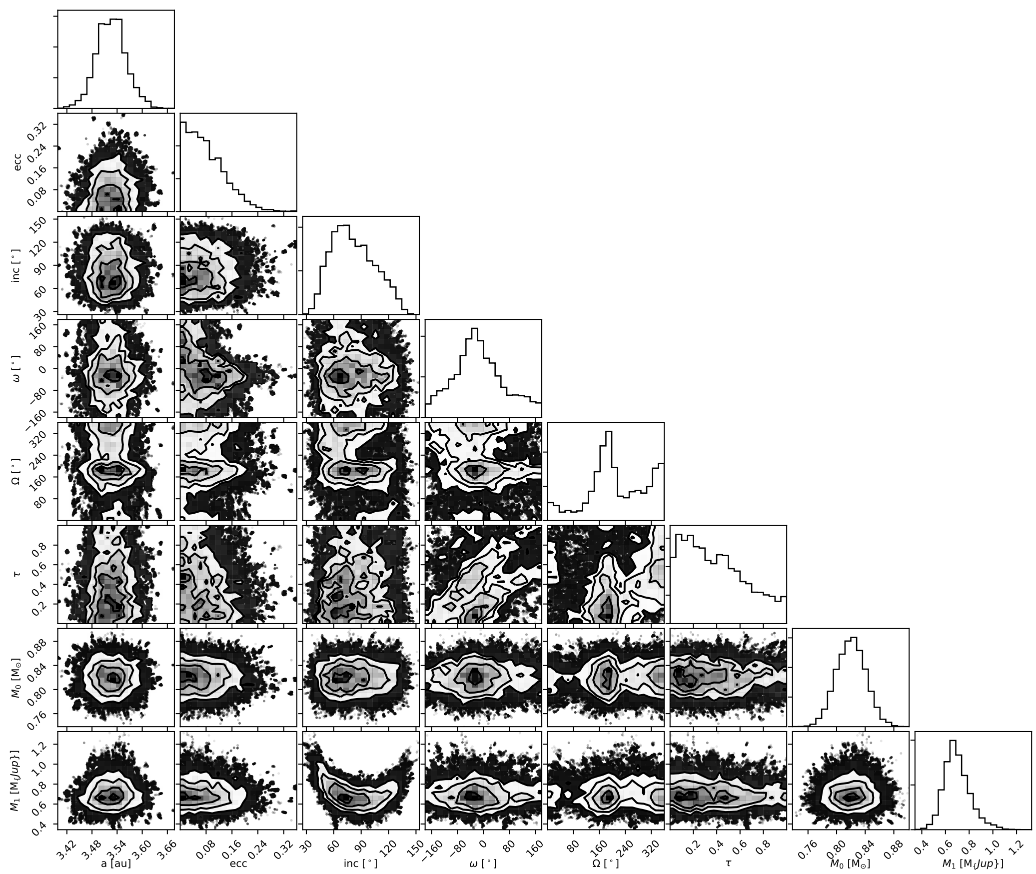

Figure 2.10 Posteriors of the orbital parameters and masses.

BIBLIOGRAPHY

Aumann, H. H. (Oct. 1985). “IRAS observations of matter around nearby stars”. In: *Publications of the ASP* 97, pp. 885–891. DOI: 10.1086/131620.

Backman, D. et al. (Dec. 2008). “EPSILON ERIDANI’S PLANETARY DEBRIS DISK: STRUCTURE AND DYNAMICS BASED ONSPITZERAND CALTECH SUBMILLIMETER OBSERVATORY OBSERVATIONS”. In: *The Astrophysical Journal* 690.2, pp. 1522–1538. DOI: 10.1088/0004-637x/690/2/1522. URL: https://doi.org/10.1088/0004-637x/690/2/1522.

Baines, E. K. and J. T. Armstrong (Dec. 2011). “CONFIRMING FUNDAMENTAL PROPERTIES OF THE EXOPLANET HOST STAR Ïµ ERIDANI USING THE NAVY OPTICAL INTERFEROMETER”. In: *The Astrophysical Journal* 744.2, p. 138. DOI: 10.1088/0004-637x/744/2/138. URL: https://doi.org/10.1088/0004-637x/744/2/138.

Baraffe, I. et al. (May 2003). “Evolutionary models for cool brown dwarfs and extrasolar giant planets. The case of HD 209458”. In: *Astronomy and Astrophysics* 402, pp. 701–712. DOI: 10.1051/0004-6361:20030252. arXiv: astro-ph/0302293 [astro-ph].

Barman, T. S. et al. (May 2015). “Simultaneous Detection of Water, Methane, and Carbon Monoxide in the Atmosphere of Exoplanet HR8799b”. In: *Astrophysical Journal* 804.1, 61, p. 61. DOI: 10.1088/0004-637X/804/1/61. arXiv: 1503.03539 [astro-ph.EP].

Beichman, C. et al. (Jan. 2020). “Searching for Planets Orbiting α Cen A with the James Webb Space Telescope”. In: *Publications of the Astronomical Society of the Pacific* 132.1007. DOI: 10.1088/1538-3873/ab5066. arXiv: 1910.09709 [astro-ph.IM].

Benedict, G. F. et al. (Oct. 2006). “The Extrasolar Planet ϵ Eridani b: Orbit and Mass”. In: *The Astronomical Journal* 132.5, pp. 2206–2218. DOI: 10.1086/508323. URL: https://doi.org/10.1086/508323.

Blunt, S., M. Endl, et al. (Nov. 2019). “Radial Velocity Discovery of an Eccentric Jovian World Orbiting at 18 au”. In: *Astronomical Journal* 158.5, 181, p. 181. DOI: 10.3847/1538-3881/ab3e63. arXiv: 1908.09925 [astro-ph.EP].

Blunt, S., J. J. Wang, et al. (Mar. 2020). “orbitize!: A Comprehensive Orbit-fitting Software Package for the High-contrast Imaging Community”. In: *Astronomical Journal* 159.3, 89, p. 89. DOI: 10.3847/1538-3881/ab6663. arXiv: 1910.01756 [astro-ph.EP].

Boccaletti, A., P.-O. Lagage, P. Baudoz, et al. (2015). In: *Publications of the Astronomical Society of the Pacific* 127, p. 633.

Bond, C. Z. et al. (July 2020). "Adaptive optics with an infrared pyramid wavefront sensor at Keck". In: *Journal of Astronomical Telescopes, Instruments, and Systems* 6, 039003, p. 039003. DOI: 10.1117/1.JATIS.6.3.039003.

Booth, M. et al. (Aug. 2017). "The Northern arc of ϵ Eridani's Debris Ring as seen by ALMA". In: *Monthly Notices of the RAS* 469.3, pp. 3200–3212. DOI: 10.1093/mnras/stx1072. arXiv: 1705.01560 [astro-ph.EP].

Brandl, B. et al. (Mar. 2021). "METIS: The Mid-infrared ELT Imager and Spectrograph". In: *The Messenger* 182, pp. 22–26. DOI: 10.18727/0722-6691/5218. arXiv: 2103.11208 [astro-ph.IM].

Brandt, T. D. (May 2021). "The Hipparcos-Gaia Catalog of Accelerations: Gaia EDR3 Edition". In: *arXiv e-prints*, arXiv:2105.11662, arXiv:2105.11662. arXiv: 2105.11662 [astro-ph.GA].

Carlomagno, B. et al. (July 2020). "METIS high-contrast imaging: design and expected performance". In: *Journal of Astronomical Telescopes, Instruments, and Systems* 6, 035005, p. 035005. DOI: 10.1117/1.JATIS.6.3.035005.

Carrion-González, Ó. et al. (Apr. 2021). "Catalogue of exoplanets accessible in reflected starlight to the Nancy Grace Roman Space Telescope. A population study and prospects for phase-curve measurements". In: *arXiv e-prints*, arXiv:2104.04296, arXiv:2104.04296. arXiv: 2104.04296 [astro-ph.EP].

Cox, A. N. (2000). *Allen's astrophysical quantities*.

Dawson, R. I., R. A. Murray-Clay, and D. C. Fabrycky (Nov. 2011). "ON THE MISALIGNMENT OF THE DIRECTLY IMAGED PLANET β PICTORIS b WITH THE SYSTEM'S WARPED INNER DISK". In: *The Astrophysical Journal* 743.1, p. L17. DOI: 10.1088/2041-8205/743/1/l17. URL: https://doi.org/10.1088/2041-8205/743/1/l17.

De Rosa, R. J., T. M. Esposito, et al. (Nov. 2019). "The Possible Astrometric Signature of a Planetary-mass Companion to the Nearby Young Star TW Piscis Austrini (Fomalhaut B): Constraints from Astrometry, Radial Velocities, and Direct Imaging". In: *The Astronomical Journal* 158.6, p. 225. DOI: 10.3847/1538-3881/ab4c9b. URL: https://doi.org/10.3847%5C%2F1538-3881%5C%2Fab4c9b.

De Rosa, R. J., E. L. Nielsen, et al. (Jan. 2020). "An Updated Visual Orbit of the Directly Imaged Exoplanet 51 Eridani b and Prospects for a Dynamical Mass Measurement with Gaia". In: *Astronomical Journal* 159.1, 1, p. 1. DOI: 10.3847/1538-3881/ab4da4. arXiv: 1910.10169 [astro-ph.EP].

Ducati, J. R. (2002). "VizieR Online Data Catalog: Catalogue of Stellar Photometry in Johnson's 11-color system." In: *VizieR Online Data Catalog* 2237.

Ertel, S. et al. (May 2018). "The HOSTS Survey Exozodiacal Dust Measurements for 30 Stars". In: *Astronomical Journal* 155, 194, p. 194. DOI: 10.3847/1538-3881/aab717. arXiv: 1803.11265 [astro-ph.SR].

Fitzgerald, M. et al. (Sept. 2019). “The Planetary Systems Imager for TMT”. In: *Bulletin of the American Astronomical Society*. Vol. 51, p. 251.

Foreman-Mackey, D. (2016). “corner.py: Scatterplot matrices in Python”. In: *Journal of Open Source Software* 1.2, p. 24. DOI: `10.21105/joss.00024`. URL: `https://doi.org/10.21105/joss.00024`.

Foreman-Mackey, D. et al. (Mar. 2013). “emcee: The MCMC Hammer”. In: *Publications of the Astronomical Society of the Pacific* 125.925, pp. 306–312. ISSN: 1538-3873. DOI: `10.1086/670067`. URL: `http://dx.doi.org/10.1086/670067`.

Fulton, B. J. et al. (Apr. 2018). “RadVel: The Radial Velocity Modeling Toolkit”. In: *Publications of the Astronomical Society of the Pacific* 130.986, p. 044504. DOI: `10.1088/1538-3873/aaaaa8`. arXiv: `1801.01947 [astro-ph.IM]`.

Gaia Collaboration (Aug. 2018). “Gaia Data Release 2. Summary of the contents and survey properties”. In: *Astronomy and Astrophysics* 616, A1, A1. DOI: `10.1051/0004-6361/201833051`. arXiv: `1804.09365 [astro-ph.GA]`.

GRAVITY Collaboration et al. (2020). “Peering into the formation history of toris b with VLTI/GRAVITY long-baseline interferometry”. In: *A&A* 633, A110. DOI: `10.1051/0004-6361/201936898`. URL: `https://doi.org/10.1051/0004-6361/201936898`.

Hatzes, A. P. et al. (Dec. 2000). “Evidence for a Long-Period Planet Orbiting É Eridani”. In: *Astrophysical Journal, Letters* 544.2, pp. L145–L148. DOI: `10.1086/317319`. arXiv: `astro-ph/0009423 [astro-ph]`.

Hinkley, S. et al. (May 2021). “Discovery of an Edge-on Circumstellar Debris Disk around BD+45° 598: A Newly Identified Member of the β Pictoris Moving Group”. In: *Astrophysical Journal* 912.2, 115, p. 115. DOI: `10.3847/1538-4357/abec6e`.

Hoeijmakers, H. J. et al. (Oct. 2018). “Medium-resolution integral-field spectroscopy for high-contrast exoplanet imaging. Molecule maps of the β Pictoris system with SINFONI”. In: *Astronomy and Astrophysics* 617, A144, A144. DOI: `10.1051/0004-6361/201832902`. arXiv: `1802.09721 [astro-ph.EP]`.

Hou, F. et al. (Jan. 2012). “AN AFFINE-INVARIANT SAMPLER FOR EXOPLANET FITTING AND DISCOVERY IN RADIAL VELOCITY DATA”. In: *The Astrophysical Journal* 745.2, p. 198. DOI: `10.1088/0004-637x/745/2/198`. URL: `https://doi.org/10.1088/0004-637x/745/2/198`.

Houlle, M. et al. (Apr. 2021). “Direct imaging and spectroscopy of exoplanets with the ELT/HARMONI high-contrast module”. In: *arXiv e-prints*, arXiv:2104.11251, arXiv:2104.11251. arXiv: `2104.11251 [astro-ph.EP]`.

Howard, A. W. et al. (Oct. 2010). “The California Planet Survey. I. Four New Giant Exoplanets”. In: *Astrophysical Journal* 721.2, pp. 1467–1481. DOI: `10.1088/0004-637X/721/2/1467`. arXiv: `1003.3488 [astro-ph.EP]`.

Huby, E., P. Baudoz, et al. (Dec. 2015). "Post-coronagraphic tip-tilt sensing for vortex phase masks: The QACITS technique". In: *Astronomy and Astrophysics* 584, A74, A74. DOI: 10.1051/0004-6361/201527102. arXiv: 1509.06158 [astro-ph.IM].

Huby, E., M. Bottom, et al. (Apr. 2017). "On-sky performance of the QACITS pointing control technique with the Keck/NIRC2 vortex coronagraph". In: *Astronomy and Astrophysics* 600, A46, A46. DOI: 10.1051/0004-6361/201630232. arXiv: 1701.06397 [astro-ph.IM].

Janson, M. et al. (Feb. 2015). "High-contrast imaging with Spitzer: deep observations of Vega, Fomalhaut, and eps Eridani". In: *Astronomy and Astrophysics* 574, A120, A120. DOI: 10.1051/0004-6361/201424944. arXiv: 1412.4816 [astro-ph.EP].

Kasper, M. et al. (Dec. 2019). "NEAR: First Results from the Search for Low-Mass Planets in α Cen". In: *The Messenger* 178, pp. 5–9. DOI: 10.18727/0722-6691/5163.

Keenan, P. C. and R. C. McNeil (Oct. 1989). "The Perkins catalog of revised MK types for the cooler stars". In: *Astrophysical Journal, Supplement* 71, pp. 245–266. DOI: 10.1086/191373.

Kervella, P. et al. (2019). "Stellar and substellar companions of nearby stars from Gaia DR2 - Binarity from proper motion anomaly". In: *A&A* 623, A72. DOI: 10.1051/0004-6361/201834371. URL: https://doi.org/10.1051/0004-6361/201834371.

Konopacky, Q. M. et al. (Mar. 2013). "Detection of Carbon Monoxide and Water Absorption Lines in an Exoplanet Atmosphere". In: *Science* 339.6126, pp. 1398–1401. DOI: 10.1126/science.1232003. arXiv: 1303.3280 [astro-ph.EP].

Lindegren, L. et al. (Aug. 2018). "Gaia Data Release 2. The astrometric solution". In: *Astronomy and Astrophysics* 616, A2, A2. DOI: 10.1051/0004-6361/201832727. arXiv: 1804.09366 [astro-ph.IM].

Lopez-Morales, M. et al. (Dec. 2016). "Kepler-21b: A Rocky Planet Around a V = 8.25 Magnitude Star". In: *Astronomical Journal* 152.6, 204, p. 204. DOI: 10.3847/0004-6256/152/6/204. arXiv: 1609.07617 [astro-ph.EP].

MacGregor, M. A. et al. (Aug. 2015). "The Epsilon Eridani System Resolved by Millimeter Interferometry". In: *Astrophysical Journal* 809.1, 47, p. 47. DOI: 10.1088/0004-637X/809/1/47. arXiv: 1507.01642 [astro-ph.SR].

Mamajek, E. E. and L. A. Hillenbrand (Nov. 2008). "Improved Age Estimation for Solar-Type Dwarfs Using Activity-Rotation Diagnostics". In: *Astrophysical Journal* 687, 1264-1293, pp. 1264–1293. DOI: 10.1086/591785. arXiv: 0807.1686.

Marley, M. et al. (July 2018). *Sonora 2018: Cloud-free, solar composition, solar C/O substellar atmosphere models and spectra*. Version nc_m+0.0_co1.0_v1.0. Zenodo. DOI: 10.5281/zenodo.1309035. URL: https://doi.org/10.5281/zenodo.1309035.

Marois, C. et al. (Nov. 2008). "Direct Imaging of Multiple Planets Orbiting the Star HR 8799". In: *Science* 322.5906, p. 1348. DOI: 10.1126/science.1166585. arXiv: 0811.2606 [astro-ph].

Mawet, D., L. Hirsch, E. J. Lee, et al. (2019). In: *Astronomical Journal* 157, p. 33.

Nielsen, E. L. et al. (Feb. 2020). "The Gemini Planet Imager Exoplanet Survey: Dynamical Mass of the Exoplanet β Pictoris b from Combined Direct Imaging and Astrometry". In: *Astronomical Journal* 159.2, 71, p. 71. DOI: 10.3847/1538-3881/ab5b92. arXiv: 1911.11273 [astro-ph.EP].

Nowak, M. et al. (Oct. 2020). "Direct confirmation of the radial-velocity planet β Pictoris c". In: *Astronomy and Astrophysics* 642, L2, p. L2. DOI: 10.1051/0004-6361/202039039. arXiv: 2010.04442 [astro-ph.EP].

Pathak, P. et al. (Apr. 2021). "High contrast imaging at 10 microns, a search for exoplanets around: Eps Indi A, Eps Eri, Tau Ceti, Sirius A and Sirius B". In: *arXiv e-prints*, arXiv:2104.13032, arXiv:2104.13032. arXiv: 2104.13032 [astro-ph.EP].

Perrin, M. D., L. Pueyo, K. Van Gorkom, et al. (2018). In: *Proceedings* 1069. URL: https://doi.org/10.1117/12.2313552.

Petit dit de la Roche, D. J. M., H. J. Hoeijmakers, and I. A. G. Snellen (Aug. 2018). "Molecule mapping of HR8799b using OSIRIS on Keck. Strong detection of water and carbon monoxide, but no methane". In: *Astronomy and Astrophysics* 616, A146, A146. DOI: 10.1051/0004-6361/201833384. arXiv: 1808.10790 [astro-ph.EP].

Quillen, A. C. and P. Faber (Dec. 2006). "Chaotic zone boundary for low free eccentricity particles near an eccentric planet". In: *Monthly Notices of the RAS* 373.3, pp. 1245–1250. DOI: 10.1111/j.1365-2966.2006.11122.x. arXiv: astro-ph/0608059 [astro-ph].

Radovan, M. V. et al. (July 2014). "The automated planet finder at Lick Observatory". In: *Ground-based and Airborne Telescopes V*. Ed. by L. M. Stepp, R. Gilmozzi, and H. J. Hall. Vol. 9145. Society of Photo-Optical Instrumentation Engineers (SPIE) Conference Series, 91452B. DOI: 10.1117/12.2057310.

Rajpaul, V. et al. (July 2015). "A Gaussian process framework for modelling stellar activity signals in radial velocity data". In: *Monthly Notices of the Royal Astronomical Society* 452.3, pp. 2269–2291. ISSN: 0035-8711. DOI: 10.1093/mnras/stv1428. eprint: https://academic.oup.com/mnras/article-pdf/452/3/2269/4912584/stv1428.pdf. URL: https://doi.org/10.1093/mnras/stv1428.

Ruffio, J.-B., B. Macintosh, J. J. Wang, et al. (June 2017). “Improving and Assessing Planet Sensitivity of the GPI Exoplanet Survey with a Forward Model Matched Filter”. In: *ApJ* 842, 14, p. 14. DOI: 10.3847/1538-4357/aa72dd. arXiv: 1705.05477 [astro-ph.EP].

Ruffio, J.-B., B. Macintosh, Q. M. Konopacky, et al. (Nov. 2019). “Radial Velocity Measurements of HR 8799 b and c with Medium Resolution Spectroscopy”. In: *Astronomical Journal* 158.5, 200, p. 200. DOI: 10.3847/1538-3881/ab4594. arXiv: 1909.07571 [astro-ph.EP].

Ruffio, J.-B., D. Mawet, et al. (Nov. 2018). “A Bayesian Framework for Exoplanet Direct Detection and Non-detection”. In: *Astronomical Journal* 156.5, 196, p. 196. DOI: 10.3847/1538-3881/aade95. arXiv: 1809.08261 [astro-ph.EP].

Serabyn, E. et al. (2017). “The W. M. Keck Observatory Infrared Vortex Coronagraph and a First Image of HIP 79124 B”. In: *Astron. J.* 153, p. 43. DOI: 10.3847/1538-3881/153/1/43.

Soummer, R., L. Pueyo, and J. Larkin (Aug. 2012). “Detection and Characterization of Exoplanets and Disks Using Projections on Karhunen-Loève Eigenimages”. In: *Astrophysical Journal, Letters* 755.2, L28, p. L28. DOI: 10.1088/2041-8205/755/2/L28. arXiv: 1207.4197 [astro-ph.IM].

Su, K. Y. L. et al. (May 2017). “The Inner 25 au Debris Distribution in the ϵ Eri System”. In: *Astronomical Journal* 153, 226, p. 226. DOI: 10.3847/1538-3881/aa696b. arXiv: 1703.10330 [astro-ph.SR].

van Leeuwen, F. (2007). *Hipparcos, the New Reduction of the Raw Data*. Vol. 350. DOI: 10.1007/978-1-4020-6342-8.

Vogt, S. S., S. L. Allen, et al. (June 1994). “HIRES: the high-resolution echelle spectrometer on the Keck 10-m Telescope”. In: *Instrumentation in Astronomy VIII*. Ed. by D. L. Crawford and E. R. Craine. Vol. 2198. Society of Photo-Optical Instrumentation Engineers (SPIE) Conference Series, p. 362. DOI: 10.1117/12.176725.

Vogt, S. S., M. Radovan, et al. (Apr. 2014). “APF The Lick Observatory Automated Planet Finder”. In: *Publications of the ASP* 126.938, p. 359. DOI: 10.1086/676120. arXiv: 1402.6684 [astro-ph.IM].

Wang, J. J., J.-B. Ruffio, et al. (June 2015). *pyKLIP: PSF Subtraction for Exoplanets and Disks*. Astrophysics Source Code Library. ascl: 1506.001.

Wang, J. J., A. Vigan, et al. (Feb. 2021). “Constraining the Nature of the PDS 70 Protoplanets with VLTI/GRAVITY $*$”. In: *The Astronomical Journal* 161.3, p. 148. DOI: 10.3847/1538-3881/abdb2d. URL: https://doi.org/10.3847/1538-3881/abdb2d.

Wilcomb, K. K. et al. (Nov. 2020). “Moderate-resolution K-band Spectroscopy of Substellar Companion κ Andromedae b”. In: *Astronomical Journal* 160.5, 207, p. 207. DOI: 10.3847/1538-3881/abb9b1. arXiv: 2009.08959 [astro-ph.EP].

Wisdom, J. (Aug. 1980). “The resonance overlap criterion and the onset of stochastic behavior in the restricted three-body problem”. In: *Astronomical Journal* 85, pp. 1122–1133. DOI: 10.1086/112778.

Xuan, W. J. et al. (Oct. 2018). “Characterizing the Performance of the NIRC2 Vortex Coronagraph at W. M. Keck Observatory”. In: *Astronomical Journal* 156.4, 156, p. 156. DOI: 10.3847/1538-3881/aadae6. arXiv: 1808.05297 [astro-ph.EP].

Chapter 3

MID-INFRARED OBSERVATIONS OF α CENTAURI WITH THE JWST

Beichman, C. et al. (Jan. 2020). "Searching for Planets Orbiting α Cen A with the James Webb Space Telescope". In: *Publications of the Astronomical Society of the Pacific* 132.1007. DOI: 10.1088/1538-3873/ab5066. arXiv: 1910.09709 [astro-ph.IM].

ABSTRACT

α Centauri A is the closest solar-type star to the Sun and offers an excellent opportunity to detect the thermal emission of a mature planet heated by its host star. The MIRI coronagraph on the James Webb Space Telescope (JWST) can search the 1-3 AU ($1''$-$2''$) region around α Centauri A which is predicted to be stable within the α Centauri AB system. We demonstrate that with reasonable performance of the telescope and instrument, a 20 hr program combining on-target and reference star observations at 15.5 μm could detect thermal emission from planets as small as ~5 $R_\oplus$. Multiple visits every 3-6 months would increase the geometrical completeness, provide astrometric confirmation of detected sources, and push the radius limit down to $\sim$ 3 $R_\oplus$. An exozodiacal cloud only a few times brighter than our own should also be detectable, although a sufficiently bright cloud might obscure any planet present in the system. While current precision radial velocity (PRV) observations set a limit of 50-100 $M_\oplus$ at 1-3 AU for planets orbiting α Centauri A, there is a broad range of exoplanet radii up to 10 $R_\oplus$ consistent with these mass limits. A carefully planned observing sequence along with state-of-the-art post-processing analysis could reject the light from α Centauri A at the level of $\sim 10^{-5}$ at $1''$-$2''$ and minimize the influence of α Centauri B located 7-$8''$ away in the 2022-2023 timeframe. These space-based observations would complement on-going imaging experiments at shorter wavelengths as well as PRV and astrometric experiments to detect planets dynamically. Planetary demographics suggest that the likelihood of directly imaging a planet whose mass and orbit are consistent with present PRV limits is small, ~5%, and possibly lower if the presence of a binary companion further reduces occurrence rates. However, at a distance of just 1.34 pc, α Centauri A is our closest sibling star and certainly merits close scrutiny.

3.1 Introduction

The detection, characterization, and search for biomarkers in the atmospheres of Earth analogs in the Habitable Zones (HZ) of their host stars are exciting goals of both ground- and space-based astronomy as described and prioritized in the National Academy's Decadal Reviews (Council, 2010), NASA's Strategic Plan[1], the Exoplanet Science Strategy Report[2] (Sciences, n.d.), and the recently announced Breakthrough Initiative[3]. The high degree of stellar rejection (10^{-10} in the visible and 10^{-7} in the thermal infrared) demanded to detect an Earth analog at small angular separations, typically 10s of milliarcsec for most nearby solar type stars, represents a daunting challenge in both reflected visible light and emitted thermal radiation. Studies of observatories capable of achieving these levels have led to designs of instruments for 30-40 m telescopes on the ground (Kenworthy et al., 2016; Mawet, Wizinowich, et al., 2016; Skemer et al., 2018; Mazin et al., 2019), 4 to 15 m telescopes in space (Habex, Mennesson et al. (2016); LUVOIR, Pueyo et al. (2017)), as well as earlier initiatives such as the TPF-C coronagraph and TPF-I/Darwin mid-IR interferometer (Leger et al. (1996), Angel et al. (1997), and Beichman, Fridlund, et al. (2007)). However, by virtue of its proximity to the Sun, α Centauri A offers an opportunity to use more modest and more near-term facilities to image directly a mature planet ranging in size from Jovian-sized to Earth-sized. Proposals exist to use ground-based 8 m telescopes (Kasper et al., n.d.) or a small visible telescope in space (Belikov et al., 2015).

At a distance of 1.34 pc, α Centauri A is 2.7 times closer than the next most favorable G star, τ Ceti. α Centauri A's luminosity of 1.5 $L_\odot$ (Thevenin et al., 2002; Kervella, Bigot, et al., 2017) puts the center of its HZ (defined here as the separation of an Earth-Equivalent level of insolation, see also Kopparapu et al. (2017)) at a physical separation of 1.2 AU which corresponds to an angular separation of $0.9''$. α Centauri A is the one stand-out exception, *primum ex parte*, in the list of solar-type host stars suitable for the eventual detection and initial characterization of a HZ Earth (Figure 3.1; Turnbull (2015)).

The 10-15 μm emission from *an isolated object* with the same brightness as a warm Earth-sized planet (20-40 μJy) would be readily detectable by MIRI. There are, of course, major challenges to be overcome: the glare of α Centauri A, the presence of α Centauri B which might remove planets from the α Centauri A system and which

[1] https://www.nasa.gov/sites/default/files/atoms/files/nasa_2018_strategic_plan.pdf
[2] https://www.nap.edu/catalog/25187/exoplanet-science-strategy
[3] https://breakthroughinitiatives.org/arewealone

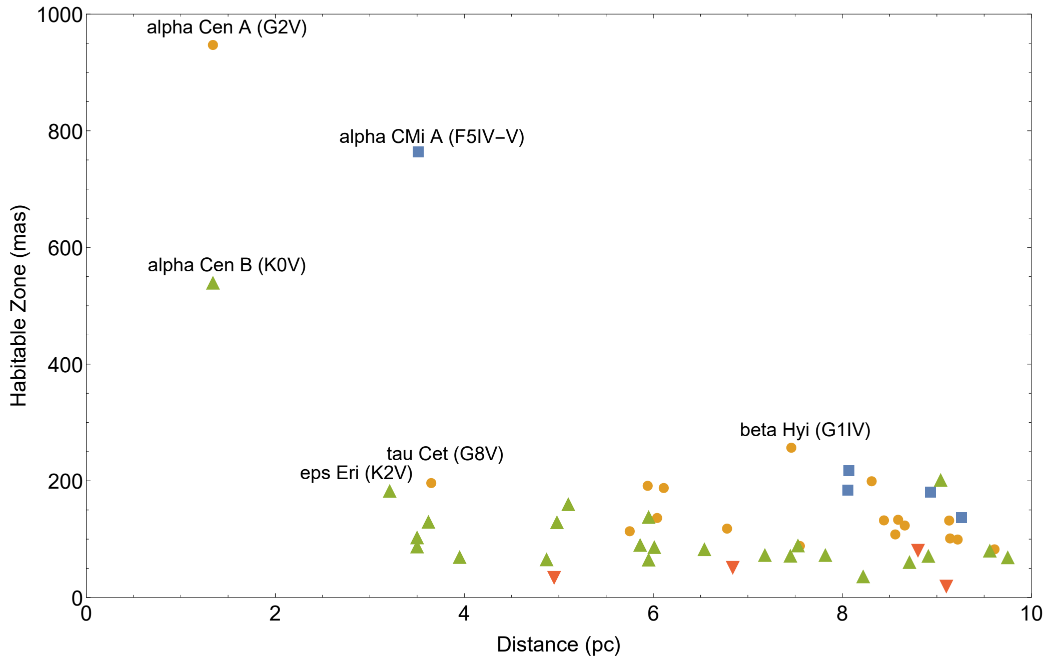

Figure 3.1 α Centauri A stands out as the most favorable star to examine due to the large angular extent of its Habitable Zone, as indicated here as the angular separation (milliarcseconds, or mas) of a planet receiving an Earth equivalent insolation from its host star (Turnbull, 2015). A few of the closest and most prominent host stars are called out individually (F stars as blue squares, G stars as orange circles, K stars as green triangles, and M stars as inverted red triangles).

introduces a second source of noise, the stability of JWST and the performance of its coronagraphs. Yet these challenges can be surmounted certainly for planets larger than the Earth. We note that a search for planets orbiting α Centauri B is less favorable due to the tight RV constraint on the presence of planets around α Centauri B (L. L. Zhao et al., 2017), its lower luminosity and correspondingly smaller HZ ($\sim 0.5''$), and to the greater deleterious effects of α Centauri A.

Current precision radial velocity (PRV) observations (L. L. Zhao et al., 2017) constrain the mass of any planet near α Centauri A to be $M\,sin(i) < 53$ $M_\oplus$ in the Habitable Zone (1.2 AU). Examination of their Figure 6 which includes their estimates for the effects of non-Gaussian noise sources ("red noise") suggests a limit between 50 and 100 $M_\oplus (2\,\sigma)$. This limit applies to the near edge-on, 79^o, orientation of the α Centauri A-B system where dynamical studies indicate the presence of a stable zone $\lesssim 3$ AU (or $2.1''$) around α Centauri A despite the presence of α Centauri B (Figure 3.2; Quarles and Lissauer (2016), Holman et al. (1999), Quarles, Lissauer, and Kaib (2018), and Quarles and Lissauer (2018)). There is a wide range of planet types possible within these mass limits, from Earth-sized planets to sub-Neptunes. In what follows we adopt an upper limit to any radial velocity signature of 5 m s^{-1} which corresponds roughly to a 2σ limit. We recognize that future PRV observations will doubtless improve on this constraint. Finally, we note that a planet's thermal emission depends on its radius, not its mass, and the range of permissible *radii* is broad due to wide range of observed planet densities.

In this paper we investigate how a modest observing program with the MIRI coronagraph could detect HZ planets larger than ~5 $R_\oplus$ orbiting α Centauri A as well as a zodiacal dust cloud only a few times brighter than our own cloud. Depending on the performance of JWST and the MIRI coronagraph, a more ambitious program could push to even lower planet sizes, ~3 $R_\oplus$.

3.2 The prospects for planets in the α Cen System

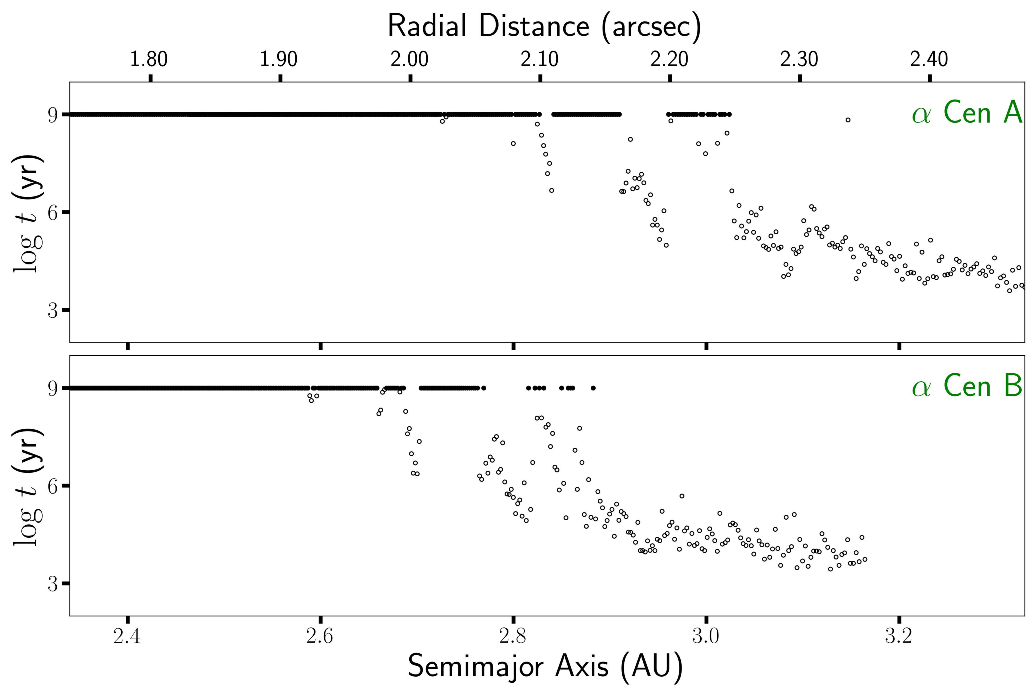

Figure 3.2 Stable regions are found within ≲3 AU for planetary systems orbiting α Centauri A and within ~2.65 AU of α Centauri B (based on work from Quarles, Lissauer, and Kaib, 2018).

Statistical studies based on radial velocity (RV) and transit surveys help to assess whether α Centauri A might host one or more planets. Unfortunately, transit surveys are incomplete in the 1-3 AU range for all radii (Thompson et al., 2018) while RV data are incomplete for masses below 100 $M_\oplus$ (Saturn) at these separations (Cumming et al., 2008; Santerne et al., 2016). Combining various estimates suggests a cumulative planet incidence for FGK stars of 3-8% for M> 100 $M_\oplus$ and P<5 yr with a five to tenfold increase for masses down to 10 $M_\oplus$. Thus, based on these statistical considerations there is a good chance (25–50%) that α Centauri A might host one or more planets in the 10-100 $M_\oplus$ range.

Fernandes et al. (2019) parameterize the joint planet occurrence rate as a function of period and mass:

$$\frac{d^2N}{dlogPdlogM} = C_0 f(P)(\frac{M}{10M_\oplus})^\gamma \tag{3.1}$$

$$f(p) = \left(\frac{P}{P_{break}}\right)^{p1} \text{ for } P < P_{break} \text{ ; or } \left(\frac{P}{P_{break}}\right)^{p2} \text{ for } P \geq P_{break} \tag{3.2}$$

While there is considerable uncertainty in the fitted parameters, Fernandes et al. (2019) find that the following values provide a reasonable fit to the available data: $P_{break} = 1581d$, $p1 = -p2 = 0.65$, $\gamma = -0.45$ and C_0=0.84. If we integrate Eqn 3.1 over periods from 10 to 1800 days (corresponding to an outer limit of 3 AU) with a minimum mass of 10 $R_\oplus$ and an upper mass consistent with an RV limit of 5 m s^{-1}, then α Centauri A has a ∼15% probability of hosting a planet with those properties. While the extrapolation to the lowest masses (∼ 10 $M_\oplus$) is quite uncertain, the population estimates in the mass/radius range which we will show are accessible to JWST (3 ∼ 5$R_\oplus$ and P<1800 d, §3.8) are reasonably well-grounded in transit and RV data (Cumming et al., 2008).

One reason for pessimism about α Centauri A's suitability as a stellar parent comes from the fact that α Centauri A & B form a relatively tight binary system. Kraus et al. (2016) have analyzed the statistics from Kepler transits and shown that detected planets are only about one-third as abundant in comparable-mass binary systems with projected separations of < 50 AU as they are around single stars. However, Quintana et al. (2002) have shown that the late stages of planet growth for a prograde disk of planetary embryos and planetesimals orbiting about either α Centauri A or B near the plane of the binary orbit would grow into a configuration of terrestrial planets comparable to that formed by an analogous disk orbiting the Sun perturbed by Jupiter and Saturn. Xie et al. (2010) and Zhang et al. (2018) have found favorable conditions for planetesimals to survive and grow to planetary embryos in disks with inclinations of up to 10° relative to the binary orbit. Simulations of Quarles and Lissauer (2016) and references therein have shown that a planet can remain in a low-inclination, low-eccentricity prograde orbit for longer than the age of the system throughout the habitable zones of both α Centauri A and B.

The population studies mentioned above are given in terms of planet masses, whereas JWST will detect thermal emission which depends on planet radius. For masses between 10-100$M_{\oplus}$, radii can range from 2 to 10 $R_{\oplus}$ (Howard, 2013) with dramatic effects on the photometric signal. We will address the sample consistent with known occurrence rate, the RV limits and detectability by JWST in a subsequent section (§3.8).

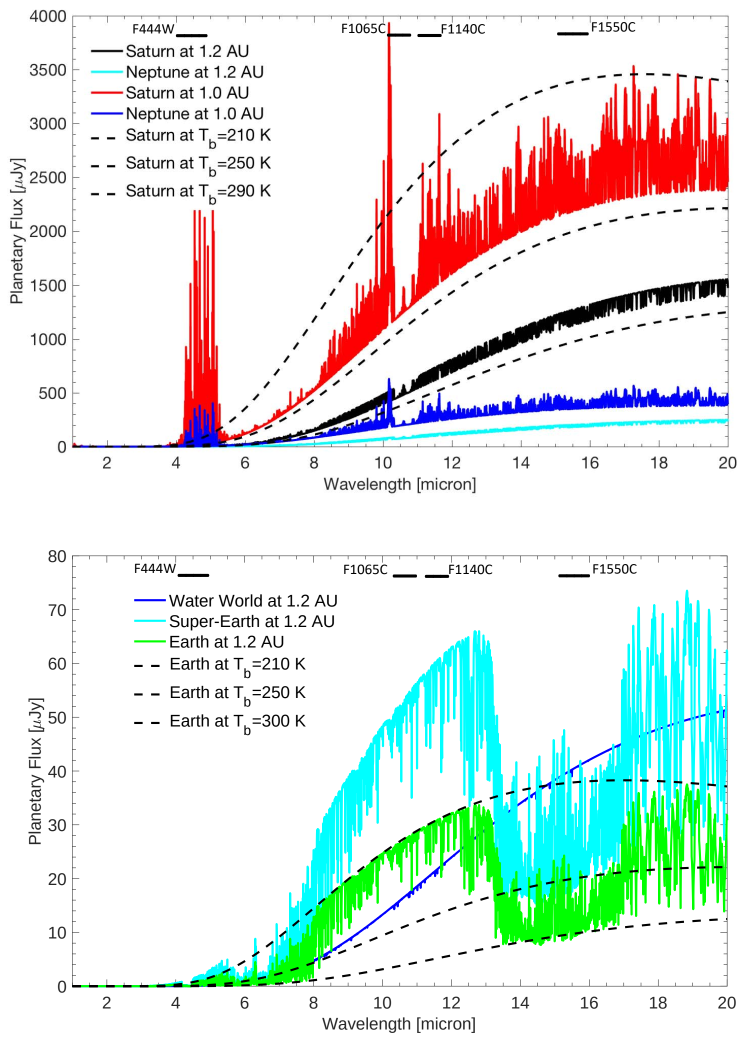

Figure 3.3 The brightness of a variety of model planets with radii between 4 to 10 $R_{\oplus}$ (a, top) and 1-2 $R_{\oplus}$ (b,bottom) over a range of orbital locations and temperatures as described in Table 3.1. The locations of the 3 MIRI coronagraphic filters and one NIRCam filter are indicated.

Table 3.1. Predicted Brightness of Possible Planets Orbiting α Centauri A

Planet Type	Radius ($R_\oplus$)	Orbit (AU)	T_{eff} (K)	F1065C (μJy)	F1550C (μJy)	F_{pl}/F_* F1550C[1]
Saturn	10	1.2	221	500	1210	1.9×10^{-5}
Warm Saturn	10	1.0	275	1370	2380	3.7×10^{-5}
Neptune	4	1.2	221	80	190	0.3×10^{-5}
Warm Neptune	4	1.0	262	220	380	0.6×10^{-5}
Mini-Neptune	2	1.2	221	20	50	0.08×10^{-5}
Warm Mini-Neptune	2	1.0	262	55	95	0.15×10^{-5}
Water World	2	1.2	215	16	40	0.06×10^{-5}
Super-Earth	1.4	1.2	250	80	40	0.06×10^{-5}
Earth	1.0	1.2	250	40	20	0.03×10^{-5}
ExoZodi Cloud[2]	–	0.75 to 1.77	250-300	2500	3000	3.6×10^{-5}

Note. — [1]Contrast F(planet)/F(star). [2]Estimated brightness of an analog of the Solar System's zodiacal cloud as discussed in Sec. 3.4.

3.3 Brightness of Habitable Zone Planets

There is a broad base of literature available to establish the expected level of brightness of exoplanets of various sizes and locations (A. Burrows et al., 2004; Seager et al., 2010; A. S. Burrows, 2014). We have used a self-consistent series of models based on the atmospheric chemistry and radiative transfer formalism developed in Hu, Seager, and Bains (2013) and Hu and Seager (2014). Table 3.1 and Figure 3.3 summarize models for 2, 4 and 10 $R_\oplus$ planets (mini-Neptunes, Neptunes, and Saturns) at 1.2 AU with a H_2-dominated atmosphere with 10× solar metallicity. The models include condensation of water, ammonia, and methane when they reach saturation in the atmosphere and are thus suitable to simulate such low-temperature atmospheres. As water condenses in the atmosphere water clouds form at a pressure of ~0.1 bar. Due to the water clouds, the mid-infrared emission spectrum is close to a 220 K black body as determined by the cloud-top temperature.

For planets at 1.0 AU which receive about 50% more irradiation than Earth our model predicts that water does not condense in its atmosphere and would likely be free of condensation clouds. The spectrum is dominated by strong H_2O, CH_4, and NH_3 absorption, as well as H_2-H_2 and H_2-He collision-induced absorption. There are infrared windows into the hot, convective part of the atmosphere, at 4-5 μm, and to a lesser extent at 10 μm.

While it is unlikely that the MIRI observations discussed here will achieve the

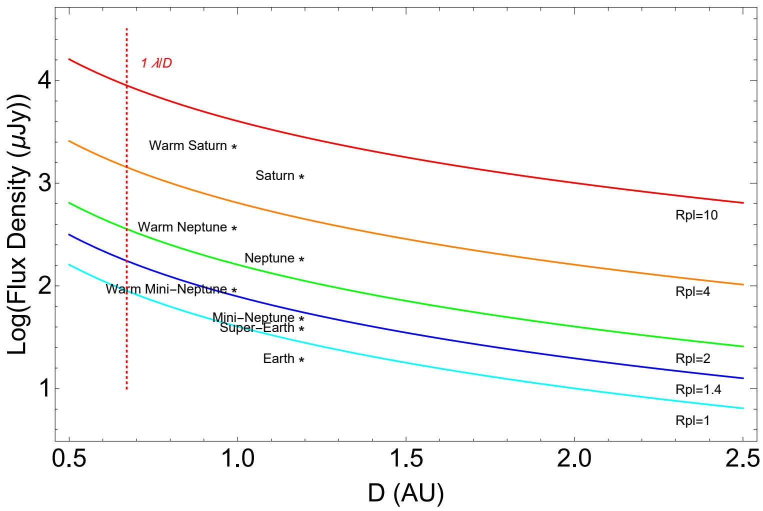

Figure 3.4 The lines show the flux density at F1550C for planets of different radii (denoted in $R_{\oplus}$ on the right) as a function of radial separation from α Centauri A based on a simple $T_{eff} \propto \mathrm{D}^{0.5}$ relationship for an albedo of 0.3. Also shown are the predicted F1550C flux densities for the detailed models specified in Table 3.1. The dotted red vertical line shows the projected location of MIRI's $1\lambda/D = 0.67''$ Inner Working Angle at 15.5 μm.

sensitivity needed to detect Earths or Super-Earths, (1-2 $R_{\oplus}$), very long observations combined with new techniques of speckle suppression may allow the detection of rocky planets. Thus, for completeness, we consider some scenarios for small planets (Figure 3.3b), for example a 2 $R_{\oplus}$ "water world" for which water is the dominant gas in the atmosphere. A thick water cloud forms with the cloud base at 0.1 bar, and the top at ~0.001 bar. Due to this thick cloud that extends to low pressures, the resulting spectrum is a black body at 215 K. We also considered an Earth-like planet, with either 1 or 1.4 $R_{\oplus}$ (an Earth or Super-Earth). We simulated the atmosphere using the standard, mid-latitude temperature-pressure profile and the full photochemistry model developed in (Hu, Ehlmann, et al., 2012). It is well known that thermal emission of Earth can be presented by a combination of cloud-free, low-altitude cloud, and high-altitude cloud atmospheres, e.g. (Marais et al., 2002; Turnbull et al., 2006). But for simplicity, we assumed a cloud-free atmosphere noting that other cloud types have smaller thermal emission features. The emission spectrum is dominated by absorption of CO_2, H_2O, and O_3.

Finally, for subsequent analyses (§3.6,3.8), we also used a simple blackbody relationship (Traub et al., 2010):

$$T_{eff} = T_* \left(\frac{1-A}{4f}\right)^{1/4} \left(\frac{R_*}{d}\right)^{1/2} = 275\, L_*^{1/4}\, (1-A)^{1/4}\, d^{-1/2}\, K \tag{3.3}$$

where L_*, T_*, R_* are the stellar luminosity, effective temperature and radius, A the planet albedo, d the planet's distance from the star in AU (Figure 3.4), and $f = 1$ is appropriate for full heat distribution. In the figure, the adopted albedo is 0.3, but in subsequent analyses, the albedo was drawn randomly between 0.15 and 0.65 appropriate to gaseous planets in our solar system, e.g. Cahoy et al. (2010).

3.4 Exozodiacal Dust Orbiting α Centauri A

The zodiacal cloud and Kuiper belt in our solar system have analogs in many other planetary systems. The recently published HOSTS survey used the nulling interferometer of the Large Binocular Telescope (LBTI) to set preliminary upper limits of 26 times the solar system zodiacal level for a sample of solar type stars (Ertel et al., 2018). Wiegert et al. (2014) find suggestive, but hardly definitive evidence for a ring of cold dust (53 K) located at ~70-105 AU around the α Centauri AB system at a level comparable to the Edgeworth-Kuiper belt in our own solar system (Teplitz et al., 1999). The HOSTS survey suggests that the level of warm zodiacal emission is higher for stars associated with cold dust emission detected at longer wavelengths by Spitzer or Herschel.

The proximity of α Centauri means that JWST/MIRI can spatially resolve a warm zodiacal dust cloud without an interferometer and thereby improve the detectability of the dust relative to purely photometric measurements (Beichman, Tanner, et al., 2006). A model of a near-edge-on "1 zodi" cloud seen around α Centauri A at 15.5 μm can be generated using ZodiPic (Kuchner, 2012). Figure 3.5 shows an $5'' \times 5''$ image of a cloud whose total dust flux density is 8.9 mJy, i.e about 10^{-4} of the stellar flux at the same wavelength. Adopting an "optimistic" HZ definition of 0.75 to 1.77 AU (Kopparapu et al., 2017) for a sun-like star and correcting for stellar luminosity, the excess flux density in the HZ is approximately 3 mJy, i.e. a total fractional excess of 3.6 x 10^{-5} between 0.92 AU and 2.18 AU. This emission would be spread over roughly 10 MIRI beams, or approximately 0.3 mJy per beam which is comparable in brightness to a "Warm Neptune" (Table 3.1). The detection of emission at this level (§3.7) is interesting for two reasons. First, observing a spatially resolved excess in the Habitable Zone would be an important contribution to our knowledge of the evolution of exoplanet systems. Second, exozodiacal emission at the few Zodi level

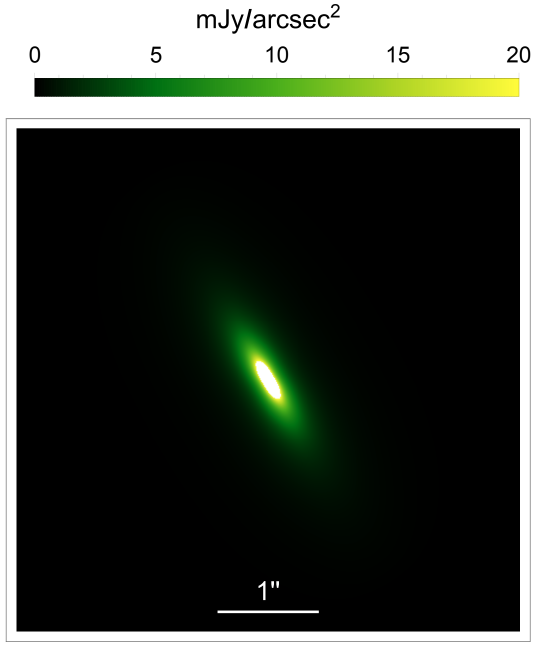

Figure 3.5 A model of a "1 zodi" cloud seen around α Centauri A at 15.5 μm, generated using ZodiPic (Kuchner, 2012) for a disk seen nearly edge-on (79^o). The image is $5''$ on a side. The total dust flux is 8.9 mJy, i.e about 10^{-4} of the stellar flux at the same wavelength.

may set a limit to the size of a HZ planet which might be detectable with MIRI's angular resolution (Beichman, Bryden, Stapelfeldt, et al., 2006).

Exactly how the exozodiacal dust is distributed is critical to its detectability and its effect on the detectability of any planets. Many exozodiacal clouds, e.g. Fomalhaut, HD69830, ϵ Eridani, have gaps rings or clumps often attributed to the presence of planets (Su et al., 2013; Beichman, Bryden, Gautier, et al., 2005; Mawet, Hirsch, et al., 2019) . A faint but homogeneous disk might simply be resolved away during the reference star subtraction while a clumpy cloud observed at the limit of JWST's angular resolution might be confused with one or more planets. Additional simulations and finally JWST observations will be required to assess these challenges.

3.5 Overcoming the Observational Challenges

The first challenge to finding one or more planets orbiting α Centauri A is to select the preferred wavelength and instrument. Compared to NIRCam's coronagraph operating at 4-5 μm with an Inner Working Angle (IWA) of 4-6 λ/D, MIRI's Four Quadrant Phase Mask (4QPM) operating at $\sim 1\,\lambda/D$ offers: comparable IWA, improved immunity to Wavefront Error (WFE) drifts and centering errors (Knight et al., 2012), more favorable planet-star contrast ratio at the expected planet temperatures at the IWA (200-300 K; Figure 3.3), and lower brightness of background stars. MIRI offers three 4QPM masks at 10.65, 11.4 and 15.5 μm. Although the shortest wavelength filter would have a smaller IWA, we have focused our discussion on F1550C for a number of reasons: longer integration time before detector saturation[4] (10 sec vs 1 sec for F1550C vs F1065C), lower impact of wavefront drifts, good sensitivity across a broad range of planet temperatures (Figure 3.3), lower confusion due to background stars, and complementarity to shorter-wavelength ground-based efforts (§3.8).

Rejecting Starlight from α Cen A

MIRI's 4QPM reduces the central brightness of a star by a factor of $\sim 10^3$, operates as close to the star as $1\ \lambda/D \sim 0.48''$ at $\lambda = 15.5\,\mu$m (where D is the telescope diameter), and achieves 10^{-4}-10^{-5} rejection at a separation of $1''$-$2''$ using standard reference star subtraction (Boccaletti et al. (2015), Figure 3.6). As we discuss in §3.6 and show in the two lower lines in Figure 3.6, it should be possible to improve on this performance with a specialized observing mode and advanced post-processing.

Rejecting Starlight from α Cen B

Complicating the issue is the presence of α Centauri B which will be located roughly 7-8$''$ away from α Centauri B during the first few years after JWST's launch. (Figure 3.7). We considered two methods for dealing with α Centauri B: 1) placing α Centauri B on the transmission gap in the 4QPM (Boccaletti et al., 2015; Danielski et al., 2018) to reduce the its central intensity at the cost of a limited selection of observing dates with the correct on-sky orientation; or 2) optimize the target-reference star observations so as to minimize wave front error drifts while accepting the deleterious effects of the full brightness of α Centauri B falling on the detector.

A positive aspect of the 4QPM coronagraphic masks is the existence of a gap, ±3 pixels (at the half power points) or ~0.3$''$, located at the phase boundaries of the four quadrants. At these locations the transmission is reduced by a factor of >8 (Danielski et al., 2018). There are semi-annual observing windows of a few days duration during which α Centauri A can be centered behind the coronagraphic mask while at the same time placing α Centauri B in one of the gaps between adjaCent quadrants, thereby reducing detector artifacts. However, as discussed in

[4] As calculated using the JWST exposure time tool. https://jwst.etc.stsci.edu/

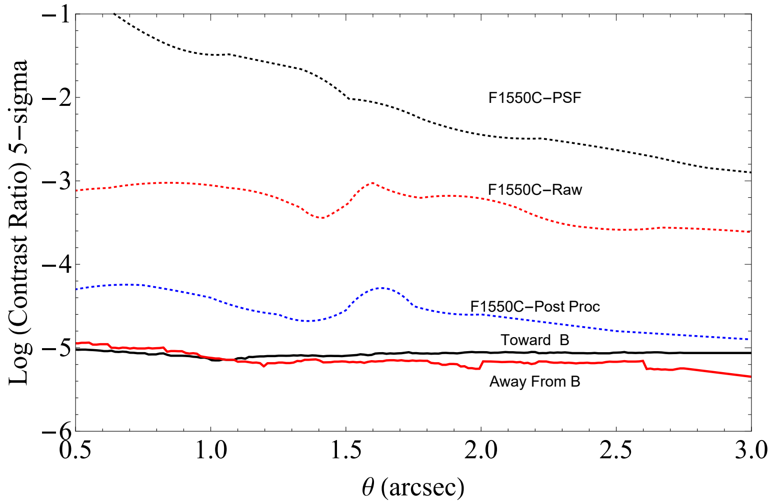

Figure 3.6 Contrast curves for the F1550C curve: PSF (dotted, black), Raw coronagraphic contrast (dotted, red), post PSF subtraction (dotted, blue) — all from (Boccaletti et al., 2015). The two solid curves show the contrast following our PCA post-processing with the upper black curve showing the influence in the direction of α Centauri B, located 7″ away, and the lower red curve the contrast in directions away from α Centauri B. The effect of α Centauri B is negligible with a few arcseconds of α Centauri A.

§3.6 this approach requires a non-optimized slew to a reference star which may induce changes in telescope's thermal environment resulting in non-zero wavefront errors and a higher level of residual speckles.

The alternative approach of placing α Centauri B in an unattenuated portion of the detector offers the advantage of a broader observing window at the cost of a greater risk of deleterious effects of the full intensity of α CentauriB.

Confusion by Background Stars and Galaxies

The high proper motion of α Centauri ($\sim 3''$ yr^{-1} due West) means that images from earlier epochs (Spitzer, HST, ground-based, etc) can be used to study the field where α Centauri will be during the JWST era and to identify background objects. Figure 3.8 shows a 8 μm (Ch 4) Spitzer/IRAC image of α Centauri AB taken in 2005 (Fazio et al., 2004) with the location of MIRI's 23″ coronagraphic field surrounding α Centauri's projected position around ~2022. The brightest stars in the vicinity are $S2$ (K_s = 11.1 mag) which will pass within 1.6″ of α Centauri A around 2023.4 and a brighter source $S5$ (K_s = 7.8 mag) which will pass within

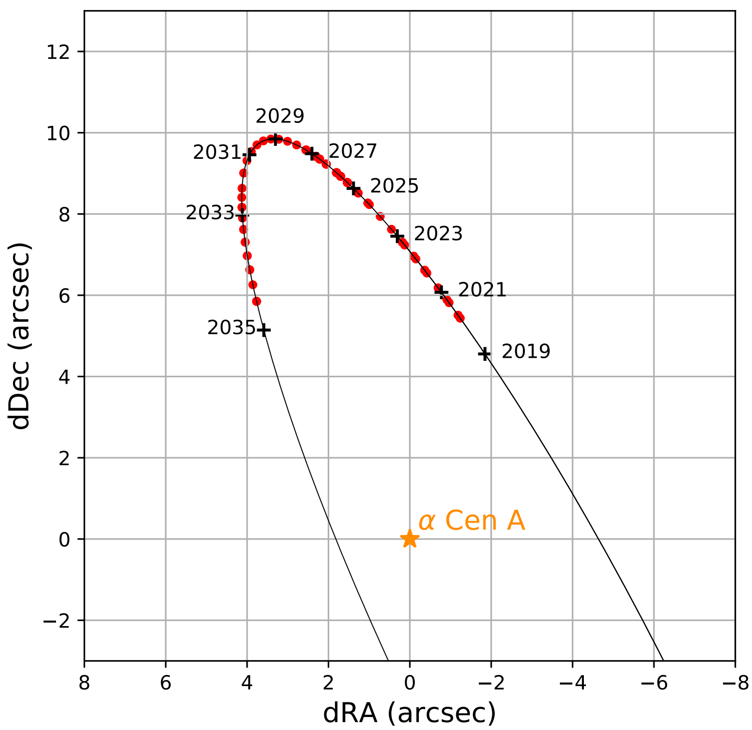

Figure 3.7 The orbit of α Centauri B around α CentauriA (Kervella, Mignard, et al., 2016) is indicated with some possible observing dates (>2021) highlighted during the early years of JWST's operation.

0.015″in 2028.4 (Kervella, Mignard, et al., 2016)). *The impending approach of $S2$ argues for observing α Centauri A soon after launch to avoid the impact of $S2$ on the observations*.

Even if there are no obvious bright stars in the coronagraphic field it is important to estimate the level of contamination of background stars and galaxies at the expected levels of emission for our hoped-for planets, e.g. F_ν(F1550C)=20 μJy for an Earth analog and 2.4 mJy for a warm Saturn (Table 1). To estimate the stellar background we take advantage of Spitzer's GLIMPSE survey (Churchwell et al., 2009) which covered a region near α Centauri. We extracted from the Deep GLIMPSE catalog[5] sources in a $r = 10'$ region located at galactic coordinates (l,b)=(-315.3^o,-0.56^o), just 0.5^o away from α Centauri, at 4.6 μm. The 4.6 μm data become confusion limited (~ 50 beams per source) at around 500 μJy (Figure 3.9), but at fluxes brighter

[5] https://irsa.ipac.caltech.edu/data/SPITZER/GLIMPSE/gator_docs/GLIMPSE_colDescriptions.html

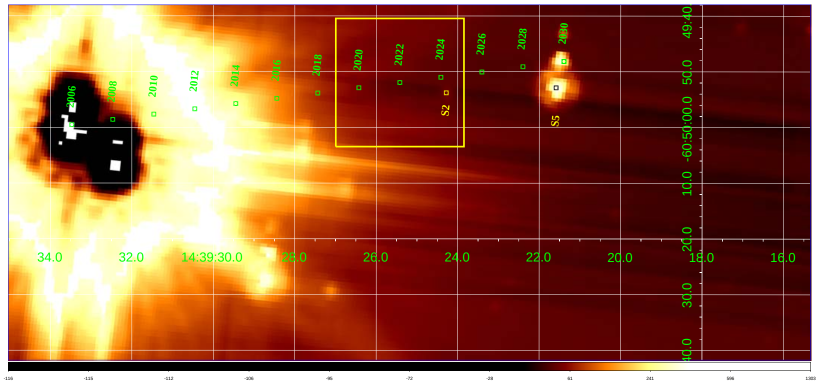

Figure 3.8 A Spitzer image (in celestial coordinates) of α Centauri AB (Fazio et al., 2004) taken in 2005 at 8.0 μm. The position of α Centauri A in 2022 is shown with a yellow square demarcating the approximate field of the 23″ MIRI coronagraph. There are no Spitzer sources within the projected MIRI field at the level of a few mJy. The approximate position of α Centauri A is shown by a series of green squares through 2030 when the source labelled "S5" (Kervella, Mignard, et al., 2016) approach α Centauri A itself.

than this level the plot of cumulative source counts, N, as a function of flux density, S, $LogN(> S)/LogS$ has a slope of -0.77, typical of a distribution of stars in the Galactic plane.

If we extrapolate the source counts to lower fluxes assuming that most of these objects have a Rayleigh-Jeans spectrum, then we can estimate the number of background sources expected within a ±2.5″ (3.3 AU) field around α CentauriA at F1550C. The extrapolated number of 15.5 μm sources is 0.004 at the 2.4 mJy brightness of a Saturn and 0.15 sources for a 20 μJy Earth (Table 1). Only at the brightness level of an Earth does the expected occurrence of background stars become a matter of concern, while for a Neptune the expected number of background sources in a ±2.5″ field is 0.03. The expected number of extra-galactic background sources is even lower at these flux levels. Using model sources counts from Cowley et al. (2018) we find that the predicted number of galaxies at 15 μm within 2″ of α CentauriA is less than 0.0035 at 20 μJy. For host stars 10 to 20 times further away than α Centauri A, the incidence of stellar and especially extra-galactic background objects will be a much more serious problem. Even though the stellar and extra-galactic sources of false positives are rare, multi-color (F1065C vs F1550C) and ultimately astrometric confirmation will be required to confidently reject background objects.

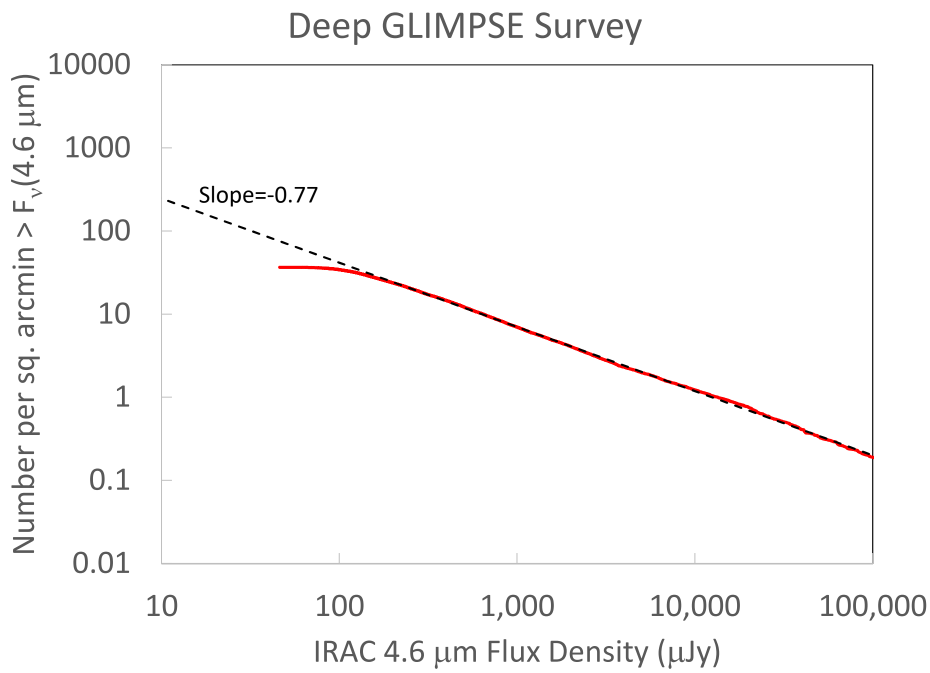

Figure 3.9 Spitzer star counts at 4.6 μm from the GLIMPSE survey at a position close to α Centauri are extrapolated below the confusion limit. The slope of the curve is typical of stellar populations in the Galactic Plane. We assume that background stars are fainter at the 15.5 μm wavelength of the MIRI coronagraph by a Rayleigh-Jeans factor of (15.5 μm/4.6 μm)^2 = 11.3.

Detector Performance Toward Bright Stars

Stars as bright as α Centauri AB present unique challenges for the MIRI detector which is a 1024×1024 arsenic-doped silicon (Si:As) IBC hybrid array (Rieke et al., 2015; Ressler, Sukhatme, et al., 2015). Even if placed behind one of the gaps in the 4QPM mask, α Centauri B would saturate portions of the detector and if not attenuated by a gap, the saturation problems would be even worse. To address detector artifacts from very bright sources, we used an instrument testbed at JPL to conduct tests on an MIRI engineering model detector using an exact copy of the flight electronics. Appendix 3.11 describes the test results in detail, but the primary conclusion is that the tests reveal no detector-based limitations to the detection of planets around the α Centauri A.

3.6 Observational Scenarios

The signal-to-noise (SNR) of a detection near α Centauri A is driven by both photon noise due to unsuppressed starlight which can be mitigated with increasing integration time and residual speckle noise which must be mitigated via improved PSF and speckle suppression. The envisioned technique of post-processing relies on the observation of a reference star with the small-grid dither technique. This technique compensates for possible jitter during the observation that slightly change the position of the target behind the coronagraph by artificially reproducing the same jitter effect while observing the reference star.

Our simulations of the observational sequence show that we achieve a reasonable balance between photon noise and residual speckle noise if we set the number integrations per dither point to keep the ratio of *total* target to reference star observing time at 1:3. This ratio depends on the difference of magnitude between the target and the reference and the stability of the observations. In particular, it is a compromise between two extreme scenarios: 1) negligible level of jitter that would require a 1:9 ratio or 2) higher level of jitter that would allow a ratio closer to 1:1, assuming two stars of the same magnitude. The adopted 1:3 ratio is a compromise that we would refine with further simulations and on-orbit information on the performance of JWST.

With this plan we can achieve detections at the levels at the 10^{-5} level at $>1''$ as discussed below. An initial reconnaissance program sufficient to detect a 5~6 $R_\oplus$ planet would require approximately 3.5 hours of on-target observing time. Adding in the $\sim 3\times$ longer duration of reference star observation plus observatory overheads leads to a total $\sim$ 20 hr program according to the JWST Exposure Time Calculator [6].

A single epoch of F1550C observations will produce a dataset which will both probe the limits of MIRI coronagraphy and result in either the detection of a planet or set limits at the $5 \sim 6\,R_\oplus$ level. MIRI might also detect solar system levels of exozodiacal emission (§3.7). Subsequent observations at multiple wavelengths would identify background objects with stellar colors and provide astrometric confirmation of detected objects.

[6] https://jwst.etc.stsci.edu/

Reference Star Selection

Coronagraphic imaging to detect a 5 $R_\oplus$ planet, not to mention 1 $R_\oplus$, presents a daunting observational challenge. The choice of a reference star is critical to removing the stellar point spread function (PSF) and residual speckles. To minimize observing time on the reference star and to maximize the level of speckle suppression it is important to find the best match in terms of brightness, spectral type and angular separation. Fortunately, on the Rayleigh-Jeans tail of photospheric emission, color effects in the narrow 6% passbands of F1550C filters are small compared with shorter wavelength observations.

There are a number of options for reference star which also affect the overall observing scenario. The closest reference to α Centauri A is, of course, α Centauri B. Using α Centauri B has the advantages of minimal change in telescope configuration and rapid target acquisition compared with choosing a more distant reference star. The disadvantage is that one can never escape the influence of the $\sim$ 1 mag (at long wavelengths) brighter α Centauri A to obtain a clean, uncontaminated PSF measurement. Ground-based programs have adopted the α Centauri B approach using rapid chopping between the two stars (§3.8). Here we examine a more conservative approach which takes a more widely separated, single star to evaluate the PSF at the positions of both α Centauri A and B. Interestingly, the two scenarios require roughly the same amount of wall clock time as determined by the JWST APT tool[7], approximately 20 hours.

For stars as bright as [F1555C] ~-1.4 mag, our choices are quite limited. We used the IRAS Low Resolution Spectrometer Catalog (Olnon et al., n.d.) to identify potential reference stars: $F_\nu(12\mu m) > 50$ Jy within 20^o of α Centauri, clean Rayleigh-Jeans photospheric emission, constant ratio (<10%) of LRS brightness (F(α Centauri)/F(star)) across the F1550C band, a low probability of variability during the 300 day IRAS mission ($VAR < 15\%$), and no bright companions within $100''$. Table 3.6 lists potential reference stars. The ratio of the LRS spectra of the (unresolved) α Centauri AB system to these stars is constant across the F1550C bandpass to < 1%.

[7] http://www.stsci.edu/scientific-community/software/astronomers-proposal-tool-apt

Table 4. Candidate Reference Stars

Star	Spec Type	Sep (deg)	[(12μm)] mag[1]
BL Cru	M4/5 III	17	-0.93
BO Mus	M6II/III	15	-1.7
DL Cha	M6III	18	-0.64
V996 Cen	Carbon Star	8	-0.70
ϵ Mus	M4III	17	-2.09
del01 Aps	M4III LPV	20	-1.36
ζ Ara	K3III	19	-1.17
α Centauri B	K1V	0.002	-0.6[2]

[1]Magnitude from IRAS Catalog; [2] estimated from shorter wavelengths

Achieving Highest Imaging Contrast

Achieving the sensitivity needed to detect planets requires aggressive post-processing techniques to reduce the residual speckles from both α Centauri A and B. We have simulated an observing scenario which places a reference star at the positions of both α Centauri A and B. The small grid 9-point dither pattern available for MIRI observations is used at the position of α Centauri A. The 15 mas micro-steps in the dither pattern combined with the 6.7 mas pointing jitter during the observation [8] improve the sampling of the point spread function (PSF) and thus the ability to remove stellar speckles (Figure 3.10). We used a Principal Component Analysis (PCA) Algorithm (Soummer et al., 2012; Amara et al., 2012) to generate a sequence of reference images using all the individual short-exposure frames obtained during the observations. For each image we generated a wavefront map realization which differed from its predecessor by a random amount and by a linear drift as described by Perrin et al. (2018) and which will be described in more detail below. The resultant wavefront maps were used to create two PSFs using the IDL version of *MIRImSIM*[9]: the on-axis PSF representing α CentauriA and an off-axis PSF at 7″ representing α CentauriB at its projected separation in ~2022. For this simulation we generated 468 exposures (52 separate pointings each with a 9 point dither pattern) for reference star at the position of A and 100 pointings (with no dither) for the reference star at the position of B. These individual reference star images were combined to generate a PSF library with 25,000 individual images (out of a possible 46,800) of the α Centauri AB system.

[8]https://jwst-docs.stsci.edu/display/JTI/JWST+Pointing+Performance
[9]https://jwst.fr/wp/?p=30

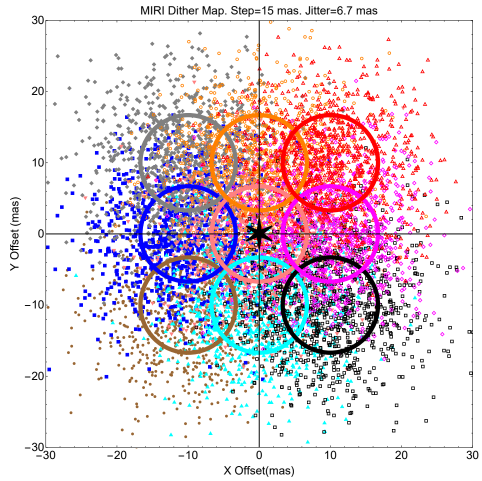

Figure 3.10 The 9 point grid dither observation strategy combined with the diversity added by the 6.7 mas jitter of the telescope (denoted by the circles) during acquisition, allows for enhanced diversity in the reference images (each denoted by a small symbol) to be used for reduction.

We also generated 200 images of α Centauri A including planets of different sizes and locations (1 to 10 $R_\oplus$, 0.5-3$''$). We also generated over 450 reference star images (§3.6). On orbit we will obtain many more images by using short exposures, ~10 sec, to avoid saturation at the core of α Centauri A and to further increase image diversity[10]. Experimenting with the PCA reductions showed that windowing the images around α Centauri A to a 5$''\times$5$''$ enhanced the performance of the PSF subtraction. Indeed, given that the region of interest does not include the region where the center of α Centauri B falls, excluding this region avoids the bias that α Centauri B induces in the reference PSF computation with PCA.

Although nominal values for readout noise, photon noise from the sky and telescope background (Ressler, Cho, et al., 2008; Rieke et al., 2015; Boccaletti et al., 2015) were added to the images, the signal from the planet itself and/or speckle noise from α Centauri A dominate the measurement within ~3$''$. The final image had a total integration time of 3.5 hr and was obtained by combining the short exposure frames for α Centauri A, α Centauri B and one of the simulated planets.

[10]The ETC shows that the wings of the unattenuated α Centauri B are not saturated beyond 1$''$-2$''$ in 10 sec.

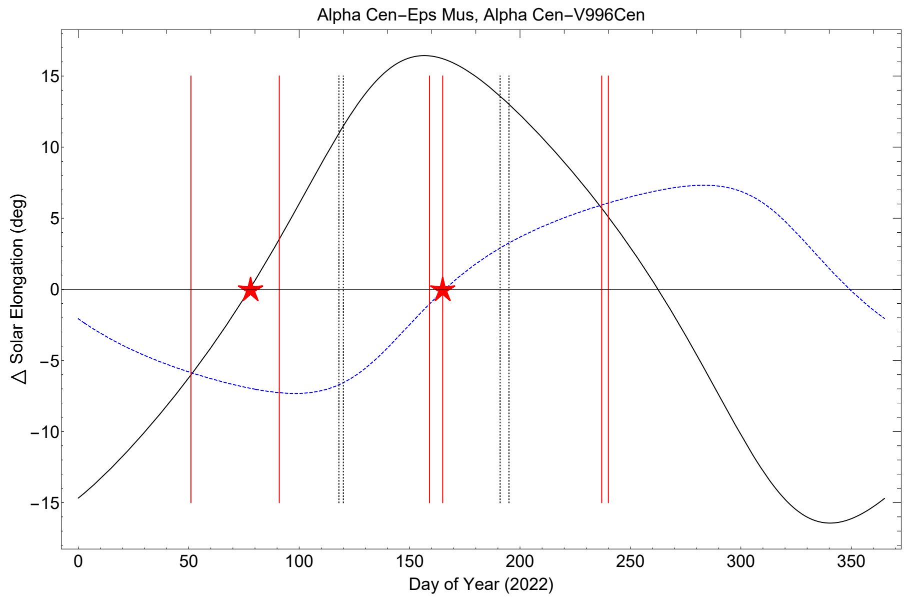

Figure 3.11 The curves show the difference between the solar elongation angles between α Centauri A and two possible reference stars (Table 3.6), ϵ Mus (solid black line) and V996 Cen (dotted blue line), through the course of one year, nominally 2022. Pairs of vertical red bars show times when α Centauri B can be located within a 4QPM quadrant while the pairs of dotted black bars show times when α Centauri B can be hidden behind one of the 4QPM gaps. Minimizing the change in solar elongation angle during a slew between α CentauriA and either star is possible on select days marked by red stars. The periods where α Centauri B can be placed behind the gap result in slews with large changes in solar elongation angle, 5^o-10^o, between the target and reference stars.

Minimizing the Effects of Wavefront Drift

The ability to detect faint companions is dominated by the stability of the nominal 132 nm of wavefront error (WFE) of the JWST telescope. According to Perrin et al. (2018), a slow-varying thermal WFE ranging from 2 to 10 nm can be expected depending on the change in solar elongation (and thus in the telescope's thermal balance). Assuming a minimal solar elongation difference as illustrated in Figure 3.11, we adopted a slow-varying thermal WFE of 2 nm RMS over the total observation of either Cen A or the reference star. The wavefront changes were distributed across small-, medium-, and large spatial scales following the prescription of Lightsey et al. (2018) and Perrin et al. (2018). For a scenario requiring a large change of solar elongation angle $> 10°$, we used initial WFE maps for the reference and target stars which differed from one another by a random 2-10 nm.

We simulated two different scenarios of wavefront evolution (Figure 3.11). In one case α Centauri B was located behind one of the 4QPM gaps while in the other α Centauri B was located at 45 degrees relative to the 4QPM boundaries. Those two scenarios have different implications for the observations. Putting α Centauri B on one of the gaps attenuates the star (Boccaletti et al., 2015; Danielski et al., 2018) with a positive effect on the level of speckles and photon noise on the final image. However, this option requires a stricter time constraint that limits our ability to optimize the solar elongation difference between the target and its reference star. Thermal models of telescope performance show that large changes in elongation angle produce sudden WFE drifts. These sudden WFEs lead to a higher level of residual speckles, which proves to be very detrimental to sensitivity. Positioning α Centauri B in between two quadrant boundaries relaxes this time constraint and enables us to optimize the difference in solar elongation. In the first scenario with α Centauri B on one of the gaps, the difference in solar elongation is estimated to $\sim 10^o$, which could result in a wavefront offset between 2-10 nm RMS between target and reference star WFE distributions (Perrin et al., 2018) whereas with α Centauri B falling between two quadrant boundaries, the difference in solar elongation can be reduced to near zero which (Perrin et al., 2018) suggests would result in a slowly evolving wavefront difference of 2 nm RMS or less.

Figure 3.12 compares the signal to noise ratio (SNR) in the PCA-processed images for different planet radii and temperatures (separations) for wavefront errors of 2 nm RMS (left). The noise at each radial offset was determined by taking the median of the values within an 1 λ/D annulus at that radius. The SNR drops for smaller planet radius and with increasing star-planet separation due to the decrease in planet temperature. The effective limit (SNR$\sim$5) of these observations is roughly 5-6 $R_\oplus$ within 1.5″. The 10 nm case (not shown) is even less favorable, strongly favoring observing scenarios which minimize WFE drifts. Figure 3.12b shows a final F1550C image showing both α Centauri B and an inset showing the PCA-corrected region with a 10 $R_\oplus$ planet at 1.5″ from α Centauri A.

Our simulations show that the scenario where α Centauri B falls on one of the gaps, the change in wavefront stability resulting from large changes solar angle greatly offsets the advantage of lower α Centauri B intensity. The scenario where α Centauri B falls within a quadrant is more favorable to the detection of small planets.

These results reinforce the fact that, in the present case of direct imaging of exoplanets around α Centauri, but also for more general cases for direct imaging of

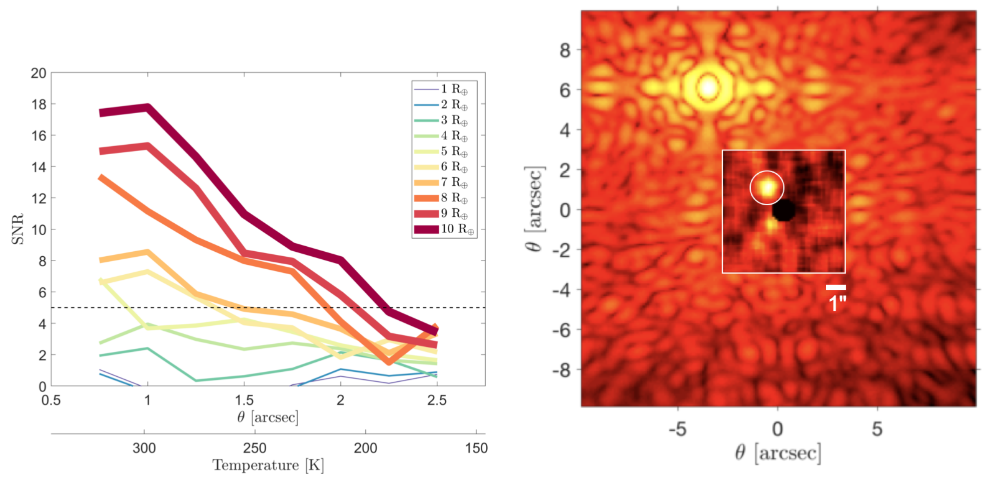

Figure 3.12 a, left) The sensitivities for different planet sizes at the expected angular separation range of detection were computed for a slow thermal varying wavefront error of 2 nm RMS (*left*). b, right) Simulation for the 2 nm case (left) for the α Centauri system with the F1550C filter centered on α Centauri A, with α Centauri B on the top left, 7 arcseconds away. The PCA reduction of the data is done on a $5'' \times 5''$ central portion of the full image (white square, the scales inside the square are different from outside). A 10 $R_\oplus$ planet is detected at $1.5''$ (white circle).

circumstellar environments, optimizing the wavefront stability through the adequate choice of reference star and optimization of observing times is crucial. On a separate note, observing sources off the gap allows observations with the (Angular Differential, ADI) strategy via rolls during a given visit or via multiple visits.

Figure 3.6 shows that in the present era, when the separation between the two stars is $\sim 7''$, the presence of α Centauri B has a relatively small effect on the ability to detect a planet orbiting α Centauri A. Not until $1.5''$ does α Centauri B appear to have a significant effect on post-processed contrast ratio, increasing from 5×10^{-5} to 8×10^{-5} on the α Centauri B facing side.

Finally, we assessed the effect of increasing the integration time *within a single visit* by a factor of 2 or more and did not see any improvement in the detectability of smaller planets. Our analysis suggests that the noise floor is set by residual speckle noise, not photon noise. Furthermore, within a given visit, the range of roll angles is modest, $\pm5^o$, so that the power of ADI is limited. The maximum 10^o roll results in only a two pixel shift at $1.5''$, compared with the $0.6''$ resolution at 15.5 μm. However, combining multiple visits with a broader range of angles and independent samples of the WFE map and drift, should produce improved sensitivity to small planets. Such visits will be necessary in any event to ensure that any planets obscured within the IWA are observed. Repeating this basic 3.5 hr observing block described here 9 times with independent wavefront realizations could result in a three-fold improvement in sensitivity and allow detections of planets down to ~3 $R_\oplus$.

3.7 Detecting and Imaging the exozodiacal Cloud

Observations of the ZodiPic model (§3.4, Figure 3.5) have been simulated using the observing scenario described above and were reduced using PCA analysis with the results shown in Figure 3.13. The figure shows the result of a 10 hour exposure. The resolved exozodiacal cloud is readily detectable at levels above ~3 Zodi (or ~5 in a single 3.5 hr exposure) and the excess integrated around the entire Habitable Zone would probably be detectable below that level. Detection of a Habitable Zone exozodiacal dust cloud at this level would be a unique contribution by JWST to our knowledge of the environment of the Habitable Zone of a solar type star.

3.8 Probability of Detecting a Planet Around α Centauri A

We use a Monte Carlo analysis (Beichman, Krist, et al., 2010) to assess the probability of finding a planet of a given radius, R_p ($R_\oplus$), and semi-major axis, SMA (AU), in the F1550C filter. The flux density of the planet is calculated from the blackbody function (Eqn 3.3) at the appropriate planet radius and orbital location, d. Figure 3.4 shows the range of planet brightness which approaches a few mJy for $10R_\oplus$ planets. For simplicity we have assumed complete redistribution of absorbed stellar energy so that there is no day-night temperature gradient and no difference in temperature as a function of phase angle. Figure 3.3 shows that a simple blackbody (Figure 3.4) over-estimates the brightness of Earth analogs with a deep CO_2 absorption feature at 15 μm. Such planets are already far below the JWST detection limit considered here, so the absorption figure was ignored in the Monte Carlo calculation.

An input population is randomly drawn from the sample described by Eqn 3.1 (§3.2) with the additional constraint of a Radial Velocity cut of 5 m s^{-1} appropriate to a $100M_\oplus$ planet at 2 AU (L. L. Zhao et al., 2017). Orbital eccentricity is randomly drawn between 0 < eccentricity< 0.5. To convert from planet mass to the planet radius needed to estimate thermal emission, we follow Wolfgang et al. (2016) and adopt $M = C(R/R_\oplus)^\gamma$ with values for C and γ from their Table 1: C=1.6 $M_\oplus$ and $\gamma = 1.8$. Similarly, we take the dispersion around the predicted radius is taken from their Eqn. (3), $\sigma = \sqrt{\sigma_1^2 + \beta(R/R_\oplus - 1)}$ with $\sigma_1 = 2.9M_\oplus$ and β=1.5.

In the simulation planets are placed at randomized locations in their orbits. Planets with apoastron greater than 3 AU are excluded due to stability arguments. An

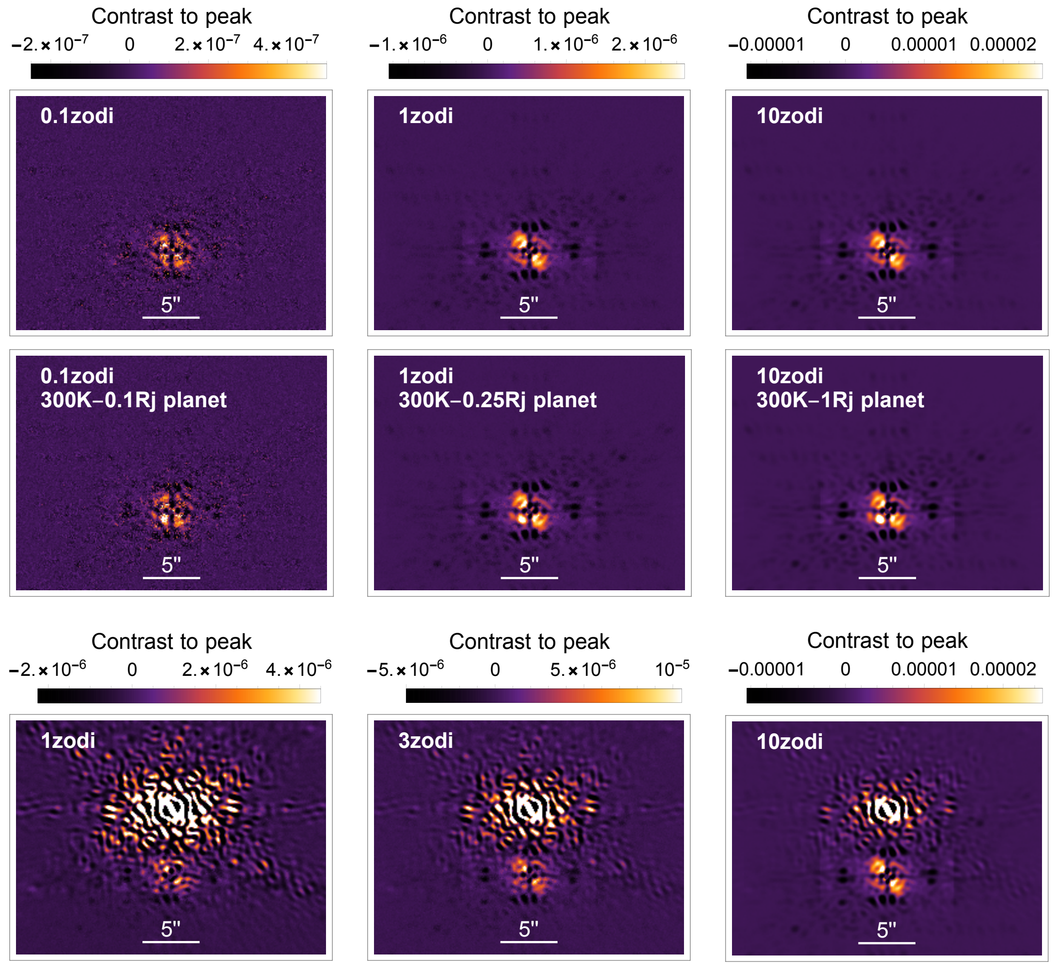

Figure 3.13 The zodi model (Figure 3.5) as observed with MIRI using the 4QPM mask in a 10 hr exposure. The top two rows show PCA reductions of observations ignoring the influence of α Centauri B. The data were taken using Small Grid Dithers for models with three different levels of zodiacal emission (0.1, 1, 10) Zodi, without and with a 300 K planet of three different radii (0.1, 0.25, and 1) R_{Jup}. The bottom panel adds in the effect of α Centauri B for the no planet case.

apoapse of 3 AU is used as a hard limit, because there appear to be no islands of stability beyond that distance (Figure 3.2, Quarles and Lissauer (2016)). The planets are confined to the plane of the α Centauri AB binary system (Kervella, Mignard, et al., 2016) with an added dispersion in the inclination of 5^o. Each planet is started on its orbit at a random time of periastron passage so that the Monte Carlo analysis samples all possible positions of planets relative to the IWA of the MIRI coronagraph. This analysis adopts the transmission of the 4QPM mask (Boccaletti et al., 2015) and the one dimensional coronagraph performance curve shown in Figure 3.6 which is based on the PCA post-processing (§3.6).

Figure 3.14a shows contours of the probability of detecting a planet of a given radius and semi-major axis in a single visit with 3.5 hours of on-target integration time. There is a broad plateau of detectability ~50% for R>5$R_\oplus$ and 1 < SMA< 2 AU. Figure 3.14b shows detectability contours based purely on photometric considerations, i.e. ignoring geometrical constraint due to planets being obscured within the IWA, and show what planets might be detected in the limit of multiple visits.

Figure 3.14 does not take into account the restriction on planets due to the RV observations. Figure 3.15a shows a smoothed histogram of all detected planets, similar to Figure 3.14b, while Figure 3.15b shows the distribution of planets which could be detected and still be consistent with the ~5 m s^{-1} PRV upper limit. Using the Fernandes et al. (2019) occurrence rates, Eqn 3.1, the fraction of all planets detectable within the 5 m s^{-1} RV limit and a 5 $R_\oplus$ MIRI limit is only 5%. A more extensive campaign of multiple visits (with independent wavefront realizations) could push to lower radii and higher completeness (§3.8). A 3 $R_\oplus$ MIRI limit could detect ~ 13% of all of the planets expected on the basis of the (poorly) known planet population and consistent with the RV limit; however, as noted in §3.2, the occurrence rates (Fernandes et al., 2019) could be a factor of 3 lower in a binary system (Kraus et al., 2016).

Sources of Incompleteness

Because α Centauri A is seen close to edge on, a planet can be missed because its semi-major axis (or apoastron for an eccentric orbit) never takes it outside the Inner Working Angle of the coronagraph or simply not far enough to be in a region of reduced speckle noise. Thus, the IWA and the contrast limit close to the IWA limit the semi-major axis at which planets can be detected. Second, planets with orbits larger than the IWA can still be missed as they pass behind the IWA in their orbit. Thus, the maximum fractional detectability for a planet at SMA=1.2 AU (0.9″) with respect to the IWA of 0.49″ at F1550C is $1 - \frac{2}{\pi}ArcSin(\frac{IWA}{SMA})$=63% in a single visit. As planets move further out, the fraction of time they are missed for geometrical reasons decreases. But, as they move further out, their temperature drops so they might be missed for reasons of low SNR. These two effects account for the general shape of the detectability in Figure 3.14a. The solution to the problems of geometrical incompleteness is carrying out multiple observations over a number of epochs as pointed out in many studies of this question (Brown, 2005; Brown, 2015).

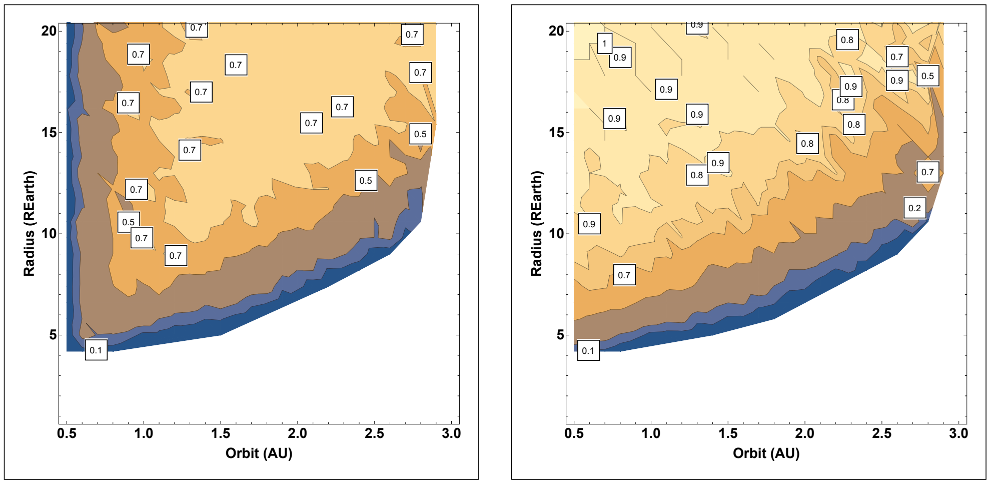

Figure 3.14 a, left) A plot showing the detectablity of planets with a specified radius and semi-major axis (SMA) in a single visit, averaged over ranges of albedo, orbital eccentricity and orientation as described in the text. The contour levels show the fraction of planets detected in a given (Radius, SMA) bin. b, right) same plot but showing sensitivity-limited detectability which ignores geometrical incompleteness due to a planet being hidden within the Inner working Angle.

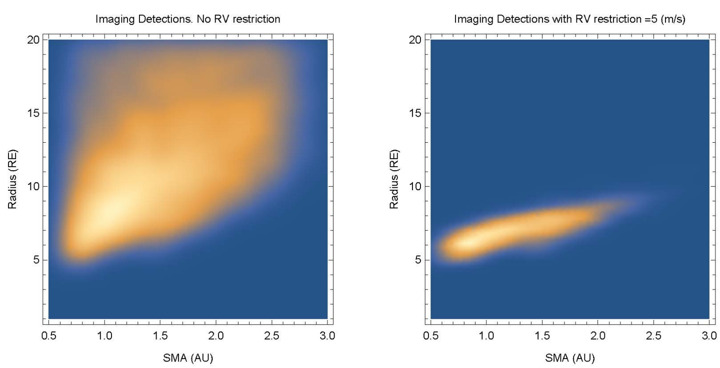

Figure 3.15 a,left) The locus of all potentially detectable planets in (Radius-SMA) space similar to Figure 3.14b. b, right) the locus of all detected planets subject to the RV limit of 5 m s^{-1}. The intensity scale is arbitrary.

Two additional sources of incompleteness are not accounted for in Figure 3.14. First is the increased noise level in the direction of α Centauri B and second from the possibility that at any one instant a planet may hide behind one of the 4QPM's quadrant gaps. Figure 3.6 shows remarkably little difference in the post-processing curves in the direction of α Centauri B relative to other directions within the region of interest, < 3 AU. α Centauri A is simply overpowering at these separations relative to α Centauri B located 7-8$''$ away.

The second source of incompleteness not taken into account in Figure 3.14 are the dead areas defined by the 4QPM gaps. We test the second source by performing numerical simulations using a modified version of the `mercury6` integration package designed to evolve planetary orbits in binary systems (Chambers et al., 2002). These simulations use the orbital solution from Pourbaix et al. (2016) for the binary orbit and evaluate the stability on 10^5 yr timescale for Earth-mass planets over a range of initial SMAs (1–3 AU), eccentricity vectors ($e_p \cos \omega_p \leq 0.9$, $e_p \cos \omega_p \leq 0.9$), and mutual inclinations ($< 90°$). Figure 3.16 shows the projection of initial conditions that are stable (survive for 10^5 yr) and binned using the expected angular resolution (~0.3 ″) at 15.5 μm to identify a normalized number density of potential orbits on the sky plane (see color scale). Projecting the gap width onto the ~2.5 AU zone of stability (Quarles and Lissauer, 2016) reveals that the incompleteness due to the gaps outside of the IWA is around 24%. This source of incompleteness can be mitigated by multiple visits at different orientations. Aligning the gaps with the α Centauri AB axis results in an incompleteness of 60%–another reason to avoid this observing scenario.

Comparison with Ground-based Initiatives

The proximity of the α Centauri system makes it a compelling target for ground-based studies in the N (10 μm) band despite the high sky background. As described in Kasper et al. (n.d.) and Kaufl et al. (2018), the European Southern Observatory (ESO) in collaboration with the Breakthrough Initiative has modified the VLT mid-IR imager VISIR to enhance its ability to search for potentially habitable planets around both components of α Centauri. The NEAR (New Earths in the Alpha Cen Region) concept combines adaptive optics using the deformable secondary mirror at UT4, a new vector vortex coronagraph (Mawet, Riaud, et al., 2005) optimized for the most sensitive spectral bandpass in the N-band, and fast chopping for noise filtering.

The recently demonstrated sensitivity of the NEAR instrument is 650 μJy (5σ in 1 hour, Kaufl et al. (2018)). Assuming no systematic errors intervene, a 100 hr observing program with NEAR could have the sensitivity to detect a 2 $R_\oplus$ planet with an Earth-like emission spectrum at $\sim 3\lambda/\mathrm{D}\sim$ 1AU and a temperature around 300 K. This result, if achieved, could complement JWST's MIRI search by extending inward to smaller, hotter planets. In the long term, the NEAR experiment is relevant for the Extremely Large Telescope/METIS instrument (Quanz et al., 2015) which would benefit from the telescope diameter (D), D^1 gain in inner working angle and

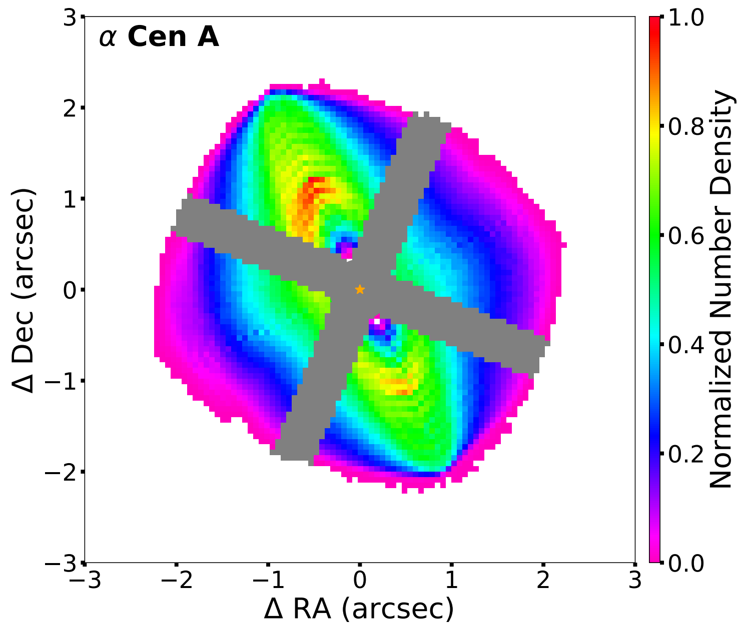

Figure 3.16 Projection of initial conditions that are stable on 10^5 yr timescales onto the sky plane. The stable initial conditions are binned for resolution at 15.5 μm, where the color scale denotes a normalized number density of stable initial conditions within each bin. Bins that do not contain any stable initial conditions are colored white. The regions defined by the 4QPM mask and the gaps between adjaCent quadrants are plotted in gray over the region of potential planet stability. These regions block roughly 24% of the coronagraphic field outside of the IWA.

the D^4 gain in photometric sensitivity due to the ELT's 39 meter aperture.

Dynamical searches for planets orbiting α CentauriA are continuing. The new generation of PRV instruments such as ESPRESSO (Hernández et al., 2018) should be able measure down to a few Earth masses, although the presence of α Centauri B presents observational challenges at binary separations smaller than a few arcseconds. On the other hand, both the ALMA and the VLT Gravity interferometers are taking advantage of this binarity by searching for a planet-induced astrometric wobble in the separation between α Centauri A and B at millimeter (Akeson et al., 2019) and near-IR wavelengths (Gravity Collaboration, 2017), respectively. Dynamical detections from any of these techniques would add critical information on the mass and orbit of any planet found via direct imaged–whether from JWST or other experiments now underway.

3.9 Conclusions

With careful observation planning and advanced post-processing techniques JWST's MIRI coronagraph could detect planets as small as 5 $R_{\oplus}$ at 15.5 μm in a single ~20 hr visit (combining ~ 3.5 hr of on-target integration plus reference star and other overheads). Multiple visits would enhance completeness, provide astrometric confirmation, and push to still lower planet radii. These additional observations would also help to refine orbital data and open a search for additional planets. Detection at MIRI wavelengths would lead to an estimate of the planet's effective temperature and thus its radius which would depend only weakly on the assumed albedo. Of course, the actual performance of JWST in terms of wavefront error and especially WFE stability remains unknown as does the performance of its detectors. A more sustained campaign could push this radius limit down to ~3 $R_{\oplus}$.

MIRI could also detect an exozodiacal dust cloud at the level of 3 ~ 5× the brightness of our own cloud. Depending on the strength and distribution of the exozodiacal dust, such emission could mask the light of any planet.

JWST data, in conjunction with ground-based observations would provide refined characterization of any detected planets: PRV measurements with both current and next generation instruments such as CHIRON and ESPRESSO (L. Zhao et al., 2018; Hernández et al., 2018) would yield a refined orbit and the planet's mass from which we would determine its bulk composition; VLT/NEAR detections at shorter wavelengths, ~ 10 μm, would refine the spectral energy distribution. Ultimately, instruments combining high contrast imaging with high spectral resolution spectroscopy on 30-40 m telescopes would open up the prospect of exoplanet spectroscopy of a planet orbiting in the Habitable Zone of a solar type star (Snellen et al., 2015; Wang et al., 2017).

3.10 Acknowledgements

Some of the research described in this publication was carried out in part at the Jet Propulsion Laboratory, California Institute of Technology, under a contract with the National Aeronautics and Space Administration.

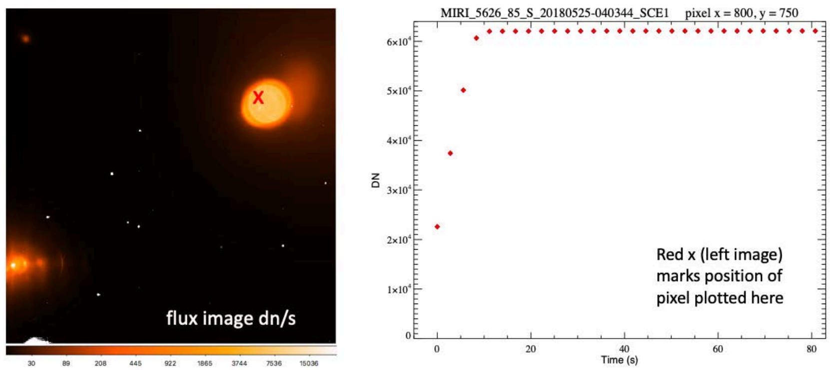

Figure 3.17 Left) Full frame MIRI engineering model detector. The tests includes two sources from a masked black body, a faint point like object in the top left, and an extended disc structure in the top right. An unfocussed LED source can be seen in the bottom left of the image. The units of the image are flux (Data Numbers, DN/s) as calculated from the slope of unsaturated frames. Right) the signal recorded from one pixel in the disc black body source.

3.11 Appendix

MIRI Detector tests

Estimates based on the JWST Exposure Time Calculator (ETC[11]) for the unattenuated signal from α Centauri B is approximately 5×10^7 electrons s^{-1} at 15.5 μm which is well above the saturation limit for the MIRI detectors. To explore the implications of such a bright source in the focal plane we carried out a series of tests using the flight-like configuration at JPL. Figure 3.17 shows the resulting image from the bright target test. The test setup was set so that it would quickly saturate the detector with a signal of a factor of 10 more than the saturation limit. Figure 3.17 plots the signal recorded for one illuminated pixel for each of the 30 groups in one integration. The test source saturated the detector in 4 groups or approximately 11 seconds for a total time per integration of 80 seconds. The total exposure time of 10 integrations was 14 minutes.

The resulting test image (Figure 3.17) shows a good detection of the 3 sources used in the test despite the “super” saturation of the detector. Other than glints and optical effects which originate in the test bench setup, there is no significant impact in the image quality from the “super-saturation” of the detector. In Figure 3.18 we set the scale of the test image to enhance the background to reveal faint structures associated with the rows and columns of the detected sources. Row profiles of the image, also presented in Figure 3.18, show that the background artifacts are 4 orders

[11] https://jwst.etc.stsci.edu/

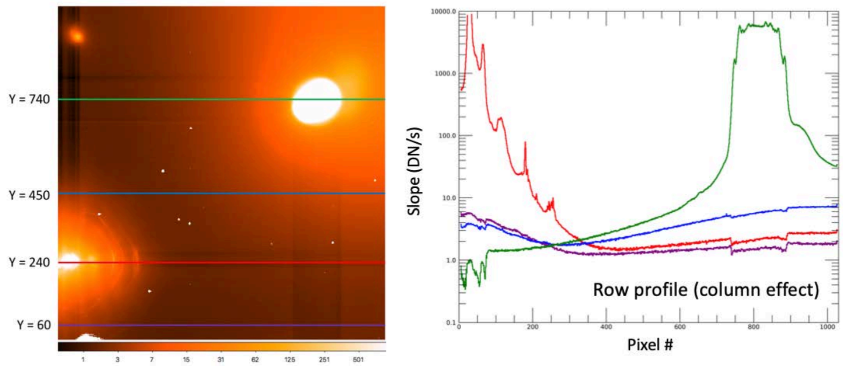

Figure 3.18 a, left) the same test data as Figure 3.17 but with the scale set to highlight faint structure in the background. b. Colored lines crossing the image horizontally mark rows whose intensities are shown on the right. b, right) The profiles of the marked rows in the detector showing the effects of the column effect in the rows underneath of brightest source.

of magnitude lower in flux than the sources in the image.

This row and column structure in the detectors had been previously identified by the MIRI test team and is associated with bright source detections (Figure 3.19). We believe the artifacts will have little impact on the detection of planets the following reasons. First, the row and column artifacts are accentuated in the JPL test images due to the very low backgrounds in the test conditions - a factor of three less than we expect at the shortest MIRI wavelength range of 5.7 microns. For the higher backgrounds expected from the MIRI 4QPMs (F1550C) the column and row effects will be significantly diluted. (Figure 3.19) also shows that, although the effect is flux dependent, it is limited to the columns in which there are bright sources, therefore the effect from α Centauri B should be limited to the columns in which it is placed.

However, the row effect extends beyond the source rows, in the read direction up the detector, with a dependence on source size. Therefore, there is a possibility that the row artifact could affect planet detection if α Centauri B were placed in a lower quadrant of the 4QPM. However, we expect the point like nature of α Centauri B will help reduce the amplitude of this artifact. Lastly, the artifacts have shown to be highly uniform in amplitude in the row and column direction, therefore preliminary efforts to correct the image based on median column and row filtering have proved promising. In summary, we find no limitations from the point of view of MIRI detectors to the detection of planets around the α Centauri AB system from MIRI ground detector testing. Including the case of "super" saturation, which is expected in the observation of the α Centauri AB system with the MIRI 4QPMs.

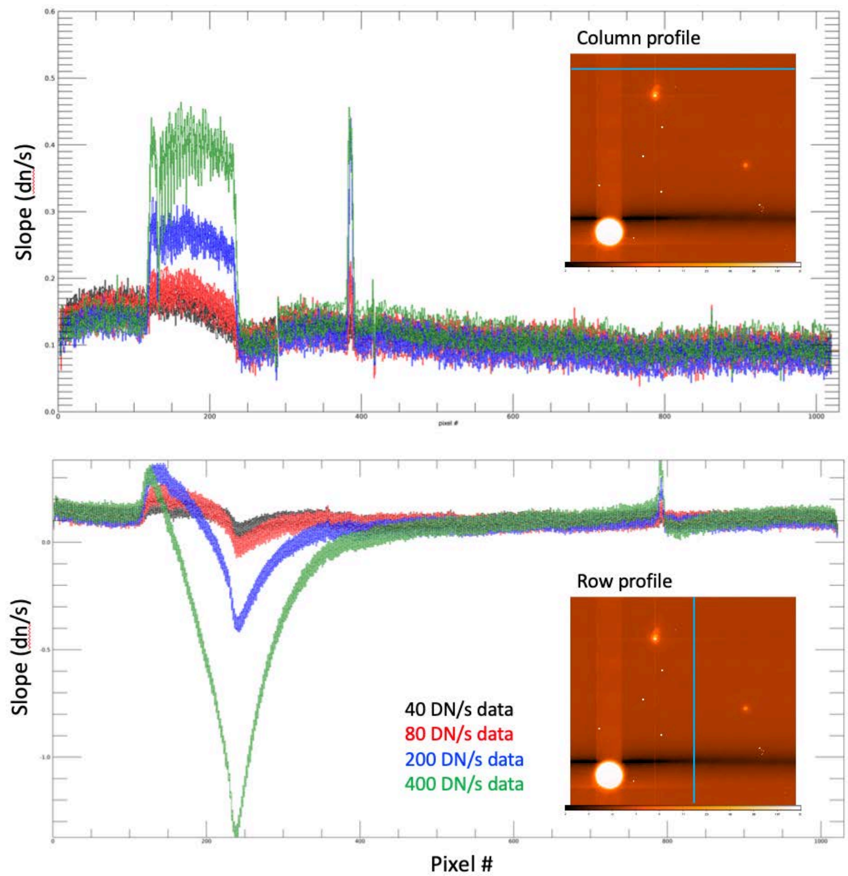

Figure 3.19 JPL MIRI test data results showing data with 3 black body sources at four different flux levels. Row (bottom) and column (top) profiles at each flux level highlight the extent of the artifacts in each direction.

BIBLIOGRAPHY

Akeson, A. et al. (2019). "presented at 2019 Astrobiology Science Conference (AbSciCon)". In: *Seattle WA* 4824.

Amara, A. and S. P. Quanz (2012). In: *Monthly Notices of the RAS* 427, p. 948.

Angel, J. R. P. and N. J. Woolf (1997). In: *Astrophysical Journal* 475, p. 373.

Beichman, C. A., G. Bryden, T. N. Gautier, et al. (2005). In: *Astrophysical Journal* 626, p. 1061.

Beichman, C. A., G. Bryden, K. R. Stapelfeldt, et al. (2006). In: *Astrophysical Journal* 652, p. 1674.

Beichman, C. A., M. Fridlund, W. A. Traub, et al. (2007). In: *Protostars and Planets V* 915.

Beichman, C. A., J. Krist, J. T. Trauger, et al. (2010). In: *Publications of the Astronomical Society of the Pacific* 122, p. 162.

Beichman, C. A., A. Tanner, G. Bryden, et al. (2006). In: *Astrophysical Journal* 639, p. 1166.

Belikov, R. et al. (2015). In: *Proceedings of the SPIE* 9605.96051, p. 7.

Boccaletti, A., P.-O. Lagage, P. Baudoz, et al. (2015). In: *Publications of the Astronomical Society of the Pacific* 127, p. 633.

Brown, R. A. (2005). In: *Astrophysical Journal* 624, p. 1010.

– (2015). In: *Astrophysical Journal* 799, p. 87.

Burrows, A., D. Sudarsky, and I. Hubeny (2004). In: *Astrophysical Journal* 609, p. 407.

Burrows, A. S. (2014). In: *Proceedings of the National Academy of Science* 111, p. 12601.

Cahoy, K. L., M. S. Marley, and J. J. Fortney (2010). In: *Astrophysical Journal* 724, p. 189.

Chambers, J. E. et al. (2002). In: *Astronomical Journal* 123, p. 2884.

Churchwell, E., B. L. Babler, M. R. Meade, et al. (2009). In: *Publications of the Astronomical Society of the Pacific* 121, p. 213.

Council, N. R. (2010). *New Worlds, New Horizons in Astronomy and Astrophysics*. Washington, DC: The National Academies Press.

Cowley, W. I. et al. (2018). In: *Monthly Notices of the RAS* 474, p. 2352.

Cumming, A., R. P. Butler, G. W. Marcy, et al. (2008). In: *Publications of the Astronomical Society of the Pacific* 120, p. 531.

Danielski, C., J.-L. Baudino, P.-O. Lagage, et al. (2018). In: *Astronomical Journal* 156, p. 276.

Ertel, S. et al. (May 2018). "The HOSTS Survey Exozodiacal Dust Measurements for 30 Stars". In: *Astronomical Journal* 155, 194, p. 194. DOI: 10.3847/1538-3881/aab717. arXiv: 1803.11265 [astro-ph.SR].

Fazio, G. and T. Megeath (2004). "A SEARCH FOR COMPANIONS AROUND STARS WITHIN FIVE PARSEC". In: *AOR Key* 3911680.

Fernandes, R. B., G. D. Mulders, I. Pascucci, et al. (2019). In: *Astrophysical Journal* 874, p. 81.

Gravity Collaboration (June 2017). "First light for GRAVITY: Phase referencing optical interferometry for the Very Large Telescope Interferometer". In: *Astronomy and Astrophysics* 602, A94, A94. DOI: 10.1051/0004-6361/201730838. arXiv: 1705.02345 [astro-ph.IM].

Hernández, G. et al. (2018). "2018". In: *Handbook of Exoplanets* 157.

Holman, M. J. and P. A. Wiegert (1999). In: *Astronomical Journal* 117, p. 621.

Howard, A. W. (2013). In: *Science* 340, p. 572.

Hu, R., B. L. Ehlmann, and S. Seager (2012). In: *Astrophysical Journal* 752, p. 7.

Hu, R. and S. Seager (2014). In: *Astrophysical Journal* 784, p. 63.

Hu, R., S. Seager, and W. Bains (2013). In: *Astrophysical Journal* 769, p. 6.

Kasper, M. et al. (n.d.). In: *The Messenger* 169 (), p. 16.

Kaufl, H.-U., M. Kasper, R. Arsenault, et al. (2018). In: *Proceedings* 1070. URL: https://doi.org/10.1117/12.2313395.

Kenworthy, M. A., O. Absil, T. Agocs, et al. (2016). In: *Proceedings of the SPIE* 9908, p. 9908.

Kervella, P., L. Bigot, A. Gallenne, et al. (2017). In: *Astronomy and Astrophysics* 597.

Kervella, P., F. Mignard, et al. (2016). In: *Astronomy and Astrophysics* 594.

Knight, J. S., P. Lightsey, and A. Barto (2012). In: *Proceedings of the SPIE* 8442, p. 84422.

Kopparapu, R. k., E. T. Wolf, G. Arney, et al. (2017). In: *Astrophysical Journal* 845, p. 5.

Kraus, A. L. et al. (2016). In: *aj* 152, p. 8.

Kuchner, M. (2012). "ZODIPIC: Zodiacal Cloud Image Synthesis". In: *Astrophysics Source Code Library* 1202, p. 002.

Leger, A., J. M. Mariotti, B. Mennesson, et al. (1996). In: *Icarus* 123, p. 249.

Lightsey, P. A., J. S. Knight, A. Barto, et al. (2018). In: *Proceedings* 1069. URL: https://doi.org/10.1117/12.2312276.

Marais, D. et al. (2002). In: *Astrobiology* 2, p. 153.

Mawet, D., L. Hirsch, E. J. Lee, et al. (2019). In: *Astronomical Journal* 157, p. 33.

Mawet, D., P. Riaud, et al. (2005). "Annular Groove Phase Mask Coronagraph". In: *Astrophys. J.* 633, pp. 1191–1200. DOI: 10.1086/462409.

Mawet, D., P. Wizinowich, R. Dekany, et al. (2016). In: *Proceedings of the SPIE* 9909, p. 99090.

Mazin, B., E. Artigau, V. Bailey, et al. (2019). In: *Bulletin of the AAS* 51, p. 128.

Mennesson, B., S. Gaudi, S. Seager, et al. (2016). In: *Proceedings of the SPIE* 9904, p. 99040.

Olnon, F. M., E. Raimond, G. Neugebauer, et al. (n.d.). "1986". In: *Astronomy and Astrophysics* 65 (), p. 607.

Perrin, M. D., L. Pueyo, K. Van Gorkom, et al. (2018). In: *Proceedings* 1069. URL: https://doi.org/10.1117/12.2313552.

Pourbaix, D. and H. M. J. Boffin (2016). In: *Astronomy and Astrophysics* 586.

Pueyo, L., N. Zimmerman, M. Bolcar, et al. (2017). In: *Society of Photo-Optical Instrumentation Engineers (SPIE) Conference Series* 398, p. 10398.

Quanz, S. P. et al. (2015). In: *International Journal of Astrobiology* 14, p. 279.

Quarles, B. and J. J. Lissauer (2016). In: *Astronomical Journal* 151, p. 111.

– (2018). In: *Astronomical Journal* 155, p. 130.

Quarles, B., J. J. Lissauer, and N. Kaib (2018). In: *Astronomical Journal* 155, p. 64.

Quintana, E. V. et al. (2002). In: *Astrophysical Journal* 576, p. 982.

Ressler, M. E., H. Cho, R. A. M. Lee, et al. (2008). In: *Proceedings* 7021. URL: https://doi.org/10.1117/12.789606.

Ressler, M. E., K. G. Sukhatme, B. R. Franklin, et al. (2015). In: *Publications of the Astronomical Society of the Pacific* 127, p. 675.

Rieke, G. H., M. E. Ressler, J. E. Morrison, et al. (2015). In: *Publications of the Astronomical Society of the Pacific* 127, p. 665.

Santerne, A., C. Moutou, M. Tsantaki, et al. (2016). In: *Astronomy and Astrophysics* 587.

Sciences, N. A. of, ed. (n.d.). *Engineering, and Medicine. 2018. Exoplanet Science Strategy*. Washington, DC: The National Academies Press. URL: https://doi.org/10.17226/25187.

Seager, S. and D. Deming (2010). In: *Annual Review of Astronomy and Astrophysics* 48, p. 631.

Skemer, A., D. Stelter, D. Mawet, et al. (2018). In: *Proceedings of the SPIE* 702, p. 10702.

Snellen, I. et al. (Apr. 2015). "Combining high-dispersion spectroscopy with high contrast imaging: Probing rocky planets around our nearest neighbors". In: *Astronomy and Astrophysics* 576, A59, A59. DOI: 10.1051/0004-6361/201425018.

Soummer, R., L. Pueyo, and J. Larkin (Aug. 2012). "Detection and Characterization of Exoplanets and Disks Using Projections on Karhunen-Loève Eigenimages". In: *Astrophysical Journal, Letters* 755.2, L28, p. L28. DOI: 10.1088/2041-8205/755/2/L28. arXiv: 1207.4197 [astro-ph.IM].

Su, K. Y. L., G. H. Rieke, R. Malhotra, et al. (2013). In: *Astrophysical Journal* 763, p. 118.

Teplitz, V. L., S. A. Stern, J. D. Anderson, et al. (1999). In: *Astrophysical Journal* 516, p. 425.

Thevenin, F., J. Provost, P. Morel, et al. (2002). In: *Astronomy and Astrophysics* 392.

Thompson, S. E., J. L. Coughlin, K. Hoffman, et al. (2018). In: *Astrophysical Journal, Supplement* 235, p. 38.

Traub, W. A. and B. R. Oppenheimer (2010). *Handbook of Exoplanets, Handbook of Exoplanets, ISBN 978-3-319-55332-0*. part of Springer Nature, 2018, id.111: Springer International Publishing AG.

Turnbull, M. C. (2015).

Turnbull, M. C., W. A. Traub, K. W. Jucks, et al. (2006). In: *Astrophysical Journal* 644, p. 551.

Wang, J., D. Mawet, G. Ruane, et al. (2017). In: *Astronomical Journal* 153, p. 183.

Wiegert, J., R. Liseau, P. Thebault, et al. (2014). In: *Astronomy and Astrophysics* 563.

Wolfgang, A., L. A. Rogers, and E. B. Ford (2016). In: *Astrophysical Journal* 825, p. 19.

Xie, J.-W., J.-L. Zhou, and J. & Ge (2010). In: *Astrophysical Journal* 708, p. 1566.

Zhang, Y., Q. Li, J.-W. Xie, et al. (2018). In: *Astrophysical Journal* 861, p. 116.

Zhao, L., D. A. Fischer, J. Brewer, et al. (2018). In: *Astronomical Journal* 155, p. 24.

Zhao, L. L., D. A. Fischer, J. M. Brewer, et al. (2017). In: arXiv: 1711.06320.

Chapter 4

CORONAGRAPH DESIGN: THE HYBRID LYOT CORONAGRAPH FOR THE ROMAN CGI

Llop-Sayson, J. et al. (2021). "Coronagraph Design with the Electric Field Conjugation Algorithm". In: *Submitted to Journal of Astronomical Telescopes, Instruments, and Systems*.

ABSTRACT

The requirements for a coronagraph instrument to image and obtain spectra of rocky planets around bright stars from space are tight. Indeed, the goal of imaging an Earth-like planet requires a starlight suppression system that cancels light to a level of 10^{-10} with sufficient stability and robustness to errors. Furthermore, the key science questions necessitate an adequate sample size; consequently, the throughput of the coronagraph drives the achievable yield of a given mission. The trade among achievable raw contrast, sensitivity to wavefront errors, and throughput poses a challenging problem in coronagraph design. The complexity of this problem drives us towards the simultaneous solving of all optical elements. In this work we present a set of methods to optimize the design of a coronagraph. We implement these for the case of the hybrid Lyot coronagraph (HLC) in the context of the Nancy Grace Roman Space Telescope Coronagraph Instrument. We discuss our findings in terms of coronagraph instrument design, and optical subsystems and performance interplay.

4.1 Introduction

The numerous techniques of detection and characterization have allowed the discovery of thousands of exoplanets of which we are just starting to grasp the diversity in planetary characteristics. Indirect techniques, such as transiting and radial velocity techniques, have been widely successful in detecting lower separation planets orbiting relatively bright and mature stars. On the other hand, direct imaging can probe wider separation planets around younger stars. Direct imaging and atmospheric characterization of exoplanets is also one of the driving science cases of NASA mission concepts HabEx (Habitable Exoplanet Observatory) (The HabEx Team, 2019) and LUVOIR (Large UV Optical Infrared Surveyor) (The LUVOIR Team, 2019). Consequently, a key technology for these observatories is the coronagraph instrument design.

Several coronagraph architectures have been demonstrated to suppress unwanted starlight for this science case (Kuchner et al., 2002; Kasdin, Vanderbei, et al., 2003; Codona et al., 2004; Mawet et al., 2005; Foo et al., 2005; Guyon, Pluzhnik, Galicher, et al., 2005; Soummer, 2005; J. T. Trauger et al., 2007). For instance, the hybrid Lyot coronagraph (HLC) (J. T. Trauger et al., 2007; J. Trauger, Moody, Krist, et al., 2016) consists of two deformable mirrors, a focal plane mask (FPM) and a Lyot stop. At the FPM a metal occulter diffracts most of the light to the outer edge in the pupil plane, where a Lyot stop filters it, cancelling most of the starlight at the final image plane. Shaped dielectric is deposited on top of the metal occulter to control the phase of the wavefront thus adding extra degrees of freedom in the design. The HLC has the best performing record in terms of raw contrast in a vacuum testbed environment (Seo, Patterson, et al., 2019), and, although it has been generally believed to suffer from sensitivity to low order errors (Krist et al., 2019), this has been mitigated through research for LUVOIR-A HLC designs. The requirements for LUVOIR and HabEx coronagraph instruments on raw contrast and sensitivity to low-order errors are remarkably strict (The LUVOIR Team, 2019; The HabEx Team, 2019). Furthermore, instruments have to allow for as high planet throughput as possible to increase the science yield of a mission (Stark et al., 2019). This is especially challenging in the presence of discontinuities in the pupil, e.g. from the telescope segmentation and from the secondary mirror. Particularly adverse to coronagraph performance is the central obscuration from the secondary mirror in an on-axis telescope (Crill et al., 2017; Stark et al., 2019). For these reasons coronagraph design optimization remains a high-priority research pathway for future direct imaging missions.

Optimizing a coronagraph design is a complex task. Many efforts in the last few years have been focused on dealing with the pupil discontinuities (Soummer et al., 2011; N'Diaye et al., 2016; Zimmerman et al., 2016; Ruane, A. J. Riggs, et al., 2018); for instance, adding an apodizer to the vortex coronagraph concept can help deal with segmentation discontinuities (Jewell et al., 2017; Ruane, Jewell, et al., 2016), or, combining the shaped pupil coronagraph concept with the apodizing phase plate coronagraph can deal with big central obscurations (Por, 2020). Ultimately, there exists a fundamental trade between the achievable raw contrast and sensitivity to low-order errors and inner working angle (IWA), and, given the current state of the art, there is still much room for improvement towards the theoretical limit (Guyon, Pluzhnik, Kuchner, et al., 2006; Belikov et al., 2019; Shaklan et al., 2019). Furthermore, much progress is still needed to understand the limitations of coronagraph systems in a testbed environment. Indeed, the physical processes taking place at the optical elements and their interplay at very high contrast are poorly understood, e.g., the chromatic effects of the DM surface errors (Krist et al., 2019), the DM actuator quantization effects (Ruane, Echeverri, et al., 2020; Prada et al., 2019), or polarization-induced aberrations (Davis et al., 2018; Krist et al., 2019; Seo, Patterson, et al., 2019). Modelling efforts at the Jet Propulsion Laboratory (JPL) have been tackling the gap between simulation and testbed performance (Zhou et al., 2020; Marx et al., 2017; Seo, Patterson, et al., 2019).

The work presented here was done in the context of optimizing the design process for the Nancy Grace Roman Space Telescope (Roman) Coronagraph Instrument's HLC. The Roman Coronagraph (Kasdin, Bailey, et al., 2020) is an advanced technology demonstrator that will pave the way for future direct imaging missions by demonstrating key coronagraph technologies in space. The HLC in the Roman Coronagraph is designed by carefully solving for the deformable mirrors shapes and the dielectric layer shape simultaneously in a small-step linearized approach. It is beyond the scope of this paper to provide the specifics of the optimal solution for the HLC design for the Roman Coronagraph; our goal is instead to publish the optimization tools we developed. These consist of the changes to the electric field conjugation (EFC) algorithm cost function and the several methods to drive EFC into the optimal design solution space. In Sec. 4.2, we lay out the EFC algorithm and its conventional cost function. In Sec. 7.2 we present the modifications to the EFC cost function. In Sec. 7.5 we present some methods on how we control the EFC design runs to seek for the optimal design points, and show the results from the modifications to the cost function. We discuss these results in Sec. 5.5. For all

EFC design run optimizations we use the Fast Linearized Coronagraph Optimizer (FALCO) (A. J. E. Riggs et al., 2018) software package[1].

4.2 The Electric Field Conjugation Algorithm

In this section we review the mathematical formalism of EFC. EFC as described by Give'On (2009) iteratively reduces the intensity in the dark hole of image plane of a coronagraphic system. Originally conceived as a wavefront control algorithm, EFC is usually implemented to optimize one or two deformable mirror (DM) shapes: the algorithm finds a vector $\Delta\mathbf{u}$ containing the change in actuator heights needed to null the E-field in the image plane.

With $\mathbf{e}_{DH}$ being the vector of complex-valued electric fields in the pixels in the region of interest, or dark hole (DH), after control iteration $k+1$, the cost function of EFC in its most fundamental mode can be expressed as:

$$J = \mathbf{e}^{\mathsf{H}}_{DH,k+1}\mathbf{e}_{DH,k+1} \tag{4.1}$$

At the core of the EFC algorithm is the linearization assumption, in which we assume that at any given control iteration the effect of the DMs is small enough that they can be approximated to first order. We can thus write the electric field at the image plane at iteration $k+1$ as the electric field in the previous iteration plus the linearized effect of the DM:

$$\begin{aligned} \mathbf{e}_{DH,k+1} &\approx \mathbf{e}_{DH,k} + \Delta\mathbf{e}_{\mathbf{u}} \\ &= \mathbf{e}_{DH,k} + \mathbf{G}\Delta\mathbf{u}, \end{aligned} \tag{4.2}$$

where $\mathbf{G}$ is the Jacobian of the system with respect to $\mathbf{u}$, $\mathbf{G} = \partial\mathbf{e}_{DH,k}/\partial\mathbf{u}$. The Jacobian contains the effect of each actuator over the electric field in the DH, and is computed by poking each actuator independently and recording the effect in a complex-valued, $n_{pixel}\times n_{actuator}$ matrix. Eq. 4.2 gives us the linearized relationship between the quantity of interest, $\mathbf{e}_{DH,k+1}$, and $\mathbf{u}$. We can use this expression with Eq. 4.1 to obtain the explicit expression of J as a function of $\Delta\mathbf{u}$, from which we can derive and apply $\partial J/\partial\Delta\mathbf{u} = 0$.

$$\mathbf{G}^{\mathsf{H}}\mathbf{G}\Delta\mathbf{u} = -\mathcal{R}\{\mathbf{G}\mathbf{e}_{DH,k}\} \tag{4.3}$$

[1] https://github.com/ajeldorado/falco-matlab, https://github.com/ajeldorado/falco-python

We solve for $\Delta\mathbf{u}$ with these equations via least squares. In practice, to ensure stability given that the problem is ill-posed, a common modification is to add Tikhonov regularization:

$$J = \mathbf{e}_{DH,k+1}^{\mathsf{H}}\mathbf{e}_{DH,k+1} + \alpha\Delta\mathbf{u}^{\intercal}\Delta\mathbf{u}, \tag{4.4}$$

where α is usually expressed as $\alpha = \alpha_0 \times 10^{\beta}$, α_0 being a scaling factor and $\beta \in \mathbb{R}$ an exponential scaling term. Including the regularization, Eq. 4.3 becomes

$$(\mathbf{G}^{\mathsf{H}}\mathbf{G} + \alpha\mathcal{I})\Delta\mathbf{u} = \mathcal{R}\{\mathbf{G}\mathbf{e}_{DH,k}\}, \tag{4.5}$$

where $\mathcal{I}$ is the identity matrix.

Using EFC as a Coronagraph Design Tool

Although EFC was conceived as a wavefront control algorithm, its formalism applies for any surface in the optical train as long as the difference in surface heights at each iteration is small, and the effect in the electric field in the DH can be linearized. Therefore, this algorithm can be used to design a coronagraph: the control vector $\mathbf{u}$ can be generalized to contain any degrees of freedom given by the designer to affect the optical propagation through the system. For instance, the cumulative control vector $\mathbf{u}$ can contain the actuators of two DMs and the parametrization of a focal plane mask's complex transmission:

$$\mathbf{u} = \begin{bmatrix} \mathbf{u}_{DM1} \\ \mathbf{u}_{DM2} \\ \mathbf{u}_{FPM} \\ \cdots \end{bmatrix} \tag{4.6}$$

Thus, the features of a hypothetical focal plane mask can be iteratively adjusted in the same way as the DM actuator heights as shown above. It is used in particular for the design of hybrid Lyot coronagraphs (HLCs), which consist of a Lyot coronagraph plus a complex-valued focal plane mask. We follow this approach in this paper.

4.3 Modifying the Cost Function

The standard EFC cost function in Eq. 4.4 is concerned only with the intensity in the DH, and ignores other key quantities that directly drive the performance of a coronagraph, namely: the throughput of an off-axis source in the DH, and the sensitivity to low-order aberrations. For the latter, a possible solution is to add channels to the electric field vector $\mathbf{e}_{DH}$ in the same way we would add wavelengths for a broadband problem (Give'on et al., 2007), but instead we add Zernike polynomials to the entrance pupil (A. E. Riggs et al., 2019). This allows the algorithm to simultaneously minimize intensity and sensitivity to low-order aberrations. As for the throughput of an off-axis source, we show in this section some modifications to the cost function to account for it.

Adding the total DM Stroke

A typical EFC design run for an HLC takes hundreds of iterations to attain the desirable DM and FPM solution in terms of raw contrast in the DH. Usually, the first iterations tackle the *easy* control modes, which require lower spatial frequencies and smaller DM stroke. At later iterations the *hard* modes are addressed. To identify easy and hard modes we do a singular value decomposition of the Jacobian matrix: the modes associated with higher energy singular values are easier to control, thus denoted easy. The modes linked lower singular values are harder or even inaccessible. The easy modes are tackled first, heavily reducing the raw contrast. When the harder modes are addressed, the DM is required to add higher frequencies in its pattern. At each iteration, the raw contrast decreases at a slower rate while rapidly increasing the RMS stroke of the DMs. The DM stroke is crudely correlated to a loss in throughput and higher sensitivity to tip and tilt errors. However, two-DM solutions often cancel each others' phase effects leaving amplitude effects, yielding less reduction in Strehl than the RMS actuator heights might otherwise produce.

A straightforward way of controlling the DM stroke is by adding a term in the EFC cost function that explicitly punishes adding excessive stroke:

$$J = \mathbf{e}_{k+1}^{\mathsf{H}} \mathbf{e}_{k+1} + \alpha \Delta \mathbf{u}^{\intercal} \Delta \mathbf{u} + \gamma \mathbf{u}^{\intercal} \mathbf{u} \tag{4.7}$$

The real-valued scalar γ regulates the strength of this new term. The total stroke being added explicitly in $\mathbf{u}^{\intercal}\mathbf{u}$ allows us to control an important parameter heavily linked to the coronagraph performance. This approach, however, has its limitations, as will be shown in Sec. 4.4. The corresponding expression for Δu in the $k+1$ iteration is:

$$\Delta \mathbf{u} = (\mathbf{G}^{\mathsf{H}} \mathbf{G} + (\alpha + \gamma) \mathcal{I})^{-\dagger} Re\{\mathbf{G}^{\mathsf{H}} \mathbf{e}_k \ + \gamma \mathbf{u}\} \tag{4.8}$$

It is worth noting that the wavefront control technique stroke minimization (Pueyo et al., 2009) and this modification to EFC are different. Moreover, stroke minimization and EFC have the same mathematical solution as EFC in Eq. 4.4, i.e. when using the Tikhonov regularization (Groff et al., 2016).

Adding the Throughput Explicitly

Another more sophisticated way of dealing with the loss of throughput is to include the change in throughput, $\Delta\mathbf{t}$, of the k^{th} iteration explicitly:

$$J = \mathbf{e}_{k+1}^{\mathsf{H}}\mathbf{e}_{k+1} + \alpha\Delta\mathbf{u}^{\intercal}\Delta\mathbf{u} + \gamma\mathbf{u}^{\intercal}\mathbf{u} - \omega\Delta\mathbf{t}^{\intercal}\Delta\mathbf{t} \tag{4.9}$$

The term $-\omega\Delta\mathbf{t}^{\intercal}\Delta\mathbf{t}$ penalizes the loss of throughput, where ω is a real-valued coefficient to regulate the strength of this term; $\mathbf{t}$ is a one-element vector in order to keep the same notation. In our optics model of the system $\Delta\mathbf{t}$ can be computed as a function of $\Delta\mathbf{u}$. Indeed, in the same way we did in Eq. 4.2 where the change of the electric field vector was expressed in terms of $\Delta\mathbf{u}$, we can do the same for the change in throughput:

$$\Delta\mathbf{t} = \mathbf{G}_{cp}\Delta\mathbf{u}, \tag{4.10}$$

where $\mathbf{G}_{cp}$ is the Jacobian of the system for the intensity of the central pixel of an unobscured PSF; cp in the subindex stands for *central pixel*. The peak intensity of an unobscured PSF is directly proportional to the throughput of the system. $\mathbf{G}_{cp}$ is computed in a similar way as the original Jacobian, as explained in Sec. 4.2, this time evaluating the peak electric field of the unobscured PSF.

From Eq. 4.9, we can express the solution for $\Delta\mathbf{u}$ for the $k+1$ iteration:

$$\Delta\mathbf{u} = (\mathbf{G}^{\mathsf{H}}\mathbf{G} + (\alpha+\gamma)\mathcal{I} - \omega\mathbf{G}_{cp}^{\mathsf{H}}\mathbf{G}_{cp})^{-\dagger}Re\{\mathbf{G}^{\mathsf{H}}\mathbf{e}_k + \gamma\mathbf{u}\}. \tag{4.11}$$

Peak-Normalized Intensity

Another way of adding the throughput constraint to the EFC cost function is by normalizing the dark hole intensity to the unocculted peak intensity. This value is closer to a key design parameter–the ratio of starlight detected to planet light detected squared, η_s/η_p^2, which is the main driver of the detectable planet yield of a mission. The peak unobscured PSF intensity is directly proportional to the system's throughput. We can write the cost function to minimize as:

$$J = (\mathbf{e}_{k+1}/p_{k+1})^{\mathsf{H}}(\mathbf{e}_{k+1}/p_{k+1}), \tag{4.12}$$

where p is a complex-valued scalar representing the peak electric field of the unocculted PSF. The Jacobian for this case is denoted $\mathbf{G_{pn}} = \partial(\mathbf{e}_k/p_k)/\partial\mathbf{u}$. We adopt an analogous linear assumption to that of conventional EFC, as in Eq. 4.2. Therefore, since the cost function J has the same form as seen in Eq. 4.1, we can rewrite Eq. 4.5 as:

$$\Delta\mathbf{u} = (\mathbf{G_{pn}}^{\mathsf{H}}\mathbf{G_{pn}} + \alpha\mathcal{I})^{-\dagger}Re\{\mathbf{G_{pn}}^{\mathsf{H}}\mathbf{e}_k/p_k\}. \tag{4.13}$$

To compute the new Jacobian $\mathbf{G_{pn}}$ we need to apply the chain rule:

$$\mathbf{G_{pn}} = \frac{\partial\mathbf{e}_k}{\partial\mathbf{u}}/p_k - \mathbf{e}_k/p_k^2\frac{\partial p_k}{\partial\mathbf{u}}. \tag{4.14}$$

The term $\frac{\partial\mathbf{e}_k}{\partial\mathbf{u}}$ is simply $\mathbf{G}$, as seen previously. To derive the term $\frac{\partial p_k}{\partial\mathbf{u}}$ we do as in Sec. 4.3 when we derived a separate Jacobian, $\mathbf{G_{cp}}$, for the changes in the peak, or central pixel, of the unocculted PSF.

4.4 Design Optimization

Our Case Study: the Roman Coronagraph HLC

The work presented in this paper was done in the context of optimizing the design for the Roman Coronagraph HLC. Using this coronagraph case to test the techniques described in Sec. 7.2 serves as a way to illustrate how difficult the problem of optimizing a coronagraph is in practice.

The Roman Space Telescope has certain characteristics that make it particularly challenging for high contrast imaging (J. Trauger, Moody, Krist, et al., 2016; Kasdin, Bailey, et al., 2020). Specifically, the central obscuration is relatively large (~30% of pupil diameter), and the six struts are several times wider (with widths of 3.2% of pupil diameter) than for any proposed mission concepts for high-contrast imaging. Discontinuities in the pupil and especially central obscurations heavily affect the performance of the system (Stark et al., 2019). The pupil version that we use is not the final, slightly asymmetric one. Instead, we use an earlier, on-axis version with 3-fold azimuthal symmetry and a perfectly circular central obscuration. Another limitation from the Roman Coronagraph that we do not consider in our study is the

DM surface stroke RMS requirement, i.e. the limit of how big the actuation of the DM actuators can be. We limit ourselves to the DM technical capabilities instead.

The specifications and other coronagraph parameters are shown in Table 4.1. Given the current mission specifications, our target contrast is 10^{-9} normalized intensity (NI). The mission specifications and predicted performance are available online[2]. The choice of Polymethylglutarimide (PMGI) as the dielectric is driven by the MDL's current HLC manufacturing capabilities; PMGI outside of the occulter mask results in incoherent light, so we limit the inclusion of dielectric to the occulter mask only. Dielectric deposition on the mask and shaping technologies limit what dielectric material is to be used (J. Trauger, Moody, Gordon, et al., 2012; Balasubramanian et al., 2013); other materials have been considered for this application (J. Trauger, Moody, and Gordon, 2013; J. Trauger, Moody, Krist, et al., 2016), we however limit ourselves to the Roman Coronagraph material. The resolution at the pupil planes drives the computing time; we compute the minimum resolution to give a reliable result at high contrast to be ~200 pixels across the pupil and use 250 pixels for margin. We use a thin-film model for the dielectric material and the metal spot in the FPM since using a complex transmission matrix and then converting the resulting matrix to a real material model is not possible in practice without losing the resultant FPM performance. We measure the contrast level with the normalized intensity, here defined as the mean intensity in the dark hole normalized to the peak intensity of the unobstructed PSF, i.e. with the FPM out of the beam, and the DMs in their current configuration. We define the throughput as the total energy within half-max isophote for a PSF offset 6 λ/D from on-axis divided by the total energy at the telescope pupil; losses from the reflectivity and transmissivity of optical surfaces are not included.

Artificial Gain for the Dielectric Actuator Vector

As explained in Sec. 4.2, the actuator control vector contains the information about the surface shape of the dielectric layer on the FPM. The FPM degrees of freedom in this vector have a significantly smaller effect on the contrast than the DM actuators. If left unweighted, the DMs are loaded with most of the work; at each iteration the controller puts most of the work on the DMs since, due to the linearization assumption, at the vicinity of the current actuator vector, only the DMs have any control over the contrast. The controller is thus blind to what the dielectric can actually achieve. To fix this we add an artificial gain to the actuator vector part

[2]https://roman.ipac.caltech.edu/sims/Param_db.html

Table 4.1. Roman Coronagraph HLC Design Parameters

Property	Value
Target Normalized Intensity	10^{-9}
Bandwidth	10%
Number of wavelengths during WFC	4
Evaluation of throughput angle	6 λ/D
Resolution in pupil planes	250 pixels
Resolution in FPM plane	3 pixels per λ/D
Correction inner & outer radius	2.8 & 10 λ/D
Deformable mirrors	Xinetics, 48×48 actuators
Metal material on FPM	Nickel
Dielectric material on FPM	Polymethylglutarimide (PMGI)

associated with the dielectric layer, which forces the controller to offload some of the work from the DMs to the FPM. This gain is defined as a multiplying factor (real-value and positive) that artificially augments the effect of the dielectric scaling the control solution, as well as to the Jacobian part associated with the dielectric degrees of freedom. Although the natural path seems to be better at the immediate iterations, we achieve a better contrast-throughput trade off overall when using this gain.

We find that tuning this artificial gain is a rather delicate task. For better results, the gain has to be higher at early iterations, and then it has to go back to the natural state, i.e. equal to one, so that the FPM effect does not impede going down in contrast. Indeed, the effect of the FPM is mostly to maintain throughput (see Sec. 4.4), so the effect of the dielectric has to be moderated to avoid getting stuck in a low contrast solution. A variable gain is found to be the best solution, but it has to be finely tuned to each case for every control variable set. It is beyond the scope of this paper to fine tune to the optimal solution, so we use a constant gain.

In Fig. 4.1 we show two EFC runs with its conventional cost function, one without the dielectric and one with. We use a gain of 10; without the gain the curve would closely follow the case of flat FPM. The other two curves in Fig. 4.1 are discussed in the following sections.

β-Scheduling

A common practice when using EFC for wavefront control is to have a scheduled regularization scheme in order to help with achieving a better contrast floor (Sidick et al., 2017; Seo, Cady, et al., 2017). This technique, known as β-scheduling, is explained in detail by Sidick et al. (2017). In Eq. 4.4, α is split into $\alpha = \alpha_0 \times 10^{\beta}$,

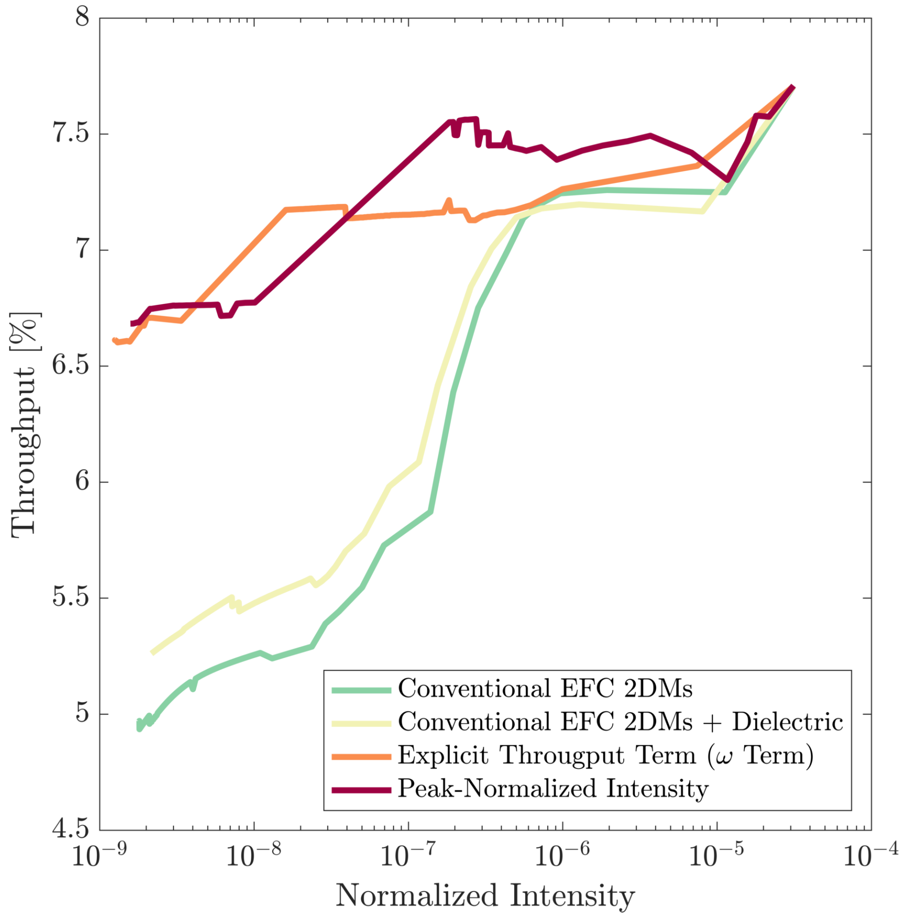

Figure 4.1 We compare different EFC cost functions to demonstrate how the methods presented in this paper can help improving the performance of a coronagraph design. With the right gain for the dielectric part of the actuator vector u, the HLC outperforms the flat FPM version. Modifying the cost function as presented in Secs. 4.3 (in Eq. 4.9) and 4.3 (in Eq. 4.12), we obtain a significant improvement (see also Table 4.3). With a more thorough treatment of the design parameters it is possible to probe more optimal areas of the parameter space; here we just illustrate the potential of the method. The DM and dielectric shapes' solutions are shown in Fig. 4.4. We do not display here the scheduled β iterations (see Sec. 4.4) to keep the figure cleaner.

where α_0 is the scaling factor and β is the exponent called out in the regularization scheduling.

The linearization performed to obtain the linear relationship between the electric field and the actuator vector (see Sec. 7.1) entails that the Jacobian of the system in this formalism intrinsically misses information. This is a form of model mismatch that also affects simulations. Indeed, although model mismatch is more severe in the case of a real system, it also affects simulations due to the linearization assumption, and results in a worse contrast floor with respect to the the actual achievable floor. A way of dealing with this is by doing β-scheduling.

To understand how β-scheduling helps with model mismatch we resort to a singular value spectrum analysis of the Jacobian, $\mathbf{G}$, for the problem laid out in Eq. 4.5. Solving for Δu, the Tikhonov regularization is to be understood as a high-pass filter that limits the controller to attack a certain amount of singular modes. The smaller (i.e., the more negative) the β, the more modes are controlled. We usually pick a β that yields the best contrast (or best contrast to throughput ratio) through a grid-search at each iteration, in which case the controller attacks bigger singular value modes, or easy modes (see Sec. 4.3), and when these are mostly done, at later iterations, the controller deals with the hard modes. A way of doing β-scheduling is by forcing the β value to be smaller than what the grid search would otherwise choose, which makes the intensity increase in the DH. However, when resuming the grid search, the contrast is significantly improved and the achievable contrast floor is lowered; this is illustrated in Fig. 6 by Sidick et al. (2017). In the singular value domain, when β is forced to small values, the intensity of the easy modes is increased, but the controller starts to deal with hard modes that were previously inaccessible. So when the controller goes back to the grid-search of β the easy modes are quickly dealt with and new hard ones are now accessible. The β-scheduling enables the carving out of harder singular modes, and thus improves the final contrast floor.

In Fig. 4.2 we illustrate the effect of performing β-scheduling by showing several EFC design runs with different schemes. By picking the right scheme, we obtain a better achievable contrast, while improving the final throughput. The design runs utilizing conventional EFC achieve an acceptable normalized intensity relatively easy. However, when modifying the cost function as seen in previous sections, a reasonable achievable contrast seems to be harder to attain. Therefore, this technique will be used when running the EFC controller for the modified cost functions.

The Tikhonov regularization is applied to the part of the Jacobian matrix associated to the DMs; there is no reason why it should not be applied to the part associated to the dielectric shape in the FPM. In Eq. 4.5, or wherever $\alpha\mathcal{I}$ is present, we substitute this term by $\mathbf{A}$, a diagonal matrix where each diagonal element is either $\alpha_{0,DM}10^{\beta_{DM}}$ or $\alpha_{0,FPM}10^{\beta_{FPM}}$. This allows us to control each regularization independently. Given the nature of the problem at hand, since the dielectric has a significantly smaller effect on the electric field in the DH with respect to the DMs, such regularization is

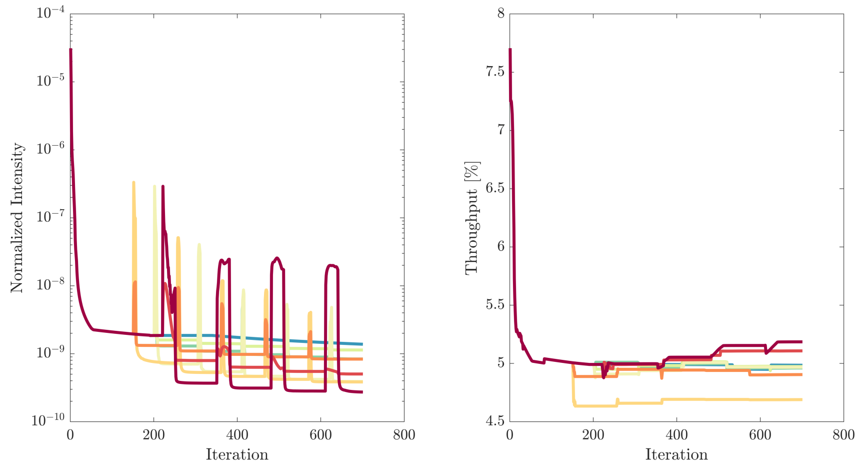

Figure 4.2 The β-scheduling helps improve the achievable contrast of the HLC design. We run several β-scheduling schemes, changing the scheduled iterations and changing the scheduled β value. The distribution of final contrast and throughput, where a better contrast does not necessarily translate into a worse throughput, speaks of the non-convexity of the problem. The cost function used for these curves is the conventional EFC cost function, shown in Eq. 4.4.

not as critical. However, since we artificially weight the dielectric effect on the DH, we rely on this new regularization as another design tool to search for the optimal coronagraph solution.

Adding the Total DM Stroke Term

As seen in Sec. 4.3, adding the γ term helps with restraining the total DM stroke, which in turn prevents an excessive loss of throughput and poor sensitivity to low-order aberrations. The effect of γ is illustrated in Fig. 4.3. For a given value of γ the effect at early iterations is relatively small, but after a certain number of iterations the run deviates from the conventional EFC curve. This is when the new term introduced in the cost function is comparable in value with the conventional EFC cost function value. In Table 4.2 we list the resultant performance metrics for different γ values. We find that γ offers a direct trade-off between achievable final contrast, and the DM stroke RMS; there appears to be an associated contrast floor that decreases monotonically with the value of γ. In all runs in Fig. 4.3 where γ is non-zero there is a change in curve direction in terms of DM surface RMS: it decreases this value when it would naturally increase. Indeed, there seems to be a point in which the γ-term initiates its effect, depending on the value of γ, up to the point of changing the curvature of the normalized intensity-DM surface RMS curve.

Table 4.2. Effect of γ in performance

γ	NI	Thput. [%]	Surf. DM1 [nmRMS]	Surf. DM2 [nmRMS]	$\lvert\Delta E\rvert^2$ for 1 nm RMS T/T
0	1.31×10^{-9}	4.82	26.55	29.36	2.2925×10^{-8}
10^{-6}	1.53×10^{-9}	5.18	20.76	22.13	2.2926×10^{-8}
10^{-5}	7.19×10^{-9}	5.45	18.13	18.98	2.2929×10^{-8}
10^{-4}	7.05×10^{-8}	6.22	14.53	14.85	2.2963×10^{-8}
10^{-3}	4.01×10^{-7}	7.02	8.91	8.93	2.3410×10^{-8}
10^{-2}	9.15×10^{-7}	6.97	7.56	7.53	2.6081×10^{-8}

A brief analysis on the units of γ can help build some intuition. Looking at Eq. 4.7, γ has units of $[NI/nm^2]$; when the normalized intensity in a design run reaches $\sim 10^{-5}$ with a DM surface RMS of $\sim$ 10 nm, it takes a γ of 10^{-2} to halt the controller from digging further. For the case of the conventional EFC cost function, we claim that there is an optimal value of γ for a given raw contrast design specification.

With other modifications of the cost function, as the ones described in Secs. 4.3 and 4.3, the EFC runs severely increase in complexity in terms of accessing different areas of the throughput-contrast space. However, the γ term effect maintains its effect of directly bounding the DM stroke RMS, which makes it a useful tool for obtaining reasonable EFC solutions. For the following sections in which we introduce more sophisticated modifications of the cost function, we work with a small value of γ that guarantees an acceptable DM stroke RMS and allows the controller to go beyond 10^{-9} in normalized intensity.

Adding the Explicit Throughput Term

Implementing the cost function in Eq. 4.9 is a direct way of bounding the loss of throughput in a similar way as done with the total stroke term (see Sec. 4.4). If the weight factor for this term, ω, is left at a fixed value, the throughput is maintained at the cost of not reaching an acceptable contrast. In practice, we leave ω as a free parameter for which a value is chosen via a grid search to give the best NI/t^2 at each iteration.

We find that this term opens a new array of accessible points in the contrast-throughput space. Depending on what the controller is allowed to do in the first iterations the grid search of the regularization (including the regularization for the dielectric actuators), and ω, and combined with the effect of the γ term, the EFC run yields a different result.

To access the best points in the contrast-throughput parameter space we require over

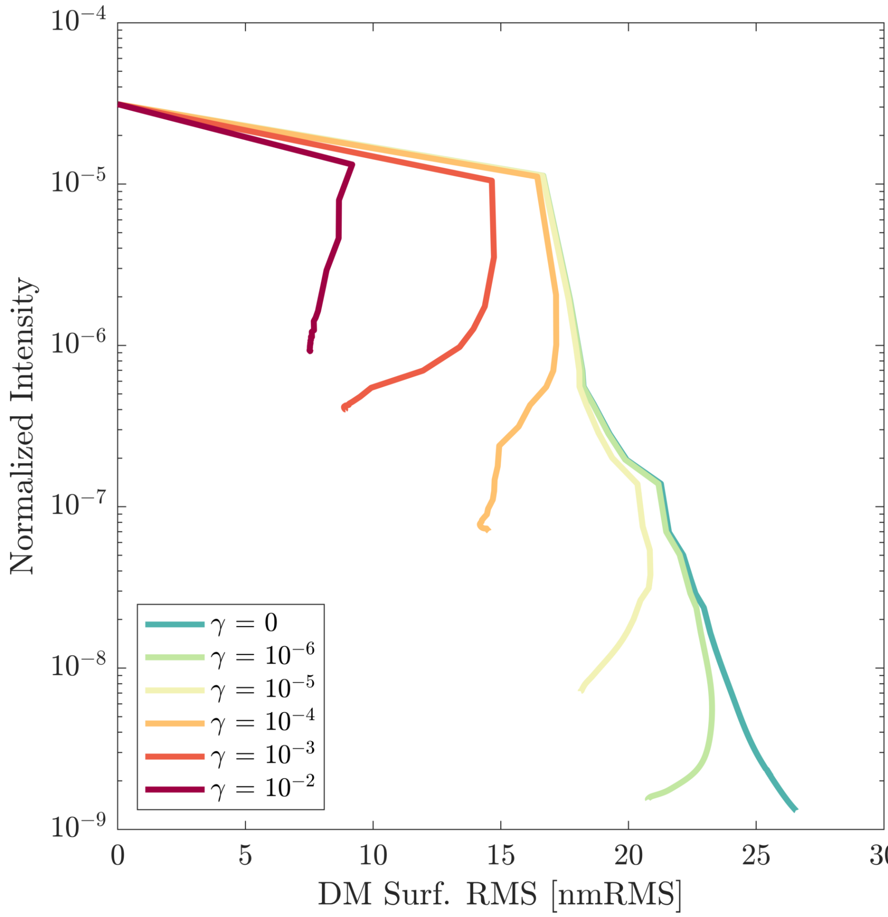

Figure 4.3 Adding the term associated with the total stroke of the DMs, the γ term, helps halt the increase in surface RMS, which in its turn helps with the throughput and sensitivity to low-order aberrations (see Table 4.2).

1000 iterations. This makes optimizing the EFC run by means of tuning several design parameters an overwhelming task. The addition of a new Jacobian for the throughput term, and the grid search over the two regularization coefficients and the ω value, makes these runs take days to complete on a powerful desktop computer.

Peak-Normalized Results

The result of implementing the cost function presented in Sec. 4.3 is shown in Fig. 4.1. For our particular problem, the controller seems to get stuck at 10^{-8} normalized intensity. We thus use the β-scheduling technique to reach better contrast results. Compared to the cost function presented in Sec. 4.3, for which the parameter ω served as a way to tweak the behaviour of the controller at every iteration, with the current cost function the user's control is more limited. We can control the final

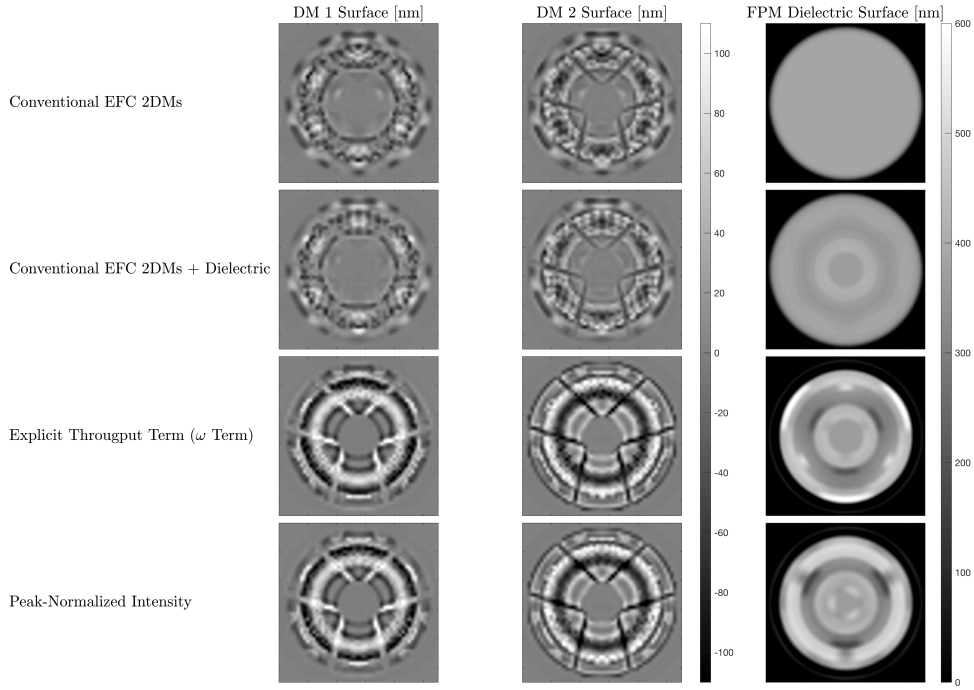

Figure 4.4 The DM shapes and dielectric layer shape solutions depend significantly on the design run and method used. The shapes displayed here correspond to the curves shown in Fig. 4.1. The throughput-conserving terms cause more pupil remapping (Guyon, Pluzhnik, Galicher, et al., 2005) to occur, as can be seen in the DM shapes.

Table 4.3. Performance comparison between different changes in the cost function.

Design Run Type	NI	Thput. [%]	DM1 [nmRMS]	DM2 [nmRMS]	$\lvert\Delta E\rvert^2$ 1nmRMS T/T
Conv. EFC 2DMs	1.79×10^{-9}	4.97	25.88	28.56	2.29×10^{-8}
Conv. EFC 2DMs + Diel.	2.16×10^{-9}	5.26	24.75	27.04	2.16×10^{-8}
Explicit Thput. Term (ω)	1.25×10^{-9}	6.61	46.16	47.00	1.34×10^{-8}
Peak-Normalized Int.	1.58×10^{-9}	6.68	44.90	46.10	2.67×10^{-8}

point in the throughput-contrast space by modifying the weight of the dielectric actuator vector, combined with the β-schedule and regularization for the dielectric vector, and γ value. However, these parameters seem to have a limited effect on the final reach in terms of throughput-contrast. The lack of a parameter equivalent to ω or γ makes this method harder to tune; for instance, these terms can be used to emphasize the throughput early or later on. However, this method is easier to implement since it does not require a multidimensional tuning.

4.5 Discussion

Problems with the linear approach

As hinted by the results presented in Sec. 7.5 the complexity of the problem at hand is titanic. Some of the reasons we identify are: (1) the high number of free variables; the DMs consist of two times 48×48 free variables, and the dielectric actuator vector although of arbitrary size, adds on the order of 200 variables. (2) the amount of controller variables, e.g. β at each iteration (see Sec. 4.4), γ (see Sec. 4.4), the weight gain on the dielectric vector (see Sec. 4.4), etc. (3) the competing nature of contrast and throughput; for the most part the gain on one is at the loss of the other. Furthermore, we are required to achieve an acceptable level of sensitivity pointing jitter. (4) The DM influence function: its tail effect, or cross talk, results in a loss of orthogonality of the DM effect. (5) The material properties of the dielectric and metal layers at the FPM, where amplitude and phase control are entangled.

Another complication comes from the limitations associated with the algorithm used, the most important of which is the linear approximation. The assumption that the step size in the DM commands is small is good enough a priori since, although some information is lost in second order effects that are not accounted for, these are fixed in further iterations, or even when doing the β-scheduling that corrects for model mismatch. However, particularly during the first iterations, when the step size is the highest given the energy displacement required, the controller places itself in a point that it did not intend given the linear assumption. This influences the following steps and, ultimately, where the controller ends in the throughput-contrast space. In particular, we find that the first iteration heavily affects where the controller follows in the throughput-contrast parameter space.

Hence, there are a large array of possibilities attainable in terms of solutions that provide an acceptable design. To illustrate this we show in Fig. 4.4 the shape solutions for the DMs and dielectric surfaces for the optimization runs of Fig. 4.1. The controller arrives at very different solutions depending on the cost function. We find that even when the cost function is the same, when tweaking certain parameters, e.g. the weighting of the dielectric actuator vector or the β-scheduling, the resulting solutions are different as well.

All of these factors contribute to making finding an optimal design a tremendous task. A solution to mitigate the problems associated with the linear approach is to use a non-linear algorithm. We have been exploring the L-BFGS-B algorithm, which has been implemented for phase retrieval (Jurling et al., 2014) providing a framework for the problem of high contrast imaging. Recently, Will et al. (2021) introduced this framework in the context of wavefront control as an alternative to EFC.

Impact of Complex Transmission in the FPM on Performance

In Fig. 4.1 we plot two conventional EFC runs: one with the actuator dielectric vector, the other without. By choosing the right artificial weight for the dielectric actuator vector (see Sec. 4.4), the runs with the dielectric perform consistently better. In the worst case, when the weight is not correctly tuned, the performance is similar to the 2 DMs only, but never worse. We find that the dielectric shape has relatively little effect on the final achievable contrast: when leaving the natural effect of the dielectric actuator vector, i.e. weight equals 1, it effectively has little effect. However, the weight helps the controller find different routes in the throughput-contrast space that end up making the dielectric do some of the work, in particular it helps with the interaction between the DMs and the Lyot stop, assisting in re-shaping the diffracted light from the struts and central obscuration into the Lyot stop. Intuitively, an additional shaped surface at the FPM helps alleviate some of the work done by the DMs. This results in a smaller stroke RMS from which a better throughput and sensitivity to jitter follow.

When accounting for the throughput in the cost function, the role of the dielectric is enhanced. The FPM now re-arranges the electric field shape at the center of the PSF attempting to retain the intensity at the center. We speculate that the dielectric, in a similar way to how it helps with the interaction of the DMs and the Lyot stop, helps reshape the PSF to interact with the part of the Lyot stop corresponding to the central obscuration in such a way that it would result in a better sensitivity.

The disparate possibilities for the dielectric shape solutions seen in Fig. 4.4 indicate that there are complex dependencies with design parameters as discussed in Sec. 4.5, and intricate interactions with the DMs. However, there seems to always be certain features on a 3-fold azimuthal symmetry associated with the strut obscurations. Ultimately, there is still much to learn on how shaping the FPM can improve performance, and how it may be used to improve the performance of future instruments.

In this work we have limited the dielectric to the current manufacturing process limits; with sharper features than currently allowed there is more room for improvement. The manufacturing process also prevents the shaping of the metal layer and using a different dielectric other than PMGI.

4.6 Conclusion

We have presented a set of tools to perform coronagraph design with the EFC algorithm. The modifications to the EFC cost function directly assist in trading off contrast, throughput, and low-order aberration sensitivities, and yield better results compared to a conventional use of EFC. We showed how, with these modifications, the controller can access the more optimal areas in the performance parameter space with careful treatment of the design run parameters. The improvements shown here amount to ~35% gain in throughput for the same normalized intensity; however, we believe there is significant room for improvement with a more thorough tuning of parameters. Some of the main findings of this work can be summarized as:

- The modifications to the EFC cost function help probe more optimal areas of the throughput-normalized intensity space.
- The explicit addition of a throughput term to the cost function (see Sec. 4.3) provides significant improvement in terms of achievable normalized intensity and throughput. It is, however, nontrivial to tune.
- The peak-normalized intensity modification to the cost function (see Sec. 4.3) is easier to tune, and also provides similar improvement in terms of normalized intensity and throughput. However, the lack of parameters to tune results in a more limited adjustment potential by the designer.
- We present the DM stroke term, or γ term, that helps with contain the throughput loss in a design run. We review the β-scheduling method that deals with model uncertainty.
- We discuss the potential and limitations of adding a designable complex transmission to the focal plane mask. This coronagraph element can re-shape the PSF to optimize the throughput with nontrivial interactions with the DMs and the Lyot stop.

One of the main limitation to these methods is the linear approximation, which hinders the controller of finding the optimal path given its limited capacity of probing the right areas in the design parameter space. A non-linear approach could address this issue and will be the subject of future work.

4.7 Appendix

Lyot Stop Size effects on Contrast and Throughput

In the Roman Coronagraph HLC, and in general in any coronagraph, the interplay between optical elements and final performance is very complex. For instance, the Lyot stop shape plays a big role in how easy is for the DMs to cancel the unwanted starlight, and has a big impact on the throughput. Although intuitively a bigger Lyot stop, i.e. a Lyot stop that blocks more light, would help driving the contrast down, the opposite effect eventually occurs: with a big Lyot stop there is not enough light in certain areas to destructively interfere at the final plane. To illustrate the complex interactions that take place we show how the Lyot stop size affects the contrast and throughput for the Roman Coronagraph case in Figs. 4.5 and 4.6. To obtain this we performed a survey of EFC runs, with a conventional cost function, for several combinations of the Lyot stop inner diameter (LSID) and outer diameter (LSOD). Some runs did not finish for unknown reasons are displayed as minus infinite in the figures.

4.8 Acknowledgments

This work was partially supported by the National Science Foundation AST-ATI Grant 1710210. The material is based upon work supported by NASA SAT under award No. 80NSSC20K0624. Part of this work was carried out at the Jet Propulsion Laboratory, California Institute of Technology, under contract with the National Aeronautics and Space Administration (NASA).

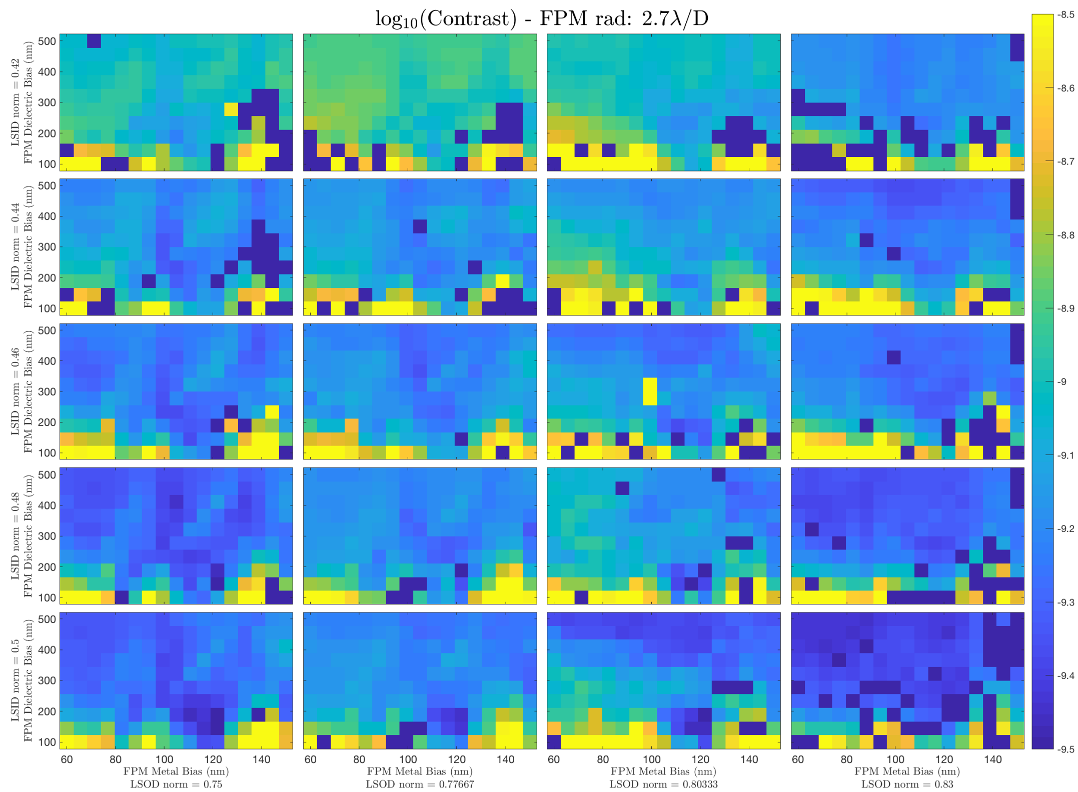

Figure 4.5 The complex interplay between optical elements in coronagraph design makes it very challenging to find a global optimal solution. To illustrate this we show here the interplay between the size of the Lyot stop (the inner radius, LSID, and the outer radius, LSOD), the FPM metal layer height, and the FPM dielectric bias height, and how it affects the final contrast after a EFC design run.

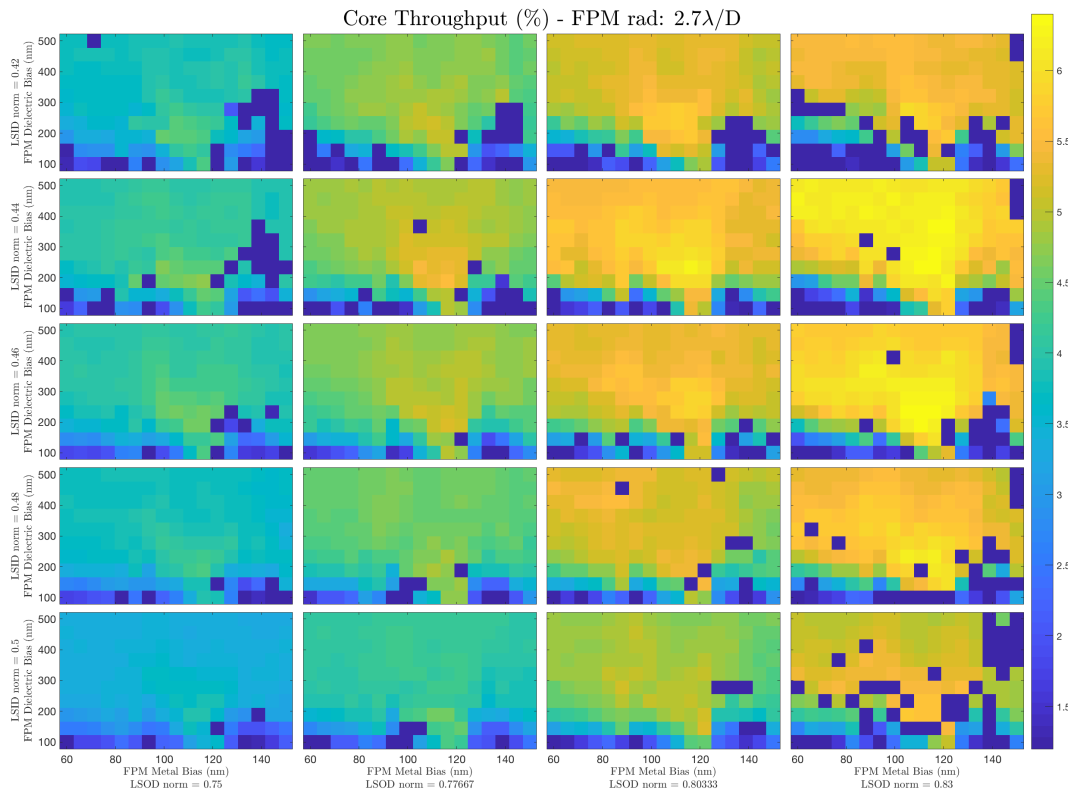

Figure 4.6 Same as Fig. 4.5 for the throughput.

BIBLIOGRAPHY

Balasubramanian, K. et al. (2013). “High contrast internal and external coronagraph masks produced by various techniques ”. In: *Techniques and Instrumentation for Detection of Exoplanets VI*. Ed. by S. Shaklan. Vol. 8864. International Society for Optics and Photonics. SPIE, pp. 644–652. URL: https://doi.org/10.1117/12.2024615.

Belikov, R. et al. (Jan. 2019). “Theoretical Limits for Exoplanet Detection with Coronagraphs on Obstructed Apertures”. In: *American Astronomical Society Meeting Abstracts #233*. Vol. 233. American Astronomical Society Meeting Abstracts, p. 237.02.

Codona, J. L. and R. Angel (Apr. 2004). “Imaging Extrasolar Planets by Stellar Halo Suppression in Separately Corrected Color Bands”. In: *Astrophysical Journal, Letters* 604.2, pp. L117–L120. DOI: 10.1086/383569. arXiv: astro-ph/0402420 [astro-ph].

Crill, B. P. and N. Siegler (2017). “Space technology for directly imaging and characterizing exo-Earths”. In: *UV/Optical/IR Space Telescopes and Instruments: Innovative Technologies and Concepts VIII*. Ed. by H. A. MacEwen and J. B. Breckinridge. Vol. 10398. International Society for Optics and Photonics. SPIE, pp. 175–195. URL: https://doi.org/10.1117/12.2275697.

Davis, J. et al. (2018). “HabEx polarization ray trace and aberration analysis”. In: *Space Telescopes and Instrumentation 2018: Optical, Infrared, and Millimeter Wave*. Ed. by M. Lystrup et al. Vol. 10698. International Society for Optics and Photonics. SPIE, pp. 1021–1039. URL: https://doi.org/10.1117/12.2313670.

Foo, G., D. M. Palacios, and G. A. Swartzlander (2005). “Optical vortex coronagraph”. In: *Opt. Lett.* 30, pp. 3308–3310. DOI: 10.1364/OL.30.003308.

Give’On, A. (2009). “A unified formailism for high contrast imaging correction algorithms”. In: *Proc. SPIE* 7440, p. 74400D. DOI: 10.1117/12.825049.

Give’on, A. et al. (2007). “Broadband wavefront correction algorithm for high-contrast imaging systems”. In: *Astronomical Adaptive Optics Systems and Applications III*. Ed. by R. K. Tyson and M. Lloyd-Hart. Vol. 6691. International Society for Optics and Photonics. SPIE, pp. 63–73. URL: https://doi.org/10.1117/12.733122.

Groff, T. D. et al. (2016). “Methods and limitations of focal plane sensing, estimation, and control in high-contrast imaging”. In: *J. Astron. Telesc. Instrum. Syst.* 2.1, p. 011009. DOI: 10.1117/1.JATIS.2.1.011009.

Guyon, O., E. A. Pluzhnik, M. J. Kuchner, et al. (Nov. 2006). "Theoretical Limits on Extrasolar Terrestrial Planet Detection with Coronagraphs". In: *Astrophysical Journal, Supplement* 167.1, pp. 81–99. DOI: 10.1086/507630. arXiv: astro-ph/0608506 [astro-ph].

Guyon, O., E. A. Pluzhnik, R. Galicher, et al. (Mar. 2005). "Exoplanet Imaging with a Phase-induced Amplitude Apodization Coronagraph. I. Principle". In: *Astrophysical Journal* 622.1, pp. 744–758. DOI: 10.1086/427771. arXiv: astro-ph/0412179 [astro-ph].

Jewell, J. et al. (2017). "Optimization of coronagraph design for segmented aperture telescopes". In: *Proc. SPIE* 10400, 104000H. DOI: 10.1117/12.2274574. URL: https://doi.org/10.1117/12.2274574.

Jurling, A. S. and J. R. Fienup (July 2014). "Applications of algorithmic differentiation to phase retrieval algorithms". In: *J. Opt. Soc. Am. A* 31.7, pp. 1348–1359. DOI: 10.1364/JOSAA.31.001348. URL: http://josaa.osa.org/abstract.cfm?URI=josaa-31-7-1348.

Kasdin, N. J., V. P. Bailey, et al. (2020). "The Nancy Grace Roman Space Telescope Coronagraph Instrument (CGI) technology demonstration". In: *Space Telescopes and Instrumentation 2020: Optical, Infrared, and Millimeter Wave*. Ed. by M. Lystrup et al. Vol. 11443. International Society for Optics and Photonics. SPIE, pp. 300–313. URL: https://doi.org/10.1117/12.2562997.

Kasdin, N. J., R. J. Vanderbei, et al. (Jan. 2003). "Extrasolar Planet Finding via Optimal Apodized-Pupil and Shaped-Pupil Coronagraphs". In: *Astrophysical Journal* 582.2, pp. 1147–1161. DOI: 10.1086/344751.

Krist, J. et al. (2019). "Numerical modeling of the Habex coronagraph". In: *Techniques and Instrumentation for Detection of Exoplanets IX*. Ed. by S. B. Shaklan. Vol. 11117. International Society for Optics and Photonics. SPIE, pp. 85–100. URL: https://doi.org/10.1117/12.2530462.

Kuchner, M. J. and W. A. Traub (May 2002). "A Coronagraph with a Band-limited Mask for Finding Terrestrial Planets". In: *Astrophysical Journal* 570.2, pp. 900–908. DOI: 10.1086/339625. arXiv: astro-ph/0203455 [astro-ph].

Marx, D. et al. (2017). "Electric field conjugation in the presence of model uncertainty". In: *Proc. SPIE* 10400, 104000P. DOI: 10.1117/12.2274541.

Mawet, D. et al. (2005). "Annular Groove Phase Mask Coronagraph". In: *Astrophys. J.* 633, pp. 1191–1200. DOI: 10.1086/462409.

N'Diaye, M. et al. (Feb. 2016). "Apodized Pupil Lyot Coronagraphs for Arbitrary Apertures. V. Hybrid Shaped Pupil Designs for Imaging Earth-like planets with Future Space Observatories". In: *ApJ* 818.2, 163, p. 163. DOI: 10.3847/0004-637X/818/2/163. arXiv: 1601.02614 [astro-ph.IM].

Por, E. H. (Jan. 2020). "Phase-apodized-pupil Lyot Coronagraphs for Arbitrary Telescope Pupils". In: *Astrophysical Journal* 888.2, 127, p. 127. DOI: 10.3847/1538-4357/ab3857. arXiv: 1908.02585 [astro-ph.IM].

Prada, C. M., E. Serabyn, and F. Shi (2019). "High-contrast imaging stability using MEMS deformable mirror". In: *Techniques and Instrumentation for Detection of Exoplanets IX*. Ed. by S. B. Shaklan. Vol. 11117. International Society for Optics and Photonics. SPIE, pp. 112–118. URL: https://doi.org/10.1117/12.2525628.

Pueyo, L. et al. (Nov. 2009). "Optimal dark hole generation via two deformable mirrors with stroke minimization". In: *Appl. Opt.* 48.32, pp. 6296–6312. DOI: 10.1364/AO.48.006296. URL: http://ao.osa.org/abstract.cfm?URI=ao-48-32-6296.

Riggs, A. J. E. et al. (Aug. 2018). "Fast linearized coronagraph optimizer (FALCO) I: a software toolbox for rapid coronagraphic design and wavefront correction". In: *Space Telescopes and Instrumentation 2018: Optical, Infrared, and Millimeter Wave*. Vol. 10698. Society of Photo-Optical Instrumentation Engineers (SPIE) Conference Series, p. 106982V. DOI: 10.1117/12.2313812.

Riggs, A. E., G. Ruane, and B. D. Kern (2019). "Directly constraining low-order aberration sensitivities in the WFIRST coronagraph design". In: *Techniques and Instrumentation for Detection of Exoplanets IX*. Ed. by S. B. Shaklan. Vol. 11117. International Society for Optics and Photonics. SPIE, pp. 136–149. URL: https://doi.org/10.1117/12.2529588.

Ruane, G., A. J. Riggs, et al. (Aug. 2018). "Review of high-contrast imaging systems for current and future ground- and space-based telescopes I: coronagraph design methods and optical performance metrics". In: *Space Telescopes and Instrumentation 2018: Optical, Infrared, and Millimeter Wave*. Ed. by M. Lystrup et al. Vol. 10698. Society of Photo-Optical Instrumentation Engineers (SPIE) Conference Series, 106982S. DOI: 10.1117/12.2312948. arXiv: 1807.07042 [astro-ph.IM].

Ruane, G., D. Echeverri, et al. (Oct. 2020). "Microelectromechanical deformable mirror development for high-contrast imaging, part 2: the impact of quantization errors on coronagraph image contrast". In: *Journal of Astronomical Telescopes, Instruments, and Systems* 6, 045002, p. 045002. DOI: 10.1117/1.JATIS.6.4.045002. arXiv: 2010.03704 [astro-ph.IM].

Ruane, G., J. Jewell, et al. (July 2016). "Apodized vortex coronagraph designs for segmented aperture telescopes". In: *Proceedings of the SPIE*. Vol. 9912. Society of Photo-Optical Instrumentation Engineers (SPIE) Conference Series, p. 99122L. DOI: 10.1117/12.2231715. arXiv: 1607.06400 [astro-ph.IM].

Seo, B.-J., E. Cady, et al. (2017). "Hybrid Lyot coronagraph for WFIRST: high-contrast broadband testbed demonstration". In: *Techniques and Instrumentation for Detection of Exoplanets VIII*. Ed. by S. Shaklan. Vol. 10400. International

Society for Optics and Photonics. SPIE, pp. 106–126. URL: https://doi.org/10.1117/12.2274687.

Seo, B.-J., K. Patterson, et al. (2019). "Testbed demonstration of high-contrast coronagraph imaging in search for Earth-like exoplanets". In: *Techniques and Instrumentation for Detection of Exoplanets IX*. Ed. by S. B. Shaklan. Vol. 11117. International Society for Optics and Photonics. SPIE, pp. 599–609. URL: https://doi.org/10.1117/12.2530033.

Shaklan, S. et al. (Sept. 2019). "Status of Space-based Segmented-Aperture Coronagraphs for Characterizing Exo-Earths Around Sun-Like Stars". In: *Bulletin of the American Astronomical Society*. Vol. 51, p. 211.

Sidick, E. et al. (2017). "Optimizing the regularization in broadband wavefront control algorithm for WFIRST coronagraph". In: *Techniques and Instrumentation for Detection of Exoplanets VIII*. Ed. by S. Shaklan. Vol. 10400. International Society for Optics and Photonics. SPIE, pp. 587–599. URL: https://doi.org/10.1117/12.2274440.

Soummer, R. (Jan. 2005). "Apodized Pupil Lyot Coronagraphs for Arbitrary Telescope Apertures". In: *Astrophysical Journal, Letters* 618.2, pp. L161–L164. DOI: 10.1086/427923. arXiv: astro-ph/0412221 [astro-ph].

Soummer, R. et al. (Mar. 2011). "Apodized Pupil Lyot Coronagraphs for Arbitrary Apertures. III. Quasi-achromatic Solutions". In: *ApJ* 729.2, 144, p. 144. DOI: 10.1088/0004-637X/729/2/144.

Stark, C. C. et al. (Apr. 2019). "ExoEarth yield landscape for future direct imaging space telescopes". In: *Journal of Astronomical Telescopes, Instruments, and Systems* 5, 024009, p. 024009. DOI: 10.1117/1.JATIS.5.2.024009. arXiv: 1904.11988 [astro-ph.EP].

The HabEx Team (2019). *The HabEx Final Report*. https://www.jpl.nasa.gov/habex/pdf/HabEx-Final-Report-Public-Release-LINKED-0924.pdf.

The LUVOIR Team (2019). *The Large UV Optical Infrared Surveyor (LUVOIR) final report*. https://asd.gsfc.nasa.gov/luvoir/resources/docs/LUVOIR_FinalReport_2019-08-26.pdf.

Trauger, J., D. Moody, and B. Gordon (Sept. 2013). "Complex apodized Lyot coronagraph for exoplanet imaging with partially obscured telescope apertures". In: *Proc.SPIE*. Vol. 8864. URL: https://doi.org/10.1117/12.2024795.

Trauger, J., D. Moody, B. Gordon, et al. (2012). "Complex apodization Lyot coronagraphy for the direct imaging of exoplanet systems: design, fabrication, and laboratory demonstration". In: *Space Telescopes and Instrumentation 2012: Optical, Infrared, and Millimeter Wave*. Ed. by M. C. Clampin et al. Vol. 8442. International Society for Optics and Photonics. SPIE, pp. 1589–1601. URL: https://doi.org/10.1117/12.926663.

Trauger, J., D. Moody, J. Krist, et al. (Jan. 2016). “Hybrid Lyot coronagraph for WFIRST-AFTA: coronagraph design and performance metrics”. In: *Journal of Astronomical Telescopes, Instruments, and Systems* 2, 011013, p. 011013. DOI: 10.1117/1.JATIS.2.1.011013.

Trauger, J. T. and W. A. Traub (Apr. 2007). “A laboratory demonstration of the capability to image an Earth-like extrasolar planet”. In: *Nature* 446.7137, pp. 771–773. DOI: 10.1038/nature05729.

Will, S. D., T. D. Groff, and J. R. Fienup (Jan. 2021). “Jacobian-free coronagraphic wavefront control using nonlinear optimization”. In: *Journal of Astronomical Telescopes, Instruments, and Systems* 7, 019002, p. 019002. DOI: 10.1117/1.JATIS.7.1.019002.

Zhou, H. et al. (2020). “Roman CGI testbed HOWFSC modeling and validation”. In: *Space Telescopes and Instrumentation 2020: Optical, Infrared, and Millimeter Wave*. Ed. by M. Lystrup et al. Vol. 11443. International Society for Optics and Photonics. SPIE, pp. 314–323. URL: https://doi.org/10.1117/12.2561087.

Zimmerman, N. T. et al. (2016). “Lyot coronagraph design study for large, segmented space telescope apertures”. In: *Space Telescopes and Instrumentation 2016: Optical, Infrared, and Millimeter Wave*. Ed. by H. A. MacEwen et al. Vol. 9904. International Society for Optics and Photonics. SPIE, pp. 668–682. URL: https://doi.org/10.1117/12.2233205.

Chapter 5

HIGH CONTRAST IMAGING WITH THE APODIZED VORTEX CORONAGRAPH

Llop-Sayson, J. et al. (Feb. 2020). "High-contrast Demonstration of an Apodized Vortex Coronagraph". In: *The Astronomical Journal* 159.3. DOI: 10.3847/1538-3881/ab6329. URL: https://doi.org/10.3847.

ABSTRACT

High contrast imaging is the primary path to the direct detection and characterization of Earth-like planets around solar-type stars; a cleverly designed internal coronagraph suppresses the light from the star, revealing the elusive circumstellar companions. However, future large-aperture telescopes (>4 m in diameter) will likely have segmented primary mirrors, which causes additional diffraction of unwanted stellar light. Here we present the first high contrast laboratory demonstration of an apodized vortex coronagraph (AVC), in which an apodizer is placed upstream of a vortex focal plane mask to improve its performance with a segmented aperture. The gray-scale apodization is numerically optimized to yield a better sensitivity to faint companions assuming an aperture shape similar to the LUVOIR-B concept. Using wavefront sensing and control over a one-sided dark hole, we achieve a raw contrast of 2×10^{-8} in monochromatic light at 775 nm, and a raw contrast of 4×10^{-8} in a 10% bandwidth. These results open the path to a new family of coronagraph designs, optimally suited for next-generation segmented space telescopes.

5.1 Introduction

The formidable task of characterizing atmospheres of nearby worlds with direct imaging techniques is one of the most challenging technological problems in modern astronomy. Future space-based observatories, such as the NASA mission concept LUVOIR (The LUVOIR Team, 2019), include among their primary science goals the detection of molecular species in the atmospheres of exoplanets. However, these exoplanets are many orders of magnitude fainter than their host star; e.g. a rocky planet such as the Earth, orbiting a Sun-like star, requires a starlight suppression system that achieves a contrast of the order of 10^{-10} to be imaged. Developments in direct imaging with coronagraph instruments are on the path to providing astronomers with the technologies to tackle these extraordinary science cases.

Many coronagraph designs have been proposed and demonstrated to deal with starlight suppression (Kuchner et al., 2002; Kasdin et al., 2003; Codona et al., 2004; Mawet, Riaud, et al., 2005; Foo et al., 2005; Guyon, Pluzhnik, et al., 2005; Soummer, 2005; J. T. Trauger et al., 2007). For instance, the vortex coronagraph (Mawet, Riaud, et al., 2005; Foo et al., 2005) is a coronagraph in which an induced azimuthal phase ramp at the focal plane diffracts the starlight towards the outer edge of the beam, where it is blocked at the following pupil plane with a Lyot stop. This concept provides high sensitivity to close-in exoplanets with its enhanced raw contrast and high-throughput at small separation angles from the host star. Vortex coronagraphs are widely used on ground-based telescopes, including the W. M. Keck Observatory where it is currently producing high contrast science with the NIRC2 camera (Serabyn et al., 2017).

However, the number of exoplanets that can be imaged is ultimately limited by the size of the telescope; at a given wavelength the minimum angular separation needed to resolve a planet and its host star is directly proportional to the telescope diameter. Large apertures will be required to undertake the most compelling science cases, e.g. habitable zones of M-type stars with extremely large telescopes from the ground, or a census on rocky planets around solar-type stars with space-based observatories. The next generation of large apertures will be segmented, which will increase the noise from unwanted stellar light due to diffraction from discontinuities in the pupil. The two concepts developed by the LUVOIR concept design team, LUVOIR-A with an on-axis 15 m primary mirror, and LUVOIR-B with an off-axis 8 m primary mirror, both segmented, have their exoplanet science yield driven by their coronagraph performance (Stark et al., 2019), which is greatly affected by the discontinuities in the pupil. Nonetheless, the last decade has seen an array of clever solutions to this problem (Mawet, Serabyn, et al., 2011; Pueyo et al., 2013; Mawet, Pueyo, et al., 2013; Carlotti et al., 2014; Guyon, Hinz, et al., 2014; G. J. Ruane, Absil, et al., 2015; G. J. Ruane, Huby, et al., 2015; Mazoyer et al., 2015; Balasubramanian et al., 2016; J. Trauger et al., 2016; Zimmerman et al., 2016; G. Ruane, Jewell, et al., 2016), and the Exoplanet Exploration Program (ExEP) Office at NASA is currently funding several groups to address this technology challenge through the Segmented Coronagraph Design and Analysis (SCDA) study (Crill et al., 2017). For instance, a deformable mirror (DM) assisted vortex coronagraph (DMVC) is baselined for the LUVOIR-B coronagraph, in which the combined work of two DMs suppresses the diffraction from the segment gaps. The same physical outcome in terms of diffraction suppression can be achieved by an apodization of the pupil (Mawet, Pueyo, et al., 2013). G. Ruane, Jewell, et al. (2016) introduced a new family of coronagraph designs, the apodized vortex coronagraph (AVC), in which a vortex coronagraph is modified by apodizing the wavefront at the pupil plane with a gray-scaled pattern optimized to provide an improved sensitivity to close-in exoplanets. The vortex mask and Lyot stop, downstream of the apodizer, suppresses the starlight.

Here we show the first laboratory demonstration of an AVC concept using the High Contrast Spectroscopy Testbed for Segmented Telescopes (HCST) in the Exoplanet Technology Laboratory (ET lab) at Caltech. A prototype apodizer was designed and fabricated for a LUVOIR-B type segmented pupil consisting of hexagonal segments with no central obscuration or support struts obscuring the aperture. In Sec. 5.2 we present simulations of the expected performance of a LUVOIR-B AVC. In Sec. 7.4 we show the laboratory setup at HCST to achieve high levels of contrast, in Sec. 5.4 we present the results of the high contrast demonstrations for monochromatic and broadband light. In Sec. 5.5 we discuss the significance of these results for the LUVOIR-B coronagraph, comparing the baselined DMVC to the AVC. Future work and conclusions are discussed in Sec. 7.6 and 7.7, respectively.

5.2 Design and Simulations

We performed simulations comparing the high contrast performance without and with the optimized apodization. These simulations were performed using the HCST layout, with no other wavefront error other than the pupil discontinuities introduced by the simulated apertures. Simulations of the AVC are performed using the Fast

Linear Least-Squares Coronagraph Optimization (FALCO) (A. J. E. Riggs et al., 2018) software package[1], the same toolbox used to run the HCST.

Our simulations show that the AVC radically improves the starlight suppression within the intended field of view. Figure 5.1 shows a comparison between the stellar residuals after the coronagraph without (left panel) and with (right panel) the optimized apodization. In theory, a vortex coronagraph provides total rejection of starlight with a flat, evenly-illuminated wavefront and a circular aperture. However, the addition of gaps between mirror segments (see Fig. 5.1a) causes points of diffracted light to appear throughout the image plane after the coronagraph (see Fig. 5.1b) whose brightness depends on the width of the gaps. The gray-scale apodization pattern (see Fig. 5.1c) is designed to minimize the diffraction from the star out to an angular separation of ~20 λ/D (see Fig. 5.1d). The numerical optimization approach is based on Jewell et al. (2017).

In the case of the AVC, the diffraction spikes originating from the presence of the hexagonal segmentation of the pupil are cancelled within the region of interest around the star. The immediate gains in raw contrast are very significant, with an improvement of $\sim$ 4 orders of magnitude for the AVC in the circular region between 3 and 10 λ/D clearly visible in the figure, and a loss in throughput of 8% (for an off-axis source at 6 λ/D from the star).

To emphasize the impact of the apodizer in terms of wavefront control performance, Fig. 5.2 shows the result of two simulations of HCST with a LUVOIR-B type aperture: on the left, without the gray-scale apodization, and on the right, with the AVC. These simulation are for HCST in its 2-DM configuration, which allows for a 360° dark hole. The AVC simulation converges to a raw contrast $\sim$ orders of magnitude better.

5.3 Laboratory Setup

The experiments were performed on the High Contrast Spectroscopy Testbed for Segmented Telescopes (HCST) (Delorme et al., 2018; Llop-Sayson, G. Ruane, Jovanovic, et al., 2019) in the Exoplanet Technology Laboratory (ET lab) at Caltech. HCST is a facility aimed at addressing the technology challenges for high contrast imaging and spectroscopy of exoplanets with large segmented telescopes. The HCST custom-made optics provide the exquisite wavefront quality required for high contrast experiments, with <0.016 waves RMS (Jovanovic et al., 2018). A

[1] https://github.com/ajeldorado/falco-matlab

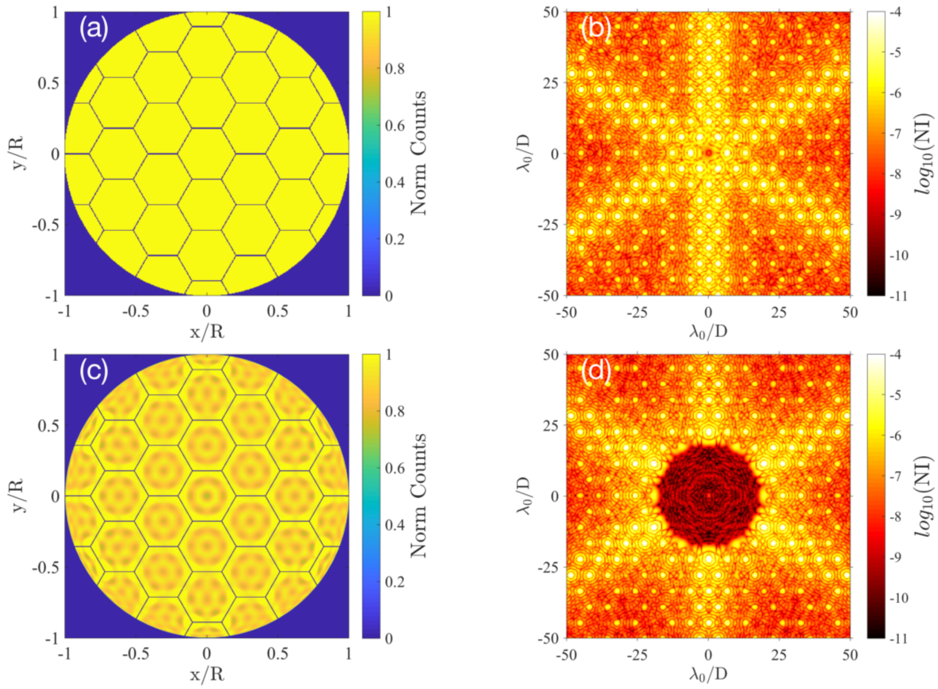

Figure 5.1 Pupil image of a hexagonally segmented LUVOIR-B type telescope aperture (a), with its correspondent simulated stellar coronagraphic PSF (b) , and a pupil image of an AVC (c) for the same aperture, with its correspondent coronagraphic PSF (d). The six diffraction spikes are caused by the hexagonal segmentation pattern. No wavefront control has been performed in either case; the dark zone around the center of the PSF for the apodized case is solely due the apodization.

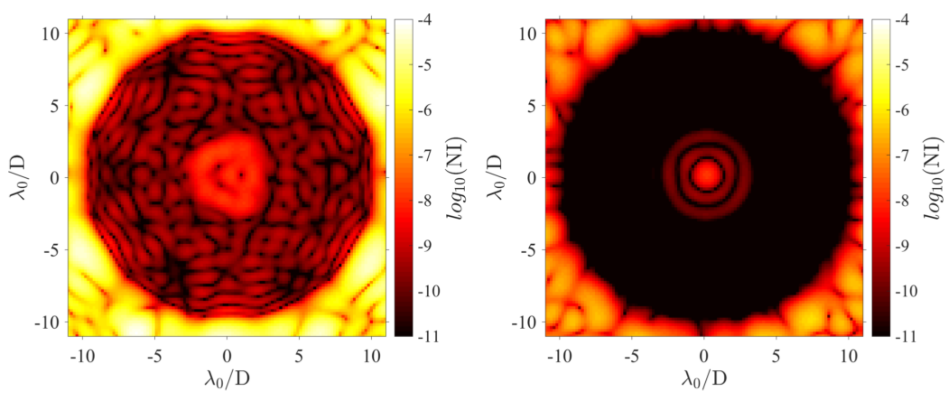

Figure 5.2 Simulated stellar PSFs after wavefront control correction, for a segmented aperture without (*left*), and with gray-scaled apodization (*right*).

custom-made enclosure consisting of sandwiched honeycomb aluminum panels ensures minimum environmental disruption from the exterior, namely air turbulence, acoustic vibrations, and temperature gradient changes. An optical table equipped with active damping isolates the setup from vibrations. The PSF jitter over a few seconds is ~2% λ/D RMS, and the slower PSF drifts, probably caused by changes in temperature gradients over the testbed, cause drifts from 0.1 to 1 λ/D over timescales of a few hours. We work with exposure times of 1 to 5 seconds and mitigate the effect of the PSF drift by periodically re-centering the camera's sub-window.

For the monochromatic light tests we used a laser (Thorlabs S1FC780), while for the broadband tests we used a supercontinuum white-light laser source (NKT Photonics SuperK EXTREME) followed by a tunable single-line filter (NKT Photonics SuperK VARIA). The light is fed to HCST through a single mode fiber (Thorlabs SM600); the light from the laser is circularly polarized and re-imaged onto a custom-made 5-μm pinhole.

The layout of the HCST can be seen in Fig. 7.3. The beam is collimated and an iris defines the outer pupil edge to avoid chromatic errors due to vignetting and back reflection from the apodizer glass substrate prototype. The AO system consists of a deformable mirror, or DM (Boston Micromachines Corporation kilo-DM) that controls the wavefront. The DM has a continuous surface membrane with 34 × 34 actuators with an inter-actuator separation of 300 μm. The apodizer is placed at a pupil plane conjugated with the DM and the entrance iris. After the apodizer, the beam is focused onto the focal plane mask (FPM). HCST uses a vortex coronagraph (Foo et al., 2005; Mawet, Riaud, et al., 2005), which provides an excellent trade-off between small inner working angle (IWA), throughput, and immunity to low-order aberrations. The vortex coronagraph induces a phase ramp at the focus of the form $e^{\pm il\theta}$, where l is the topological charge of the vortex.Given an arbitrary phase aberration at the pupil plane described as a linear combination of Zernike polynomials, Z_n^m, the VC is insensitive to aberrations such that $|l| > n + |m|$. Here we used a charge $l = 8$ mask, we are thus insensitive of tip and tilt, astigmatism, coma, trefoil, and spherical aberrations. However, a higher charge reduces the throughput at close-in angles, pushing away the IWA. The theoretical IWA for a charge $l = 8$ VC is $\sim 3.5\lambda/D$. A more in-depth analysis of this trade-off can be found on G. Ruane, Mawet, et al. (2018). After the FPM, the beam is then collimated and clipped at the pupil by the Lyot stop, a circular laser-cut aluminum mask with a 15.4 mm diameter hole that blocks ~93% of the incoming beam diameter. The remaining light is imaged with a ~f/50 beam onto the camera (Oxford Instruments Andor Neo 5.5). In order to do photometric calibration, we used a filter wheel with an neutral density filter when necessary (Thorlabs NE20B, OD=2.0).

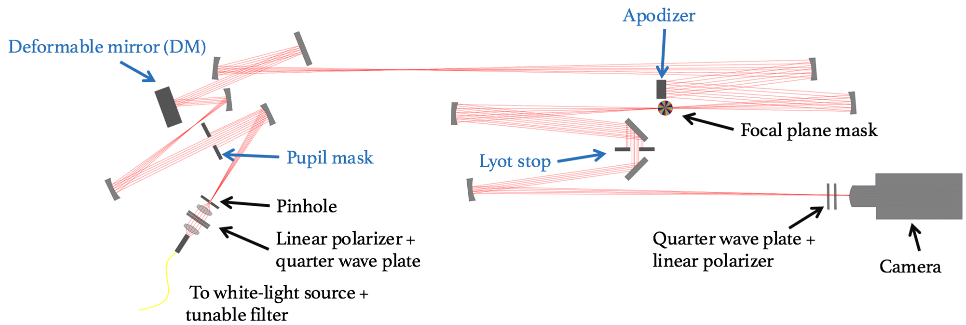

Figure 5.3 Layout of HCST for the apodized vortex coronagraph concept demonstration. Blue font and arrows indicate conjugated pupil planes.

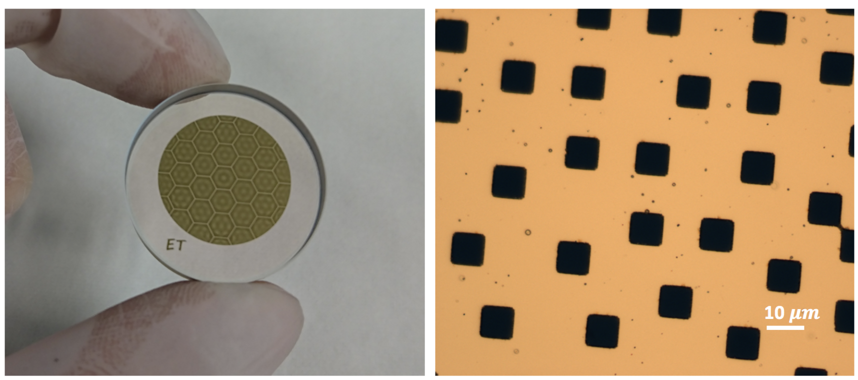

Figure 5.4 Picture of an apodizer prototype (*left*), and a microscope image of the microdot pattern on the apodizer surface (*right*). This design is optimized for a LUVOIR-B type aperture, with the gray-scaled apodization achieved with the microdot technique, in which a pattern of $\sim 10 \times 10$ μm square dots of gold is evaporated onto the substrate surface.

Figure 5.4 shows the picture of the apodizer prototype used in these experiments, manufactured by Opto-Line. The prototype consists of an AR-coated 6 mm thick BK7 substrate with a microdot pattern on the reflective surface; in this binary mask, the density of microdots on the surface provides the desired gray-scaled apodization. The reflective layer is 400 nm thick with gold evaporated on a thin sub-layer of chrome with 10×10 μm square voids where the AR coating is exposed.

5.4 Laboratory Results

Results for the AVC in monochromatic light

With the laboratory setup described in Sec. 7.4 we first demonstrated the AVC concept with monochromatic light. The pupil images with the prototype apodizer aligned in the system are shown in Fig. 5.5, upstream (left) and downstream (right) from the focal-plane mask. As expected, with the vortex mask aligned to the beam, the light tends to concentrate in the segment gaps in the pupil downstream of the focal plane mask (G. Ruane, A. Riggs, et al., 2018), still this effect is mitigated by the apodization, which aims to send this light out of the beam. The right panel in Figure 5.5, was taken with the DM turned off (i.e. zero volts applied to the actuators). As such, the azimuthal asymmetry beyond the Lyot stop seen in the image is due to low-order aberrations introduced by the shape of the DM when unpowered. Furthermore, the clipping of the extended beam downstream of the vortex mask is caused by the collimating OAP before the Lyot stop.

In Fig. 5.6 we show the AVC PSF for both an off-axis source and the coronagraphic PSF. The main diffraction effects (other than the Airy ring pattern) that can be identified prior to wavefront control are listed below:

1. The six-fold diffraction spikes is caused by the hexagonal segmentation of the pupil (see Fig. 5.5).

2. The gray-scaled apodization creates a diffraction spike-free area around the simulated star. Without an optimized apodization the diffraction spikes would cover the full FOV and would be difficult to suppress achromatically with the AO system alone.

3. The DM quilting, i.e. the phase pattern on the DM surface, induces a square grid of bright spots at $\sim 30\ \lambda/D$. This effect is only concerning at levels of raw contrast below 1×10^{-9} (Krist et al., 2019).

4. Strong horizontal diffraction features around the simulated star can be seen which are due to phase errors on the OAP surfaces due to tooling marks at fabrication. Upon inspection with a laser interferometer, all OAPs show vertical stripe-like features with <10 nmRMS. The horizontal diffraction is consistent with the surface errors measurements.

All major effects before correction with the AO system are thus well understood, namely, the apodizer behaves as predicted creating an area with improved raw

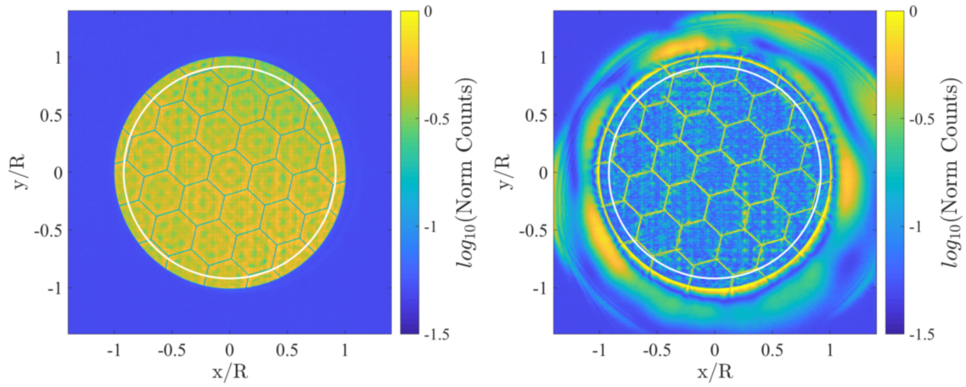

Figure 5.5 Pupil image of the Lyot plane, with focal plane mask out (*left*), and aligned (*right*). The white circle indicates the extent of the Lyot stop when aligned to the beam.

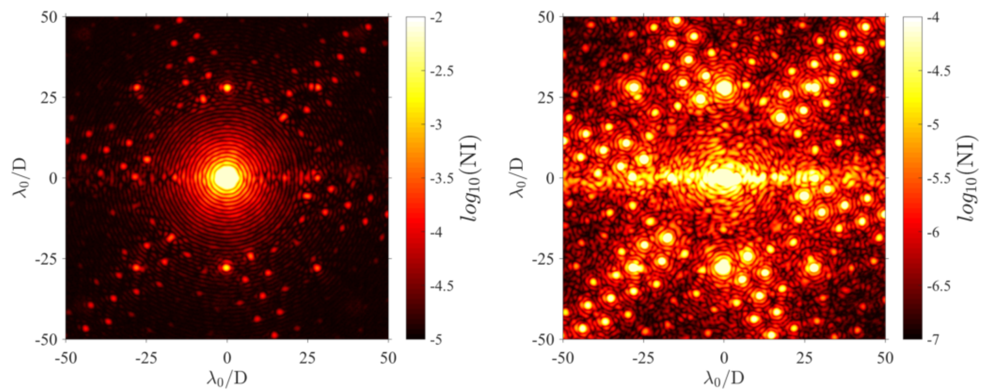

Figure 5.6 AVC PSF (*left*), and coronagraphic PSF (*right*). The coronagraphic PSF obtained in the testbed has the same appearance as predicted by simulations in terms of diffraction spikes, and apodized area (see Fig. 5.1). Two other major effects can be seen from these images besides the diffraction caused by the hexagonal segmentation: the BMC DM phase error pattern induces a square grid of bright spots at $\sim 30\ \lambda/D$, and a strong horizontal diffraction stripe can be seen which is due to phase errors on the the OAPs from tooling during fabrication.

contrast (see Fig. 5.1). The starting raw contrast after image sharpening, performed with Zernike tuning with the DM, and with a full-control-area wavefront control run, is below 10^{-6} beyond $5\lambda/D$.

We performed wavefront sensing and control (WFSC) with the electric field conjugation (EFC) (Give'On, 2009) algorithm to further suppress residual starlight creating a dark area, or dark hole (DH), around the simulated star. EFC is a model-based algorithm that iteratively finds the DM shape that minimizes the energy in a region of the image plane. It uses a model of the optical system to compute the effect of each DM actuator on the image plane to estimate the electric field on that plane, and to solve for the DM shape that minimizes the energy on the DH. Fig. 5.7 shows the DH image and the resulting DM solution for the correction; the best high contrast result with laser light is 2×10^{-8}. In contrast, for previous experiments on the HCST, in which we performed WFSC with EFC with a circular clear aperture, i.e. without the apodizer, we achieved an average raw contrast over a DH of 1×10^{-8} for $\sim 1\%$ narrowband light (Llop-Sayson, G. Ruane, Jovanovic, et al., 2019). Although the limitation to HCST's performance with the clear aperture configuration is not fully understood, the most probable cause is a combination of: model uncertainty, PSF drift, incoherent light in the system from ghosts, and the limitation from the least significant bit of the DM electronics, which sets the limit of HCST to 7×10^{-9} (see Echeverri et al. in prep). The discrepancy of a factor of two between HCST's best results with and without the AVC could be explained by a combination of a few factors that result from implementing the AVC:

- Model uncertainty associated with the apodizer. For instance, the model mismatch associated with errors from the DM actuator position with respect to the beam may be larger with the apodizer. Indeed, a discrepancy between the DM actuator position relative to the apodizer in the model and the actual relative position in the testbed, considering unaccounted magnification between the two planes, will certainly exacerbate the uncertainty in the model.

- Incoherent light from back-reflection at the back of the apodizer substrate. Although the substrate of the prototype apodizer is AR-coated, and the beam is circularly clipped at the entrance pupil to match the apodizer circular edge, a small percentage of light is still back-reflected, $< 1\%$, and could be an issue at levels of 10^{-8} raw contrast.

- Lyot plane leakage. For the clear aperture experiments the Lyot stop would block $\sim 83\%$ of the radius of the beam, 10% more than for the AVC experiment. This makes leakage at the Lyot plane worse, given that the beam is clipped after the vortex mask (see Fig. 5.5, right image).

- Defects in the microdot matrix (Zhang et al., 2018), and/or subtle non-linear vector diffraction effects due to the sub-wavelength feature size of microdot edges (Sivaramakrishnan et al., 2013).

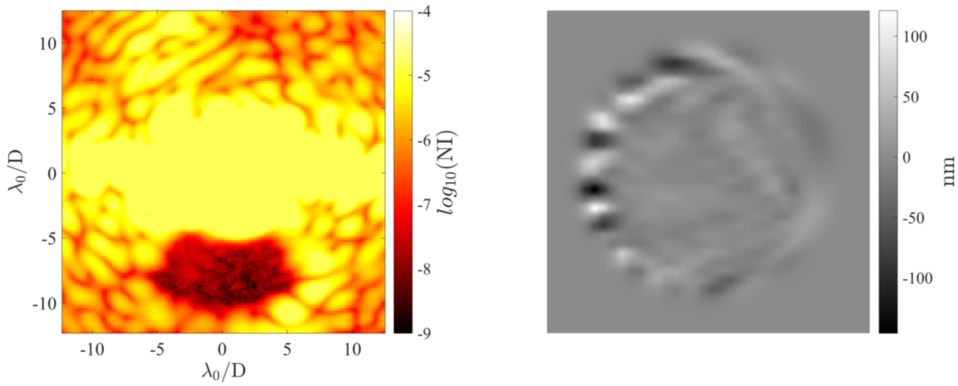

Figure 5.7 Result of an EFC run at HCST with the AVC: coronagraphic PSF with a dark hole (*left*), and the corresponding DM solution (*right*). The best raw contrast achieved is 2×10^{-8} with the apodizer prototype used in this experiment; the dark hole is a 60° aperture arc from 6 λ/D to 10 λ/D. We suspect that the high stroke of the actuators behind the Lyot stop is due to a combination of 1) a positioning error of the Lyot stop in the model with respect to the testbed position, and 2) an effect of the control algorithm dealing with PSF jitter and PSF drift.

Results for the AVC in broadband light

For the broadband demonstration, we chose a 10% bandwidth at 775 nm, and used the NKT VARIA tunable filter to sequentially select equidistant ~ 3 nm intermediate bands to perform multi-wavelength wavefront control with EFC as in Groff et al. (2016). In Fig. 5.8 we show the result of a corrected coronagraphic PSF with the AVC for broadband light, the best result is of 4×10^{-8} average raw contrast for a 60° aperture arc going from 6 λ/D to 10 λ/D DH.

The average raw contrast for the same DH presented here for the clear circular aperture configuration is currently limited at 3×10^{-8} for the same bandpass. As discussed in Sec. 5.4, different factors associated with the AVC, specifically the apodizer, could explain the discrepancy in the contrast floor. Furthermore, in the case of broadband light, model errors are harder to trace and tackle.

5.5 Discussion: The AVC vs. the DMVC

The LUVOIR-B baseline coronagraph is a DM-assisted vortex coronagraph (DMVC) (The LUVOIR Team, 2019). A DMVC uses two DMs in series to help suppress the starlight diffracted by the mirror segmentation. Indeed, a 2-DM configuration, with both a pupil-plane DM, and an out-of-pupil DM, can correct amplitude discontinuities such as segment gaps. The net remapping effect of the DMVC is strictly equivalent to the gray-scaled apodization of the AVC. The DMVC is all reflective

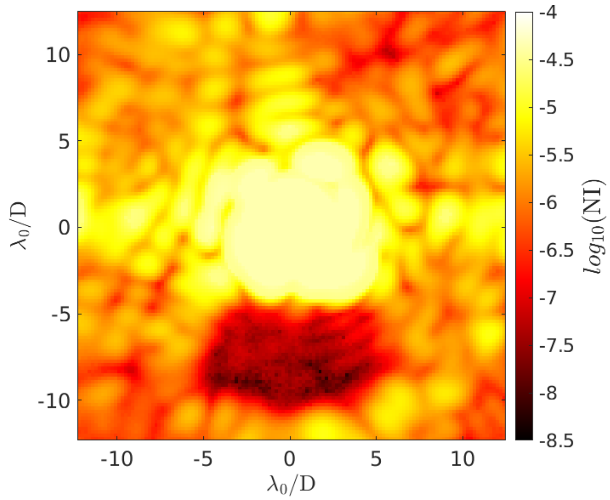

Figure 5.8 Broadband coronagraphic PSF with a dark hole obtained with EFC . The deepest level of raw contrast achieved at HCST for the AVC with 10% broadband light at 775 nm is 4×10^{-8} for a 60° aperture arc from 6 λ/D to 10 λ/D dark hole.

and thus lossless. However, beamwalk on the second out-of-pupil DM makes the DMVC generally more sensitive to low-order aberrations.

The improved robustness to tip and tilt errors for the AVC comes somewhat at the expense of throughput due to the reduced transmittance of the gray-scale apodizer. For a LUVOIR-B like aperture the throughput loss is a marginal $\sim$ 9% (G. Ruane, A. Riggs, et al., 2018) compared to the DMVC. From the extensive yield analysis of Stark et al. (2019), we found that an AVC on board of LUVOIR-B, has an exoEarth yield 96% that of the DMVC, which corresponds to a loss approximately 1 exoEarth. The trade between the sensitivity to low-order aberrations and throughput for LUVOIR-B in terms of exoEarth yield will be the matter of future work.

Other factors to consider include the associated risk of the DM technology maturity, the appearance of bright spots on the resulting coronagraphic PSF for the DMVC, or the relative alignment error tolerance between the DMs. Furthermore, the DMVC can only deal with a limited segment gap size; the larger the gap, the more DM stroke is needed, and high contrast at the requirement levels of the LUVOIR mission concept, i.e. 10^{-10} average raw contrast, is hardly achievable for segment gaps with thickness of 0.1% of the telescope diameter (G. Ruane, A. Riggs, et al., 2018).

5.6 Perspectives

We plan on using a System Identification, or System ID (Sun et al., 2018), algorithm based on a neural network to address the model uncertainties in the system. Poorly understood effects at high contrast levels, such as surface quality and edge effects from the apodizer microdots, or the interplay between actuator positioning in the beam and the segment gaps, could be addressed by this approach. System ID was successfully implemented at HCST (Llop-Sayson, G. Ruane, Jovanovic, et al., 2019) and has the potential of dealing with the issues associated with performing model-based WFSC with an AVC, namely the uncertainties coming from the apodizer and segment gaps. At a more general level, demonstrating System ID for the AVC is directly applicable to any instrument dealing with discontinuities in the pupil of any kind. Such is the case of next generation ELTs, in which effective model-based WFSC is the pathway to reaching the highest possible number of directly imaged exoplanets.

Plans to improve the performance of HCST are currently underway (Llop-Sayson, G. Ruane, Jovanovic, et al., 2019), which include: 1) a new source architecture with a new mount, more stable to make the system more robust to PSF jitter and drift, 2) a field stop at the image plane to avoid incoherent light from ghosts, and 3) a tip and tilt sensing and control system. With this upgrades we expect to improve the performance and the limiting factors and thus surpass our current contrast floor.

A fiber injection unit is planned for HCST, with which we will perform WFSC through a single mode fiber (SMF) with the purpose of paving the way for high dispersion coronagraphy (Sparks et al., 2002; Kawahara et al., 2014; Kok et al., 2014; Snellen et al., 2015; Wang et al., 2017; Mawet, G. Ruane, et al., 2017). Indeed, using an SMF to recover the planet signal improves the sensitivity to planet signal in the presence of starlight noise by virtue of the modal selectivity of the fiber. We previously demonstrated WFSC through an SMF for a clear open aperture (Mawet, G. Ruane, et al., 2017; Llop-Sayson, G. Ruane, Mawet, et al., 2019), we now plan to use the AVC to demonstrate the capabilities of using an SMF with segmented apertures. Moreover, a custom-made multi-core fiber has been purchased to test a multi-object wavefront control approach recently introduced by Coker et al. (2019).

In this paper we have presented an AVC design optimized for a segmentation-only type of aperture, however, although segment gaps are a major concern in coronagraph design, more severe discontinuities, particularly from central obscurations and support struts, pose a more challenging difficulty for high contrast imaging (Jewell et al., 2017; Stark et al., 2019). Future work will involve efforts on design and testing AVC apodizers optimized for central obscurations and support strut discontinuities.

5.7 Conclusion

We have demonstrated the apodized vortex coronagraph (AVC) concept in the laboratory to high levels of contrast with both monochromatic and 10% bandwidth light. The predictions from the AVC model and design process have been validated, as the prototype manufactured for the testbed effectively deals with diffraction emerging from the segmentation from the pupil. Furthermore, WFSC has been successfully implemented with the AVC, consistently reaching levels of 10^{-8} raw contrast; for a 60° arc-shaped aperture from 6 λ/D to 10 λ/D dark hole, we achieve 2×10^{-8} raw contrast for monochromatic light at 780 nm, and 4×10^{-8} for 10% bandwidth at the same wavelength. From previous experiments at HCST with a clear circular aperture, we know that the level of incoherent light is below $1{\times}10^{-8}$ (Llop-Sayson, G. Ruane, Jovanovic, et al., 2019). We thus plan to address this discrepancy, namely by tackling model uncertainties with a System Identification approach, and attempting to minimize incoherent light in the system. Furthermore, future experiments with a fiber injection unit will aim to yield improved results in terms of contrast and bandwidth, thus leading the way for future high dispersion coronagraphy instruments on large segmented telescopes. Indeed, the results presented in this paper, and the envisioned improved performance at HCST with the incoming upgrades, are a testimony of the potential of high contrast technology in next generation space-based observatories such as the NASA mission concept LUVOIR, and ground-based observatories, such as the Thirty Meter Telescope.

5.8 Acknowledgments

The first author J. Llop-Sayson is partially supported by the National Science Foundation AST-ATI Grant 1710210. Part of this work was carried out at the Jet Propulsion Laboratory, California Institute of Technology, under contract with the National Aeronautics and Space Administration (NASA).

BIBLIOGRAPHY

Balasubramanian, K. et al. (Jan. 2016). “WFIRST-AFTA coronagraph shaped pupil masks: design, fabrication, and characterization”. In: *Journal of Astronomical Telescopes, Instruments, and Systems* 2, 011005, p. 011005. DOI: 10.1117/1.JATIS.2.1.011005.

Carlotti, A., L. Pueyo, and D. Mawet (June 2014). “Apodized phase mask coronagraphs for arbitrary apertures. II. Comprehensive review of solutions for the vortex coronagraph”. In: *Astronomy and Astrophysics* 566, A31, A31. DOI: 10.1051/0004-6361/201323258. arXiv: 1404.2845 [astro-ph.IM].

Codona, J. L. and R. Angel (Apr. 2004). “Imaging Extrasolar Planets by Stellar Halo Suppression in Separately Corrected Color Bands”. In: *Astrophysical Journal, Letters* 604.2, pp. L117–L120. DOI: 10.1086/383569. arXiv: astro-ph/0402420 [astro-ph].

Coker, C. T. et al. (July 2019). “Simulations of a High-Contrast Single-Mode Fiber Coronagraphic Multi-Object Spectrograph for Future Space Telescopes”. In: *arXiv e-prints*, arXiv:1907.03921, arXiv:1907.03921. arXiv: 1907.03921 [astro-ph.IM].

Crill, B. P. and N. Siegler (2017). “Space technology for directly imaging and characterizing exo-Earths”. In: *UV/Optical/IR Space Telescopes and Instruments: Innovative Technologies and Concepts VIII*. Ed. by H. A. MacEwen and J. B. Breckinridge. Vol. 10398. International Society for Optics and Photonics. SPIE, pp. 175–195. URL: https://doi.org/10.1117/12.2275697.

Delorme, J. R. et al. (2018). “High-contrast spectroscopy testbed for segmented telescopes”. In: *Proc. SPIE* 10400, p. 104000X. DOI: 10.1117/12.2274893.

Foo, G., D. M. Palacios, and G. A. Swartzlander (2005). “Optical vortex coronagraph”. In: *Opt. Lett.* 30, pp. 3308–3310. DOI: 10.1364/OL.30.003308.

Give’On, A. (2009). “A unified formailism for high contrast imaging correction algorithms”. In: *Proc. SPIE* 7440, p. 74400D. DOI: 10.1117/12.825049.

Groff, T. D. et al. (2016). “Methods and limitations of focal plane sensing, estimation, and control in high-contrast imaging”. In: *J. Astron. Telesc. Instrum. Syst.* 2.1, p. 011009. DOI: 10.1117/1.JATIS.2.1.011009.

Guyon, O., P. M. Hinz, et al. (Jan. 2014). “High Performance Lyot and PIAA Coronagraphy for Arbitrarily Shaped Telescope Apertures”. In: *Astrophysical Journal* 780.2, 171, p. 171. DOI: 10.1088/0004-637X/780/2/171. arXiv: 1305.6686 [astro-ph.IM].

Guyon, O., E. A. Pluzhnik, et al. (Mar. 2005). "Exoplanet Imaging with a Phase-induced Amplitude Apodization Coronagraph. I. Principle". In: *Astrophysical Journal* 622.1, pp. 744–758. DOI: 10.1086/427771. arXiv: astro-ph/0412179 [astro-ph].

Jewell, J. et al. (2017). "Optimization of coronagraph design for segmented aperture telescopes". In: *Proc. SPIE* 10400, 104000H. DOI: 10.1117/12.2274574. URL: https://doi.org/10.1117/12.2274574.

Jovanovic, N. et al. (2018). "High-contrast spectroscopy testbed for Segmented Telescopes: instrument overview and development progress". In: *Proc. SPIE* 10702, 107024E. DOI: 10.1117/12.2314325.

Kasdin, N. J. et al. (Jan. 2003). "Extrasolar Planet Finding via Optimal Apodized-Pupil and Shaped-Pupil Coronagraphs". In: *Astrophysical Journal* 582.2, pp. 1147–1161. DOI: 10.1086/344751.

Kawahara, H. et al. (June 2014). "Spectroscopic Coronagraphy for Planetary Radial Velocimetry of Exoplanets". In: *The Astrophysical Journal Supplement Series* 212.2, p. 27. DOI: 10.1088/0067-0049/212/2/27.

Kok, R. J. de et al. (Jan. 2014). "Identifying new opportunities for exoplanet characterisation at high spectral resolution". In: *Astronomy and Astrophysics* 561, A150, A150. DOI: 10.1051/0004-6361/201322947. arXiv: 1312.3745.

Krist, J. et al. (2019). "Numerical modeling of the Habex coronagraph". In: *Techniques and Instrumentation for Detection of Exoplanets IX*. Ed. by S. B. Shaklan. Vol. 11117. International Society for Optics and Photonics. SPIE, pp. 85–100. URL: https://doi.org/10.1117/12.2530462.

Kuchner, M. J. and W. A. Traub (May 2002). "A Coronagraph with a Band-limited Mask for Finding Terrestrial Planets". In: *Astrophysical Journal* 570.2, pp. 900–908. DOI: 10.1086/339625. arXiv: astro-ph/0203455 [astro-ph].

Llop-Sayson, J., G. Ruane, N. Jovanovic, et al. (2019). "The high-contrast spectroscopy testbed for segmented telescopes (HCST): new wavefront control demonstrations". In: *Techniques and Instrumentation for Detection of Exoplanets IX*. Ed. by S. B. Shaklan. Vol. 11117. International Society for Optics and Photonics. SPIE, pp. 610–619. URL: https://doi.org/10.1117/12.2530670.

Llop-Sayson, J., G. Ruane, D. Mawet, et al. (2019). "Demonstration of an electric field conjugation algorithm for improved starlight rejection through a single mode optical fiber". In: *Journal of Astronomical Telescopes, Instruments, and Systems* 5.1. DOI: 10.1117/1.JATIS.5.1.019004. URL: https://doi.org/10.1117/1.JATIS.5.1.019004.

Mawet, D., L. Pueyo, et al. (Nov. 2013). "Ring-apodized Vortex Coronagraphs for Obscured Telescopes. I. Transmissive Ring Apodizers". In: *Astrophysical Journal, Supplement* 209.1, 7, p. 7. DOI: 10.1088/0067-0049/209/1/7. arXiv: 1309.3328 [astro-ph.IM].

Mawet, D., P. Riaud, et al. (2005). “Annular Groove Phase Mask Coronagraph”. In: *Astrophys. J.* 633, pp. 1191–1200. DOI: 10.1086/462409.

Mawet, D., G. Ruane, et al. (2017). “Observing Exoplanets with High-dispersion Coronagraphy. II. Demonstration of an Active Single-mode Fiber Injection Unit”. In: *Astrophys. J.* 838, p. 92. DOI: 10.3847/1538-4357/aa647f.

Mawet, D., E. Serabyn, et al. (Apr. 2011). “Improved high-contrast imaging with on-axis telescopes using a multistage vortex coronagraph”. In: *Optics Letters* 36.8, p. 1506. DOI: 10.1364/OL.36.001506. arXiv: 1103.1909 [astro-ph.IM].

Mazoyer, J. et al. (Sept. 2015). “Active correction of aperture discontinuities (ACAD) for space telescope pupils: a parametic analysis”. In: *Proceedings of the SPIE*. Vol. 9605. Society of Photo-Optical Instrumentation Engineers (SPIE) Conference Series, p. 96050M. DOI: 10.1117/12.2188692. arXiv: 1710.03510 [astro-ph.IM].

Pueyo, L. and C. Norman (June 2013). “High-contrast Imaging with an Arbitrary Aperture: Active Compensation of Aperture Discontinuities”. In: *Astrophysical Journal* 769.2, 102, p. 102. DOI: 10.1088/0004-637X/769/2/102. arXiv: 1211.6112 [astro-ph.IM].

Riggs, A. J. E. et al. (Aug. 2018). “Fast linearized coronagraph optimizer (FALCO) I: a software toolbox for rapid coronagraphic design and wavefront correction”. In: *Space Telescopes and Instrumentation 2018: Optical, Infrared, and Millimeter Wave*. Vol. 10698. Society of Photo-Optical Instrumentation Engineers (SPIE) Conference Series, p. 106982V. DOI: 10.1117/12.2313812.

Ruane, G., A. Riggs, et al. (Aug. 2018). “Fast linearized coronagraph optimizer (FALCO) IV: coronagraph design survey for obstructed and segmented apertures”. In: *Proceedings of the SPIE*. Vol. 10698. Society of Photo-Optical Instrumentation Engineers (SPIE) Conference Series, 106984U. DOI: 10.1117/12.2312973. arXiv: 1807.06758 [astro-ph.IM].

Ruane, G. J., E. Huby, et al. (Nov. 2015). “Lyot-plane phase masks for improved high-contrast imaging with a vortex coronagraph”. In: *Astronomy and Astrophysics* 583, A81, A81. DOI: 10.1051/0004-6361/201526561. arXiv: 1509.05750 [astro-ph.IM].

Ruane, G., J. Jewell, et al. (July 2016). “Apodized vortex coronagraph designs for segmented aperture telescopes”. In: *Proceedings of the SPIE*. Vol. 9912. Society of Photo-Optical Instrumentation Engineers (SPIE) Conference Series, p. 99122L. DOI: 10.1117/12.2231715. arXiv: 1607.06400 [astro-ph.IM].

Ruane, G., D. Mawet, et al. (Jan. 2018). “Vortex coronagraphs for the Habitable Exoplanet Imaging Mission concept: theoretical performance and telescope requirements”. In: *Journal of Astronomical Telescopes, Instruments, and Systems* 4, 015004, p. 015004. DOI: 10.1117/1.JATIS.4.1.015004. arXiv: 1803.03909 [astro-ph.IM].

Ruane, G. J., O. Absil, et al. (Sept. 2015). "Optimized focal and pupil plane masks for vortex coronagraphs on telescopes with obstructed apertures". In: *Proceedings of the SPIE*. Vol. 9605. Society of Photo-Optical Instrumentation Engineers (SPIE) Conference Series, p. 96051I. DOI: 10.1117/12.2187236. arXiv: 1509.05794 [astro-ph.IM].

Serabyn, E. et al. (Jan. 2017). "The W. M. Keck Observatory Infrared Vortex Coronagraph and a First Image of HIP 79124 B". In: *The Astronomical Journal* 153.1, 43, p. 43. DOI: 10.3847/1538-3881/153/1/43. arXiv: 1612.03093 [astro-ph.SR].

Sivaramakrishnan, A. et al. (Sept. 2013). "Calibrating apodizer fabrication techniques for high-contrast coronagraphs on segmented and monolithic space telescopes". In: *Proceedings of the SPIE*. Vol. 8860. Society of Photo-Optical Instrumentation Engineers (SPIE) Conference Series, 88600W. DOI: 10.1117/12.2024091.

Snellen, I. et al. (Apr. 2015). "Combining high-dispersion spectroscopy with high contrast imaging: Probing rocky planets around our nearest neighbors". In: *Astronomy and Astrophysics* 576, A59, A59. DOI: 10.1051/0004-6361/201425018.

Soummer, R. (Jan. 2005). "Apodized Pupil Lyot Coronagraphs for Arbitrary Telescope Apertures". In: *Astrophysical Journal, Letters* 618.2, pp. L161–L164. DOI: 10.1086/427923. arXiv: astro-ph/0412221 [astro-ph].

Sparks, W. B. and H. C. Ford (Oct. 2002). "Imaging Spectroscopy for Extrasolar Planet Detection". In: *Astrophysical Journal* 578, pp. 543–564. DOI: 10.1086/342401. eprint: astro-ph/0209078.

Stark, C. C. et al. (Apr. 2019). "ExoEarth yield landscape for future direct imaging space telescopes". In: *Journal of Astronomical Telescopes, Instruments, and Systems* 5, 024009, p. 024009. DOI: 10.1117/1.JATIS.5.2.024009. arXiv: 1904.11988 [astro-ph.EP].

Sun, H., N. J. Kasdin, and R. Vanderbei (2018). "Identification and adaptive control of a high-contrast focal plane wavefront correction system". In: *Journal of Astronomical Telescopes, Instruments, and Systems* 4.4, pp. 1 - 15 –15. DOI: 10.1117/1.JATIS.4.4.049006. URL: https://doi.org/10.1117/1.JATIS.4.4.049006.

The LUVOIR Team (2019). *The Large UV Optical Infrared Surveyor (LUVOIR) final report*. https://asd.gsfc.nasa.gov/luvoir/resources/docs/LUVOIR_FinalReport_2019-08-26.pdf.

Trauger, J. et al. (Jan. 2016). "Hybrid Lyot coronagraph for WFIRST-AFTA: coronagraph design and performance metrics". In: *Journal of Astronomical Telescopes, Instruments, and Systems* 2, 011013, p. 011013. DOI: 10.1117/1.JATIS.2.1.011013.

Trauger, J. T. and W. A. Traub (Apr. 2007). "A laboratory demonstration of the capability to image an Earth-like extrasolar planet". In: *Nature* 446.7137, pp. 771–773. DOI: 10.1038/nature05729.

Wang, J. et al. (Apr. 2017). "Observing Exoplanets with High Dispersion Coronagraphy. I. The Scientific Potential of Current and Next-generation Large Ground and Space Telescopes". In: *Astron. J.* 153, 183, p. 183. DOI: 10.3847/1538-3881/aa6474. arXiv: 1703.00582 [astro-ph.EP].

Zhang, M. et al. (July 2018). "Characterization of microdot apodizers for imaging exoplanets with next-generation space telescopes". In: *Proceedings of the SPIE*. Vol. 10698. Society of Photo-Optical Instrumentation Engineers (SPIE) Conference Series, p. 106985X. DOI: 10.1117/12.2312831. arXiv: 1807.06761 [astro-ph.IM].

Zimmerman, N. T. et al. (Jan. 2016). "Shaped pupil Lyot coronagraphs: high-contrast solutions for restricted focal planes". In: *Journal of Astronomical Telescopes, Instruments, and Systems* 2, 011012, p. 011012. DOI: 10.1117/1.JATIS.2.1.011012. arXiv: 1601.05121 [astro-ph.IM].

Chapter 6

WAVEFRONT SENSING AND CONTROL WITH A SINGLE MODE FIBER I: PROOF OF CONCEPT

Llop-Sayson, J. et al. (2019). "Demonstration of an electric field conjugation algorithm for improved starlight rejection through a single mode optical fiber". In: *Journal of Astronomical Telescopes, Instruments, and Systems* 5.1. DOI: 10.1117/1.JATIS.5.1.019004. URL: https://doi.org/10.1117/1.JATIS.5.1.019004.

ABSTRACT

Linking a coronagraph instrument to a spectrograph via a single mode optical fiber is a pathway towards detailed characterization of exoplanet atmospheres with current and future ground- and space-based telescopes. However, given the extreme brightness ratio and small angular separation between planets and their host stars, the planet signal-to-noise ratio will likely be limited by the unwanted coupling of starlight into the fiber. To address this issue, we utilize a wavefront control loop and a deformable mirror to systematically reject starlight from the fiber by measuring what is transmitted through the fiber. The wavefront control algorithm is based on the formalism of electric field conjugation (EFC), which in our case accounts for the spatial mode selectivity of the fiber. This is achieved by using a control output that is the overlap integral of the electric field with the fundamental mode of a single mode fiber. This quantity can be estimated by pair-wise image plane probes injected using a deformable mirror. We present simulation and laboratory results that demonstrate our approach offers a significant improvement in starlight suppression through the fiber relative to a conventional EFC controller. With our experimental setup, which provides an initial normalized intensity of 3×10^{-4} in the fiber at an angular separation of $4\lambda/D$, we obtain a final normalized intensity of 3×10^{-6} in monochromatic light at $\lambda = 635$ nm through the fiber (100x suppression factor) and 2×10^{-5} in $\Delta\lambda/\lambda = 8\%$ broadband light about $\lambda = 625$ nm (10x suppression factor). The fiber-based approach improves the sensitivity of spectral measurements at high contrast and may serve as an integral part of future space-based exoplanet imaging missions as well as ground-based instruments.

6.1 Introduction

Directly detecting the spectral signatures of molecules in the atmosphere of exoplanets, including biosignatures on temperate Earth-size planets, poses an immense technical challenge. Noise due to stray starlight diffracted from the telescope aperture as well as static and dynamic aberrations throughout the optical system limit the detection significance of the planet's spectral features. Furthermore, the wavefront quality and stability requirements for detecting and characterizing Earth-size exoplanets around solar-type stars with space-based missions such as the Habitable Exoplanet Observatory (HabEx)(Gaudi et al., 2018) and Large UV/Optical/IR Surveyor (LUVOIR)(The LUVOIR Team, 2018) mission concepts (Wang, Mawet, Hu, et al., 2018), and around M-type stars with the next-generation giant segmented mirror telescopes (GSMTs) on the ground, will be at the limits of current wavefront sensing and control techniques and technologies(Guyon, 2018).

Fiber-fed spectrographs have been used in astronomy since the 1980s(Hill et al., 1980). In the last decades, advances in adaptive optics (AO) have enabled diffraction-limited imaging and spectroscopy with 8-10 meter class ground-based telescopes and made the use of single mode fibers an advantageous option(Jovanovic, Guyon, et al., 2014; Schwab et al., 2014; Jovanovic, Schwab, et al., 2017). Recently, we introduced a practical concept that allows for the spectroscopic characterization of known exoplanets by linking the final focal plane of a coronagraph to a spectrograph via a single mode optical fiber(Mawet, Ruane, et al., 2017). A fiber injection unit (FIU) collects the known exoplanet's signal by coupling its light into a single mode fiber (SMF). In most cases, the signal-to-noise ratio (SNR) of the planet spectrum is limited by speckle and photon noise sources from starlight. Minimizing the stellar electric field that couples into the fiber reduces these noise sources such that the faint planet signal can be spectroscopically analyzed. The motivation for using a single mode fiber is to exploit its mode selectivity to further reject unwanted starlight.

Wavefront control techniques aim to eliminate stellar speckles and reduce contamination of the companion's signal using adaptive optics (AO). A deformable mirror (DM) placed at a pupil plane modifies the incoming wavefront to create a dark, speckle-free region in the image plane using one of several approaches that have been implemented successfully in previous laboratory demonstrations (Groff, A. Riggs, et al., 2016). A notable example is the electric field conjugation (EFC) algorithm (Give'On, 2009), which is the baseline wavefront control algorithm for the WFIRST Coronagraph Instrument (CGI) (Spergel et al., 2015). By finding the minimum of the electric field, EFC solves for the shape of the DM, which is characterized by $N \times N$ actuator heights.

Here, we introduce a new algorithm based on the EFC formalism that modifies the wavefront to minimize the speckles coupling into a SMF. We present the modified formalism of EFC that accounts for the modal selectivity of the SMF, results from simulations, as well as supporting laboratory experiments.

6.2 Electric field sensing

EFC iteratively reduces stellar intensity in a region of the image plane using an estimate of the electric field. In the case of a SMF, the measured intensity at the output of the fiber is the overlap integral of the electric field at the input of the fiber multiplied by the fundamental mode of the fiber:

$$I \propto \left| \iint E_{im} \Psi_{SMF} da \right|^2 , \tag{6.1}$$

where E_{im} is the electric field, Ψ_{SMF} is the fiber mode shape, and da is the differential area element in the image plane. The control algorithm presented here relies on the sensing of the real and imaginary parts of the electric field through the mode of the fiber. The procedure for sensing the overlap integral is based on the pair-wise probing method introduced by Give'On et al. 2009 (Give'On, 2009) and further developed by Groff et al. 2016 (Groff, A. Riggs, et al., 2016). However, instead of sensing the field at a set of pixels, the resolution element in this case is the overlap integral for the SMF referred to in this work as a *fibxel*.

We write the electric field in the image plane as the output of the coronagraph operator $C\left\{\cdot\right\}$:

$$E_{im} = C\left\{A\ e^{\alpha + i\beta} e^{i\phi}\right\} , \tag{6.2}$$

where A is the pupil field, α and β are respectively the amplitude and phase aberrations, and ϕ is the phase delay introduced by the DM. Assuming small changes in DM shapes, we use a truncated Taylor series expansion about $\phi = 0$ to find the linear relationship between the DM actuator heights and the field at the fiber. That is,

$$E_{im} \approx C\left\{A\ e^{\alpha + i\beta}\right\} + iC\left\{\phi\right\} = E_{Sp} + Gu, \tag{6.3}$$

where E_{Sp} is the speckle field we seek to sense, G is the control matrix, or Jacobian of the system, and u contains the changes in DM actuator heights. The intensity measured at the output of a fiber is

$$I = \left| \int (E_{Sp} + Gu)\Psi_{SMF} da \right|^2 \tag{6.4}$$

$$= \left| \int \Psi_{SMF} E_{Sp} da \right|^2 + \left| \int \Psi_{SMF} Gu da \right|^2 + 2\mathrm{Re}\left\{ \int \Psi_{SMF} E_{Sp} da \times \int \Psi_{SMF} Gu da \right\}. \tag{6.5}$$

For a pair of probes, $\pm Gu$, the difference between intensities of the positive and negative probe images is

$$\Delta I = 4\mathrm{Re}\left\{ \int \Psi_{SMF} E_{Sp} da \times \int \Psi_{SMF} Gu da \right\} \tag{6.6}$$

$$= 4 \int \Psi_{SMF} \mathrm{Re}\left\{E_{Sp}\right\} da \int \Psi_{SMF} \mathrm{Re}\left\{Gu\right\} da \tag{6.7}$$

$$+ 4 \int \Psi_{SMF} \mathrm{Im}\left\{E_{Sp}\right\} da \int \Psi_{SMF} \mathrm{Im}\left\{Gu\right\} da. \tag{6.8}$$

For n different pairs of probes:

$$\begin{bmatrix} \Delta I_1 \\ \vdots \\ \Delta I_n \end{bmatrix} = 4 \begin{bmatrix} \int \Psi_{SMF} \mathrm{Re}\left\{Gu_1\right\} da & \int \Psi_{SMF} \mathrm{Im}\left\{Gu_1\right\} da \\ \vdots & \vdots \\ \int \Psi_{SMF} \mathrm{Re}\left\{Gu_n\right\} da & \int \Psi_{SMF} \mathrm{Im}\left\{Gu_n\right\} da \end{bmatrix} \begin{bmatrix} \int \Psi_{SMF} \mathrm{Re}\left\{E_{Sp}\right\} da \\ \int \Psi_{SMF} \mathrm{Im}\left\{E_{Sp}\right\} da \end{bmatrix}, \tag{6.9}$$

or more simply, $z = H\, x$. Taking the pseudo-inverse of the observation matrix H, we find an estimate of the fibxel electric field $\hat{x} = H^{-\dagger}\, z$, where $\hat{x}$ is specifically the estimate of the complex-valued overlap integral. This estimate is computed at each control iteration. For a system equipped with more than one SMF in the image plane, a larger number of fibxels is used in the matrices above.

6.3 EFC through a single mode fiber

Once the overlap integral of the electric field in the image plane is estimated, we use a similar approach to the conventional EFC algorithm(Give'On, 2009). Assuming a linear relationship between the DM actuators and field in the image plane (see Eqn. 6.3), we calculate the DM shape that minimizes, in the least squares sense with a cost function given by $W = \left|\int (E_{Sp} + Gu)\Psi_{SMF} da\right|^2$, the overlap integral. This is done by $u = -G^{-\dagger}\hat{x}$, where

$$\hat{x} = \begin{bmatrix} \int \Psi_{SMF} \mathrm{Re}\left\{E_{Sp}\right\} da \\ \int \Psi_{SMF} \mathrm{Im}\left\{E_{Sp}\right\} da \end{bmatrix}. \tag{6.10}$$

In conventional EFC, G accounts for the effect of each actuator on the signal measured by pixels in the dark hole. In the case of an SMF, G accounts for the effect of each actuator on the overlap integral(s). Hence, similar to conventional EFC, G is computed using a model of the optical system, where each DM actuator is poked and its effect on the overlap integral is stored in G. The computation of the shape of the DM, u, is done iteratively until the starlight coupling into the SMF is minimized. Here, we report the performance of the EFC algorithm in terms of normalized intensity.

6.4 Definitions of normalized intensity

For the sake of clarity, we define the following metrics used in this paper to evaluate contrast performance:

- **Mean normalized intensity.** The mean intensity in the dark hole divided by the peak intensity of the non-coronagraphic star PSF. This is a commonly used metric to measure, and is often found in literature as simply *normalized intensity*. In this paper, we will only use this definition in Sec. 6.7, in the context of conventional, camera-based EFC.

- **SMF normalized intensity.** The power measured at the output of the SMF divided by the intensity measured at the output of the SMF centered on the non-coronagraphic star PSF. This is the main metric we use in this paper to assess the performance of the new algorithm.

- **Pixel Aperture normalized intensity.** The total intensity measured on an aperture on the camera of the size of the SMF, divided by the total intensity of the same aperture centered on the non-coronagraphic star PSF. We use this metric to effectively compare the new algorithm in terms of the intensity at the position of the fiber. This metric can be thought as the fiber normalized intensity of a multi-mode fiber, with an aperture the same size as the experiment's SMF.

The normalized intensity is equivalent to raw contrast when the throughput of the off-axis PSF at the angular separation of the planet is unaffected by the coronagraph.

6.5 Simulations

In order to validate the control algorithm presented above, we performed simulations in an end-to-end testbed simulation of the High Contrast Spectroscopy for Segmented

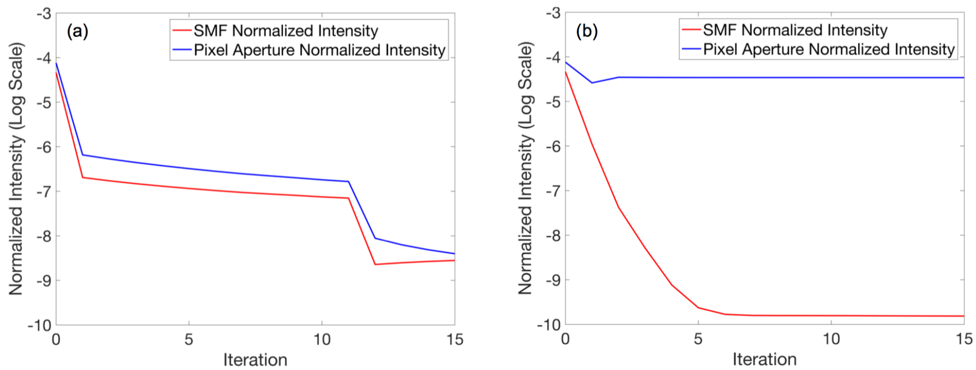

Figure 6.1 Simulations comparing (a) conventional EFC and (b) the new fiber-based algorithm. In both cases, the SMF normalized intensity (red line) is lower than the pixel aperture normalized intensity (blue line). The fiber-based EFC algorithm consistently yields deeper nulls in fewer iterations. The G matrix is recomputed at iteration number 11 in both cases. In the conventional EFC case in (a), the improvement is clearly seen. For the new algorithm, in (b), there is no significant improvement after the recalculation of the G matrix. All of the simulations assume polychromatic light with a spectral bandwidth of $\Delta\lambda/\lambda = 10\%$.

Telescopes Testbed (HCST) (Delorme et al., 2018; Jovanovic, Ruane, et al., 2018) in the Exoplanet Technology Laboratory (ET Lab) at Caltech where we have carried out the experimental tests described in the next section. This model is based on a MATLAB code that uses the PROPER (Krist, 2007) library to perform realistic propagations for coronagraph and adaptive optics systems. This model assumes a point source for the star and static aberrations. We use surface errors of 3 nm RMS per optic with randomly generated error maps based on a power spectral density function, calculated from measurements of HCST's optics. The model for the SMF is a 2D Gaussian of $1.4\lambda_0/D$ FWHM.

For monochromatic light at $\lambda = 650$ nm, we obtain almost perfect suppression of the coupling of the speckles through the SMF. In theory, the DM at the pupil plane has full control authority over the coupling of any monochromatic speckle through an SMF placed within the control area on the image plane.

We also simulated the new algorithm with polychromatic light with a $\Delta\lambda/\lambda = 10\%$ bandwidth, centered at $\lambda_0 = 650$ nm, and compared it to the performance of conventional EFC on the same setup and speckle field (see Fig. 6.1). In both simulations, we compute the power at the output of a SMF and the intensity read from the pixels of a simulated camera in the same image plane. We compare the SMF normalized

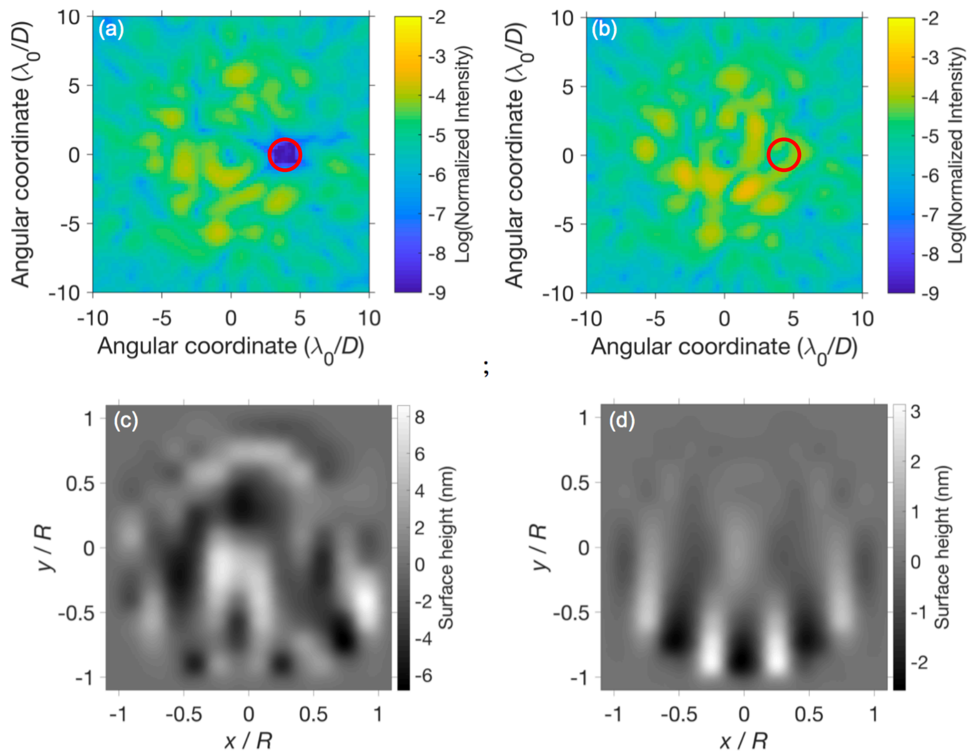

Figure 6.2 (a)-(b) Simulated stellar PSFs in log normalized intensity after running (a) conventional and (b) fiber-based EFC. (c)-(d) The corresponding DM shapes. The red circle indicates the control area for the case of conventional EFC and the position of the fiber for the case of fiber-based EFC, both centered at 4 λ_0/D from the center of the PSF.

intensity, calculated with the SMF, to the pixel aperture normalized intensity, calculated by integrating intensity over pixels (see Sec. 6.4). The performance of the new algorithm is consistently better in terms of final normalized intensity for different surface error maps on the optics than conventional EFC.

As we discussed in Sec. 6.3, the new algorithm does not try to eliminate the electric field at the fiber position; instead, it minimizes the overlap integral of the speckles with the fundamental mode of the SMF. Figure 6.2 shows the outcome of this important difference between the new algorithm presented here and conventional EFC. Although more light falls on the region of the SMF for the new algorithm (Fig. 6.2b) with respect to the conventional EFC result (Fig. 6.2a), there is less light coupling into the fundamental mode of the SMF, which is the ultimate goal. Since the cost function is less restrictive and the algorithm is not required to move the same amount of light from the region of the fiber, the DM strokes are also smaller.

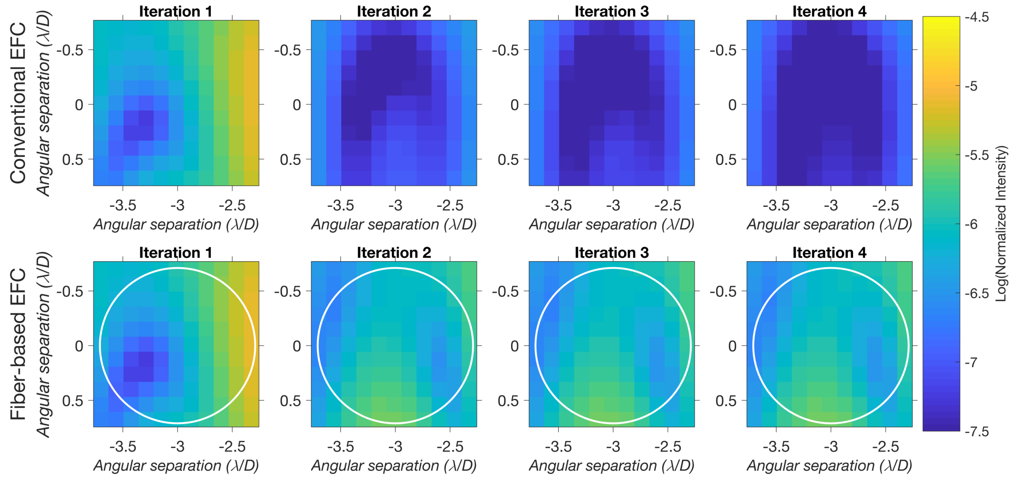

Figure 6.3 Zoom in on the region of the fiber for the simulations in Figs. 6.1-6.2. The first 4 iterations on a conventional EFC run (*top row*) show how EFC tries to suppress the intensity over the region. However, the new algorithm (*bottom row*) does not create a dark hole since it is only minimizing the overlap integral and converges to a solution is only a few steps. The white circle indicates the size of the mode of the fiber

Two main factors cause the difference in DM stroke: (1) the modal selectivity of the SMF helps relieve the overall work of the DM and (2) conventional EFC uses several resolution elements to effectively suppress the diffracted starlight in the region of the fiber making its cost function more restrictive.

In Figs. 6.3 and 6.4, we zoom in on the region of the fiber and compare the intensity and phase, respectively, for both a conventional and fiber-based EFC example case. Figure 6.3 shows that conventional EFC tries to suppress the amplitude of the electric field, and thus the intensity, creating a dark hole in the stellar speckle field. On the other hand, the fiber-based algorithm leaves a small amount of stellar intensity at the fiber position. However, comparing the phase of the residual stellar fields (see Fig. 6.4) demonstrates that the fiber-based algorithm converges to a state where the phase becomes asymmetric or singular at the fiber tip preventing the starlight from coupling into the SMF.

Response to tip-tilt errors

We analyze the sensitivity of the null to post-coronagraphic tip-tilt errors by adding offsets to the fiber before and after the nulling with the fiber-based EFC algorithm. When adding small position errors to the SMF before running the algorithm, the achieved normalized intensity remains on the order of the performance of the per-

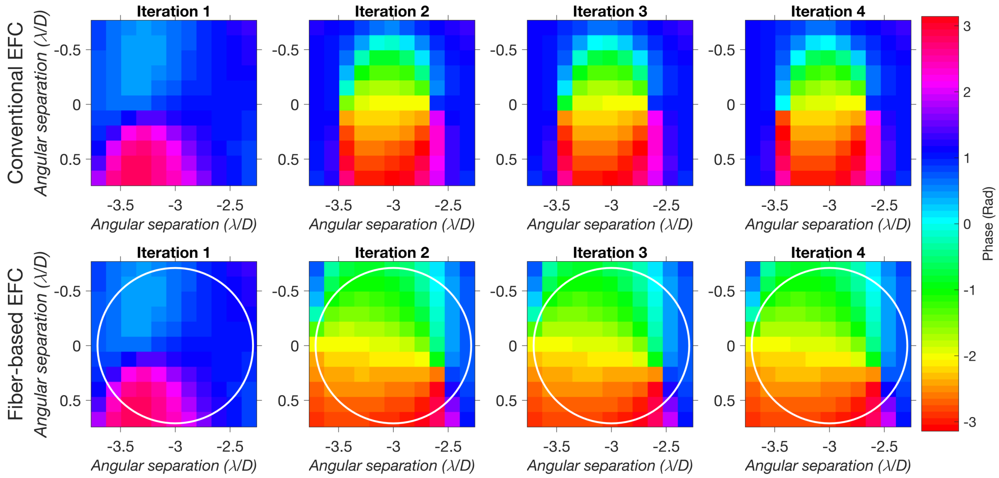

Figure 6.4 Same as Fig. 6.3, but showing the phase of the stellar field. In the conventional EFC case (*top row*), the phase over the region of the fiber does not obey any particular pattern since EFC works on suppressing the intensity at every position the region. On the other hand, the fiber-based algorithm (*bottom row*) converges to a field that is asymmetric across the fiber tip.

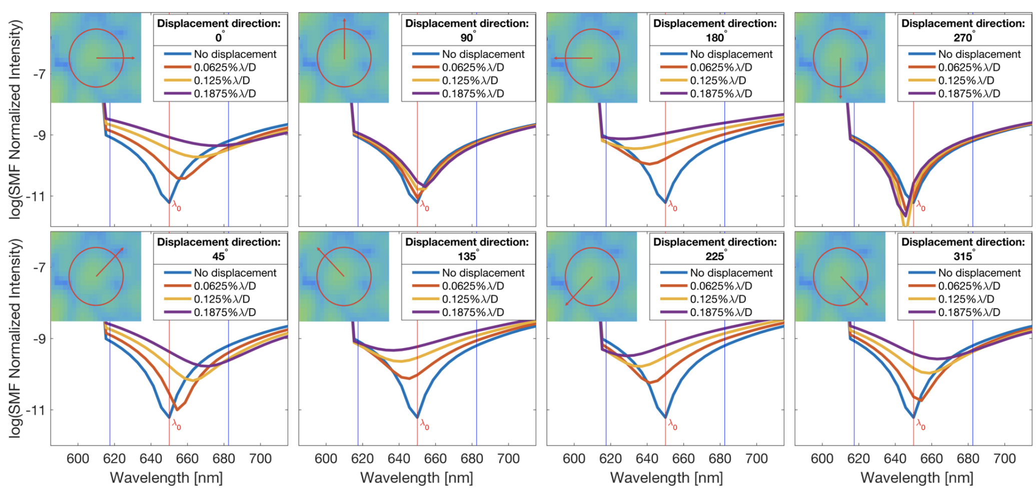

Figure 6.5 Simulation showing the effect of moving the SMF from its original position where the starlight is nulled in eight directions. We find the change in normalized intensity is chromatic and direction dependent. The red and blue lines indicate the central wavelength and the limits of the controlled bandwidth, respectively.

fectly aligned case. For instance, a position displacement of the order 1% of λ/D causes the algorithm to converge slower if the offset is not accounted for in the model and the final SMF normalized intensity is within a factor of two compared to the perfectly aligned case.

The response to tip-tilt errors after the null is produced is significantly worse. We simulate this by generating the null at a nominal position and, with the DM solution applied, we introduce small displacements to the SMF without further wavefront correction. Figure 6.5 shows eight cases corresponding to different displacement directions. We find that the response in the terms of normalized intensity is very chromatic under tip-tilt errors and that the direction of displacement has a significant effect on the degradation of the normalized intensity (compare e.g. 0° and 90° displacements). This is due to the structure of the phase that the DM solution induces in the image plane; some directions will still have a phase pattern that nulls the overlap integral. However, most directions of displacement are very sensitive, with a deterioration of one order of magnitude in the normalized intensity for a displacement of 0.2% of λ/D, and over two orders of magnitude for a displacement error of 1% of λ/D.

The phase solution that the DM induces at the tip of the fiber has to be asymmetric (see Fig. 6.4), as discussed by Por et al. (2018), this asymmetry can be of first order, second order, etc. depending on the phase structure that achieves the null. In general, the phase structure found by the algorithm is of first order, i.e., a phase ramp across the fiber tip, which causes a significant leak of light for small misalignments, and thus it is a more sensitive solution to tip-tilt errors. Although this is a limitation with respect to conventional EFC, future work will explore methods to reduce the tip-tilt sensitivity of the fiber-based solutions, including using a controller that initially reduces the intensity at the fiber before finding the best null using the overlap integral. For the purpose of this work, we demonstrate the current algorithm without attempting to reduce the sensitivity of the solution to tip-tilt errors.

6.6 Laboratory Setup

To validate the algorithm we performed experiments using the HCST-T (Mawet, Ruane, et al., 2017), an optical testbed consisting of an AO system, a coronagraph, and a FIU (see Fig. 6.6). The optics are mainly off-the-shelf transmissive lenses that are readily available.

For the monochromatic tests we use a laser diode at 635 nm; for the broadband tests we use a supercontinuum white light laser source (NKT Photonics SuperK EXTREME), filtered to provide a $\Delta\lambda/\lambda = 8\%$ bandpass at 625 nm. The light is fed into HCST-T by two source fibers (Thorlabs SM600 fibers), which simulate the star and planet. For this work, we will only make use of the star source. A

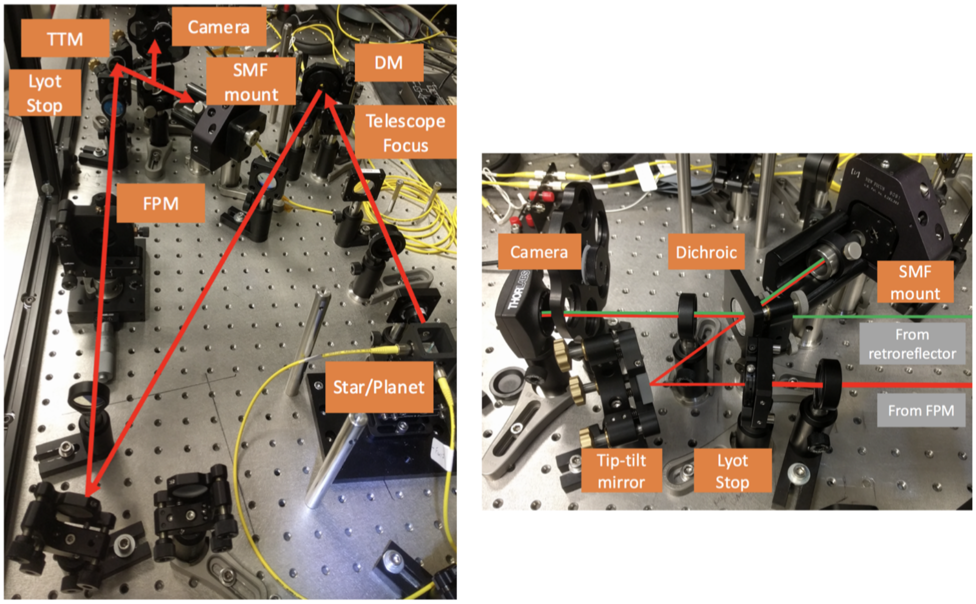

Figure 6.6 The HCST-T layout (*left image*) consists of two fiber-coupled sources to simulate a star and planet, an AO system with a deformable mirror (DM), a coronagraph with a focal plane mask (FPM) and a Lyot Stop, and a fiber injection unit (FIU) with a tip-tilt mirror (TTM), SMF mount, and a tracking camera. At the FIU (*right image*), the beam is steered by the TTM to align it with the SMF while the dichroic sends part of the incoming light to the tracking camera. The SMF can be used to back-propagate light into the system where it is reflected by the dichroic to a retroreflector such that the SMF is also imaged by the tracking camera for alignment and calibration purposes.

telescope simulator, with an aperture diameter of 4 mm, images the simulated star. In the AO system, a DM (Boston Micromachines Corporation multi-DM) controls the incoming wavefront. The DM has a continuous membrane surface with 12×12 actuators and a 400 μm actuator pitch. The beam illuminates a circular region 10 actuators in diameter. The specified average step size of the actuators is <1 nm.

The beam then passes through a 3-plane coronagraph, where the light is focused on to the focal plane mask (FPM). Our setup is equipped with a vortex coronagraph, which enables high-throughput, high-contrast imaging at small angular separations (Foo et al., 2005; Mawet, Riaud, et al., 2005). We use a charge 4 liquid crystal polymer vector vortex mask, which applies a phase ramp at the focus of the form $e^{\pm i4\theta}$. This FPM is optimized around 600 nm. The quality of a vector vortex phase mask is characterized by measuring the transmission between parallel circular polarizers to estimate the fraction of starlight with the incorrect phase. For the mask used here, the leakage is less than 0.15% and 0.11% for 635 nm and 625 nm, corresponding to the central wavelengths of the monochromatic and broadband experiments respectively. The beam is then collimated and clipped by an adjustable iris that serves as the Lyot stop and blocks approximately 15-20% of the full pupil area. The beam magnification between the DM and Lyot stop is 1:1.

Finally, a tip-tilt mirror (TTM) sends the beam into the FIU. The FIU system is nearly identical to the one described by Mawet, Ruane, et al. (2017) (see Fig. 6.6). The TTM is actuated in order to accurately align the beam to the SMF. A dichroic lets the majority of the light go through to the SMF and reflects some light to the tracking camera (Thorlabs CMOS DCC1545M). The camera is used for positioning the fiber, aligning the coronagraph mask, and to perform conventional pixel-based EFC, as shown in Sec. 6.7. The SMF is mounted on a five-axis stage (Newport 9091) behind a 7.5-mm focal length lens. At the output end of the SMF, the power coupled into the SMF is measured with a silicon photodiode (FEMTO OE-200-SI).

We measured the throughput of the FIU to be 55% by comparing the power measured upstream of the focusing lens to the output of the SMF. However, the ideal coupling for a circular aperture into a SMF with perfect optics is 82%. We identify various sources to account for the loss of throughput: the transmission of the focusing lens, transmission losses in the SMF, and the mismatch between the focal ratio, $F\#$, of the incoming beam and the optimum for our SMF. To isolate these effects, we removed all of the optics between the source and FIU and measured the low order aberrations upstream of the focusing lens using a Shack-Hartmann wavefront sensor (Thorlabs WFS150-5C). In our numerical simulation, we introduced the measured aberrations to the simulated wavefront and took into account the mismatch between the $F\#$ of the last lens and the optimal $F\#$ for the fiber. The result was consistent with the measured losses in our system; the main cause of throughput loss being the coupling of the suboptimal $F\#$.

6.7 Results

Conventional EFC Tests

In order to assess the wavefront control capabilities of HCST-T, we first performed conventional camera-based EFC tests. Although speckle nulling has been previously demonstrated by our team using this setup, both using the camera and an SMF (Mawet, Ruane, et al., 2017), EFC is a significantly different algorithm. EFC relies on an estimate of the electric field at the image plane, an accurate model of the system, and low level of aberrations so that the response of the system to changes in the plane of the DM is linear in image plane field amplitude (Give'On, 2009). Given that HCST-T consists of off-the-shelf transmissive optics, the low order aberration regime is not guaranteed; indeed, our starting focal plane location at 4 λ/D is of the order of 10^{-4} normalized intensity. Besides, although the DM has a total of 12×12 actuators, the pupil is clipped at the DM plane and only 10×10 actuators are available, therefore, the control radius is limited to 5 λ/D.

In Fig. 6.7, we show the results for the tests on conventional camera-based EFC. The control area, or dark hole (DH), is a 3×3 pixel box centered at approximately 4 λ/D from the PSF; the resolution at the camera is of 3.2 pixels per λ/D approximately. We achieve a modest normalized intensity of 10^{-4}. The limited performance is attributed to having a low fidelity model of the physical system, to both estimate the electric field and to compute the G matrix of the system.

The shape of the DM, according to our model, agrees well with our expectation for a small DH at 4 λ/D, consisting of a distinct sinusoidal shape at the corresponding spatial frequency (see Fig. 6.7 (b)). The discrepancy between this shape and the shapes found via simulations (see Fig. 6.2 (c)) can be explained by the fact that in the laboratory, after achieving a certain normalized intensity, an order of magnitude lower than the vicinity of the control area, the electric field becomes increasingly hard to sense: the intensity modulation starts to worsen, and the limited dynamic range of the detector makes it harder to calibrate the probes. Therefore the algorithm fails to find a better shape for the DM. The RMS surface height of the DM solution within the pupil is $3.3nmRMS$.

Monochromatic Light Results

Figure 6.8 shows a laboratory demonstration of the new algorithm, in which a suppression of a factor of ∼100 is achieved through the SMF. The final SMF normalized intensity is 3×10^{-6}. Figs. 6.8 (c) and (d) show the coronagraphic PSF before and after correction, and Fig. 6.8 (b) shows the solution for the DM. The SMF is placed at approximately 4 λ/D to avoid PSF distortion effects at smaller angular separations due to the FPM and to stay within the 5 λ/D control radius afforded by the available 10×10 actuators at the DM plane.

The improved performance of the new algorithm compared to the tests presented in Sec. 6.7 can be explained by the two reasons discussed in Sec. 6.5. Indeed, the nature of the problem is different and the DM is only restricted to one control

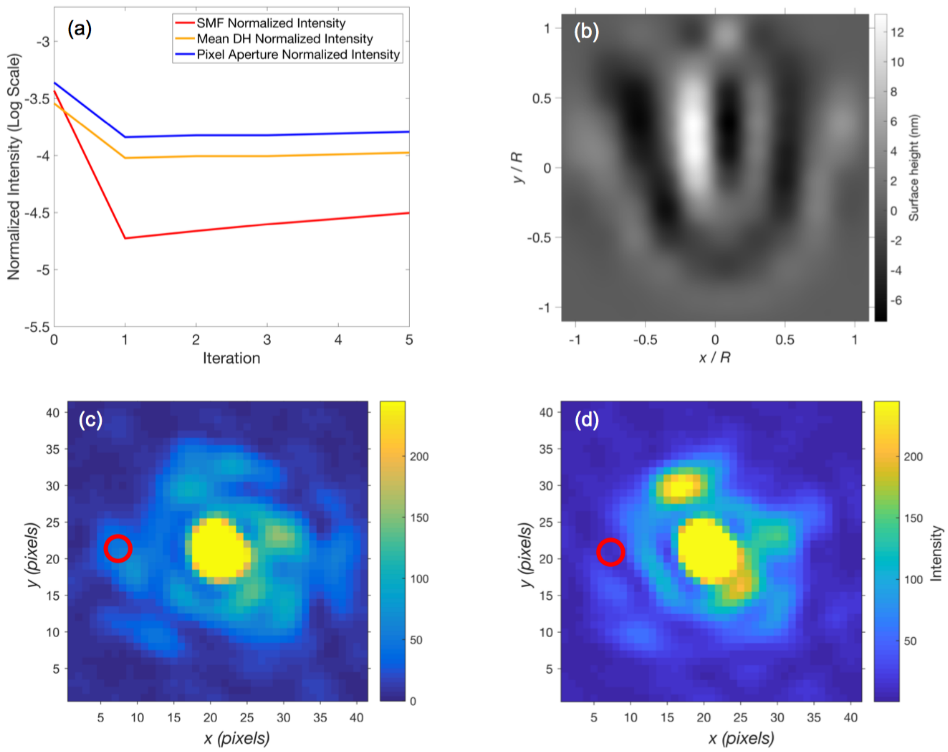

Figure 6.7 Laboratory results for conventional EFC experiments on HCST-T. (a) normalized intensity versus iteration, (b) the DM shape solution according to our model, and (c)-(d) the coronagraphic PSF before and after correction, respectively. The normalized intensity achieved is likely limited by the high levels of aberration and the model uncertainty. In (a), the SMF normalized intensity is also plotted although the control is entirely done with the camera. The SMF normalized intensity is always better thanks to the modal selectivity of the SMF. The final solution of the DM (b) has the expected shape, given the small size of the dark hole (DH), with a distinct sinusoidal shape at the spatial frequency corresponding to the position of the DH. In (c) and (d), a 3×3 pixel box located at the center of the red circle is the control area, or the DH in which EFC is trying to null.

element. Furthermore, the sensing of the electric field is more favorable when using the new algorithm. This is because the probes used to sense the overlap integral are just sinusoids on the DM, or satellite speckles at the image plane. Their effect on the change on the overlap integral is more robust, given the modal selectivity of the SMF. As found via simulations (see Sec. 6.5), the values of the actuator strokes on the DM are significantly smaller, with respect to the solution for conventional camera based EFC. The RMS surface height of the DM solution within the pupil is $2.2nmRMS$. Hence, the effect of this DM solution on the Strehl ratio will be more favorable with respect to conventional EFC. However, the presence of the

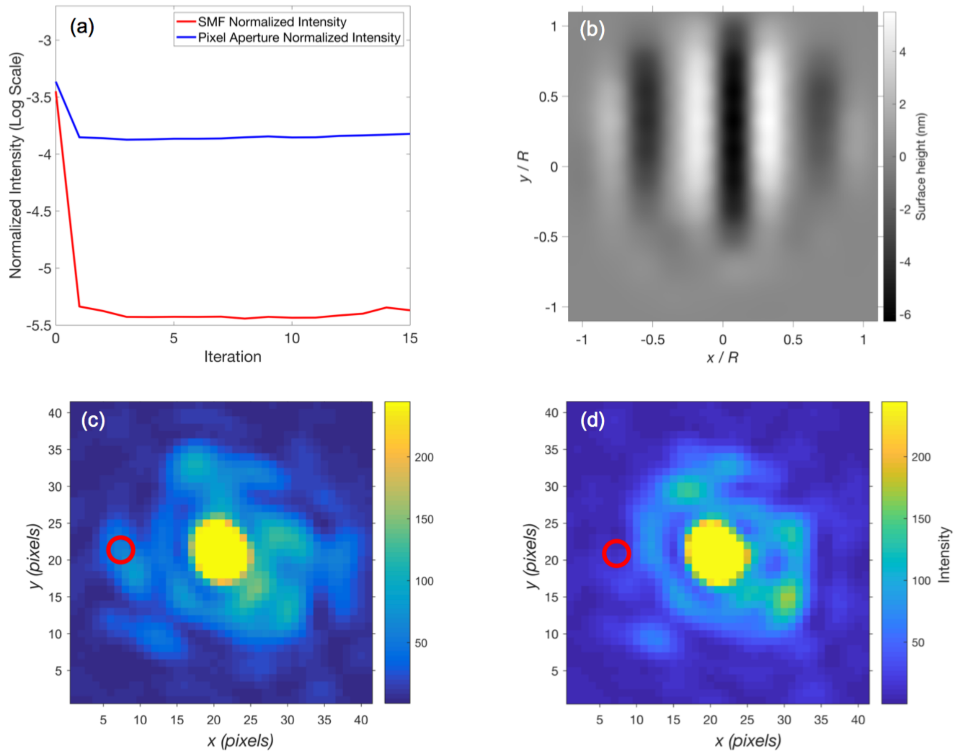

Figure 6.8 Same as Fig. 6.7, but for monochromatic fiber-based EFC experiments. The main features of the curves in (a) are as predicted by the simulations: the algorithm reaches its final normalized intensity after only a few iterations and the normalized intensity on the camera is >10× the SMF normalized intensity. The DM solution in (b) is very similar to the solutions found via simulations. The main features of the DM shape are found at the first iteration, the following iterations are just minimal adjustments. The red circle in (c) and (d) indicates the position of the SMF.

vortex coronagraph, and the fact that we work at 4 λ/D, will degrade the coupling efficiency into the fiber. The difference between achieved normalized intensity for the intensity and for the SMF normalized intensity as expected from the simulations is reproduced in the laboratory (see Fig. 6.8(a)).

Polychromatic Light Results

We performed polychromatic light experiments with the new algorithm using a $\Delta\lambda/\lambda$=8% bandwidth centered at λ_0=625 nm. The algorithm remains unchanged; i.e., it only aims at controlling the central wavelength while the full band of the light is fed into system at once. The only change in the setup is the use of a different light source; we connected the supercontinuum source with a 50 nm bandpass filter.

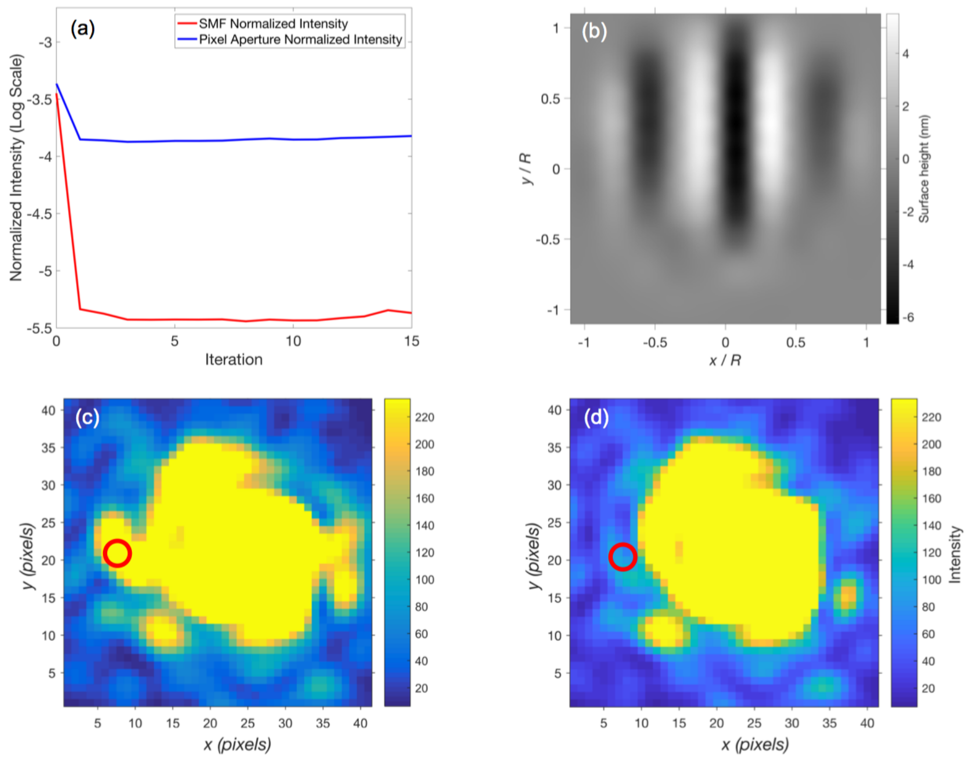

Figure 6.9 Same as Fig. 6.8, but for polychromatic light. The normalized intensity achieved is 5 times worse than the monochromatic experiment. The fact that we are controlling only the central wavelength is a primary cause of the deteriorated performance. The DM solution in (b) remains almost identical to the case of monochromatic light. The camera images of the coronagraphic PSF (c) and (d) show how more light gets leaked into the image plane.

We show in Fig. 6.9 that we obtained a SMF normalized intensity of 1.6×10^{-5}, a degradation of a factor of 5 in terms of normalized intensity with respect to the monochromatic case. Due to the larger bandwidth, the effect of the FPM is significantly limited, and more light passes through the mask due to the chromatic leakage. However, the algorithm is still able to control some of the light as can be seen from the contrast curves. The RMS surface height of the DM solution within the pupil is $2.0 nmRMS$.

Considerations on the control performance

The achieved normalized intensity in the experiments presented in the previous sections is far from reaching the noise floor of the detector, which sets the limit of SMF normalized intensity to a level of $\sim 1 \times 10^{-12}$. Furthermore, the simulations for the new algorithm predict an almost perfect suppression of residual starlight in monochromatic light. The limitations on the performance of our experiments can be explained by discrepancies between the model used in the algorithm and the real optical system. EFC needs an accurate model to build the G matrix of the system and to get an accurate estimation of the electric field (or overlap integral). Discrepancies between model and optical system are a commonly known problem when implementing EFC, and an important limitation for the achievable contrast (Marx et al., 2017).

We identify some specific sources of model uncertainty on HCST-T:

- The vector vortex coronagraph imparts conjugated $e^{\pm i4\theta}$ phase ramps on input orthogonal circular polarization states. Our EFC-based controller can only control one state and thus one phase ramp at a time, leaving non-common path aberrations uncorrected.
- The quality of the transmissive optics coupled with the uncertainties on the alignment of the system. Since the model used for running the control algorithm relies on Fourier transforms for a flat wavefront, the model uncertainties arising from the aberrations on the optics and the errors in the alignment are not properly accounted for.
- The Lyot stop position and shape. There is uncertainty on the exact position of the Lyot stop with respect to the conjugated entrance pupil plane. In our model the aperture plane is perfectly conjugated with the Lyot stop plane. Furthermore, the aperture of the Lyot stop is a manual, adjustable iris, which results in an uncertainty on the amount of light clipped by the Lyot stop. In the model, the beam is assumed to be perfectly circular, but in the real setup the beam may be somewhat noncircular. This has an effect on the shape of the PSF and, thus, on the coupling with the SMF.
- The DM shape uncertainty. Although we do not find any limitation in our simulations in monochromatic light, which assumes a perfect DM, there may be shape errors in the form of actuator response errors, or inter-actuator coupling related errors. The influence function used is not measured from our DM; rather, we use a smooth shape similar to a Gaussian.
- The uncertainties regarding the coupling of the light with the SMF. Although we can account for the losses in the coupling at the FIU, as discussed in Sec. 6.6, the effect on the algorithm of factors such as the modeling of the

fundamental mode of the SMF, or the photonic effects in the SMF itself, are poorly understood.

Some other suspected reasons for the limitation in the laboratory performance of the algorithm are:

- The DM control authority. A 12×12 actuator DM is severally limited in the range of shapes it can reproduce, specially at high spatial frequencies near the Nyquist limit.
- The limitations on the SMF position. As discussed in Sec. 6.7, the range of positions in which we can place the SMF with respect to the PSF is limited by the number of DM actuators across the pupil and the inner working angle of the FPM. In practice, we place the SMF at approximately 4 λ/D from the central PSF. At this spatial frequency, if we apply a satellite speckle with the DM in both the laboratory and the model, we can see a significant difference in the shape of the speckle due to the effect of the FPM.
- The stability of the setup. Although HCST-T is equipped with a full solid enclosure and the PSF in the camera appears to be very stable, the coupling into the SMF is extremely sensitive. The deviations of the SMF from its original position are not monitored, but the effect of changes in the SMF position could be detrimental, especially in the sensing stage. In Sec. 6.5, we found the null through the SMF to be very sensitive to jitter, which imposes strict requirements on post-coronagraph tip-tilt control.

6.8 Perspectives

After having demonstrated this new algorithm on the HCST-T, we plan to move the experiment to the superior HCST-R(Jovanovic, Ruane, et al., 2018). Equipped with custom reflective optics and a BMC kilo-DM with 34 actuators across the pupil, HCST-R has excellent potential for exploring novel high-contrast technologies. We have achieved a normalized intensity of 5×10^{-8} using a simple camera-based speckle nulling technique, our plan is to include an FIU at the image plane of HCST-R and achieve very high contrast in polychromatic light through an SMF.

A Kalman Filter was implemented for speckle nulling by Xin et al. (Xin et al., 2018), in which the control history, and previous measurements, were used to achieve a more stable null through the SMF and an overall better normalized intensity. A

Kalman Filter Estimator for EFC was demonstrated by Groff et al. 2013 (Groff and Kasdin, 2013), for a faster suppression of the electric field of the starlight in an EFC dug dark hole, with further improvement by adding an extended Kalman Filter by Riggs et al. 2016(A. J. E. Riggs et al., 2016). This technique may be directly applied to the case of EFC for an FIU, and we plan to demonstrate this on HCST-R. Predictive control is particularly important in the presence of atmospheric turbulence and other types of disturbances such as vibrations and thermal drifts; a Kalman Filter approach, which can account for the nature of the speckle evolution in the image plane, is a very promising technique.

We also plan on demonstrating this technique on sky with the Keck Planet Imager and Characterizer (KPIC) (Mawet, Delorme, et al., 2017) at the W.M. Keck Observatory. KPIC consists of a series of upgrades to the Keck II adaptive optics system and instrument suite, including an FIU to high-resolution infrared spectrograph NIRSPEC. In addition to its unique science capabilities, KPIC is also intended as a path to mature key technologies, such as high dispersion coronagraphy (HDC) (Kawahara et al., 2014; Sparks et al., 2002; Snellen et al., 2015; Kok et al., 2014; Wang, Mawet, Ruane, et al., 2017; Mawet, Ruane, et al., 2017), for future space based telescopes and large ground-based telescopes such as the Thirty Meter Telescope. KPIC is a perfect instrument to test this algorithm on sky.

In the limiting case where stellar photon noise originating from quasi-static aberrations is dominating (e.g. HR8799's planet infrared spectroscopy with KPIC), the corresponding exposure time gain is $\tau \propto \eta_s/\eta_p^2$ (see Ruane et al. (2018)), where η_s, and η_p are the fraction of residual star and detected planet light, respectively. The achieved stellar signal suppression of $\sim$100 shown in this paper, would translate into a reduction of $\sim$100 in necessary exposure time. This algorithm, if running fast enough, and/or combined with a Kalman filter could also address dynamic atmospheric residuals. This will be the subject of a forthcoming paper.

6.9 Conclusion

We have presented an algorithm, based on EFC, to achieve improved suppression through a SMF. We performed simulations to assess the performance of the algorithm and its sensitivity to position errors and jitter, and tested it in the laboratory where we obtained a normalized intensity through the SMF of 3×10^{-6} in monochromatic light at 635 nm, and 2×10^{-5} in 8% broadband light at 625 nm. The wavefront control algorithm presented here is designed to take advantage of the SMF's spatial selectivity, thus is perfectly suited for an HDC system (Wang, Mawet, Ruane, et al., 2017; Mawet, Ruane, et al., 2017). The promising results obtained from simulations, and the lessons learned from applying EFC in the laboratory on HCST-T, will help us achieve the significantly deep contrast levels on our improved HCST-R testbed. The stellar suppression gains obtained by this technique directly reduce the exposure time needed for stellar photon noise limited cases (see Sec. 6.8), since the Strehl ratio is practically unaffected by the DM solution (see Sec. 6.7). Applying this algorithm in practice on future telescopes may enable the detection of spectral signatures associated with individual molecules and potential signs of life (Wang, Mawet, Hu, et al., 2018).

BIBLIOGRAPHY

Delorme, J. R. et al. (2018). “High-contrast spectroscopy testbed for segmented telescopes”. In: *Proc. SPIE* 10400, p. 104000X. DOI: 10.1117/12.2274893.

Foo, G., D. M. Palacios, and G. A. Swartzlander (2005). “Optical vortex coronagraph”. In: *Opt. Lett.* 30, pp. 3308–3310. DOI: 10.1364/OL.30.003308.

Gaudi, B. S. et al. (2018). “The Habitable Exoplanet Observatory (HabEx) Mission Concept Study Interim Report”. In: *ArXiv e-prints*, p. 1809.09674.

Give’On, A. (2009). “A unified formailism for high contrast imaging correction algorithms”. In: *Proc. SPIE* 7440, p. 74400D. DOI: 10.1117/12.825049.

Groff, T. D. and N. J. Kasdin (2013). “Kalman filtering techniques for focal plane electric field estimation”. In: *J. Opt. Soc. Am. A* 30, p. 128. DOI: 10.1364/JOSAA.30.000128.

Groff, T. D., A. Riggs, et al. (2016). “Methods and limitations of focal plane sensing, estimation, and control in high-contrast imaging”. In: *J. Astron. Telesc. Instrum. Syst.* 2.1, p. 011009. DOI: 10.1117/1.JATIS.2.1.011009.

Guyon, O. (2018). “Extreme Adaptive Optics”. In: *Annu. Rev. Astron. Astrophys.* 56, pp. 315–355. DOI: 10.1146/annurev-astro-081817-052000.

Hill, J. M. et al. (Dec. 1980). “Multiple object spectroscopy - The Medusa spectrograph”. In: *Astrophysical Journal, Letters* 242, pp. L69–L72. DOI: 10.1086/183405.

Jovanovic, N., O. Guyon, et al. (July 2014). “How to inject light efficiently into single-mode fibers”. In: *Proc. SPIE*. Proceedings of the SPIE 9147, 91477P, 91477P. DOI: 10.1117/12.2057210.

Jovanovic, N., G. Ruane, et al. (2018). “High-contrast spectroscopy testbed for Segmented Telescopes: instrument overview and development progress”. In: *Proc. SPIE* 10702, 107024E. DOI: 10.1117/12.2314325.

Jovanovic, N., C. Schwab, et al. (Aug. 2017). “Efficient injection from large telescopes into single-mode fibres: Enabling the era of ultra-precision astronomy”. In: *Astronomy and Astrophysics* 604, A122, A122. DOI: 10.1051/0004-6361/201630351. arXiv: 1706.08821 [astro-ph.IM].

Kawahara, H. et al. (June 2014). “Spectroscopic Coronagraphy for Planetary Radial Velocimetry of Exoplanets”. In: *The Astrophysical Journal Supplement Series* 212.2, p. 27. DOI: 10.1088/0067-0049/212/2/27.

Kok, R. J. de et al. (Jan. 2014). “Identifying new opportunities for exoplanet characterisation at high spectral resolution”. In: *Astronomy and Astrophysics* 561, A150, A150. DOI: 10.1051/0004-6361/201322947. arXiv: 1312.3745.

Krist, J. E. (2007). "PROPER: an optical propagation library for IDL". In: *Proc. SPIE* 6675, 66750P. DOI: 10.1117/12.731179.

Marx, D. et al. (2017). "Electric field conjugation in the presence of model uncertainty". In: *Proc. SPIE* 10400, 104000P. DOI: 10.1117/12.2274541.

Mawet, D., J. R. Delorme, et al. (2017). "A fiber injection unit for the Keck Planet Imager and Characterizer". In: *Proc. SPIE* 10400, p. 1040029. DOI: 10.1117/12.2274891.

Mawet, D., P. Riaud, et al. (2005). "Annular Groove Phase Mask Coronagraph". In: *Astrophys. J.* 633, pp. 1191–1200. DOI: 10.1086/462409.

Mawet, D., G. Ruane, et al. (2017). "Observing Exoplanets with High-dispersion Coronagraphy. II. Demonstration of an Active Single-mode Fiber Injection Unit". In: *Astrophys. J.* 838, p. 92. DOI: 10.3847/1538-4357/aa647f.

Por, E. H. and S. Y. Haffert (Mar. 2018). "The Single-mode Complex Amplitude Refinement (SCAR) coronagraph: I. Concept, theory and design". In: *arXiv e-prints*. arXiv: 1803.10691 [astro-ph.IM].

Riggs, A. J. E., N. J. Kasdin, and T. D. Groff (2016). "Recursive starlight and bias estimation for high-contrast imaging with an extended Kalman filter". In: *J. Astron. Telesc. Instrum. Syst.* 2.1, p. 011017. DOI: 10.1117/1.JATIS.2.1.011017.

Ruane, G. et al. (Jan. 2018). "Vortex coronagraphs for the Habitable Exoplanet Imaging Mission concept: theoretical performance and telescope requirements". In: *Journal of Astronomical Telescopes, Instruments, and Systems* 4, 015004, p. 015004. DOI: 10.1117/1.JATIS.4.1.015004. arXiv: 1803.03909 [astro-ph.IM].

Schwab, C. et al. (Apr. 2014). "Single Mode, Extreme Precision Doppler Spectrographs". In: *Proc. SPIE*. IAU Symposium 293. Ed. by N. Haghighipour.

Snellen, I. et al. (Apr. 2015). "Combining high-dispersion spectroscopy with high contrast imaging: Probing rocky planets around our nearest neighbors". In: *Astronomy and Astrophysics* 576, A59, A59. DOI: 10.1051/0004-6361/201425018.

Sparks, W. B. and H. C. Ford (Oct. 2002). "Imaging Spectroscopy for Extrasolar Planet Detection". In: *Astrophysical Journal* 578, pp. 543–564. DOI: 10.1086/342401. eprint: astro-ph/0209078.

Spergel, D. et al. (2015). "Wide-Field InfrarRed Survey Telescope-Astrophysics Focused Telescope Assets WFIRST-AFTA 2015 Report". In: *ArXiv e-prints*, p. 1503.03757.

The LUVOIR Team (2018). "The LUVOIR Mission Concept Study Interim Report". In: *ArXiv e-prints*, p. 1809.09668.

Wang, J., D. Mawet, R. Hu, et al. (2018). “Baseline requirements for detecting biosignatures with the HabEx and LUVOIR mission concepts”. In: *J. Astron. Telesc. Instrum. Syst.* 4.3, p. 035001. DOI: 10.1117/1.JATIS.4.3.035001.

Wang, J., D. Mawet, G. Ruane, et al. (Apr. 2017). “Observing Exoplanets with High Dispersion Coronagraphy. I. The Scientific Potential of Current and Next-generation Large Ground and Space Telescopes”. In: *Astron. J.* 153, 183, p. 183. DOI: 10.3847/1538-3881/aa6474. arXiv: 1703.00582 [astro-ph.EP].

Xin, Y. et al. (2018). “Demonstration of a Speckle Nulling Algorithm and Kalman Filter Estimator with a Fiber Injection Unit for Observing Exoplanets with High-dispersion Coronagraphy”. In: *Proc. SPIE* 10703, 107036Z.

Chapter 7

WAVEFRONT SENSING AND CONTROL WITH A SINGLE MODE FIBER II: BROADBAND EXPERIMENTS

Llop-Sayson, J. et al. (2021). “Laboratory Demonstration of Wavefront Control through a Single Mode Fiber over a 20% Bandwidth for the Characterization of Exoplanet Atmospheres”. In: *Submitted to Journal of Astronomical Telescopes, Instruments, and Systems*.

ABSTRACT

To address the fundamental questions of exoplanetary science, future space-based observatories will have to obtain quality spectra of a large enough set of Earth-like planets around main sequence stars. Although coronagraph instruments provide the necessary observational efficiency to probe many systems with respect to a starshade observation, they typically suffer from a limited achievable bandwidth at the necessary contrast and relatively poor throughput to off-axis sources. This is mainly due to the fact that the starlight is suppressed within the optical system, so the quasi-static aberrations from optical imperfections are the dominant term and need to be dealt with deformable mirrors. The DMs have limited capabilities to achieve large bandwidths, and their high stroke after corrections is highly detrimental to the Strehl ratio of off-axis sources. A technological path to overcome these issues is the use of single mode fibers (SMFs). Coupling the planet light into an SMF to feed a high resolution spectrograph has been shown to improve the final signal-to-noise ratio. Furthermore, it has been shown that it is more favorable to do broadband wavefront control with SMFs when exploiting their modal selectivity; the DMs have to work less so the bandwidth is improved and the off-axis throughput is better. Here we demonstrate the potential of this technology by performing wavefront control through an SMF over a 20% bandwidth at the High Contrast Spectroscopy Testbed achieving 2.5×10^{-8} raw contrast.

7.1 Introduction

The answer to some of the fundamental questions in exoplanetary science seems to be within our reach in the next decades. Is there life on other planets? How common are Earth-like planets? How do other worlds come to be? NASA mission concepts HabEx (The HabEx Team, 2019) and LUVOIR (The LUVOIR Team, 2019) intend to address these questions. To do so, these missions will probe nearby planetary systems with the aim of obtaining an effective census of the galactic vicinity's ecosystem. Of particular interest are solar-type stars, which may host planets analogous to our own. The outcome of such missions, combined with future ground-based observatories scientific output (Lopez-Morales et al., 2019; Fitzgerald et al., 2019; Carlomagno et al., 2020; Brandl et al., 2021), will determine the success of comparative exoplanet research.

Detecting and characterizing Earth-like exoplanets (or exoEarths) poses an enormous technological challenge. An Earth-sized planet orbiting a Sun-like star is of the order of 10^{-10} fainter than its host. Furthermore, to detect biosignatures in their atmospheres, spectra have to be obtained over large bandwidths with high resolution. For HabEx and LUVOIR it is estimated that the detection of the most compelling molecules in an exo-atmosphere will typically take over 100 hours (J. Wang et al., 2018). Moreover, it is not sufficient to detect biomarkers in one exoEarth candidate, our conclusions on the fundamental questions mentioned above depend on the sample size of these candidates (Stark et al., 2019). Given these considerations, HabEx and LUVOIR teams have examined the benefits of a hybrid coronagraph and starshade mission. A coronagraph instrument, given its observation efficiency, would obtain astrometry of exoEarth candidates for their orbital characterization, and atmospheric spectra at modest bandwidths, and the starshade would follow up obtaining high resolution spectra more efficiently given its higher throughput. The expected yield of these missions is 10-50 Earth-like planets in the habitable zone around main sequence stars, depending on telescope and general mission parameters (Stark et al., 2019; Sandora et al., 2020).

The use of single mode fiber (SMF) technology provides a potential path to increasing the yield of exoplanet census missions with internal coronagraphs. An SMF in the image plane is used to retrieve the light from the exoplanet and send it to a spectrograph. Improved signal-to-noise ratio can be achieved in this way due to the mode selectivity of the fiber (Jovanovic, Schwab, et al., 2017; Mawet, Ruane, et al., 2017), which helps filter out the stellar speckles. This concept is already in use at the Keck observatory with the Keck Planet Imager and Characterizer (KPIC) (J.-R. Delorme et al., 2021). KPIC is already producing spectroscopic exoplanet science thanks to its unprecedented capabilities (J. J. Wang et al., 2021). In addition, an SMF in the image plane of a coronagraph instrument has been shown to be more favorable to broadband light when it comes to doing active wavefront control as well (Coker et al., 2019). This is particularly interesting to the subject of maximizing the yield for a given mission since coronagraph instruments typically suffer from not being able to achieve high contrast over broad bandwidths.

In this work we demonstrate a 20% bandwidth null through an SMF at 10^{-8} raw contrast levels in an in-air testbed environment. This result illustrates the potential of SMFs for broadband light wavefront control. In Sec. 7.2 we give an overview of the wavefront control algorithm we use. In Sec. 7.3 we present an evaluation of one of the main limitations of SMF, which is tip and tilt errors. In Sec. 7.4 the laboratory setup is presented, and in Sec. 7.5 we report the results.

7.2 Wavefront Sensing and Control Algorithm

The wavefront control algorithm we use to null the intensity that couples into the fiber is an adaptation of the electric field conjugation (EFC) (Give'on et al., 2007) algorithm. EFC, as originally conceived, uses an estimation of the electric field in the image plane to produce a deformable mirror (DM) solution that cancels that electric field. The intensity is thus minimized in a given set of pixels, or dark hole. The modified EFC algorithm for an SMF (abbreviated here to EFC-SMF) follows the same formalism as conventional EFC with the key difference being that, instead of addressing the actual electric field in the image plane, the main focus is on the overlap integral of this electric field with the fundamental mode of the fiber. Indeed, the intensity at the output of an ideal SMF is:

$$I_{SMF} = \left| \int E_{im} \Psi_{SMF} da \right|^2 , \tag{7.1}$$

where Ψ_{SMF} is the shape of the fundamental mode of the fiber and E_{im} is the electric field at the image plane. We refer to our previous paper, Llop-Sayson, Ruane, Mawet, Jovanovic, Calvin, et al. (2019), for a more detailed explanation of the algorithm.

Therefore, EFC-SMF is unconcerned with the intensity in the image plane; in other words, there is no dark hole digging, the controller finds a solution that cancels the overlap integral. This algorithm finds a phase pattern at the tip of the SMF that impedes the coupling of diffracted light into the fiber. For instance, the DM generates a phase ramp which, given its asymmetry over the fiber tip, cancels the overlap integral. In general, any asymmetric phase solution with respect to the SMF center ensures zero coupling. This kind of solutions are typically easier to achieve with the wavefront controller: (1) since the SMF corresponds to a single location in the focal plane, the controller needs only to control the corresponding spatial frequency in the pupil (as opposed to many for normal size DH, and (2) the null condition through the overlap integral is relaxed and allows for multiple DM solutions. Therefore, the DM requires significantly less stroke to achieve a high contrast solution through the SMF with respect to digging a DH (Llop-Sayson, Ruane, Mawet, Jovanovic, Calvin, et al., 2019; Llop-Sayson, Jovanovic, et al., 2020). Furthermore, with EFC-SMF, the broadband solution is easier to obtain over broader bandwidths for the same reasons (Coker et al., 2019).

The implementation of EFC-SMF to work with broadband light follows the exact same approach as in conventional EFC (Give'on et al., 2007); sub-bandpass channels are added to the control matrix, and the solution is the optimal DM solution, in the least-squares sense. The algorithm presented in this section is implemented with the Fast Linear Least-Squares Coronagraph Optimization (FALCO) (Riggs et al., 2018) software package[1], which is used for simulations and testbed experiments.

7.3 Control bandwidth effect on tip and tilt error robustness

An important limitation in achieving and maintaining high contrast levels through an SMF is the tip and tilt (abbreviated T/T) errors (Coker et al., 2019). We find that monochromatic results of EFC-SMF are very sensitive to T/T errors (as is discussed in Sec. 7.5), and multi-wavelength results, given the averaging nature of the EFC solution regarding multi-wavelength treatment, are more robust. We simulate different bandwidths to evaluate post-control T/T errors and verify this: the broader the bandpass in EFC-SMF, the more robust the solution is to post-control T/T errors. In Fig. 7.1 we illustrate this with simulations, we plot the wavefront control results for 4 different bandwidths where the SMF has moved with respect to the original null position and the raw contrast is evaluated at those error positions. The 20% bandwidth solution, although its original null is not as high, is clearly superior in terms of robustness to smaller bandwidths. These simulations are performed with FALCO; the entrance pupil is a defined amplitude map based on a pupil image from the laboratory, all simulations run for 10 EFC-SMF iterations, and

[1] https://github.com/ajeldorado/falco-matlab

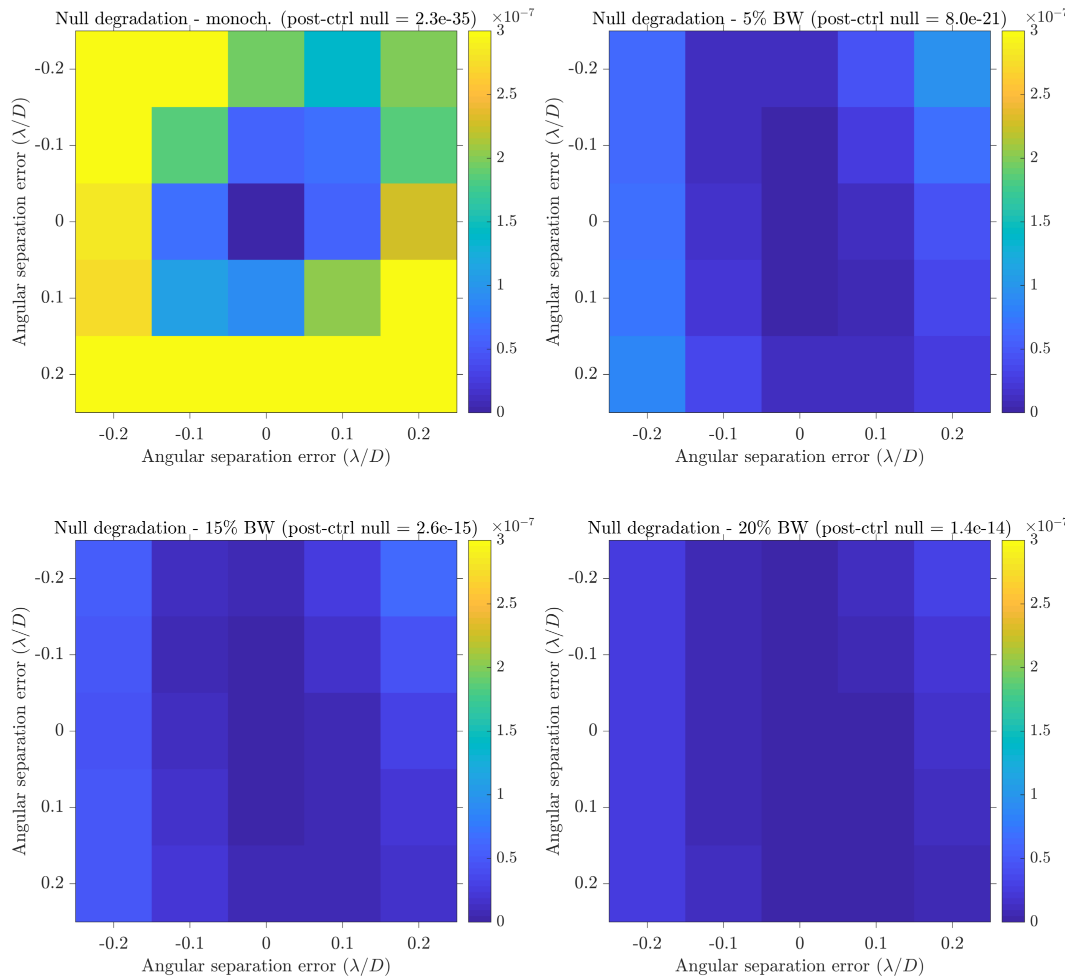

Figure 7.1 We run EFC-SMF simulations for 4 different bandwidths for a set number of iterations and evaluate the solution moving the SMF on a 3×3 grid of positions around the original SMF center. While the final solution is deeper in contrast for smaller bandwidths, the robustness to these errors is clearly improved with larger bandwidth: the broader the control bandwidth the more robust the solution is to tip and tilt errors.

depending on the bandwidth we select a number of sub-bandpasses, for instance, the 20% bandwidth run is performed with 11. The evaluation of the raw contrast is done with the same amount of sub-bandpasses, more details on how we measure raw contrast are given in Sec. 7.5.

In Fig. 7.2 we take a closer look at the case of 20% bandwidth. After obtaining a null via EFC-SMF, we can tolerate a T/T error of 0.1 λ/D before reaching a null degradation greater than 1×10^{-8}.

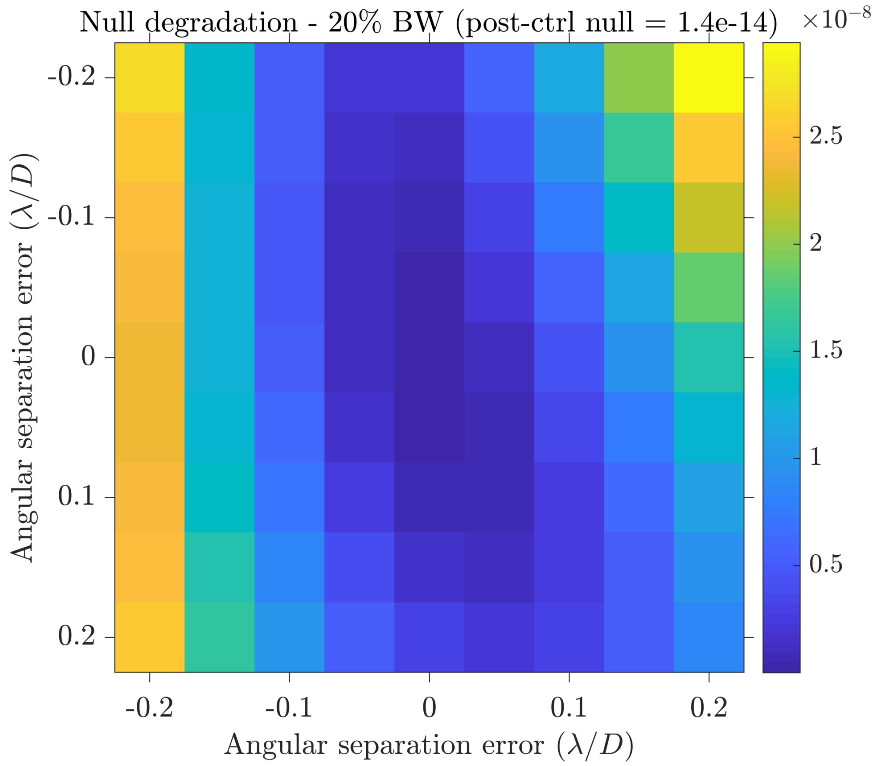

Figure 7.2 We inspect the T/T sensitivity for the case of a 20% bandwidth EFC-SMF result, same as in bottom-right of Fig 7.1 but higher resolution. The resulting null is robust enough to allow for a T/T error of 0.1 λ/D before reaching $1{\times}10^{-8}$.

7.4 Laboratory Setup

The experiments presented here were performed at the High Contrast Spectroscopy Testbed (HCST) (J. R. Delorme et al., 2018). HCST was designed to demonstrate high contrast imaging and spectroscopic technologies for future ground-based and space-based observatories. Its custom-made optics ensure the exquisite wavefront quality required for these kind of experiments; we measured an overall wavefront error of <0.016 waves RMS at 630 nm throughout the system until the field stop plane (Jovanovic, Ruane, et al., 2018). An enclosure consisting of sandwiched honeycomb aluminum panels prevents air turbulence, acoustic vibrations and temperature gradients from interfering with the setup. Furthermore, a floating optical table provides passive vibration isolation. The humidity is controlled inside the enclosure to stay below 30%. All this results in a PSF jitter that remains under 0.02 λ/D RMS.

The optical layout of HCST can be seen in Fig. 7.3. The light source system consists of a supercontinuum white-light laser source (NKT Photonics SuperK EXTREME) connected to a tunable filter (NKT Photonics SuperK VARIA), which we use to select the wavelength and bandpass sent to the instrument. We check the output of the source and tunable filters with an optical sprectrum analyzer (Thorlabs OSA202C) to validate the wavelength coverage. An SMF (Thorlabs SM600) feeds the light into the testbed, and is re-imaged onto a custom-made 4-μm pinhole. A circular polarizer is placed upstream of the pinhole and ensures the correct polarization state needed to conduct wavefront control with the HCST's Vector Vortex Coronagraph (VVC) (Llop-Sayson, Kappel, et al., 2021) is selected. An iris defines the pupil after the first collimating off-axis parabola (OAP). The DM is a Boston Micromachines Corporation kilo-DM; it consists of a continuous surface membrane with 34×34 actuators with an inter-actuator separation of 300 μm. At the focal plane mask we use a VVC; a vortex coronagraph imprints the beam with a phase ramp of the form $e^{\pm il\theta}$, where l is the topological charge of the vortex. For this experiment, we used a charge $l = 8$ mask. At the following pupil plane, a Lyot stop removes the on-axis diffracted light. Our Lyot stop is a laser-cut 15.4 mm diameter aluminum mask that blocks ~84% of the incoming beam diameter. At the focal plane following the Lyot stop, a custom-made field stop from Shimifrez Inc. blocks most of the coronagraphic PSF except the area of interest where either the dark hole or the tip of the SMF was placed.

At the core of the experiments presented in this work is the fiber injection unit (FIU). The FIU allows the positioning of the SMF to do wavefront control, photometric calibration and injection optimization. The light is picked off with a dichroic mirror (Thorlabs BSX11) and sent to the SMF. The SMF is mounted on a three-axis stage consisting of piezo-linear stages (Physik Instrumente Q-545.240) that provide nanometer precision positioning. To measure the output of the SMF we re-image the tip of the fiber onto a camera (Oxford Instruments Andor Neo 5.5), which reads the intensity transmitted through the SMF. The light transmitted through the dichroic is focused onto the same camera with an ~f/50 beam, and used for tracking. The retroreflector is used for calibration purposes when back-feeding light into the testbed through the SMF. We use a filter wheel with a neutral density filter (Thorlabs NE50B, OD=5.0) for photometric calibration.

We measure the jitter and drift of the setup to be 0.02 λ/D RMS, and the PSF drift to vary depending on the time of day and date; typically there is PSF drift of 0.1 λ/D over several hours.

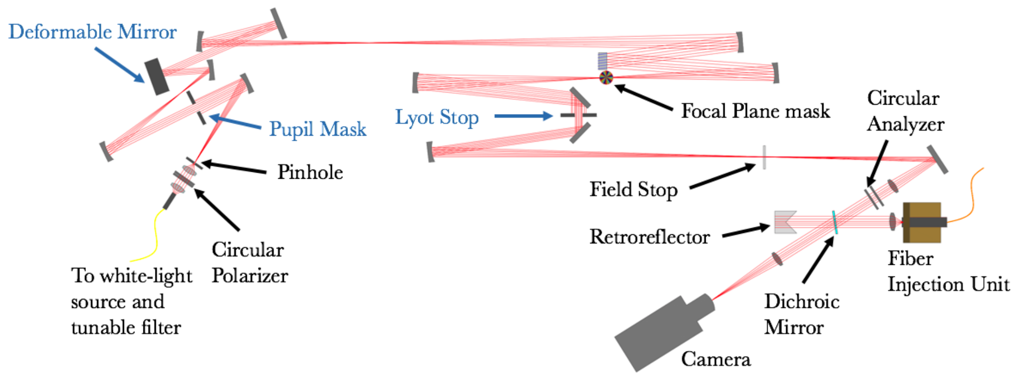

Figure 7.3 Layout of HCST for the single mode fiber experiments. Blue font and arrows indicate conjugated pupil planes.

7.5 Laboratory Results

In this section we present the testbed results of the SMF wavefront control experiments at HCST.

Measure of contrast: the SMF raw contrast

Our measure of contrast is the raw contrast over the SMF, or SMF raw contrast, which is defined as the intensity read at the output of the SMF, with SMF input end centered on the speckle field, divided by the output intensity of the SMF with the SMF centered at the center of the pseudo-stellar PSF with the focal plane mask off center. These two measurements are done with the same optical settings, e.g. Lyot stop position, source brightness, and DM shape. This is the contrast measure directly comparable to the typically used raw contrast, the difference being the added SMF coupling consideration. This measure is the most relevant regarding contrast since it directly drives the SNR of a planet detection. Indeed, the time to achieve a given SNR is $t_{SNR} \propto \eta_s/\eta_p^2$, where η_s, and η_p are the fraction of detected star and planet light, respectively, and these values both depend on the same optical configuration, in particular, the DM shape.

Previous results: monochromatic experiments

In Llop-Sayson, Jovanovic, et al. (2020) we presented the first EFC-SMF results at HCST with monochromatic light, where we achieved SMF raw contrast levels of $1{\times}10^{-8}$ and beyond. The EFC-SMF runs where negatively affected by tip and tilt issues; the fluctuating shape of the contrast vs. iteration curves shown in Fig. 2

of Llop-Sayson, Jovanovic, et al. (2020) were attributed to PSF jitter. Indeed, an SMF in a speckle field is very sensitive to tip and tilt errors (Jovanovic, Schwab, et al., 2017; Hottinger et al., 2018). Moreover, a monochromatic EFC-SMF solution suffers more from tip and tilt errors with respect to multi-wavelength EFC-SMF solutions (see Sec. 7.3).

We made several changes to decrease the jitter and PSF drift in the testbed. For instance, we changed the protocol of operation in HCST for doing EFC experiments to avoid temperature gradients and heat emissions near the beam. Actuators, encoders and any heat source are now carefully shielded and only powered for operation. Paneling within the testbed that was added to screen out stray light was thoroughly analyzed in terms of vibration and its effects on beam disturbance.

20% bandwidth results

The 20% bandwidth EFC-SMF control runs are performed with the multiwavelength version of the EFC-SMF algorithm discussed in Sec. 7.2 using FALCO. We use 7 wavelength channels of ~1-2% bandwidths each that span the whole bandpass, but cover 80% of the total bandpass; in other words, although the lower and upper wavelength do account for a 20% bandwidth stretch, the 7 wavelength sub-bandpasses cover 80% of the whole bandpass. This is done to speed up the control iterations while still controlling most of the bandpass. To evaluate the actual results that we present in this work, we use 11 sub-bandpasses of ~1-2% bandwidths each that cover the whole bandwidth.

Before starting the EFC-SMF run, we dig a DH around the position of the SMF with conventional EFC using the camera. We do the wavefront control over a small aperture of 60° from 5.5 to 9.5 λ/D, which, combined with the use of our field stop that blocks the light outside this zone, removes most of the light from the image plane. This is done given the sensitivity to T/T of an EFC-SMF solution; we find that it is important to dig a DH beforehand around the position of the SMF to ensure there is minimal leakage of light that couples into the fiber. This preliminary EFC is done at 15% bandwidth reaching typically ~6×10^{-8} average raw contrast over the DH.

The SMF is placed at 7.5 λ/D from the center of the PSF. With the initial DH, the starting SMF raw contrast is of ~6×10^{-8}. Then EFC-SMF is implemented and the SMF raw contrast is brought down to $2.5 - 3\times10^{-8}$. Figure 7.4 shows the post-control performance of the EFC-SMF result for the 11 sub-bandpasses that

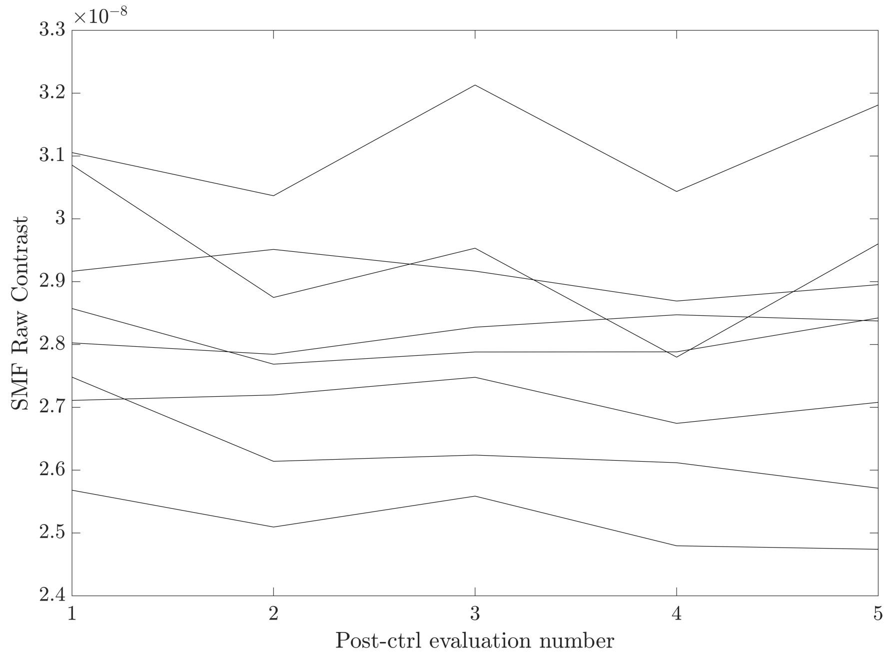

Figure 7.4 We consistently achieve a raw contrast over the SMF of $2.5-3\times10^{-8}$ with 20% bandwidth at 780 nm. We run several independent EFC-SMF runs and evaulate the result 5 times with the corresponding DM solution, each line represents an independent EFC-SMF solution. The DM is maintained at the same configuration for the evaluation.

span the whole 20% bandwidth. We evaluate the SMF raw contrast 5 times with the DM control solution. In Fig. 7.5 we show a camera image of the raw contrast in the image plane after a typical EFC-SMF run. The fact that the raw contrast on the camera pixels is still $\sim10^{-7}$ although the SMF raw contrast through the fiber is $\sim10^{-8}$ illustrates that the SMF is unconcerned with the actual intensity in the image plane as long as the phase distribution yields a null through the fiber. In Fig. 7.6 we show the null degradation through the SMF as a result of leaving the EFC-SMF DM solution stationary; after 4 hours the SMF raw contrast has degraded by a factor of ~2. A small PSF drift and speckle changes due to temperature gradient variations are believed to be the main causes for this deterioration.

Incoherent light limitation

The raw contrast limitation is unmodulated incoherent light that couples into the SMF. We find the same limitation when doing conventional EFC. We hypothesize two possible explanations for this: (1) chromatic leakage through the VVC mask, (2) a DM control limitation regarding the least significant bit (LSB). The first is a known

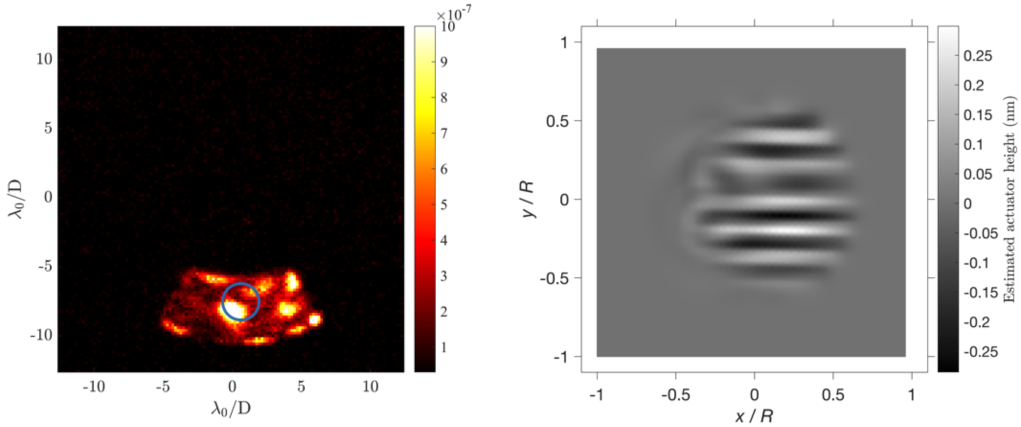

Figure 7.5 *Left:* camera picture of the image plane after performing wavefront control with the EFC-SMF algorithm. Beforehand, we run conventional EFC with the camera pixels to get rid of most of the light in the image plane. Although the raw contrast in the image plane is $\sim 10^{-7}$, the raw contrast through the SMF is actually $\sim 10^{-8}$. The field stop at a focal plane (see Fig. 7.3) blocks most of the coronagraphic PSF except a 60° arc around the SMF position. The blue circle indicates the center of the fiber. *Right:* model of the DM solution. Since we use a linear gain to estimate the height of the DM, and the DM voltage to actuator height is non-linear especially at low voltage, the actual heights in the DM are most likely larger.

effect of the VVC given the way it imprints the vortex ramp through polarization changes (Mawet, Serabyn, et al., 2009; Ruane, Serabyn, et al., 2020). Although there are ways to reduce the chromatic leakage with modifications to the polarization state that enters the testbed (Llop-Sayson, Kappel, et al., 2021), the leakage due to imperfect retardance in the VVC is inherent to the mask fabrication process, so it depends on the fabrication quality. We refer to Ruane, Serabyn, et al. (2020) for a more thorough analysis on this issue. If the polarization leakage in the mask is the main limitation, either a better mask or better polarization management with the circular polarizer and analyzer can solve this problem.

Regarding the DM control limitation, the LSB issue affects the achievable DM shape features. Indeed, certain features that the controller aims at applying to the DM are not possible given that the LSB limits the actuators minimal step. This quantization error results in an incoherent component; for a given set of DM electronics there is an inherent contrast floor (Ruane, Echeverri, et al., 2020). Our 14-bit electronics are estimated to give a raw contrast floor of $\sim 5\times10^{-9}$, however, given the non-linear nature of the DM actuation at low voltage levels, it is possible that this limitation

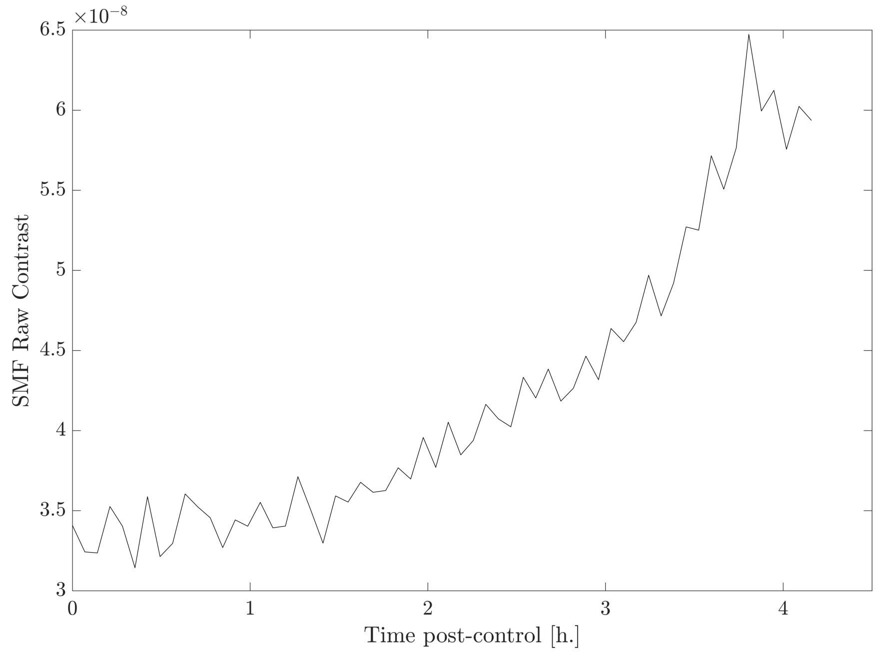

Figure 7.6 Degradation of the raw contrast through the SMF after having performed wavefront control with the EFC-SMF algorithm. The DM is left at the configuration corresponding to the wavefront control solution. PSF drift and changes in the quasi-static speckles over the fiber are thought to be the main factors for this null degradation.

may be emerging at higher contrast levels than expected.

7.6 Perspectives

Doing broadband wavefront control for SMFs is more favorable with respect to conventional camera pixels wavefront control (Coker et al., 2019); the natural next step is to go to larger bandwidths. We intend to demonstrate the same algorithm used in this work to do 30% bandwidth wavefront control. In line with these experiments is the laboratory demonstration of a new concept for multi-object wavefront control using multiple SMFs on the image plane and doing simultaneous wavefront control through all fibers. This will demonstrate the possibility of gathering high contrast spectra from multiple objects with SMFs. We purchased a custom made multi-core SMF to do this experiment as detailed in Coker et al. (2019). Furthermore, to demonstrate the viability of SMF wavefront control for segmented apertures, we will repeat similar experiments using the apodized vortex coronagraph (AVC) concept (Ruane, Jewell, et al., 2016; Jewell et al., 2017) in HCST. This concept deals with light diffraction from telescope discontinuities such as segmentation. We demonstrated raw contrast levels of 10^{-8} at HCST with a prototype AVC mask (Llop-Sayson, Ruane, Mawet, Jovanovic, Coker, et al., 2020). We expect to obtain improved raw contrast through an SMF with a new apodizer prototype.

7.7 Conclusion

We have demonstrated the potential of using single mode fibers for high contrast spectroscopic characterization of exoplanets with broadband light. We have achieved a raw contrast of 2.5×10^{-8} at 20% bandwidth (780 nm) with HCST, an in-air testbed equipped with a vector vortex coronagraph, a high-order DM and a fiber injection unit. This result at such large bandpass, relative to what other laboratory demonstrations typically work with, illustrates the potential of single mode fiber wavefront control. Their mode selectivity, combined with the DM frequencies requirements relaxation, are their biggest advantage with respect to doing high contrast on a camera. We have also analyzed what was been believed to be one of the main limitations with this approach: tip and tilt errors. We have demonstrated via simulations that a broadband solution is less sensitive to tip and tilt aberrations, and have shown in the lab that in an in-air environment the null through the fiber degrades relatively slowly; a factor of ~2 over 4 hours. Continuing to mature this technology is a path to increasing the estimated yield of characterizable Earth-like candidates for mission concepts such as HabEx and LUVOIR.

7.8 Acknowledgments

The material is based upon work supported by NASA SAT under award No. 80NSSC20K0624. Part of this work was carried out at the Jet Propulsion Laboratory, California Institute of Technology, under contract with the National Aeronautics and Space Administration (NASA).

BIBLIOGRAPHY

Brandl, B. et al. (Mar. 2021). "METIS: The Mid-infrared ELT Imager and Spectrograph". In: *The Messenger* 182, pp. 22–26. DOI: 10.18727/0722-6691/5218. arXiv: 2103.11208 [astro-ph.IM].

Carlomagno, B. et al. (July 2020). "METIS high-contrast imaging: design and expected performance". In: *Journal of Astronomical Telescopes, Instruments, and Systems* 6, 035005, p. 035005. DOI: 10.1117/1.JATIS.6.3.035005.

Coker, C. T. et al. (July 2019). "Simulations of a High-Contrast Single-Mode Fiber Coronagraphic Multi-Object Spectrograph for Future Space Telescopes". In: *arXiv e-prints*, arXiv:1907.03921, arXiv:1907.03921. arXiv: 1907.03921 [astro-ph.IM].

Delorme, J. R. et al. (2018). "High-contrast spectroscopy testbed for segmented telescopes". In: *Proc. SPIE* 10400, p. 104000X. DOI: 10.1117/12.2274893.

Delorme, J.-R. et al. (2021). "Keck Planet Imager and Characterizer: a dedicated single-mode fiber injection unit for high-resolution exoplanet spectroscopy". In: *Journal of Astronomical Telescopes, Instruments, and Systems* 7.3, pp. 1–25. DOI: 10.1117/1.JATIS.7.3.035006. URL: https://doi.org/10.1117/1.JATIS.7.3.035006.

Fitzgerald, M. et al. (Sept. 2019). "The Planetary Systems Imager for TMT". In: *Bulletin of the American Astronomical Society*. Vol. 51, p. 251.

Give'on, A. et al. (2007). "Broadband wavefront correction algorithm for high-contrast imaging systems". In: *Astronomical Adaptive Optics Systems and Applications III*. Ed. by R. K. Tyson and M. Lloyd-Hart. Vol. 6691. International Society for Optics and Photonics. SPIE, pp. 63–73. URL: https://doi.org/10.1117/12.733122.

Hottinger, P. et al. (July 2018). "Micro-lens arrays as tip-tilt sensor for single mode fiber coupling". In: *Advances in Optical and Mechanical Technologies for Telescopes and Instrumentation III*. Ed. by R. Navarro and R. Geyl. Vol. 10706. Society of Photo-Optical Instrumentation Engineers (SPIE) Conference Series, p. 1070629. DOI: 10.1117/12.2312015. arXiv: 1808.03190 [astro-ph.IM].

Jewell, J. et al. (2017). "Optimization of coronagraph design for segmented aperture telescopes". In: *Proc. SPIE* 10400, 104000H. DOI: 10.1117/12.2274574. URL: https://doi.org/10.1117/12.2274574.

Jovanovic, N., G. Ruane, et al. (2018). "High-contrast spectroscopy testbed for Segmented Telescopes: instrument overview and development progress". In: *Proc. SPIE* 10702, 107024E. DOI: 10.1117/12.2314325.

Jovanovic, N., C. Schwab, et al. (Aug. 2017). “Efficient injection from large telescopes into single-mode fibres: Enabling the era of ultra-precision astronomy”. In: *Astronomy and Astrophysics* 604, A122, A122. DOI: 10.1051/0004-6361/201630351. arXiv: 1706.08821 [astro-ph.IM].

Llop-Sayson, J., N. Jovanovic, et al. (2020). “Wavefront control experiments with a single mode fiber at the High-Contrast Spectroscopy Testbed for Segmented Telescopes (HCST)”. In: *Space Telescopes and Instrumentation 2020: Optical, Infrared, and Millimeter Wave*. Ed. by M. Lystrup et al. Vol. 11443. International Society for Optics and Photonics. SPIE, pp. 517–523. URL: https://doi.org/10.1117/12.2562973.

Llop-Sayson, J., C. Kappel, et al. (2021). “New method to achieve the proper polarization state for a vector vortex coronagraph”. In: *Techniques and Instrumentation for Detection of Exoplanets X*. Ed. by S. B. Shaklan and G. J. Ruane. Vol. 11823. International Society for Optics and Photonics. SPIE, pp. 230–237. URL: https://doi.org/10.1117/12.2594871.

Llop-Sayson, J., G. Ruane, D. Mawet, N. Jovanovic, B. Calvin, et al. (2019). “Demonstration of an electric field conjugation algorithm for improved starlight rejection through a single mode optical fiber”. In: *Journal of Astronomical Telescopes, Instruments, and Systems* 5.1. DOI: 10.1117/1.JATIS.5.1.019004. URL: https://doi.org/10.1117/1.JATIS.5.1.019004.

Llop-Sayson, J., G. Ruane, D. Mawet, N. Jovanovic, C. T. Coker, et al. (Feb. 2020). “High-contrast Demonstration of an Apodized Vortex Coronagraph”. In: *The Astronomical Journal* 159.3. DOI: 10.3847/1538-3881/ab6329. URL: https://doi.org/10.3847.

Lopez-Morales, M. et al. (May 2019). “Detecting Earth-like Biosignatures on Rocky Exoplanets around Nearby Stars with Ground-based Extremely Large Telescopes”. In: *Bulletin of the AAS* 51.3, 162, p. 162. arXiv: 1903.09523 [astro-ph.EP].

Mawet, D., G. Ruane, et al. (2017). “Observing Exoplanets with High-dispersion Coronagraphy. II. Demonstration of an Active Single-mode Fiber Injection Unit”. In: *Astrophys. J.* 838, p. 92. DOI: 10.3847/1538-4357/aa647f.

Mawet, D., E. Serabyn, et al. (Feb. 2009). “Optical Vectorial Vortex Coronagraphs using Liquid Crystal Polymers: theory, manufacturing and laboratory demonstration”. In: *Opt. Express* 17.3, pp. 1902–1918. DOI: 10.1364/OE.17.001902. URL: http://www.opticsexpress.org/abstract.cfm?URI=oe-17-3-1902.

Riggs, A. J. E. et al. (Aug. 2018). “Fast linearized coronagraph optimizer (FALCO) I: a software toolbox for rapid coronagraphic design and wavefront correction”. In: *Space Telescopes and Instrumentation 2018: Optical, Infrared, and Millimeter Wave*. Vol. 10698. Society of Photo-Optical Instrumentation Engineers (SPIE) Conference Series, p. 106982V. DOI: 10.1117/12.2313812.

Ruane, G., D. Echeverri, et al. (Oct. 2020). "Microelectromechanical deformable mirror development for high-contrast imaging, part 2: the impact of quantization errors on coronagraph image contrast". In: *Journal of Astronomical Telescopes, Instruments, and Systems* 6, 045002, p. 045002. DOI: 10.1117/1.JATIS.6.4.045002. arXiv: 2010.03704 [astro-ph.IM].

Ruane, G., J. Jewell, et al. (July 2016). "Apodized vortex coronagraph designs for segmented aperture telescopes". In: *Proceedings of the SPIE*. Vol. 9912. Society of Photo-Optical Instrumentation Engineers (SPIE) Conference Series, p. 99122L. DOI: 10.1117/12.2231715. arXiv: 1607.06400 [astro-ph.IM].

Ruane, G., E. Serabyn, et al. (Dec. 2020). "Experimental analysis of the achromatic performance of a vector vortex coronagraph". In: *Society of Photo-Optical Instrumentation Engineers (SPIE) Conference Series*. Vol. 11443. Society of Photo-Optical Instrumentation Engineers (SPIE) Conference Series, 114432O. DOI: 10.1117/12.2561593. arXiv: 2012.07728 [astro-ph.IM].

Sandora, M. and J. Silk (June 2020). "Biosignature surveys to exoplanet yields and beyond". In: *Monthly Notices of the RAS* 495.1, pp. 1000–1015. DOI: 10.1093/mnras/staa1284. arXiv: 2005.04005 [astro-ph.EP].

Stark, C. C. et al. (Apr. 2019). "ExoEarth yield landscape for future direct imaging space telescopes". In: *Journal of Astronomical Telescopes, Instruments, and Systems* 5, 024009, p. 024009. DOI: 10.1117/1.JATIS.5.2.024009. arXiv: 1904.11988 [astro-ph.EP].

The HabEx Team (2019). *The HabEx Final Report*. https://www.jpl.nasa.gov/habex/pdf/HabEx-Final-Report-Public-Release-LINKED-0924.pdf.

The LUVOIR Team (2019). *The Large UV Optical Infrared Surveyor (LUVOIR) final report*. https://asd.gsfc.nasa.gov/luvoir/resources/docs/LUVOIR_FinalReport_2019-08-26.pdf.

Wang, J. et al. (2018). "Baseline requirements for detecting biosignatures with the HabEx and LUVOIR mission concepts". In: *J. Astron. Telesc. Instrum. Syst.* 4.3, p. 035001. DOI: 10.1117/1.JATIS.4.3.035001.

Wang, J. J. et al. (July 2021). "Detection and Bulk Properties of the HR 8799 Planets with High Resolution Spectroscopy". In: *arXiv e-prints*, arXiv:2107.06949, arXiv:2107.06949. arXiv: 2107.06949 [astro-ph.EP].

Chapter 8

SUMMARY AND FUTURE OUTLOOK

8.1 Summary

Chapters 2 and 3 dealt with two preeminent nearby systems, the proximity of which makes them ideal targets for direct imaging observations: ϵ Eridani and α Centauri. ϵ Eridani hosts a confirmed companion that has long eluded direct detection. In Chapter 2 a study of this planet is reproduced in which we used the data from three different detection techniques, RV, astrometry and direct imaging, to constrain ϵ Eridani b mass and orbit. Although a non-detection in the direct imaging data, the flux estimations from the coronagraph images sets an upper limit on the mass and age of the planet. New RV data is presented which constrains all but two of the orbital parameters, both of which are available to the astrometry data. We used the intermediate astrometry data from *Hipparcos*, and the *Gaia* data releases DR2 and eDR3. This data helps further constrain the mass and gives a new probability distribution for the inclination. In Chapter 3, the prospects of imaging a companion in the infrared around α Centauri with the JWST were evaluated. The complementarity of JWST observations with RV and astrometry is explored, and, although the sensitivity of this observations is highly dependent on the observatory performance, it is expected that companion sizes of ~0.5 R_{Jup} will be readily detectable.

The rest of the chapters deal with technology development and laboratory demonstrations of high contrast imaging and spectroscopy instrumentation. Chapter 4 presents new coronagraph design tools based on a popular linearized approach for doing wavefront sensing and control (WFSC): the electric field conjugation (EFC) algorithm. We modified the EFC cost function to address the loss of throughput (of planet signal) during the computation of optical surfaces. The tools presented yield a better performance in terms of achievable raw contrast and throughput. Coronagraph design is a complex minimization problem that has been identified as a key technology development pathway for future observatories. Chapter 5 deals with a similar issue: the laboratory demonstration of a coronagraph concept that tackles the problem of diffraction associated with telescope segmentation, the apodized vortex coronagraph (AVC). We demonstrated the viability of an AVC in the laboratory achieving levels of 10^{-8} raw contrast in narrowband and 10% bandwidth light.

In the last two chapters, a novel WFSC algorithm for single mode fibers (SMFs) is introduced and demonstrated. This WFSC concept is developed in the context of using an SMF in the image plane of a coronagraph to enhance the signal-to-noise ratio (SNR) of the planet. The SMF then feeds the planet light into a high resolution spectrograph. Chapter 6 presents the mathematical formalism, which is based on the EFC algorithm and adapted to exploit the complementarity between the coronagraph and the modal selectivity of an SMF. The new algorithm was demonstrated to suppress light through the fiber with a laser source. In Chapter 7 the same algorithm is demonstrated at 20% bandwidth reaching raw contrast levels of 10^{-8}.

8.2 Future outlook

The field of exoplanet science is looking at exciting prospects in the next years. Gaia's currently available data releases have offered a glimpse of the sensitivity this mission will offer. Its final release is projected to allow the detection of 10000s of new exoplanets. As seen in Chapter 2, astrometry is a powerful method capable of constraining mass and all orbit parameters. Gaia is expected to set a major turning point in the field of exoplanet science. Regarding direct imaging, the JWST observatory, set to launch at the end of this year, will offer unprecedented sensitivity in the near- and mid-infrared. The NIRCam and MIRI instruments will be equipped with optimized coronagraphs, and NIRSpec will have an integral field spectrograph (IFS). In Chapter 2 we explored the possibility of imaging ϵ Eridani b with these instruments, NIRSpec being a promising one given that, in the speckle limted case, the spectroscopic capabilities of an IFS offer enhanced speckle rejection. In Chapter 3 a thorough analysis of MIRI capabilities at low separations, <1", was presented, and although the study was done for a possible companion in the α Centauri system, the contrast curves produced are relevant for any system (provided that the contamination from the binary behaves as expected). The performance of JWST, regarding high contrast imaging, will depend on many factors, namely the telescope stability and wavefront error changes due to temperature drifts. Nonetheless, the sensitivity at relatively wider separations will be unmatched. The Roman Space Telescope, with its Coronagraph Instrument (Roman Coronagraph), is expected to launch in 2025. The Roman Coronagraph is conceived as a technology demonstrator to test high contrast imaging and spectroscopy technologies. In particular, it will assess the challenges and limitations of wavefront sensing and control (WFSC) in space; it will be equipped with state of the art coronagraph technology, namely two DMs, and is expected to reach raw contrast levels of 10^{-9} (Kasdin et al., 2020). Although conceived as a technology pathfinder, the Roman Coronagraph is predicted to achieve also amazing science (Bailey et al., 2018). Jupiter-like planets will be not only imaged, but also spectrally analyzed revealing atmosphere and cloud properties.

KPIC at Keck (Delorme et al., 2021), in its upcoming phases, is an exciting prospect regarding the technology discussed in Chapters 6 and 7. KPIC is already producing outstanding science (J. J. Wang et al., 2021). The integration of a high-order DM will allow the implementation of WFSC through an SMF. This will further enhance the planet's SNR and allow for improved high resolution spectroscopy.

A particularly important prospect is the imminent resolution of the Astronomy and Astrophysics Decadal Survey (Astro2020), which will mark the path forward of this field for the next decades. The scientific community highlighted the importance of extremely large telescopes (ELTs) to carry out the challenges in astronomy for the next decades. ELTs will push the sensitivities of ground-based observatories to super-Earths (Dragomir et al., 2019; J. Wang et al., 2019; Carlomagno et al., 2020) and will possibly be able to detect biosignatures in rocky planets (Lopez-Morales et al., 2019). For instance, the MODHIS instrument at the Thirty Meter Telescope (TMT), will be equipped with SMFs that can feed directly imaged planet light into its high resolution spectrograph (Mawet et al., 2019). The work presented in Chapters 6 and 7 could help maximize the efficiency of next generation fiber-fed spectrographs.

A particularly important resolution of Astro2020 will be the recommendation on the next great space observatory. NASA presented mission concepts HabEx (The HabEx Team, 2019) and LUVOIR (The LUVOIR Team, 2019) both of which include an important exoplanet science program. The work presented in this thesis is directly relevant to these concepts, in particular the last four chapters. The direction of research efforts in the future will greatly depend on the recommendations from Astro2020.

BIBLIOGRAPHY

Bailey, V. P. et al. (Dec. 2018). "Potential exoplanetary system science with the Wide Field Infrared Survey Telescope Coronagraph Instrument". In: *AGU Fall Meeting Abstracts*. Vol. 2018, P51B–01.

Carlomagno, B. et al. (July 2020). "METIS high-contrast imaging: design and expected performance". In: *Journal of Astronomical Telescopes, Instruments, and Systems* 6, 035005, p. 035005. DOI: 10.1117/1.JATIS.6.3.035005.

Delorme, J.-R. et al. (2021). "Keck Planet Imager and Characterizer: a dedicated single-mode fiber injection unit for high-resolution exoplanet spectroscopy". In: *Journal of Astronomical Telescopes, Instruments, and Systems* 7.3, pp. 1–25. DOI: 10.1117/1.JATIS.7.3.035006. URL: https://doi.org/10.1117/1.JATIS.7.3.035006.

Dragomir, D. et al. (May 2019). "Characterizing the Atmospheres of Irradiated Exoplanets at High Spectral Resolution". In: *Bulletin of the AAS* 51.3, 422, p. 422. arXiv: 1903.09173 [astro-ph.EP].

Kasdin, N. J. et al. (2020). "The Nancy Grace Roman Space Telescope Coronagraph Instrument (CGI) technology demonstration". In: *Space Telescopes and Instrumentation 2020: Optical, Infrared, and Millimeter Wave*. Ed. by M. Lystrup et al. Vol. 11443. International Society for Optics and Photonics. SPIE, pp. 300–313. URL: https://doi.org/10.1117/12.2562997.

Lopez-Morales, M. et al. (May 2019). "Detecting Earth-like Biosignatures on Rocky Exoplanets around Nearby Stars with Ground-based Extremely Large Telescopes". In: *Bulletin of the AAS* 51.3, 162, p. 162. arXiv: 1903.09523 [astro-ph.EP].

Mawet, D. et al. (Sept. 2019). "High-resolution Infrared Spectrograph for Exoplanet Characterization with the Keck and Thirty Meter Telescopes". In: *Bulletin of the American Astronomical Society*. Vol. 51, p. 134. arXiv: 1908.03623 [astro-ph.IM].

The HabEx Team (2019). *The HabEx Final Report*. https://www.jpl.nasa.gov/habex/pdf/HabEx-Final-Report-Public-Release-LINKED-0924.pdf.

The LUVOIR Team (2019). *The Large UV Optical Infrared Surveyor (LUVOIR) final report*. https://asd.gsfc.nasa.gov/luvoir/resources/docs/LUVOIR_FinalReport_2019-08-26.pdf.

Wang, J. J. et al. (July 2021). "Detection and Bulk Properties of the HR 8799 Planets with High Resolution Spectroscopy". In: *arXiv e-prints*, arXiv:2107.06949, arXiv:2107.06949. arXiv: 2107.06949 [astro-ph.EP].

Wang, J. et al. (May 31, 2019). "New Frontiers for Terrestrial-sized to Neptune-sized Exoplanets In the Era of Extremely Large Telescopes". In: *Bulletin of the AAS* 51.3. https://baas.aas.org/pub/2020n3i200. URL: https://baas.aas.org/pub/2020n3i200.